

**Application of 3D Marine Controlled-Source  
Electromagnetic Finite-Element Forward Modelling to  
Hydrocarbon Exploration in the Flemish Pass Basin  
Offshore Newfoundland and Labrador, Canada**

by

© Michael W. Dunham

A thesis submitted to the School of Graduate Studies in partial fulfillment of the  
requirements for the degree of

**Master of Science**

**Department of Earth Sciences**

Memorial University of Newfoundland

**May 2017**

St. John's, Newfoundland and Labrador

# Abstract

The Flemish Pass Basin located 450 km east offshore St. John's, Newfoundland, Canada has seen an increase in exploration activity over the past decade. Risk mitigation is important for deepwater drilling, and marine CSEM interpretation techniques have the potential help de-risk reservoirs in an offshore exploration setting. This thesis uses 3D marine CSEM finite-element forward modeling with comparisons to measured data to (1) show the finite-element forward modeling code can synthesize data from real complex models built using unstructured grids, and (2) use this forward modeling technique to provide additional support and interpretations for two offshore exploration fields in the Flemish Pass Basin: Mizzen and Bay du Nord.

In summary, the finite-element forward modeling code was able to synthesize good quality results from complex models built from real data. Sensitivity to the Mizzen reservoir was found, but it is likely below the detectability threshold. This is likely a result of the reservoir being too small and containing uneconomic volumes of hydrocarbons. However, the Bay du Nord reservoir is much larger and is predicted to contain much higher volumes of hydrocarbons. Numerical analysis confirmed a much greater sensitivity to the Bay du Nord reservoir exists.

# Acknowledgements

I am forever indebted to my high school calculus and physics teachers, Anne Swanson and Linda Flohr, who instilled my passion for mathematics and physics. My post-secondary education was made possible by Mrs. Swanson because she believed in my ability to succeed, when others did not. My first choice undergraduate university, Colorado School of Mines, initially deemed me unfit for admittance based on low standardized test scores. The potential and ability of a human being to achieve great things go far beyond a single number, and I think Mrs. Swanson recognized this. She contacted the university, and two weeks later I received an acceptance letter, which still remains in a frame to this day. Mrs. Swanson was truly someone who cared about her students, and I am forever thankful for the opportunities she made possible for me.

I would like to thank Dr. Yaoguo Li, my undergraduate research supervisor who inspired my curiosity for electromagnetic methods and helped me develop essential research skills. When I began my undergraduate research project, I struggled severely with performing many components of my research, but Dr. Li was very helpful by pointing me in the right direction and helped me build the necessary research skills for graduate school.

The accomplishments of this thesis were made possible through the contributions and support from many companies and individuals. I am especially grateful for the

internship opportunity provided by Nalcor Energy – Oil and Gas mid-way through my thesis. This internship provided me with the data and tools necessary to build *real* models which are what made the results of this thesis quite powerful. Deric Cameron and Ian Atkinson deserve personal recognition as they were both very helpful with this project. I would also like to thank everyone on the exploration team at Nalcor for their collaboration and assistance with software.

Electromagnetic Geoservices (EMGS) also had a significant contribution to this thesis. I am ever so thankful for EMGS allowing me to use their marine CSEM data from the Flemish Pass Basin as a comparison tool. Without this data, I would not have been able to establish the resistivities of my real models or interpret my final forward modeling results from a practical perspective. I would like to specifically recognize Svein Ellingsrud for his input and personal communication regarding the results of my thesis. Also, I am thankful for Bjørn Petter Lindom for ultimately permitting the inclusion of their marine CSEM data in my thesis.

TGS-NOPEC Geophysical Company and Petroleum Geo-Services (PGS) had important contributions to this thesis as well. 2D seismic data from the Flemish Pass was used to help build the reservoir bodies for my models, and I am grateful for TGS and PGS permitting me to use this data in my thesis.

Members of the Memorial University of Newfoundland Earth Sciences Department have been very helpful and are important contributors to this thesis. I am deeply grateful to Dr. SeyedMasoud Ansari for being able to use his finite-element code for

my thesis. Dr. Ansari's code made this project possible, and I deeply appreciate all his collaboration and the changes he made to this code to accommodate my needs. I would also like to thank Peter Lelièvre for his model building software which greatly simplified the process of building complex models. Dr. Lelièvre was very helpful and he also made changes to his software to accommodate my needs for which I am deeply thankful for.

My final acknowledgement goes to my supervisor, Dr. Colin G. Farquharson. The relationship between student and supervisor is an important one and communication, to me, is the most important factor. Colin was prompt and always made an effort regarding communication, and I valued this greatly. His knowledge and expertise were essential through the progression of this project, but his enthusiasm, quirkiness, and personable nature are the qualities that truly make him unique. How this man manages to have enough time to mentor nearly a dozen graduate students, write grant proposals, and teach courses while still reserving time to help raise his family, is truly remarkable. Colin is certainly a rare individual and I could not have had a better supervisor to mentor this project.

# Table of Contents

Abstract.....	ii
Acknowledgements.....	iii
List of Tables.....	xi
List of Figures.....	xii
Chapter 1 Introduction.....	1
1.1 Motivation.....	1
1.2 Historical Development of Marine CSEM.....	3
1.3 Thesis focus .....	6
1.4 Outline.....	8
Chapter 2 Methods.....	11
2.1 The Marine CSEM Method.....	11
2.1.1 The Physics of Electromagnetics.....	11
2.1.2 Marine CSEM Acquisition .....	14
2.1.3 Data Processing .....	17
2.1.4 Conceptual Explanations of the CSEM response .....	19
2.1.5 Electrical Anisotropy .....	21
2.1.6 The Receiver Response.....	23
2.1.6.1 Near offsets .....	24
2.1.6.2 Mid offsets .....	24
2.1.6.3 Far offsets .....	25
2.1.7 Limitations.....	28
2.2 Forward Modeling Techniques .....	29
2.2.1 Integral Equation Method.....	30

2.2.2	Finite Difference Method .....	31
2.2.3	Finite Element Method .....	34
2.2.4	3D Forward Modeling in the Context of Marine CSEM .....	38
2.2.5	CSEM3DFWD .....	40
2.2.5.1	Computational requirements .....	42
Chapter 3	Model Building and Forward Modeling .....	44
3.1	The Five-Step Forward Modeling Process .....	46
3.1.1	Step I: Gathering Information.....	47
3.1.2	Step II: Building the Model.....	49
3.1.3	Step III: Generating the Unstructured Mesh .....	52
3.1.4	Step IV: Visualization .....	55
3.1.5	Step V: Data Simulation.....	56
Chapter 4	Synthetic Forward Models.....	59
4.1	Marine Halfspace Model.....	59
4.1.1	Test I .....	60
4.1.2	Test II .....	61
4.1.3	Test III.....	64
4.1.4	Test IV.....	66
4.1.5	Remarks .....	68
4.2	Marine Layered Earth Reservoir Model.....	70
4.2.1	In-line halfspace .....	71
4.2.2	Broadside halfspace.....	74
4.2.3	In-line reservoir .....	75
4.2.4	Broadside reservoir.....	78
4.2.5	Remarks .....	80
Chapter 5	The Mizzen Study in the Flemish Pass Basin.....	83

5.1	Geology of the Mizzen field.....	83
5.2	Motivation.....	86
5.3	Preliminary 1D modeling .....	90
5.4	3D Model Building at Mizzen .....	95
5.4.1	Seafloor model.....	97
5.4.2	Base Tertiary model.....	103
5.4.3	Base Cretaceous model.....	107
5.4.3.1	Attempt I.....	107
5.4.3.2	Attempt II .....	112
5.4.4	Base Jurassic (basement) model.....	116
5.5	Observation Location Refinement .....	120
5.5.1	Transmitter parameters .....	120
5.5.2	Electromagnetic reciprocity.....	121
5.5.3	Seafloor model simulation I.....	123
5.5.4	Seafloor model simulation II .....	124
5.5.5	Seafloor model simulation III .....	128
5.5.6	Seafloor model simulation IV .....	132
5.6	The Mizzen Reservoir.....	133
5.6.1	Verification of hydrocarbon volumes.....	140
5.7	Preliminary Numerical Results .....	143
5.8	Modifying Resistivities .....	153
5.8.1	Updated 1D sensitivities .....	163
5.9	Final Results .....	166
5.9.1	Results for RX41.....	166
5.9.2	Sensitivity summaries .....	172
5.10	Mizzen Conclusions .....	175

5.10.1	Assumptions.....	178
Chapter 6	The Bay du Nord Study in the Flemish Pass Basin .....	182
6.1	Bay du Nord.....	183
6.1.1	Motivation .....	190
6.2	Preliminary 1D modeling .....	191
6.3	3D Model Building at Bay du Nord.....	194
6.3.1	Establishing the VOI .....	194
6.3.2	Geochronologic surfaces .....	195
6.3.3	Incremental mesh generation .....	201
6.4	Building the Bay du Nord Reservoir Model.....	206
6.4.1	Creating the Bay du Nord surfaces.....	206
6.4.2	Assembling the Bay du Nord reservoir within FacetModeller.....	210
6.4.3	Bay du Nord reservoir mesh .....	217
6.5	Debugging the Bay du Nord Reservoir mesh.....	222
6.5.1	Test I: Translation to the mid-Jurassic.....	222
6.5.2	Test II: Mid-Jurassic and reservoir constraint .....	225
6.5.3	Test III: No attachment with reservoir constraint .....	227
6.5.4	Test IV: Attached with reservoir constraint .....	228
6.5.5	Summation and verdict.....	232
6.6	Verification of Hydrocarbon Volumes .....	233
6.7	Establishing Resistivities at RX15 .....	237
6.7.1	Simulations with longitudinal resistivities.....	237
6.7.2	Recovery of vertical resistivities.....	242
6.7.3	Updated 1D sensitivities .....	246
6.8	Final results.....	249
6.8.1	Results for RX15.....	249

6.8.2	Results for RX59.....	252
6.8.3	Sensitivity summaries .....	256
6.9	Bay du Nord Conclusions.....	264
6.9.1	Assumptions.....	268
Chapter 7	Conclusions.....	270
7.1	Modeling conclusions.....	270
7.2	Improvements and considerations .....	272
References	.....	274
Appendix A	Triangle.....	284
Appendix B	TetGen.....	287
Appendix C	Refinement at Observation Locations .....	289
Appendix D	Results of Mizzen Study.....	290
RX42	.....	291
RX43	.....	294
RX44	.....	297
RX45	.....	299

# List of Tables

Table 5-1: Mesh statistics for the five Mizzen models at RX44.....	146
Table 6-1: Mesh statistics for the four Bay du Nord background models .....	203
Table 6-2: A summary of all five simulation tests performed on variants of the Bay du Nord reservoir model .....	232
Table 6-3: The start, step, and end values for four parameters needed to calculate the OOIP and recoverable oil for the Bay du Nord reservoir .....	235
Table 6-4: A summary of the strongest sensitivities at both offset ranges and at the three frequencies considered for the Mizzen and Bay du Nord reservoirs .....	267

# List of Figures

Figure 1.1: Seismic P-wave velocity and electrical resistivity of a porous (50%) sandstone as a function of gas saturation in the pore fluid .....	2
Figure 1.2: A map showing basins located offshore Newfoundland .....	7
Figure 2.1: The marine CSEM concept.....	14
Figure 2.2: The horizontal electric dipole (HED) geometry.....	15
Figure 2.3: A typical marine CSEM multicomponent receiver .....	16
Figure 2.4: The three mechanisms which influence electromagnetic signals.....	20
Figure 2.5: A 1D layered earth example which shows that vertical and horizontal fields treat the layers as resistors in series and parallel respectively .....	22
Figure 2.6: The amplitude and phase from the 1D canonical disk model.....	24
Figure 2.7: The marine CSEM airwave.....	26
Figure 2.8: The staggered grid for the finite-difference (FD) method .....	31
Figure 2.9: The common non-uniform rectilinear grid used for 3D FD solutions...	32
Figure 2.10: Differences between structured and unstructured meshes .....	35
Figure 2.11: A hexahedral cell illustrating nodal-element basis functions.....	36
Figure 2.12: A hexahedral cell illustrating edge-element basis functions.....	37
Figure 2.13: Computational requirements of CSEM3DFWD .....	43
Figure 3.1: An example of a marine CSEM complex synthetic model.....	45
Figure 3.2: The five-step forward modeling process used throughout the thesis ....	46
Figure 3.3: Example topography of the seafloor in of the Flemish Pass Basin.....	48

Figure 3.4: The seafloor surface from Figure 3.3 imported into a 3D FacetModeller session with boundary facets included .....	51
Figure 3.5: The TetGen command line statistics of the mesh created from the input model shown in Figure 3.4 .....	54
Figure 3.6: The unstructured mesh from the model in Figure 3.4.....	56
Figure 3.7: The residual norm and the in-line electric field amplitude for the mesh shown in Figure 3.6.....	58
Figure 4.1: The mesh from halfspace Test I. The mesh contains 27,985 cells .....	61
Figure 4.2: The Test I halfspace mesh slice, electric field amplitude, phase, and the calculated residuals for the amplitude and phase .....	62
Figure 4.3: The Test II halfspace mesh slice, electric field amplitude, phase, and the calculated residuals for the amplitude and phase .....	63
Figure 4.4: The Test III halfspace mesh slice, electric field amplitude, phase, and the calculated residuals for the amplitude and phase. ....	65
Figure 4.5: The Test IV halfspace mesh slice, electric field amplitude, phase, and the calculated residuals for the amplitude and phase .....	67
Figure 4.6: The convergence curves for each of the halfspace tests .....	69
Figure 4.7: The 1D representation of the marine layered earth reservoir.....	71
Figure 4.8: Various 2D slices of the halfspace mesh (with air) at $y = 0$ km .....	73
Figure 4.9: The computed amplitude and phase from the halfspace model (with air) using an in-line transmitter orientation .....	74
Figure 4.10: The computed amplitude and phase from the halfspace model (with air) using a broadside transmitter orientation .....	75
Figure 4.11: The dimensions of the reservoir slab (14 km x 10 km) and its superposition on the meshed seafloor surface for the in-line reservoir model .....	76
Figure 4.12: Views of the in-line reservoir mesh .....	77
Figure 4.13: The computed amplitude and phase from the reservoir model using an in-line transmitter orientation.....	77

Figure 4.14: The dimensions of the reservoir slab (14 km x 14 km) and its superposition on the meshed seafloor surface for the broadside reservoir model....	79
Figure 4.15: The computed amplitude and phase results from the reservoir model using a broadside transmitter orientation.....	79
Figure 4.16: A summary of all responses for the halfspace and reservoir models ...	81
Figure 5.1: A seafloor map of offshore Newfoundland indicating the location of the Flemish Pass Basin and the seismic/CSEM data surrounding Mizzen L-11 .....	84
Figure 5.2: The lithostratigraphic geology of the Flemish Pass Basin.....	85
Figure 5.3: The Mizzen L-11 well log.....	87
Figure 5.4: The four different amplitude-versus-offset (AVO) classes.....	88
Figure 5.5: The near and far angle seismic data stacks from the seismic line that passes over Mizzen L-11.....	89
Figure 5.6: The 1D resistivity model from blocking the L-11 resistivity log .....	91
Figure 5.7: 1D in-line amplitudes and sensitivities from the 1D model in Figure 5.6 for four different frequencies .....	93
Figure 5.8: A map of the seafloor surface surrounding Mizzen L-11 .....	97
Figure 5.9: Statistics of the seafloor mesh without edge-length constraints .....	99
Figure 5.10: A 3D view of the seafloor mesh without edge-length constraints.....	99
Figure 5.11: A 2D slice of the seafloor mesh (without edge-length constraints) zoomed in to show the pulses of nodes created on the seafloor surface. ....	100
Figure 5.12: A 2D slice of the seafloor mesh with 500m edge-length constraints imposed on the seafloor nodes.....	100
Figure 5.13: Statistics of the seafloor mesh with 500m edge-length constraints .....	100
Figure 5.14: Residual norm for the seafloor model with the 500m edge-length constraint imposed on the seafloor surface nodes .....	102
Figure 5.15: A map of the base Tertiary surface surrounding Mizzen L-11 .....	103
Figure 5.16: Statistics of the base Tertiary mesh with 500m edge-length constraints imposed on the seafloor and base Tertiary surface nodes.....	104

Figure 5.17: A 3D view of the base Tertiary mesh .....	105
Figure 5.18: Residual norm for the base Tertiary model .....	106
Figure 5.19: A map of the base Cretaceous surface surrounding Mizzen L-11 .....	108
Figure 5.20: Statistics of the base Cretaceous mesh (attempt I) with variable edge-length constraints imposed.....	109
Figure 5.21: A 3D view of the base Cretaceous mesh (attempt I).....	109
Figure 5.22: A thickness map of the Cretaceous surrounding Mizzen L-11.....	110
Figure 5.23: A 2D slice of the base Cretaceous mesh (attempt I) .....	111
Figure 5.24: Residual norm for the base Cretaceous model (attempt I).....	112
Figure 5.25: 3D view of the base Cretaceous surface after meshing (attempt II)..	113
Figure 5.26: A 2D slice of the base Cretaceous mesh (attempt II).....	114
Figure 5.27: Residual norm for the base Cretaceous model (attempt II) .....	115
Figure 5.28: A map of the base Jurassic surface surrounding Mizzen L-11 .....	117
Figure 5.29: Statistics of the base Jurassic mesh with 500m edge-length constraints imposed on the nodes for all three surfaces. ....	118
Figure 5.30: A 3D view of the base Jurassic mesh.....	119
Figure 5.31: Residual norm for the base Jurassic model.....	119
Figure 5.32: Reciprocity of marine CSEM acquisition .....	122
Figure 5.33: The in-line amplitude for seafloor model simulation I using the real transmitter and receiver locations surrounding RX42 .....	124
Figure 5.34: A segment of the connected chain of nodes required for enclosing the receiver locations surrounding RX42 in regular tetrahedra .....	125
Figure 5.35: Plan view images of the seafloor mesh with the edge-length constraints imposed on all seafloor nodes.....	127
Figure 5.36: Plan view images of the seafloor mesh with the edge-length constraints removed from seafloor nodes surrounding the observation locations.....	127
Figure 5.37: The in-line amplitude for seafloor model simulation II using regular tetrahedra to enclose all 2401 observation locations surrounding RX42 .....	128

Figure 5.38: The deviation of the observation locations from a line connecting the start and end points .....	130
Figure 5.39: The in-line amplitude for seafloor model simulation III using observations at 200m spacing and refinement tetrahedra with 10m edge lengths ..	131
Figure 5.40: The in-line amplitude for seafloor model simulation IV using observations at 200m spacing and refinement tetrahedra with 5m edge lengths...	132
Figure 5.41: Cross-section of the dipping slab representations of the Mizzen reservoirs superimposed on far angle stack .....	134
Figure 5.42: The nodes used to create the three Mizzen sands.....	137
Figure 5.43: The entire mesh including the three Mizzen slabs and observation location refinement around RX44 .....	138
Figure 5.44: Two perspective views of the Mizzen slabs along the EMGS transmitter line (shown in Figure 5.1) .....	138
Figure 5.45: A zoomed-out 2D slice along the EMGS transmitter line .....	139
Figure 5.46: A 2D slice of the mesh along the seismic line .....	140
Figure 5.47: 2D slices of five different Mizzen models with incremental changes..	144
Figure 5.48: The starting resistivities derived from the Mizzen L-11 well log.....	146
Figure 5.49: Residual norm for the five models at RX44 and $f = 0.50$ Hz. ....	147
Figure 5.50: The preliminary in-line electric field amplitudes for the five models at RX44 for $f = 0.50$ Hz. The measured mCSEM data is shown for comparison .....	149
Figure 5.51: The same image from Figure 5.50, but zoomed in to show detail. ....	149
Figure 5.52: The sensitivity of the Mizzen hydrocarbons at RX44 for $f = 0.50$ Hz. The noise level from the measured mCSEM data is shown for comparison .....	151
Figure 5.53: The preliminary phase for each of the five models at RX44 for $f = 0.50$ Hz. The measured mCSEM data is shown for comparison. ....	152
Figure 5.54: The amplitude and phase responses for varying the value of the Tertiary region in the seafloor model at RX44 for $f = 0.50$ Hz .....	154
Figure 5.55: The amplitude and phase responses for varying the value of the Cretaceous/Jurassic region in the tertiary model at RX44 for $f = 0.50$ Hz .....	157

Figure 5.56: The amplitude and phase responses for varying the value of the basement region in the basement model at RX44 for $f = 0.50$ Hz .....	159
Figure 5.57: The computed responses for each of the five models, and the reservoir sensitivity at RX44 for $f = 0.50$ Hz using the final resistivities .....	162
Figure 5.58: 1D models of the horizontal resistivities derived from the L-11 well log and the vertical resistivities determined through incremental simulation .....	164
Figure 5.59: The 1D sensitivities to the Mizzen hydrocarbon bearing slabs for the horizontal and vertical resistivities and also for three different frequencies. ....	165
Figure 5.60: The final in-line amplitude for each of the five models, and the sensitivity to the Mizzen hydrocarbons at RX41 for $f = 0.50$ Hz.....	167
Figure 5.61: The final in-line amplitude and phase for three of the models, and the sensitivity to the Mizzen hydrocarbons at RX41 for $f = 0.25$ Hz.....	169
Figure 5.62: The final in-line amplitude and phase for two of the models, and the sensitivity to the Mizzen hydrocarbons at RX41 for $f = 1.00$ Hz.....	170
Figure 5.63: The sensitivity summaries to the Mizzen slab hydrocarbons, and the measured noise levels at all five receivers for $f = 0.25, 0.50,$ and $1.00$ Hz.....	173
Figure 6.1: A map of the data surrounding Bay du Nord C-78.....	184
Figure 6.2: The Bay du Nord C-78 well log.....	185
Figure 6.3: The near and far angle stacks for seismic line #1 in Figure 6.1 .....	187
Figure 6.4: The near and far angle stacks for seismic line #2 in Figure 6.1 .....	188
Figure 6.5: The near and far angle stacks for seismic line #3 in Figure 6.1 .....	189
Figure 6.6: The 1D resistivity model from blocking the C-78 resistivity log.....	192
Figure 6.7: The sensitivities from the model in Figure 6.6 at three frequencies....	192
Figure 6.8: A map of the seafloor surface surrounding Bay du Nord .....	197
Figure 6.9: A map of the base Tertiary surface surrounding Bay du Nord.....	198
Figure 6.10: A map of the base Cretaceous surface surrounding Bay du Nord .....	199
Figure 6.11: A map of the base Jurassic surface surrounding Bay du Nord.....	200
Figure 6.12: A 3D mesh of the base Jurassic model along transmitter line #09...	204

Figure 6.13: Residual norm for four different meshes incrementally containing one (seafloor model) to four (base Jurassic model) surfaces.....	204
Figure 6.14: Depth slices of the in-line mCSEM inversion from EMGS.....	208
Figure 6.15: The top-of-sand surface for the Bay du Nord reservoir .....	209
Figure 6.16: The top and base-of-sand reservoir surfaces within FacetModeller ...	211
Figure 6.17: The original base Cretaceous surface, and the base Cretaceous surface with refinement modifications needed to the attach the two reservoir surfaces ....	213
Figure 6.18: The facets used to connect the two reservoir surfaces to the base Cretaceous in the region circled in <i>green</i> from Figure 6.16 .....	215
Figure 6.19: The facets used to connect the two reservoir surfaces to the base Cretaceous in the region circled in <i>yellow</i> from Figure 6.16 .....	215
Figure 6.20: A view of the Bay du Nord reservoir within FacetModeller.....	216
Figure 6.21: A view of the modified base Cretaceous surface after meshing .....	218
Figure 6.22: The entire 3D Bay du Nord reservoir mesh.....	220
Figure 6.23: A 2D slice of the Bay du Nord reservoir mesh along the CSEM transmitter #9 and the observation locations trend northeast from RX15.....	220
Figure 6.24: Residual norm of the Bay du Nord reservoir mesh.....	221
Figure 6.25: A 2D slice of the <i>mid-Jurassic</i> Bay du Nord reservoir mesh along CSEM transmitter #9.....	224
Figure 6.26: Residual norm of the <i>mid-Jurassic</i> Bay du Nord mesh .....	224
Figure 6.27: A 2D slice of the <i>constrained mid-Jurassic</i> Bay du Nord reservoir mesh along CSEM transmitter #9.....	226
Figure 6.28: Residual norm of the <i>constrained mid-Jurassic</i> Bay du Nord mesh..	226
Figure 6.29: A 2D slice of the <i>shallow constrained</i> Bay du Nord reservoir mesh along CSEM transmitter #9.....	229
Figure 6.30: Residual norm of the <i>shallow constrained</i> Bay du Nord mesh .....	229
Figure 6.31: A 2D slice of the <i>attached and constrained</i> Bay du Nord reservoir mesh along CSEM transmitter #9.....	231
Figure 6.32: Residual norm of the <i>attached and constrained</i> Bay du Nord mesh..	231

Figure 6.33: A histogram of recoverable oil calculations for the Bay du Nord reservoir body in the model .....	236
Figure 6.34: 2D slices along $x = 25.0$ km for five different Bay du Nord models with incremental changes between each model.....	238
Figure 6.35: The preliminary in-line amplitude and phase responses from the five meshes, and the Bay du Nord sensitivity at RX15 for $f = 0.50$ Hz.....	240
Figure 6.36: The in-line amplitude and phase responses for varying the value of the basement region in the base Jurassic mesh at RX15 for $f = 0.50$ Hz.....	243
Figure 6.37: The final in-line amplitude and phase responses from the five meshes, and the Bay du Nord sensitivity at RX15 for $f = 0.50$ Hz .....	245
Figure 6.38: 1D models of the horizontal resistivities derived from the C-78 well log and the vertical resistivities determined through incremental simulation .....	247
Figure 6.39: The 1D sensitivities of the Bay du Nord reservoir for the horizontal and vertical resistivities and also for three different frequencies. ....	248
Figure 6.40: The final in-line amplitude and phase responses from the five meshes, and the Bay du Nord sensitivity at RX15 for $f = 0.25$ Hz .....	250
Figure 6.41: The final in-line amplitude and phase responses from the five meshes, and the Bay du Nord sensitivity at RX15 for $f = 1.00$ Hz .....	251
Figure 6.42: The final in-line amplitude and phase responses from the background and reservoir meshes, and the Bay du Nord sensitivity at RX59 for $f = 0.25$ Hz.	253
Figure 6.43: The final in-line amplitude and phase responses from the background and reservoir meshes, and the Bay du Nord sensitivity at RX59 for $f = 0.50$ Hz.	254
Figure 6.44: The final in-line amplitude and phase responses from the background and reservoir meshes, and the Bay du Nord sensitivity at RX59 for $f = 1.00$ Hz.	255
Figure 6.45: The sensitivity summaries for the Bay du Nord reservoir and the measured noise levels at six of the twenty receivers for the three frequencies .....	258
Figure 6.46: The mid-offset and far-offset sensitivity maps for $f = 0.25$ Hz.....	261
Figure 6.47: The mid-offset and far-offset sensitivity maps for $f = 0.50$ Hz.....	262
Figure 6.48: The mid-offset and far-offset sensitivity maps for $f = 1.00$ Hz.....	263

# Chapter 1

## Introduction

### 1.1 Motivation

The geophysical tool primarily used for the exploration of marine hydrocarbon reservoirs is the seismic reflection method. Seismic reflection provides the highest resolution of subsurface structure when compared to other methods, but like any geophysical method, it has its deficiencies. In particular, seismic reflection analysis techniques are limited in their ability to distinguish between hydrocarbon and gas-charged brine reservoirs (Wright et al., 2002). As Figure 1.1 shows, small fractions of gas in pore fluid, i.e. fizz gas, can cause significant changes to seismic velocity resulting in a false hydrocarbon indicator (Lee, 2004). Therefore, a reservoir that is largely brine with small fractions of gas can have a strong seismic reflection. Such reservoirs, however, will be electrically conductive overall, in contrast to when they are hydrocarbon saturated. This is a motivation for the use of electromagnetic methods in marine hydrocarbon exploration.

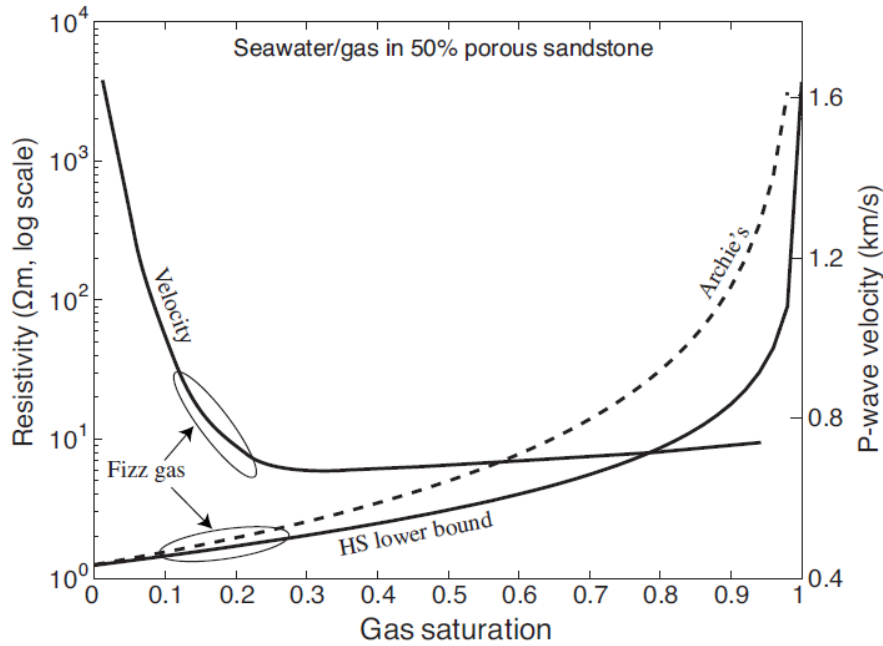


Figure 1.1: Seismic P-wave velocity (from Lee, 2004) and electrical resistivity of a porous (50%) sandstone as a function of gas saturation in the pore fluid. Hashin-Shtrikman (HS) and Archie's law are used for determining the resistivity of gas bubbles in water (image from Constable, 2010).

Measurements of electrical resistivity have historically been obtained through wire-line logging of wells, and have played a crucial role in hydrocarbon exploration (Eidesmo et al., 2002). If a reservoir is hydrocarbon saturated it typically is a few orders of magnitude more electrically resistive than brine reservoirs and surrounding shales. Resistivity logs provide excellent vertical resolution, but the lateral sampling density is limited due to obvious cost reasons. As hydrocarbon exploration moves more towards deepwater environments, the economic challenges associated with drilling will continue to increase (Constable and Srnka, 2007). Therefore, collecting any additional data will be beneficial if it has the potential to de-risk a given prospect. A practical supplemental method is marine controlled-source electromagnetics (CSEM).

## 1.2 Historical Development of Marine CSEM

The histories of marine controlled-source electromagnetics (CSEM) and marine magnetotellurics (MT) are intimately linked because both techniques image resistivity and rely on the measurement of electric and magnetic fields (Constable, 2010). The marine MT method was first introduced for prospecting in a seminal paper by Cagniard (1953), however, the difficulty associated with taking measurements on the seafloor meant that the theory predated practice for marine applications. In the following decade, Charles Cox and Jean Filloux of Scripps Institution of Oceanography developed the first equipment suitable for deep seafloor MT soundings (Constable, 2010). In 1961, they deployed both electric and magnetic field sensors in 1000-2000m water offshore California and in 1965 they also deployed similar instruments in 4000m water (Filloux, 1967b). The fields measured in the 1965 experiment were referenced to land magnetic measurements and a seafloor MT response was produced.

The MT method was developed as an academic tool to study the oceanic lithosphere and mantle because of the low-frequency content in MT data (Constable, 2010). When MT receivers are placed on the seafloor the MT source fields must propagate down through the electrically conductive seawater which filters out the higher frequencies (Behrens, 2005). If higher frequency MT source fields are absent then MT cannot image shallow subsurface resistivity. This motivates the use of an active source near the seafloor to replace the relatively high-frequency energy lost to MT field decay (Behrens, 2005; Constable and Srnka, 2007); this high-frequency void is what marine CSEM was and is meant to fill.

The first publication associated with marine CSEM theory is probably that of Bannister (1968), who proposed a theory for frequency-domain, seafloor dipole-dipole measurements to determine seabed resistivity. Bannister had recognized the noise issues associated with magnetic sources and consequently recommended the horizontal electric dipole (HED) source that is commonly used today. The deepwater marine CSEM method used today was developed by Charles Cox of Scripps in the late 1970s (Cox, 1981), and the very first CSEM experiment took place in 1979 out on a mid-ocean ridge in the Pacific (Spiess et al., 1980; Young and Cox, 1981). Despite the academic development of marine CSEM that occurred in the 1970s, industry adoption of the method did not occur until the late 1990s (Constable, 2010).

In the late 1990s, hydrocarbon exploration moved to deepwater where drilling wells became extremely expensive and interpreting seismic also became more challenging. Therefore, it was financially beneficial to have additional information and data to reduce risk (Constable and Srnka, 2007). In the late 1990s, exploration was being routinely carried out in water 1000m deep and Statoil and ExxonMobil both began examining marine CSEM as a tool for hydrocarbon exploration (Constable and Srnka, 2007). Statoil conducted an internal research project which showed that under certain conditions a buried oil-filled reservoir in a marine setting could be detected with marine CSEM. The positive results of this study were sufficient enough for Statoil to follow through with the first CSEM field trials in offshore Angola in November 2000 (Constable, 2010; Constable and Srnka, 2007). Around

the same time, ExxonMobil was investigating survey design, acquisition, data processing, inversion, and interpretation techniques for 3D marine CSEM data. Soon after, ExxonMobil started their own field programs with trials offshore Scotland in late 2001 and West Africa in January 2002 (Constable and Srnka, 2007).

Over the past decade, marine CSEM data have been acquired to help supplement seismic data in marine basins across the globe (Constable, 2010). Figure 1.1 illustrates how marine CSEM has already been used as a de-risking tool. Small fractions of gas in pore fluid can increase seismic velocities by a significant amount (Constable, 2010; Fanavoll et al., 2014). Consequently, this can cause a false direct hydrocarbon indicator (DHI) in seismic data (i.e. not all seismic anomalies are indicative of hydrocarbon saturations). Electrical resistivity, what marine CSEM is sensitive to, is determined by the pore content, and the measured resistivity is higher when pores are filled with oil or gas (Vieira da Silva et al., 2012). Consequently, a useful application of marine CSEM has been pre-drill appraisal of seismicly identified DHIs to avoid drilling dry holes associated with structures characterized by strong seismic reflections, but appear to be conductive from marine CSEM data (Constable, 2010).

Two common and problematic lithologies in hydrocarbon exploration (for seismic methods) are salt and basalt. Both have fast seismic velocities and scatter seismic energy, often resulting in poor seismic resolution beneath them (Hoversten et al., 2000; Maresh and White, 2005). Marine CSEM and MT are additional sources that

can aid in determining geological structure beneath these two problematic units (Jegen et al., 2009; Colombo et al., 2012).

There are clear advantages to collecting additional non-invasive geophysical data, such as marine CSEM, which is capable of detecting resistivity variations at a similar lateral coverage to seismic methods, but at a lower vertical resolution (Constable and Weiss, 2006; Eidesmo et al., 2002). Despite the lower resolution of marine CSEM, all of these examples demonstrate why the oil and gas exploration industry has been investing in marine CSEM for the past decade.

### **1.3 Thesis focus**

The Flemish Pass Basin offshore Newfoundland, Canada is situated between the Grand Banks and the Flemish Cap (see Figure 1.2). Within close proximity to the Flemish Pass are the major producing fields in the Jeanne d’Arc Basin: Hibernia, White Rose, and Terra Nova. In recent years, there has been significant seismic exploration in the Flemish Pass Basin which was subsequently followed by three discoveries – Mizzen, Harpoon, and Bay du Nord – and their locations are indicated in Figure 1.2.

Historically, exploration wells have been drilled based solely on seismic data targeting four-way enclosures or fault-bounded structures (Wu et al., 2015). However, as mentioned previously, marine CSEM data can be used as a supplemental interpretation tool combined with seismic to assist de-risking prospects. Recent 3D CSEM results in the Barents Sea show how integrated

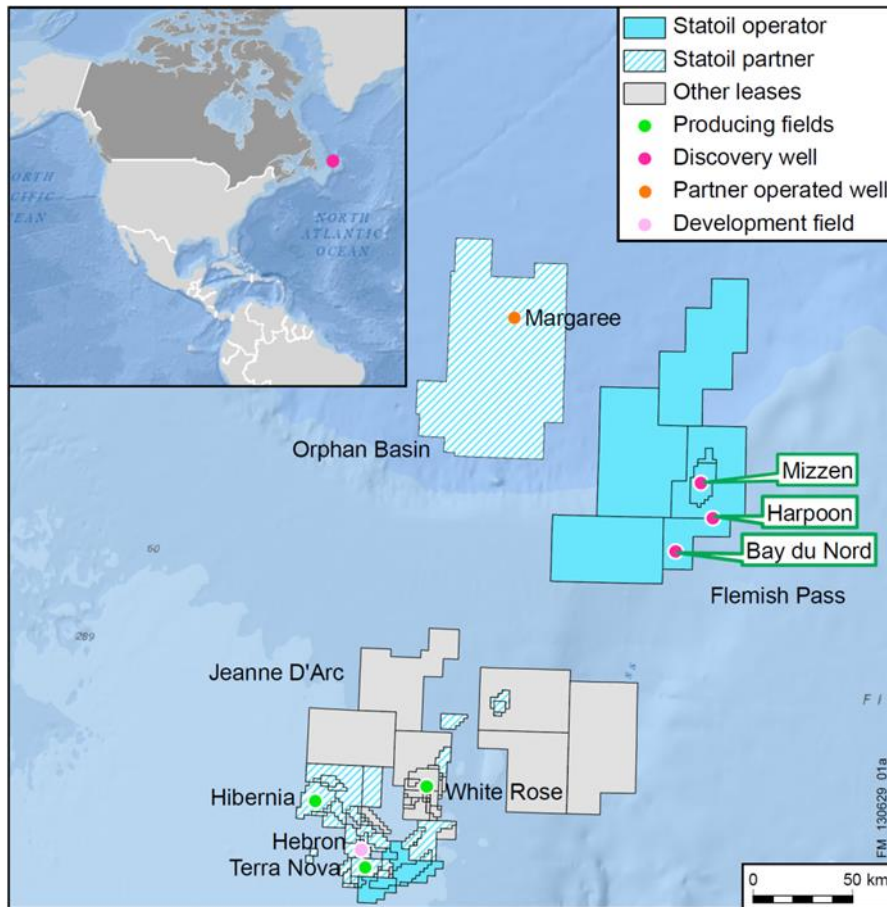


Figure 1.2: The Flemish Pass, Orphan, and Jeanne D'Arc basins located offshore Newfoundland. Recent seismic exploration in the Flemish Pass Basin has led to three Statoil discoveries: Mizzen, Harpoon, and Bay du Nord (image courtesy <http://www.statoil.com/>).

interpretation can be powerful in the exploration phase (Gabrielsen et al., 2013; Fanavoll et al., 2014). As these studies show, the marine CSEM interpretation technique common in industry is 3D finite-difference inversions on rectilinear meshes to recover resistivity distributions. Inversions are practically useful because the inverse process recovers physical properties, but the inversion of EM data for resistivity is usually *very low resolution*. An alternative approach is *forward modeling*, which assumes the resistivity model is known, and consists of an

iterative process of simulating data based on that model, making a comparison to measured data, and updating the model as needed.

This thesis applies a marine CSEM forward modeling method to the Mizzen and Bay du Nord fields in the Flemish Pass Basin (see Figure 1.2). A 3D finite-element forward modeling code, given by Ansari and Farquharson (2014), is used to simulate marine CSEM data based on resistivity models reflective of the 3D structure surrounding these two fields. EMGS has also acquired a multi-client 3D wide-azimuth marine CSEM survey around the Flemish Pass Basin covering a total of 1986 km<sup>2</sup> (Wu et al., 2015). The data from this survey provides the necessary basis of comparison for the simulated forward model data. The practical motivation of this thesis is to provide additional support and interpretations for two real exploration scenarios (the Mizzen and Bay du Nord fields) in the Flemish Pass Basin. However, an important underlying research motive of this thesis is to show the finite-element code can synthesize data from real complex models built using *unstructured meshes*. It is common in literature to see 3D finite-element codes applied to simplistic, synthetic models for code verification purposes, and complex synthetic models in some studies; however, this study takes the logical next step by synthesizing 3D marine CSEM data from complex models built from *real data*.

## 1.4 Outline

In the coming chapters of this thesis, the finite-element forward modeling code will be used to synthesize data from various models. Following this chapter, the details

of the marine CSEM method will be described so the reader understands why and how this method is used to detect marine hydrocarbon reservoirs. After this, a discussion of the various forward modeling techniques is given and an argument is made as to why the finite-element method considered for this thesis is the preferred choice. A high level summary for the mathematical basis of the finite-element code from Ansari and Farquharson (2014) is also given.

In Chapter 3, the forward modeling process is described. This process shows the progression of steps needed to build a model and simulate marine CSEM data based on that model for the studies performed in the three preceding chapters. Chapter 4 shows the results from synthesizing marine CSEM data from a synthetic marine halfspace model and layered earth model. The forward modeling workflow is first applied to simple synthetic models in order to become familiar with the modeling process and the software involved.

Chapter 5 applies the 3D finite-element forward modeling method to the first real complex model at the Mizzen field. The series of steps required for building the model are described. Comparisons to the measured data are made after generating the unstructured meshes. Chapter 6 applies the same method to the second real complex model at the Bay du Nord field. This model contains additional complexities in comparison the Mizzen model and subsequently requires more steps in the modeling process.

Finally, Chapter 7 summarizes the results of the thesis and provides suggestions for improvements and considerations. At the end of this thesis there are a series of appendices that provide the command line switches for Triangle (Appendix A), the command line switches for TetGen (Appendix B), a MATLAB code used for determining refinement nodes surrounding observation locations (Appendix C), and a summary of the results for the Mizzen forward modeling study (Appendix D).

# Chapter 2

## Methods

The focus of this thesis involves 3D marine CSEM forward modeling on unstructured grids. Knowledge of the marine CSEM method, from the underlying physics to qualitative comprehension, is needed in order to understand how this method is used in a hydrocarbon exploration context. Furthermore, forward modeling forms an integral component of this thesis so it is important to understand the three main modeling schemes to recognize the merits of each, and ultimately why the finite-element approach was chosen for this project.

### 2.1 The Marine CSEM Method

#### 2.1.1 The Physics of Electromagnetics

In the discussion of any electromagnetics method, it is useful to begin with the physics and mathematics (refer to Stratton, 1941; Ward and Hohmann, 1988).

Electromagnetics can be easily described starting with Faraday's and Ampere's laws shown as Equations 2.1 and 2.2 respectively:

$$\nabla \times E = \frac{-\partial B}{\partial t} \quad (2.1)$$

$$\nabla \times B = \mu J + \mu \varepsilon \frac{\partial E}{\partial t} \quad (2.2)$$

where,

$$J = \sigma E \quad (2.3)$$

is the constitutive relationship, otherwise known as Ohm's law. Equations 2.1 and 2.2 can be combined into one partial differential equation (PDE) for the electric field by taking the curl of Equation 2.1 and transforming it to the frequency domain assuming an  $e^{-i\omega t}$  dependency:

$$\nabla \times \nabla \times E = i\omega\mu\sigma E - \omega^2\mu\varepsilon E \quad (2.4)$$

The quasi-static approximation states that the electromagnetic field is dominated by the diffusion portion of the field and not the wave portion (i.e. when the ratio  $|\sigma/\omega\varepsilon|$  is high). In summation, the quasi-static approximation ignores the wave portion of the field ( $\omega^2\mu\varepsilon E$ ) in its entirety and this is a reasonable assumption when considering the non-negligible conductivities and low frequencies pertinent to marine CSEM (Weaver, 1994). The relevant *conservation of charge* can be found by taking the divergence of Equation 2.2 and neglecting any displacement currents:

$$\nabla \cdot J = 0 \quad (2.5)$$

The quasi-static approximation also simplifies Equation 2.4 to the following,

$$\nabla \times \nabla \times E = -k^2 E \quad (2.6)$$

taking  $k^2 = -i\omega\mu\sigma$  where  $k$  is the complex wavenumber. When solving for  $k$ , there are real and imaginary components as indicated by Equation 2.7 and the real and imaginary components are both equal as shown in Equation 2.8:

$$k = \beta - i\alpha \quad (2.7)$$

$$\beta = \alpha = \sqrt{\frac{\omega\mu\sigma}{2}} \quad (2.8)$$

The simplest solution to the PDE in Equation 2.6 is to consider a region of uniform conductivity ( $\sigma$ ) and a plane wave of angular frequency ( $\omega$ ) propagating along the z-axis while oscillating in the x-y plane (Behrens, 2005):

$$E = E_o e^{-i(kz - \omega t)} \quad (2.9)$$

The expression for  $k$  in Equation 2.7 can be substituted for  $k$  in Equation 2.9 and the result becomes:

$$E = E_o e^{-\alpha z} e^{i(\omega t - \beta z)} \quad (2.10)$$

where  $e^{i(\omega t - \beta z)}$  represents the oscillatory part of the field (recall from Euler's formula  $e^{iz} = \cos(z) + i\sin(z)$ ) and  $e^{-\alpha z}$  represents the attenuation (and controls the amplitude) part of the field. A simple examination of the attenuation portion of the field reveals an important concept of electromagnetics called the *skin depth*. When  $z=0.0\text{m}$  the attenuation part of the field is unity which implies there has been no attenuation. The skin depth refers to the depth at which the fields reduce to  $1/e$  of the original amplitude. Some simple algebra:

$$e^{-1} = e^{-\sqrt{\omega\mu\sigma/2}z} \quad 1 = \sqrt{\omega\mu\sigma/2} z$$

shows that the depth at which the amplitude reduces to  $1/e$ , or the skin depth ( $z_s$ ), can be represented as the following (Constable, 2010):

$$z_s = \frac{1}{\alpha} = \frac{1}{\beta} = \sqrt{\frac{2}{\omega\mu\sigma}} \approx \frac{500}{\sqrt{\sigma f}} \quad (2.11)$$

The skin depth in Equation 2.11 shows that the attenuation of electromagnetic fields is dependent on conductivity and frequency. Consequently, different electromagnetic sources at varying frequencies will contain different sensitivities to

earth structure, such as marine CSEM and magnetotellurics (MT). Consider a scenario with marine sediment conductivity  $\sigma = 1.0$  S/m, a CSEM frequency of  $f_{csem} = 1.0$  Hz, and a MT frequency of  $f_{MT} = 0.01$  Hz. The corresponding skin depths for CSEM and MT are  $Z_{csem} = 500$ m and  $Z_{MT} = 5,000$ m which again illustrates why marine CSEM is more sensitive to shallow structure.

### 2.1.2 Marine CSEM Acquisition

Figure 2.1 from Constable (2010) illustrates the typical marine CSEM method. The electromagnetic signal is emitted from a horizontal electric dipole transmitter 50–300m long and 25–100m above the seafloor. The transmitter is towed close to the seafloor to ensure the best coupling between the signal and the subsurface as the seawater is conductive and attenuates the signal through the process of induction.

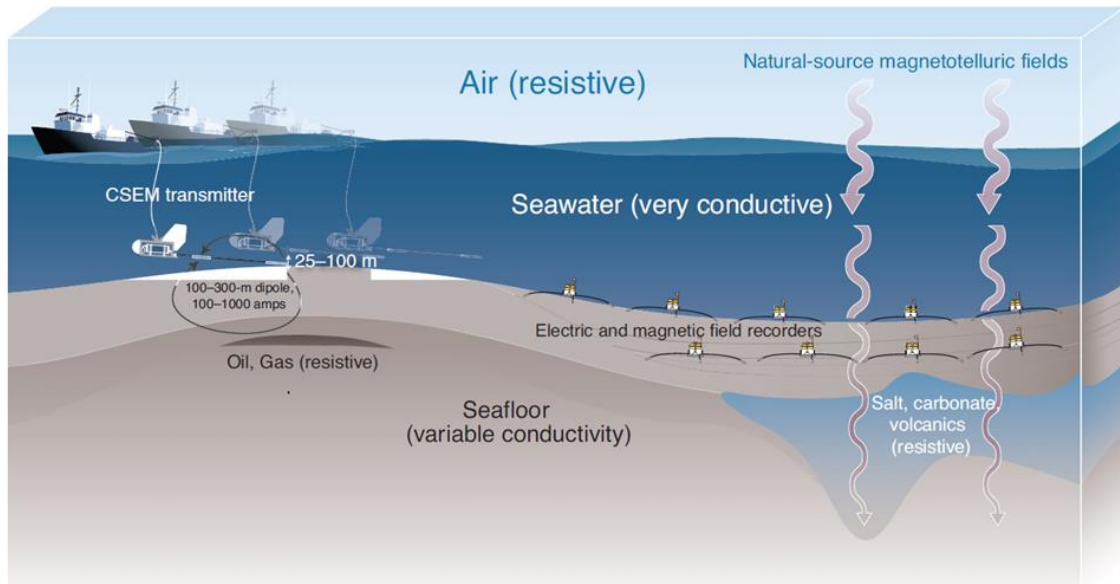


Figure 2.1: The marine CSEM concept. Electric and magnetic receivers are deployed on the seafloor and a towed horizontal electric dipole transmitter emits the primary field (from Constable, 2010).

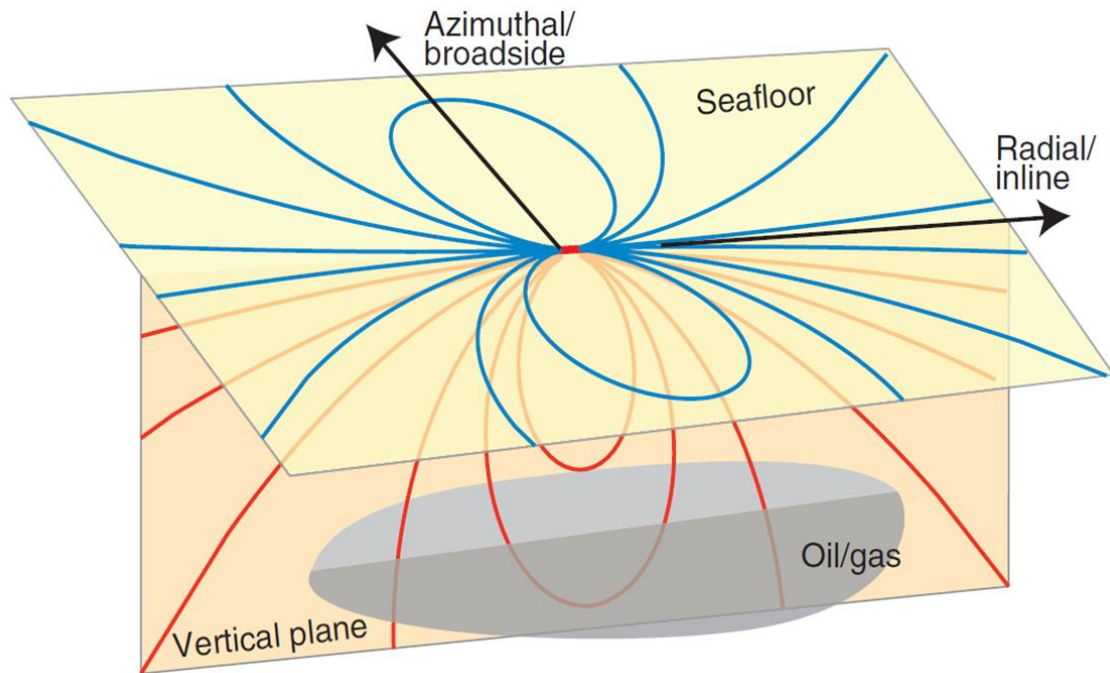


Figure 2.2: The horizontal electric dipole (HED) geometry. The in-line fields are largely vertical and the broadside fields are largely horizontal (Constable, 2010).

A high voltage at low current is fed down a winch cable to the main body of the transmitter where it is transformed into a low voltage at high current. The high current is fed to the source electrode and the seawater provides the return path for the current to travel to the sink electrode (Behrens, 2005). Figure 2.2 shows a schematic of the horizontal electric dipole (HED) which has an inherent complex 3D geometry. The fields in the vertical plane of the transmitter (i.e. inline) are largely vertical and the fields in the plane horizontal to the transmitter (i.e. broadside) are largely horizontal. The current emitted by these transmitters can be onwards of 100–1000A or larger.

Marine CSEM is commonly operated in the frequency domain with frequencies varying depending on the target depth, but typically ranging from 0.1 – 10.0 Hz.

MT frequencies will vary largely based on seawater depth and typically range from 0.0001 to 1.0 Hz (Constable, 2010). This correlates to the previous statement in Section 1.2 that CSEM frequencies are commonly chosen to encompass frequencies not contained in MT data to image shallower targets. The common approach for marine CSEM receiver coverage is to deploy limited amounts of receivers to the seafloor by anchors (Constable, 2010). The receivers then measure the time-varying signal for both the electric and magnetic fields as the transmitter is towed from zero to several kilometers from the receivers (Constable and Srnka, 2007). Figure 2.3 shows a schematic of a typical marine CSEM multicomponent receiver. All of the data is recorded in time and must be processed in order for the data to be understood and interpreted.

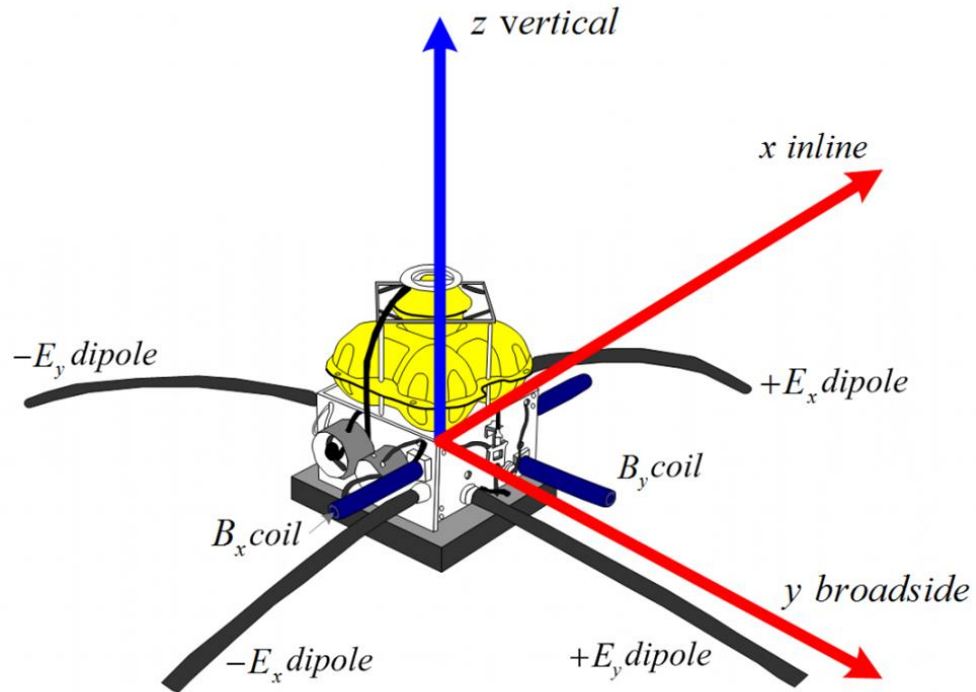


Figure 2.3: A typical marine CSEM multicomponent receiver illustrating the different fields and components measured. This is the Scripps Institution of Oceanography Mark III design (courtesy of [www.digitalearthlab.com](http://www.digitalearthlab.com)).

### 2.1.3 Data Processing

A processing routine given by Behrens (2005) begins by first loading the raw time series data recorded by the receivers. Instead of using a Fourier transform to convert the data from time to frequency domain, a different approach is used. A given data point in time,  $d(t)$ , can be represented as a continuous sinusoid, or more specifically, the sum of two orthogonal harmonic basis functions scaled by coefficients:

$$d(t) = A\cos(\omega t) + B\sin(\omega t). \quad (2.12)$$

However, since the measured data is a series of electric field stack frames in time, the data is actually a vector,  $d$ . Therefore, Equation 2.12 can be represented as a system of equations

$$\begin{bmatrix} \cos(\omega_j t_1) & \sin(\omega_j t_1) \\ \cos(\omega_j t_2) & \sin(\omega_j t_2) \\ \vdots & \vdots \\ \cos(\omega_j t_n) & \sin(\omega_j t_n) \end{bmatrix} \begin{bmatrix} A_j \\ B_j \end{bmatrix} = \begin{bmatrix} d_1 \\ d_2 \\ \vdots \\ d_n \end{bmatrix} \quad (2.13)$$

where  $n$  is the number of data in the time series, and  $j$  is the number of frequencies (in this case just one). This system is overdetermined and thus no exact solution for the two coefficients  $(A_j, B_j)$  exists. Equation 2.13 can be rewritten in a short form

$$MC = d \quad (2.14)$$

where  $M$  is the basis function matrix and  $C$  is the coefficient vector. A least squares solver can be used to solve for the two coefficients. Once the coefficients are solved for, the data can be represented in a different manner to characterize the amplitude and phase of the signal at a particular frequency,  $\omega_j$ :

$$\tilde{d}_{i,j} = \left( \sqrt{A_j^2 + B_j^2} \right) \cos \left( \omega_j t_i - \tan^{-1} \frac{B_j}{A_j} \right) = |E_j| \cos(\omega_j t_i - \varphi_j). \quad (2.15)$$

This least squares process determines approximate values for the amplitude  $|E_j| = \sqrt{A_j^2 + B_j^2}$  and phase  $\varphi_j = \tan^{-1} \frac{B_j}{A_j}$  of the recorded time signal, which are what is used for interpretation. The data in Volts are normalized by the receiver's antenna length and nominal gain to give the electric field amplitude in Volts per metre.

The next step in the process given by Behrens (2005) involves normalizing, more stacking, and rotating the data. The data from the previous step are normalized by the transmitter source dipole moment and adjusted to remove the receiver amplifier transfer function. CSEM receivers fall freely to the seafloor and as a consequence, their orientations are unknown (Lu et al., 2006). One method to determine receiver orientation and project the measured fields into a preferred direction is using a polarization ellipse (Behrens, 2005). The parameters determined by the polarization ellipse are used to rotate the data to the desired coordinate system (i.e.  $E_x$  and  $E_y$ ).

The final processing step is to merge the electric field data with the navigation and time data. The receiver and navigation data are recorded separately and are combined together by aligning their respective time vectors. This entire process illustrated by Behrens (2005) shows how time series data that have 'multiple' data points for one source-receiver separation change to have one electric field amplitude and one phase data point in the frequency domain.

### 2.1.4 Conceptual Explanations of the CSEM response

It is important to understand *how* changes in measured marine CSEM fields can be an indication of hydrocarbon presence. Constable (2010) elaborates on three mechanisms that are critical to understanding what produces changes in the amplitude and phase of any measured electromagnetic field and they are illustrated in Figure 2.4.

The first is geometric spreading which represents the characteristic dipole decay as the fields propagate further from the source. The second is the galvanic effect associated with the conservation of the normal component of current across a conductive boundary. If the current, or current density, must be preserved when crossing a boundary then the electric field must change. If current is traveling from layer 1 to layer 2 and layer 2 is more conductive (as shown in Figure 2.4), then this causes a *decrease* in the electric field; if layer 2 is more resistive then this causes an *increase* in the electric field. Both the geometric and galvanic effects have no associated changes in phase. The third is the inductive effect. If the fields travel sufficiently through a given layer where the distance traveled is comparable to the skin depth, then inductive attenuation and a phase shift occurs. A phase shift occurs because the expression for skin depth not only shows up in the attenuation part of the field but also in the oscillatory part of the field,  $e^{-i(\omega t - \beta z)}$  (i.e. one skin depth is equivalent to a change in 1 radian  $\approx 57^\circ$ ).

So the question becomes, is the marine CSEM response of a reservoir (thin resistor) going to be dominated by galvanic or inductive effects? Hydrocarbon reservoirs are

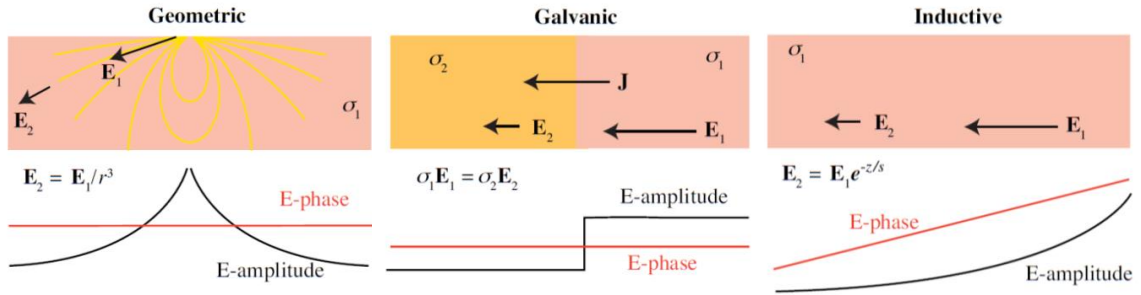


Figure 2.4: The three mechanisms which influence the amplitude and phase of electromagnetic signals: geometric, galvanic, and inductive. All three cause changes in amplitude, but only induction causes a change in phase (Constable, 2010).

typically very laterally extensive, but relatively thin in thickness. As a consequence of reservoirs being relatively thin, the distance the electromagnetic fields have to travel to get through the reservoir will in most cases be much less than the skin depth. Therefore, inductive effects will most likely *not* drive the CSEM response. However, galvanic effects can cause a response in a thin resistor. As the fields travel from marine sediments to a hydrocarbon reservoir there is typically a significant increase in resistivity which would cause an increased electric field response.

When these three concepts described by Constable (2010) are combined with the knowledge of transmitter geometry (Figure 2.2), the sensitivity of marine CSEM to hydrocarbon reservoirs is easily understood. The electric field lines associated with the in-line orientation of the transmitter are purely radial and plunge into the seafloor with a *significant vertical component* (Constable, 2010). As a consequence of hydrocarbon reservoirs being laterally extensive, the in-line fields will normally intersect a reservoir causing galvanic distortions of the electric field which can be measured by the receivers. Despite the 3D nature of the dipole, it is noted that the

in-line (radial) geometry contains the strongest galvanic effect (Eidesmo et al., 2002). In the direction broadside to the transmitter, electric field lines are purely azimuthal and largely horizontal which will not produce galvanic effects at horizontal boundaries (Constable, 2010). In general, inductive effects dominate broadside (azimuthal) geometries and the attenuative effects are governed by skin depth (Eidesmo et al., 2002). These phenomena as a whole result in a significant difference in the sensitivity of in-line and broadside CSEM components when mapping thin resistors, or hydrocarbons.

### 2.1.5 Electrical Anisotropy

The difference in reservoir sensitivity between in-line and broadside marine CSEM transmitter components can also be explained in terms of electrical anisotropy on the macro scale. The horizontal electric dipole produces horizontal and vertical fields and this implies that horizontal and vertical currents flow through the subsurface as well (i.e. Ohm's law). When considering a layered earth scenario, the resolution of EM fields is not adequate enough to be able to discern each individual layer; instead, the fields will treat a sequence of layers as a single *bulk* unit. The direct consequence of this is shown in Figure 2.5. When a vertical field (via an in-line transmitter direction) approaches a sequence of layers, the field treats the layers as if they are resistors in series. In circuit theory, the equivalent resistance of a circuit array with resistors in series is simply the *sum* of the resistances of each resistor, as shown in Equation 2.16. This same theory can be applied to determine the *equivalent resistivity* of a sequence of layers. The result is a depth-averaged

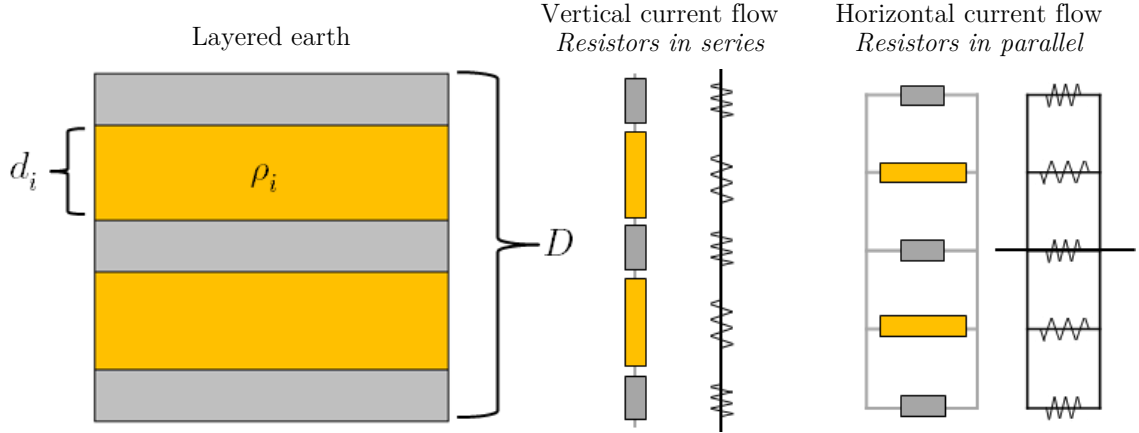


Figure 2.5: A 1D layered earth example which shows that vertical and horizontal fields treat the layers as resistors in series and parallel respectively. As a consequence, vertical fields are more sensitive to resistors and horizontal fields are more sensitive to conductors.

resistivity termed the vertical resistivity ( $\rho_v$ ) which has an *emphasis on beds with high resistivity* and is a result from vertical fields:

$$R_{Total} = R_1 + R_2 \dots + R_n \quad \rightarrow \quad \rho_v = \frac{1}{D} \sum_i \rho_i d_i \quad (2.16)$$

The same process can be applied to horizontal fields (via broadside transmitter directions) as shown in Figure 2.5. Except in this case, the horizontal fields treat the sequence of layers as resistors in parallel and there is an inverse relationship to calculate the effective resistance (Equation 2.17). The equivalent resistivity from horizontal fields is termed the horizontal resistivity ( $\rho_h$ ), but it has an *emphasis on beds with high conductivity*:

$$\frac{1}{R_{Total}} = \frac{1}{R_1} + \frac{1}{R_2} + \dots + \frac{1}{R_n} \quad \rightarrow \quad \frac{1}{\rho_h} = \frac{1}{D} \sum_i \frac{d_i}{\rho_i} \quad (2.17)$$

These two considerations of vertical and horizontal fields imply the equivalent resistivity has directional dependence, and therefore the equivalent *bulk* unit is electrically anisotropic. This macro anisotropy is a direct consequence of the

inadequate resolution of the EM method to discern the individual layers. The degree of anisotropy,  $\lambda$ , is given by,

$$\lambda = \sqrt{\frac{\rho_v}{\rho_h}} \quad (2.18)$$

but it is not uncommon to see the expression given without the square root depending on the source. The expressions shown in Equations 2.16 – 2.18 are part of the Dar Zarrouk parameters given by Maillet (1947).

This phenomenon of electrical anisotropy can be used to justify and explain why certain electrical geophysical methods are sensitive to certain targets. Consider MT for example. The far-field approximation assumes that MT fields are plane-waves, and therefore, the fields are horizontal. It is widely known that MT fields are sensitive to horizontal conductors, but there is little sensitivity to thin horizontal resistors. However, this analysis shows that vertical marine CSEM source fields will be sensitive to horizontal resistors, and by extension, also hydrocarbons.

### 2.1.6 The Receiver Response

The previous sections describe the factors that influence a marine CSEM response and this information is the foundation of being able to understand and interpret the response measured in a receiver. It is not explicitly stated in the literature, but the marine CSEM response consists of three distinguishable data ranges: the near, mid, and far offsets. A 1D forward modeling example of the common canonical disk model (Constable and Weiss, 2006; Key, 2009) is shown in Figure 2.6 and is used to help illustrate the factors that contribute to each offset interval. Panels (b) and

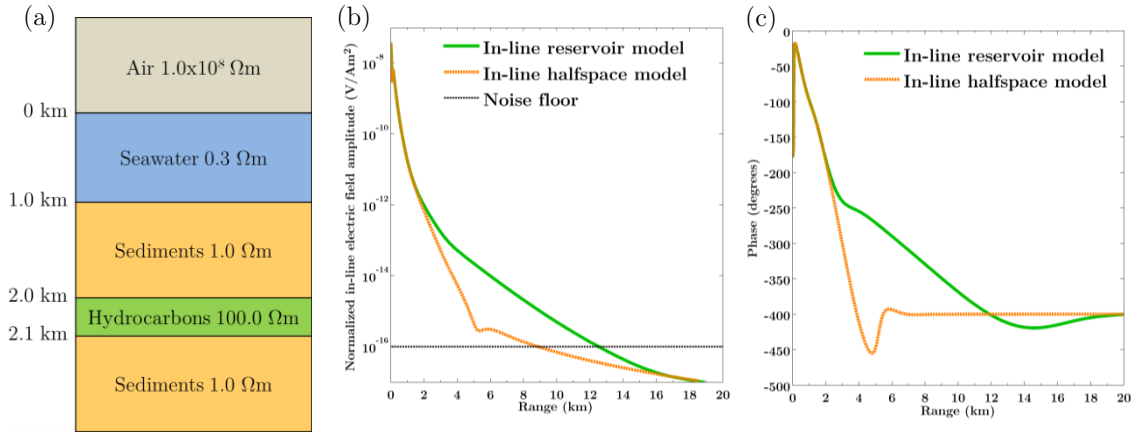


Figure 2.6: (a) The 1D canonical disk model used for 1D marine CSEM forward modeling which was achieved by using DIPOLE1D (Key, 2009), (b) the in-line amplitude, and (c) phase responses for the 1D reservoir model and the halfspace model without hydrocarbons.

(c) are 1D computations for the in-line amplitude and phase respectively. The green curves are computations coming directly from the model depicted in panel (a), whereas the orange curves represent computations *without* the hydrocarbon layer (i.e. the halfspace model).

### 2.1.6.1 Near offsets

The near offsets are dominated by the *seawater response*. Similar to seismic, there is also a *direct wave* in marine CSEM where the EM waves travel directly from the transmitter to the receiver within the seawater column. However, this direct wave does decay quickly as it is only propagating in seawater which has a high conductivity and small skin depth. The signature of the direct wave will have a very steep slope in the amplitude (see the 0-1km range in Figure 2.6b).

### 2.1.6.2 Mid offsets

The data recorded at mid offsets has had enough time for the primary field to propagate into the subsurface and refract back up to the receivers. The direct wave

is still present, but the seawater acts as a natural filter and its contribution to the total field diminishes quickly as the offset increases. Once the fields propagate into the seafloor, the fields will decay less because they are traveling through more resistive media. This is clearly shown by the amplitude *and* phase plots shown in Figure 2.6. There is clearly a decrease in slope for the amplitude of the halfspace response from 2-5km which is the response coming from the 1.0 $\Omega$ m sediments. Furthermore, there is a distinctive increase for the in-line amplitude of the reservoir response and this matches the predictions discussed in Sections 2.1.4 and 2.1.5. The presence of the hydrocarbon layer prevents the fields from decaying too quickly in the subsurface which is also observed by the shallower slope in the phase.

### **2.1.6.3 Far offsets**

At far offsets, there are two phenomena that complicate marine CSEM data interpretation. As Figure 2.7(a) shows, it is common for transmitter signals to follow a propagation path upwards through the water column to the surface, horizontally through the air at the speed of light, and back down through the water column to a seafloor receiver (Eidesmo et al., 2002). This is called the *airwave*. The airwave can contribute significantly to the recorded signal because it has a lack of attenuation in the atmosphere where *only* geometric spreading is reducing the signal with distance (Constable, 2010). Figure 2.7(b) demonstrates that the contribution of the airwave becomes significant with shallow seawater depths, long source-receiver offsets, and conductive sub-seafloor sediments. In shallow water, the fields taking Path III in Figure 2.7(a) will not decay as much as if the seawater column was deeper. At large offsets, the subsurface response will

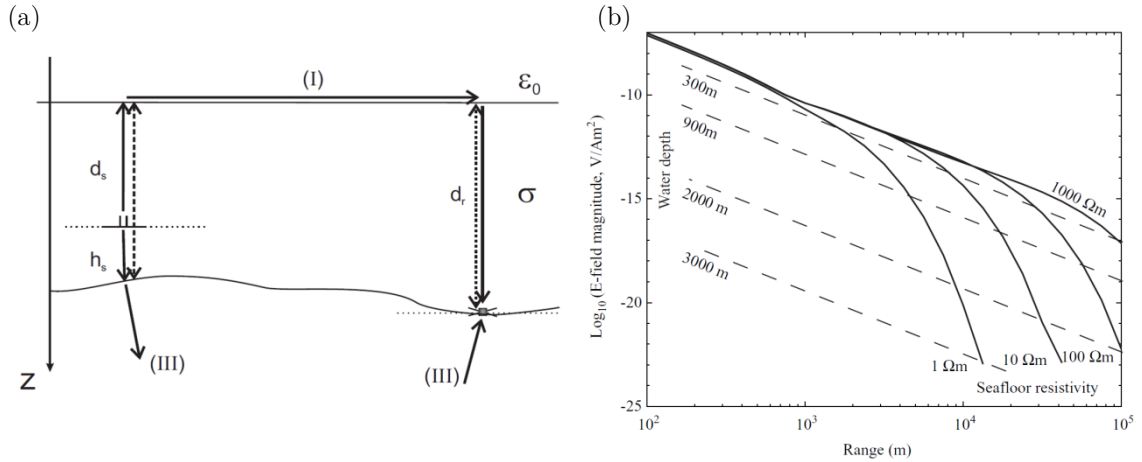


Figure 2.7: (a) A sketch of marine CSEM signal propagation given by Løseth (2007) showing at a given offset the total field can comprise of fields that propagated in the air (Path I) and the subsurface (Path III). The (b) radial electric field amplitudes as a function of range and half-space resistivity without an air layer, and the airwave contribution for various water depths (from by Constable and Weiss, 2006).

begin to decay and the contribution of the airwave to the total signal will become significant. Furthermore, if the sub-seafloor sediments are more conductive, then the *geological* contribution to the total field will decay more quickly and the airwave will once again begin to dominate.

Airwave signals are essentially noise because they contain no information regarding the sub-seafloor resistivity. The influence of the airwave on marine CSEM data can be shown by observing the phase in Figure 2.6. *The airwave has no phase lag* because the wave is traveling at the speed of light at the air-water interface. In other words, there is an instantaneous travel-time for the EM wave at the air-water interface regardless of offset. Therefore, the travel time for an airwave essentially only comes from the path the wave takes going up and then back down through the water column ( $d_s + d_r$  in Figure 2.7a). This is easily observed by the halfspace response where the phase remains constant at  $-400^\circ$  starting at 6km offset

and this is the offset at which the airwave begins to dominate. The presence of the reservoir increases the amplitude of the electric field such that the airwave does not begin to influence the data until about 14km offset.

The second phenomenon that occurs at larger offsets is the noise floor of the transmitter/receiver system. Sources of noise in the receiver include the electrodes, water motion, instrument motion, and the magnetotelluric signal (Constable and Weiss, 2006). The signal to noise ratio can be improved with a larger source dipole moment, stacking bandwidth, and the length of the receiver antenna, but a noise floor of  $10^{-16}$  V/(Am<sup>2</sup>) appears to be the lower bound (Constable and Weiss, 2006). The noise level plays an important role in survey design and data interpretation because starting at a given range, the signal-to-noise ratio will be too poor to trust. With a noise level of  $10^{-16}$  V/(Am<sup>2</sup>) in Figure 2.6, the amplitudes cannot be trusted beyond 9km offset and 13km offset for the halfspace and reservoir responses.

The near offsets are dominated by source-related direct waves and the far offsets are dominated by airwaves and noise. The mid-offset range is the only portion of the data that is interpretable and useful. For the example discussed in this section, the mid-offset range for the halfspace model appears to lie approximately on the interval 1-5km and 1-13km for the reservoir model. In summation, there appears to be only a *window* of useful data in a marine CSEM data set and this range will vary greatly depending on seawater depth, subsurface geology, and acquisition geometry.

### 2.1.7 Limitations

The previous sections show that there are benefits to using marine CSEM for hydrocarbon exploration and conceptually state that the method can be sensitive to thin resistors, but there are still some practical limitations of the method. Marine CSEM is sensitive to resistivity, and unfortunately, not all resistive anomalies are hydrocarbons. Carbonates and low porosity zones are *lithological* examples of high resistivity zones. As a consequence, marine CSEM is only sensitive to resistivity and may not be able to distinguish between lithological and fluid effects.

There is also an underlying resolution deficiency with marine CSEM. In general, it is understood that the higher the frequency, the higher the resolution. However, marine CSEM is forced to use lower frequencies to reduce attenuation, and this is at the expense of resolution. As an example, some common frequencies for marine CSEM would lie between 0.25 – 1.00Hz, whereas a peak seismic frequency might be 25.0Hz. This is one explanation as to why the seismic method has a much better resolution than marine CSEM, but the underlying reason is the loss of the harmonic term in the transformation from the wave to the diffusion equation (Constable, 2010). The inherent lower resolution of marine CSEM has other implications as well. The burial depth, lateral extent, and resistivity-thickness product (transverse resistance) are important for the detection of hydrocarbons (Constable and Weiss, 2006). So, if the reservoir is buried too deep, is too small, or is too thin, then the method may not be able to detect the reservoir at all.

Sources of noise are also important considerations for the marine CSEM method. Section 2.1.6 discussed the airwave and noise floor which can render the far offsets uninterpretable. It is important to take these factors into consideration when seeking to utilize the marine CSEM method for hydrocarbon exploration. In specific relation to this thesis, many of these factors and limitations proved to be critical in providing accurate interpretations and conclusions for the forward modeling studies performed in the Flemish Pass Basin (see Chapters 5 and 6).

## 2.2 Forward Modeling Techniques

The development from the previous sections conceptually described at a high level what the CSEM response of a hydrocarbon reservoir should be, but in order to observe the true limitations and capabilities of CSEM data, it is valuable to have more than just qualitative understanding. A quantitative approach to understanding 3D resistivity structures is needed which gave rise to 3D forward modeling of geophysical EM problems. There are three common techniques for modeling 3D EM problems: integral equation (IE), finite-difference (FD), and finite-element (FE). All three of these methods are trying to solve the same Maxwell's equations (Equations 2.19 and 2.20 below are similar to Equations 2.1 and 2.2 but with the source and quasi-static approximation taken into account), but each method does so differently:

$$\nabla \times E = i\omega\mu H \quad (2.19)$$

$$\nabla \times H = \sigma E + J^s \quad (2.20)$$

### 2.2.1 Integral Equation Method

The IE approach to solving Maxwell's differential equations (Equations 2.19 and 2.20) is to reduce them to a Fredholm integral equation of the second kind with respect to the electric field where a Green's function technique is applied (Avdeev, 2005):

$$E(r) = E_o(r) + \int_{V^s} G(r; r')(\tilde{\sigma} - \tilde{\sigma}_o)E(r')dr' \quad (2.21)$$

In Equation 2.21,  $E_o$  is the known background electric field,  $G$  is the dyadic for the Green's function, and  $V^s$  is the volume where  $(\tilde{\sigma} - \tilde{\sigma}_o)$  is non-zero. Initially, IE methods received the most attention (Raiche, 1974; Hohmann, 1975; Ting and Hohmann, 1981; Wannamaker et al., 1984; Newman and Hohmann, 1988; Wannamaker, 1991; Avdeev et al., 1997). These IE methods are for models consisting of localized regions of anomalous conductivity in a simple background. The upside of this method is only the anomalous region requires discretization, fewer unknowns are involved, and a smaller system of equations is solved compared to other methods (Farquharson and Miensopust, 2011). This approach makes IE practical for compact bodies and simple problems. However, as model complexity increases the computational intensity increases as well because the system matrices are dense for the IE method (Streich, 2009). Despite these difficulties, the IE method was the most practical option given the computing resources at the time. As computer speed and memory increased, differential equation methods (FD and FE) received more attention (Farquharson and Miensopust, 2011).

## 2.2.2 Finite Difference Method

To solve Maxwell's equations using the finite-difference (FD) method, the staggered grid scheme (Yee, 1966) shown in Figure 2.8 is typically used to solve the vector Helmholtz equation

$$\nabla \times \nabla \times \mathbf{E} + i\omega\mu_o\sigma\mathbf{E} = -i\omega\mu_o\mathbf{J}_s \quad (2.22)$$

where  $J_s$  is the source current density. Conventionally, the Helmholtz equation is solved because solving the coupled Maxwell's equations (Equations 2.19 and 2.20) in the air can result in slow convergence (Newman and Alumbaugh, 1995).

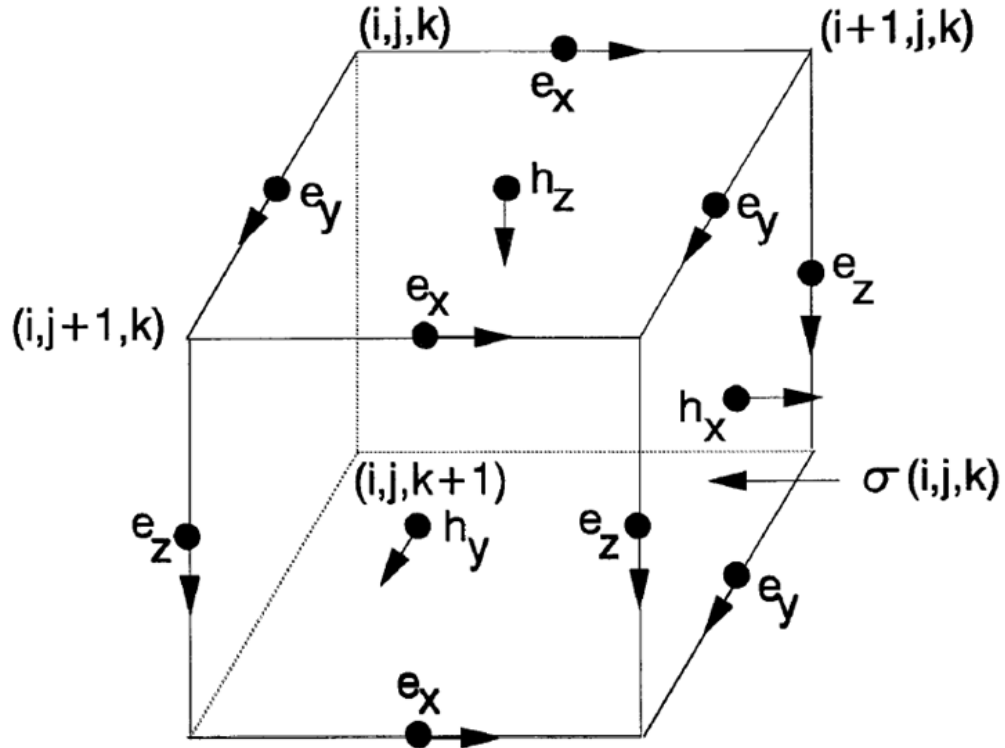


Figure 2.8: The staggered grid (Yee, 1966) assignments of the electric and magnetic fields to cell  $(i,j,k)$ . H-fields are assigned to face centers and E-fields to edges (Newman and Alumbaugh, 1995).

The staggered grid is critical for solving EM problems because it explicitly enforces: (1) continuity of tangential electric field, (2) discontinuity of normal electric field and (3) the divergence-free condition. Equation 2.22 is solved for the electric field,  $E$ , by replacing the  $\nabla \times \nabla \times$  operator with finite-differences according to the staggered scheme shown in Figure 2.8. The result is a system of equations  $A_{FD} x = b$  where  $A_{FD}$  is the stiffness matrix containing the discrete information about the  $\nabla \times \nabla \times$  operator and the  $i\omega\mu_0\sigma$  term on a 3D mesh (see Figure 2.9 for an example),  $x$  is the vector of unknown electric field values, and  $b$  is associated with the source.

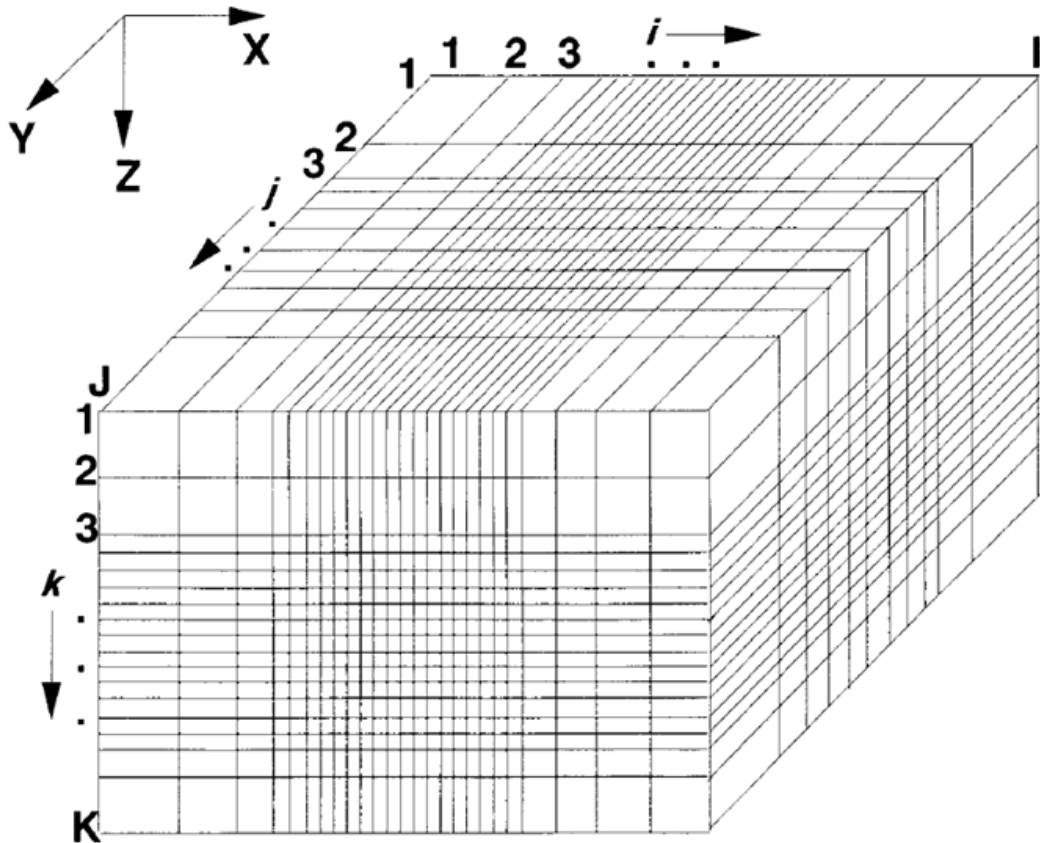


Figure 2.9: The common non-uniform rectilinear grid used for 3D finite-difference solutions (Newman and Alumbaugh, 1995).

This FD scheme using staggered grids has been used to solve EM forward problems since the 1980s. Solving Maxwell's equations in the time domain involve time stepping which removes the need to solve a linear system of equations. The 2D time-domain FD method by Oristaglio and Hohmann (1984) was later generalized to 3D (Wang and Hohmann, 1993; Commer and Newman, 2004; Maaø, 2007). The FD method was also extended to the frequency domain (Newman and Alumbaugh, 1995; Weaver et al., 1999; Fomenko and Mogi, 2002; Streich, 2009) and to incorporate electrical anisotropy (Weiss and Newman, 2002; Newman et al., 2010).

When comparing the FD and IE methods there are evident complications and advantages. FD (and FE) methods require discretization of the whole 3D domain whereas IE methods discretize only anomalous regions. Consequently, electric and magnetic fields must be solved for everywhere on the grid as opposed to just anomalous regions. The resulting matrix system is sparse and diagonally banded (Newman and Alumbaugh, 1995). Many more unknowns than the IE method are therefore involved, but discretization of the entire 3D domain allows for more complicated, general models to be considered (Farquharson and Miensoopust, 2011). As the size of the 3D model increases, the computation time for the unknown fields scales much better than the IE method because the matrix system is sparse for FD methods (Newman and Alumbaugh, 1995). However, a disadvantage of the FD method is the weighted conductivity averaging required because one edge is shared by four cells in a rectilinear mesh. Despite its imperfections, FD methods are quite favorable for their relatively straightforward implementation on 3D rectilinear meshes.

### 2.2.3 Finite Element Method

Even though the models considered by the FD method are an improvement compared to those possible by the IE method, the traditional FD method is limited to a rectilinear mesh formation like those shown in Figure 2.9. Unstructured tetrahedral meshes enable a more faithful representation of topography and realistic subsurface interfaces than rectilinear grids (Farquharson and Miensopust, 2011). The finite-element (FE) method has recently received more attention because it is far better suited to support unstructured meshes than the FD method. The FE approach is a useful tool for modeling complex structures because its flexibility enables simulation of geometric complexity while minimizing the number of solution variables (Nam et al., 2007). This is illustrated by panels (a) and (b) in Figure 2.10. A structured rectilinear mesh struggles to represent this complex body and its curved surfaces, whereas the complex body is easily represented on an unstructured tetrahedral mesh.

The FE method allows local grid refinement whereas the FD method does not (Puzyrev et al., 2013). Figure 2.10(d) shows how an unstructured mesh has the ability to refine at regions of interest and coarsen near the boundaries. Refinement is important for modeling purposes because electromagnetic fields can have high gradients in target areas (i.e. hydrocarbon reservoirs can be orders of magnitude higher in resistivity than the surrounding medium) and locally around sources and receivers. Consequently, the computed fields can be more accurately represented with a refinement in these areas while maintaining coarser cells elsewhere in the

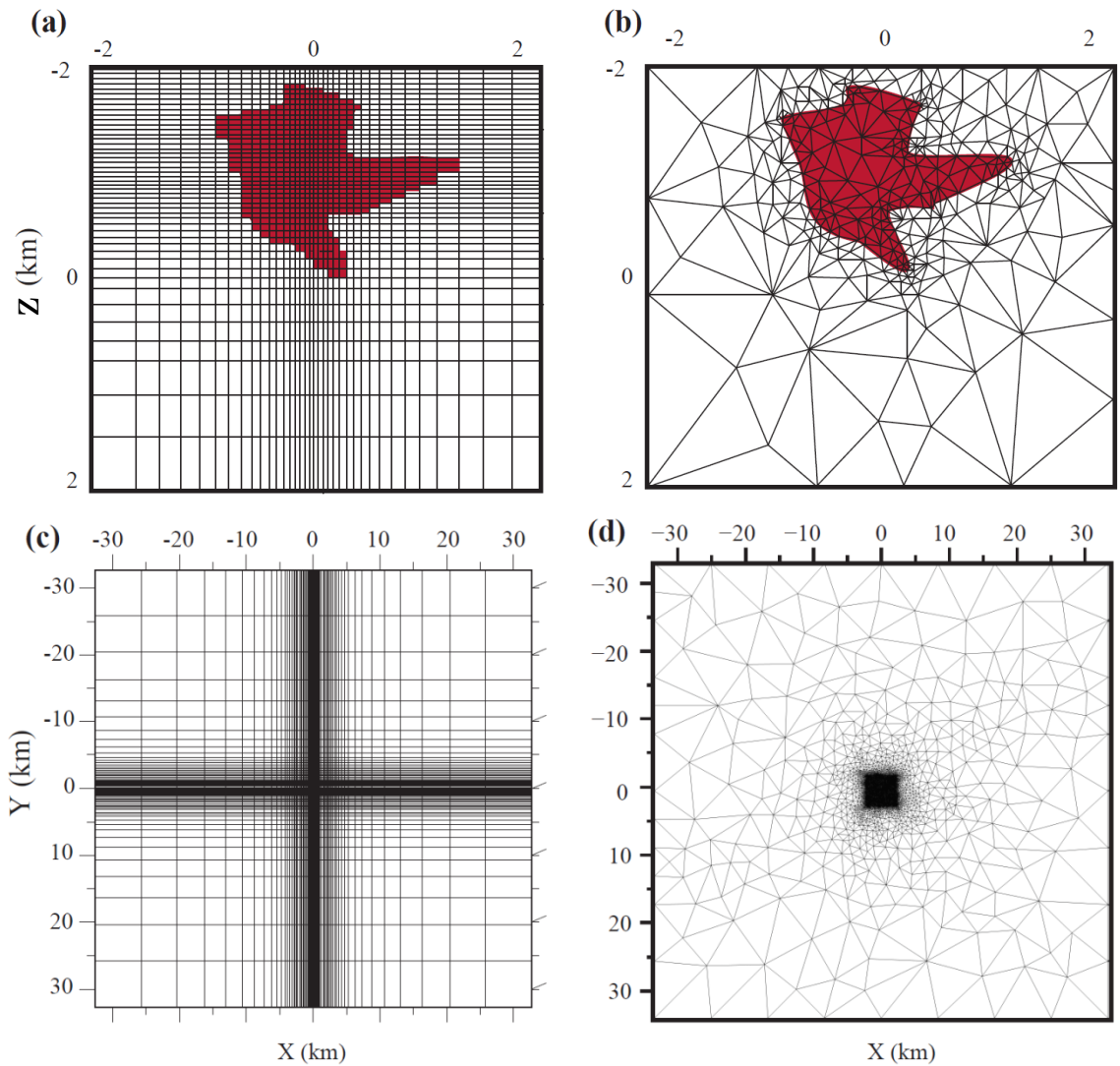


Figure 2.10: Generating a complex underground body using (a) structured rectilinear and (b) unstructured tetrahedral grids. A plan view of the entire mesh subdivided into (c) structured and (d) unstructured elements (images courtesy SeyedMasoud Ansari).

mesh. Refinement in a structured mesh causes cells to emanate out from the refined region in a cross pattern throughout the entire mesh to the boundary (see Figure 2.10c) For practical reasons, this is inefficient because small cells are forced to be in areas where they are not needed, and small cells near the boundary of the mesh can result in computational inefficiencies. However, since the FE method is

more involved, it is more mathematically challenging, complicated, and not as straightforward to implement as the FD method.

The formulation of the FE method is based on the principle of energy minimization (Coggon, 1971) and the first applications of the FE method computing electromagnetic fields for a 3D conductivity model used nodal elements on a rectilinear mesh (Pridmore et al., 1981; Livelybrooks, 1993; Mogi, 1996). The nodal element approach contains scalar basis functions located at cell vertices and is non-zero only in the cells that share the vertex as shown in Figure 2.11. The basis function is equal to unity at the vertex, decreases linearly in each direction, and is equal to zero in all surrounding cells. However, if nodal basis functions are used for solving the Helmholtz equation (Equation 2.22), then the divergence free and discontinuous normal electric field conditions will not be satisfied (Jin, 2002).

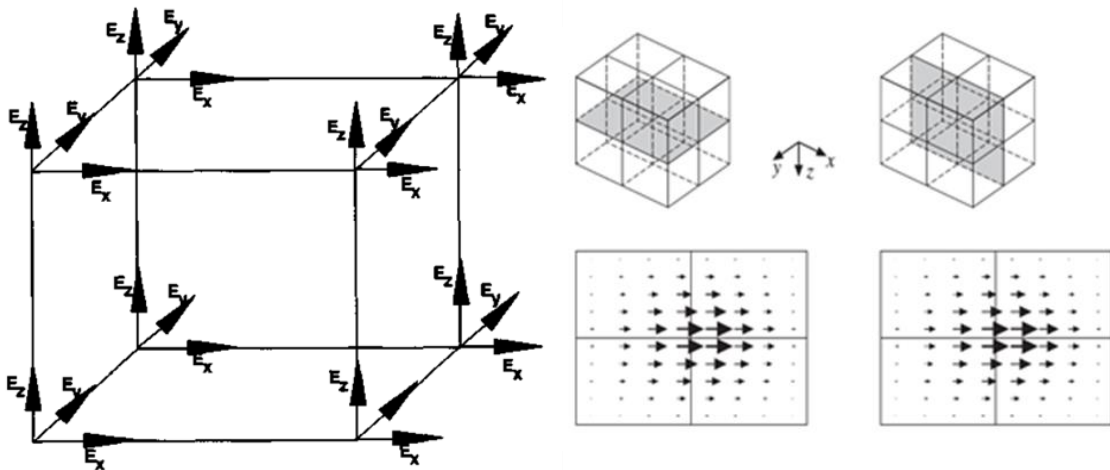


Figure 2.11: (left) A standard hexahedral cell illustrating the *nodal-element approach* (Sugeng, 1998), and (right) a nodal basis function for the x-component of the field shown for  $xy$  and  $xz$  planes (Farquharson and Miensopust, 2011).

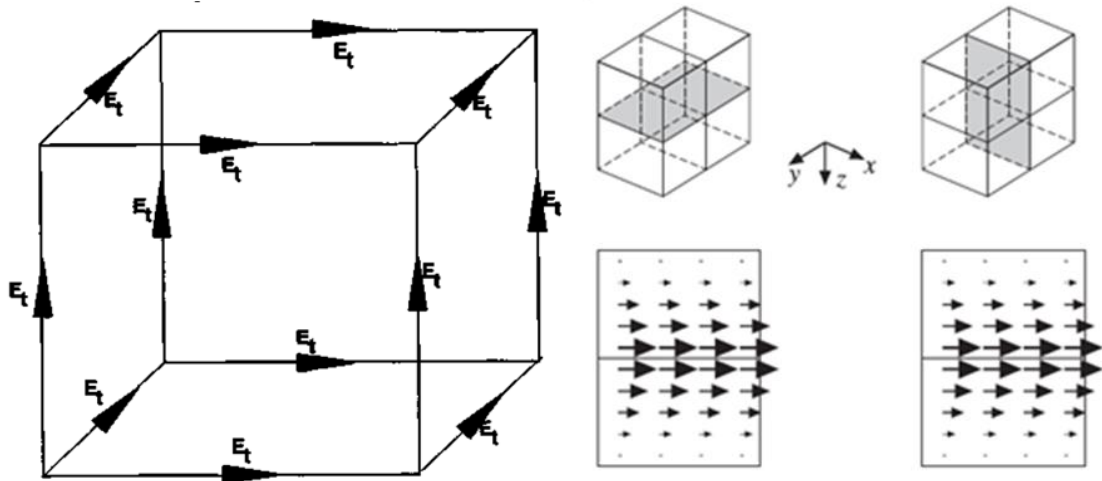


Figure 2.12: (left) A standard hexahedral cell illustrating the *edge-element approach* (Sugeng, 1998) and (right) an *x*-directed edge-element basis function shown for *xy* and *xz* planes through the shared edge (Farquharson and Miensopust, 2011).

The solution to this problem is to use Nédélec's vector edge elements instead (Nédélec, 1980). These vector basis functions are associated with a particular edge and are nonzero only in the cells that share the edge as shown in Figure 2.12. The vector basis function has a magnitude of unity along the edge, varies linearly in directions perpendicular to the shared edge, invariant in the direction of the shared edge, and is equal to zero on all edges of surrounding cells. This basis function formulation allows for the normal component of the electric field to be discontinuous, the divergence free condition is satisfied, and the numerical computation is reduced as the number of unknowns per hexahedral element is 12 instead of 24 (Sugeng, 1998).

There have been many studies using this edge-element approach to solve for the electric field on structured grids (Sugeng, 1998; Nam et al., 2007; Farquharson and

Miensopust, 2011) and unstructured grids (Liu et al., 2008; Schwarzbach et al., 2011; Vieira da Silva, 2012). These studies express the vector Helmholtz equation solely in terms of the electric or magnetic field which can result in computational inefficiencies when very low frequencies are considered (Ansari and Farquharson, 2014). However, studies have shown that decomposing the primary fields into vector and scalar ( $\mathbf{A}$ ,  $\Phi$ ) potentials can help alleviate this inefficiency (e.g., Badea et al., 2001; Mitsuhata and Uchida, 2004; Puzyrev et al., 2013). Badea et al. (2001) and Puzyrev et al. (2013) use nodal basis functions for both vector and scalar potentials, but this approach violates the necessity, from the Coulomb gauge condition, of the vector potential being divergence free in a source-free element (Ansari and Farquharson, 2014). Mitsuhata and Uchida (2004) decompose the magnetic field into vector and scalar potentials and expand them using edge-element and nodal-element basis functions respectively which satisfies the condition just mentioned, but this formulation is limited to the magnetotelluric forward problem. Ansari and Farquharson (2014) present a FE solution to the 3D EM forward problem by decomposing the electric field into vector and scalar potentials and expanding them using edge-element and nodal-element basis functions. This formulation satisfies the necessary conditions mentioned previously and is suitable for marine CSEM applications.

#### **2.2.4 3D Forward Modeling in the Context of Marine CSEM**

Over the past two decades, there has been much advancement in the literature regarding improvements to modeling 3D EM problems and some of these studies

have been tailored to the application of marine CSEM. A seminal paper given by Constable and Weiss (2006) applied a 3D FD method to a simple marine CSEM model with a flat seafloor and a buried disk representing a hydrocarbon reservoir (i.e. the *canonical disk model*). Li and Key (2007) developed an adaptive FE solver and applied it to a complex synthetic salt model with multiple topographical layers, but this solver was *limited to 2D models*. This 2D code of Li and Key (2007) was later extended to 2D joint inversion with MT (Key, 2016) and this code was applied to another complex synthetic salt model. Um et al. (2010) used a 3D time-domain FE method on a rendition of the canonical disk model that was extended to contain a dipping seafloor. Schwarzbach et al. (2011) developed a 3D adaptive FE method and applied it to a synthetic seafloor topography model. Um et al. (2013) used a 3D FE solver on a modified version of the SEG salt model which contained seafloor topography, a salt body, and a dipping cylindrical disk for the hydrocarbon reservoir. Puzyrev et al. (2013) applied a 3D parallel FE method to a complex synthetic model with seafloor bathymetry and subsurface topographical layers. Most recently, Zhang and Key (2016) developed a 3D parallel adaptive FE method, but their published examples thus far appear to be limited (i.e. seafloor bathymetry models). What all these examples appear to be lacking is the application of a 3D forward modeling method to *real* complex models *built from real data*.

### 2.2.5 CSEM3DFWD

The code chosen for this thesis is the 3D FE forward modeling code, CSEM3DFWD, using vector and scalar potentials ( $\mathbf{A}$ ,  $\Phi$ ) on unstructured grids given by Ansari and Farquharson (2014). This code was chosen because it is readily available (developed in-house) and the finite-element method supports the utilization of unstructured meshes. An unstructured mesh is important to model complex geologies and incorporate local refinements which are necessary for marine CSEM data simulation. A high level summary of the mathematical basis of the code is given below.

This formulation still assumes the fields operate in the quasi-static regime and in the frequency domain, so the Helmholtz equation (Equation 2.22) is still appropriate. However, this approach uses potentials and not the fields themselves. Recall that the magnetic field must be divergence-free ( $\nabla \cdot \mathbf{B} = 0$ ) and consequently it can be expressed as the curl of a vector potential,  $\mathbf{A}$ :

$$\mathbf{B} = \nabla \times \mathbf{A}. \quad (2.23)$$

Substituting this into Faraday's law gives,

$$\mathbf{E} = -i\omega\mathbf{A} - \nabla\Phi \quad (2.24)$$

where  $\Phi$  is the scalar potential (Ward and Hohmann, 1988). The vector-scalar potential equation (Equation 2.24) is substituted into the Helmholtz equation (Equation 2.22):

$$\nabla \times \nabla \times \mathbf{A} + i\omega\mu_o\sigma\mathbf{A} + \mu_o\sigma\nabla\Phi = \mu_o\mathbf{J}_s \quad (2.25)$$

where a new Helmholtz equation is formed, but in terms of vector and scalar potentials ( $\mathbf{A}$ ,  $\Phi$ ). Unfortunately, this new equation contains four unknowns ( $\mathbf{A}_x$ ,  $\mathbf{A}_y$ ,  $\mathbf{A}_z$ ,  $\Phi$ ) instead of three ( $\mathbf{E}_x$ ,  $\mathbf{E}_y$ ,  $\mathbf{E}_z$ ), so an additional equation is needed. The equation for the conservation of charge

$$\nabla \cdot \mathbf{J} = -\nabla \cdot \mathbf{J}_s \quad (2.26)$$

is used, and substituting in Ohm's law and Equation 2.24 gives,

$$-i\omega\nabla \cdot (\sigma\mathbf{A}) - \nabla \cdot (\sigma\nabla\Phi) = -\nabla \cdot \mathbf{J}_s. \quad (2.27)$$

The natural boundary conditions are used for Equations 2.25 and 2.27 and the system of equations is discretized using the FE approach. First, vector and scalar residuals are formed from Equations 2.25 and 2.27 respectively

$$\mathbf{r} = \nabla \times \nabla \times \tilde{\mathbf{A}} + i\omega\mu_o\sigma\tilde{\mathbf{A}} + \mu_o\sigma\nabla\tilde{\Phi} - \mu_o\mathbf{J}_s \quad (2.28)$$

$$r = -i\omega\nabla \cdot (\sigma\tilde{\mathbf{A}}) - \nabla \cdot (\sigma\nabla\tilde{\Phi}) + \nabla \cdot \mathbf{J}_s \quad (2.29)$$

where  $\tilde{\mathbf{A}}$  and  $\tilde{\Phi}$  are the approximated vector and scalar potentials. The inner products of the vector and scalar residuals with a weight function ( $\mathbf{W}$ ,  $\nu$ ) for each are integrated over the entire domain and equated to zero so a good solution can be obtained. The *surface terms* are removed to arrive at the following expressions,

$$\int_{\Omega} (\nabla \times \mathbf{W}) \cdot (\nabla \times \tilde{\mathbf{A}}) d\Omega + i\omega\mu_o \int_{\Omega} \sigma \mathbf{W} \cdot \tilde{\mathbf{A}} d\Omega + \mu_o \int_{\Omega} \sigma \mathbf{W} \cdot \nabla \tilde{\Phi} d\Omega = \mu_o \int_{\Omega} \mathbf{W} \cdot \mathbf{J}_s d\Omega \quad (2.30)$$

$$i\omega \int_{\Omega} \nabla \nu \cdot \sigma \tilde{\mathbf{A}} d\Omega + \int_{\Omega} \nabla \nu \cdot \sigma \nabla \tilde{\Phi} d\Omega = - \int_{\Omega} \nu \nabla \cdot \mathbf{J}_s d\Omega \quad (2.31)$$

To solve these two equations (Equation 2.30 and 2.31), the computational domain is subdivided into a grid of unstructured tetrahedral elements. Within each element, the approximated vector and scalar potentials are expressed in terms of vector and scalar basis functions:

$$\tilde{\mathbf{A}} = \sum_{j=1}^{n_A} \tilde{\mathbf{A}}_j N_j \quad \tilde{\Phi} = \sum_{k=1}^{n_{\Phi}} \tilde{\Phi}_k N_k \quad (2.32)$$

where  $\mathbf{N}_j$  and  $N_k$  are vector and scalar basis functions respectively, and the parameters  $\tilde{\mathbf{A}}_j$  and  $\tilde{\Phi}_k$  are the unknown vector and scalar coefficients to be determined. The Galerkin method of weighted residuals is used where the weighting functions  $(\mathbf{W}, \nu)$  are chosen to be equal to the basis functions  $(\mathbf{N}_j, N_k)$  and  $\tilde{\mathbf{A}}_j$  and  $\tilde{\Phi}_k$  in Equations 2.30 and 2.31 are replaced with their basis function representations in Equation 2.32. This forms a system of equations that is ultimately solved using an iterative solver called generalized minimal residual (GMRES) from SPARSKIT (Saad, 1990). Once the system solves for the vector and scalar potentials, the electric field is obtained using Equation 2.24.

### 2.2.5.1 Computational requirements

GMRES, as mentioned above, is an iterative solver and the  $n$ th iterate minimizes the residual in the Krylov subspace  $K_n$ . The dimension of this Krylov subspace and the number of cells in a mesh determine the maximum amount of running memory required to solve the system of equations. Computational resources are not unlimited, so all meshes in this thesis were created with this in mind.

Figure 2.13 shows this relationship between the amount of cells, the Krylov subspace, and the required memory encountered in this thesis. The small squares for each Krylov subspace represent memory requirements for meshes actually used in this work. An interpolation/extrapolation for each Krylov subspace shows a linear relationship between memory and number of cells.

At different stages in this thesis, the threshold of available memory (i.e. RAM) was set by limitations of the code and the actual computational resources used. In

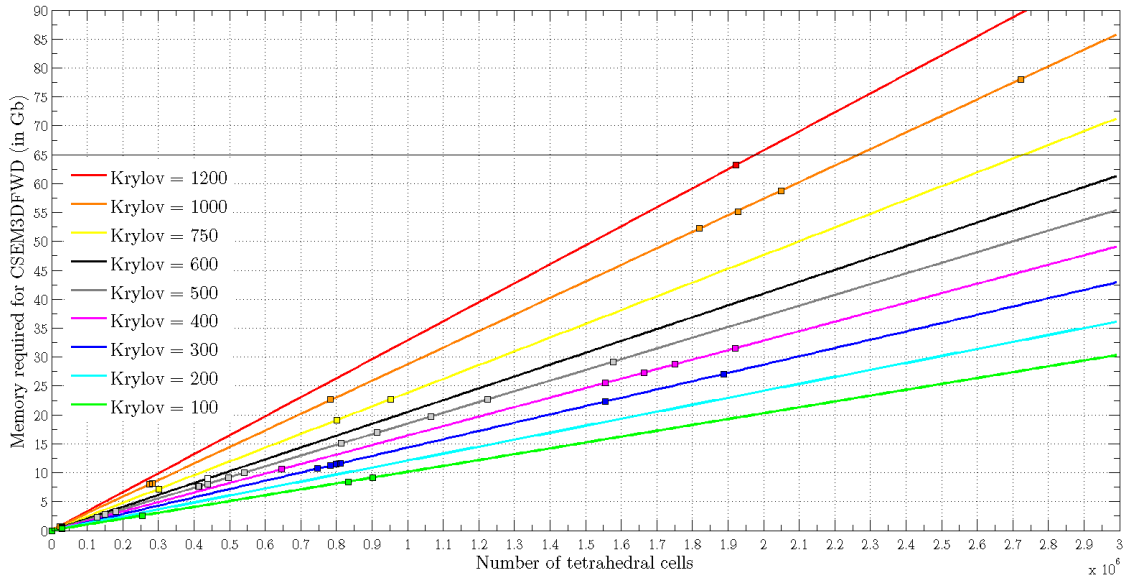


Figure 2.13: The computational requirements of the GMRES iterative solver for the finite-element forward modeling code given by Ansari and Farquharson (2014). The maximum memory required to solve the system of equations is plotted against the number of cells in a mesh for varying degrees of the Krylov subspace. The small squares indicate the memory required for the size of meshes used throughout this thesis.

Chapter 4, all numerical simulations were performed on a Dell Optiplex 9020 desktop computer (3.2 GHz Intel Core i5 processor) with 16GB RAM. However, for Chapter 5 all numerical simulations were performed on a cluster containing CPU nodes with 24GB RAM and GPU nodes with 64GB RAM. Unfortunately, at this point there was a bug in the code that prevented simulations from requiring more than 32GB RAM. This bug was fixed for the simulations in Chapter 6 and the solver could utilize the full memory capacity of the GPU nodes. Refer back to Figure 2.13 to determine the memory requirements for a given Krylov subspace and mesh size because this information is not always given explicitly in the text.

# Chapter 3

## Model Building and Forward Modeling

Many numerical methods for solving electromagnetic problems have been developed in the past couple of decades as discussed above, and research is likely to continue in these areas to achieve more efficient and accurate solutions. Applying these codes to model realistic geology is also a growing area of interest. However, a majority of the 3D EM forward modeling literature develop codes to only (1) compare results with known analytical or published results, or (2) extend their codes to simple (sometimes novel) models. Most researchers start by comparing their results to very simple models with known analytical solutions for validation. The other standard procedure is to compare results to published results such as the COMMEMI prism models (Zhdanov et al., 1997) or the canonical disk model for marine CSEM (Constable and Weiss, 2006).

These are always important starting points to show that a forward modeling code is accurate and efficient; however, once this is achieved, it is necessary to apply the code to more complex and realistic models. The studies discussed in Section 2.2.4

showed that there have been many investigations applying 3D forward modeling algorithms to synthetic (and sometimes complex) models. The most noteworthy is the study conducted by Puzyrev et al. (2013) where they used a 3D parallel FE method to simulate marine CSEM data from a complex *synthetic* model as shown in Figure 3.1. The focus of this thesis is to simulate marine CSEM data from models of this nature, but taking one step further, they will be *real* models based on *real* data from the Flemish Pass Basin.

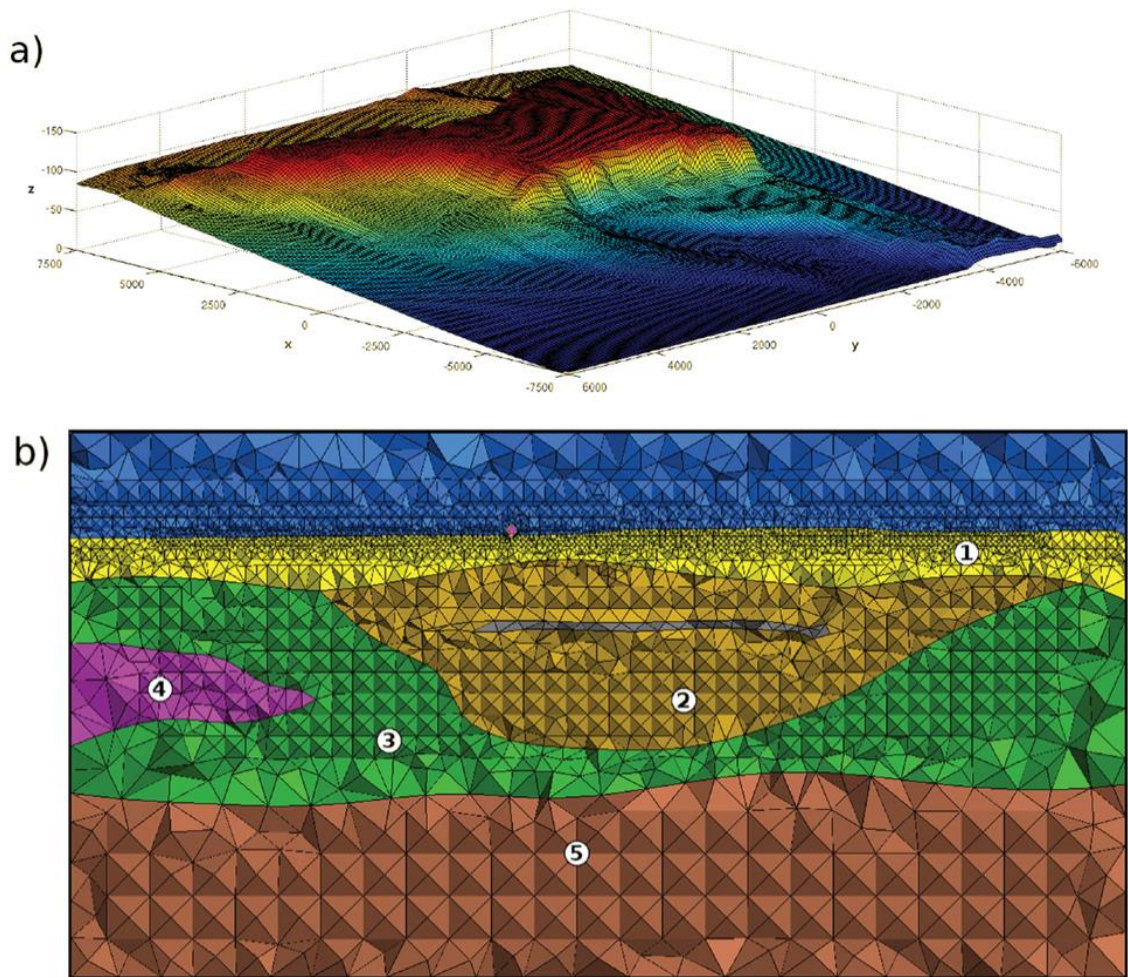


Figure 3.1: An example of a marine CSEM complex synthetic model showing the (a) seafloor bathymetry and (b) an X-Z slice through the center of the mesh (Puzyrev et al., 2013).

### 3.1 The Five-Step Forward Modeling Process

The integral processes behind this thesis are the sequence of steps necessary to simulate marine CSEM data from *any* model. Specifically, this is an *iterative* process consisting of five main steps as depicted in Figure 3.2. This process shows the progression of steps needed to build a model and simulate marine CSEM data based on that model for the studies performed in the three subsequent chapters (Chapters 4, 5, and 6). A general explanation of each of the steps is given below.

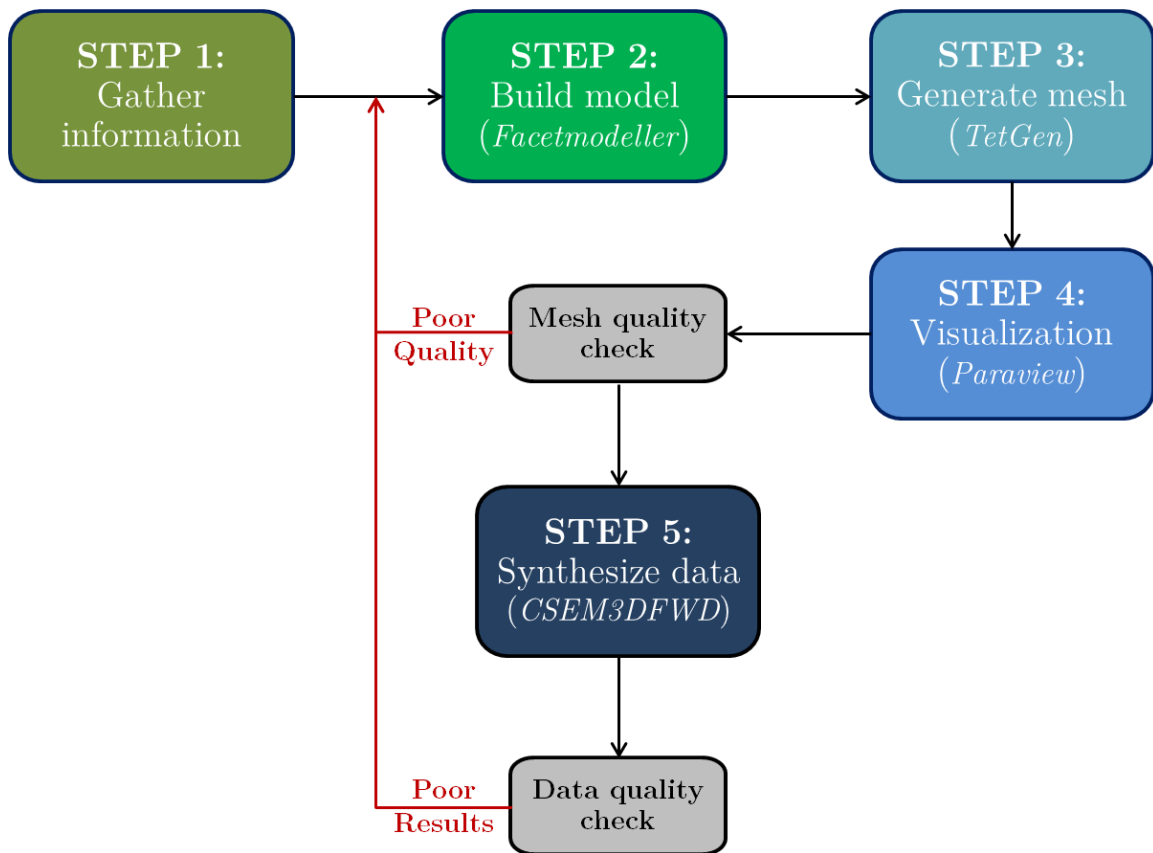


Figure 3.2: A diagram depicting the iterative five-step process used to progress through the sequence of steps necessary to build a model and simulate marine CSEM data based on that model. The five steps include (1) gathering information, (2) building the model, (3) generating the mesh, (4) visualizing the mesh, and (5) simulating data.

### 3.1.1 Step I: Gathering Information

The first step necessary for the forward modeling process is gathering the information required to build the model. For any model, the dimensions of the whole model, referred to as the volume of interest (VOI), need to be established. The dimensions for x, y, and z varied for the models considered in this thesis, but as a general rule, the lateral extents were chosen such that the boundaries of the model were *8-10 skin depths* away from the transmitter. This is needed because the CSEM3DFWD code assumes a *zero* boundary condition, and the transmitter needs to be sufficiently far from the boundary for that condition to hold. However, in order to know what the skin depth is (see Equation 2.11), the intended frequencies and approximate resistivities of the model must be known. For the synthetic models considered in this study, the resistivities were pre-determined in order to match responses with published results. Conversely, the real models require concrete data to determine the resistivities, and this was done by using resistivity logs from the appropriate regions.

Another component that is critical to know prior to model building is the model geometry (i.e. layers). For the synthetic models, this only required knowledge of the desired depth to certain layers because the layers were assumed to be flat. However, this was a much more complicated process for the real models. Geochronologic surfaces (seafloor, base Tertiary, etc.) were created by Nalcor Energy via Petrel (a software platform used in the exploration and production sector of the petroleum industry) by combining horizons on many 2D seismic lines

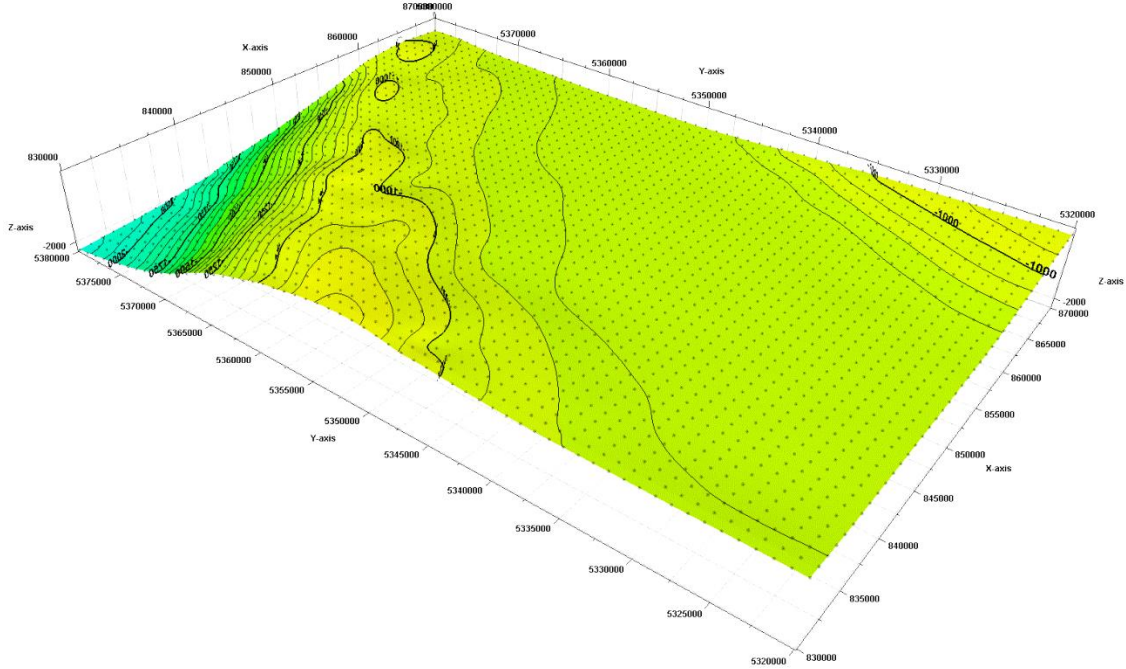


Figure 3.3: An example schematic showing the topography of the seafloor in a region of the Flemish Pass Basin. The vertical exaggeration is 7.5x. The black dots are points (or nodes) used to represent the surface and serve as an input for reproducing this surface in the modeling building stage.

in the Flemish Pass Basin and then interpolating. An example of a seafloor surface in the Flemish Pass derived from 2D seismic lines and interpolation is shown in Figure 3.3. Some minor processing had to be done to these surfaces to prepare them for the model building stage. The surfaces were passed through de-spiking filters to remove any interpolation artifacts. Unfortunately, the surfaces themselves cannot be directly imported to the model building software. However, the surface can be represented with discrete XYZ points (see the black dots on the surface in Figure 3.3). These points (or nodes) can be exported into a file which is needed for Step II.

One of the last things to have prepared for model building is determining the acquisition information. This includes considering the transmitter position and orientation, and also the placement for the observation locations. For the synthetic examples, these parameters were chosen to mimic those in the literature, or they were made up. However, for the real models, the transmitter and receiver information was extracted from the EMGS acquisition data files. These three pieces of data and information are the primary inputs needed to begin building a model.

### **3.1.2 Step II: Building the Model**

The model itself was built using in-house software called FacetModeller developed by Peter Lelièvre. To start, a 3D model must be defined by establishing the VOI. The *building* of the 3D model is accomplished through a manual process of adding points (nodes) and facets (planar shape in 3D, segments in 2D).

An integral part of building the real models was actually importing the 3D surfaces into the VOI and the process to accomplish this was quite involved. First of all, the XYZ topography file of a surface from Petrel only contains nodes, but facets are needed in order to connect the nodes and truly make it a surface that FacetModeller can recognize. This involved importing the XYZ points into a 2D FacetModeller session in order to generate a file which could be triangularized (filled with triangles) using a piece of public-domain software called Triangle (Shewchuk, 1996). After using Triangle, the files needed to import the 3D surface

into FacetModeller are obtained. A step-by-step description of this process is given below.

- 1) The XYZ points file of the surface from Petrel is imported into a *2D FacetModeller* session.
- 2) Linear facets are added around the boundary of the surface connecting all nodes along the boundary (to enclose the surface).
- 3) A .poly file is exported from FacetModeller that contains all XY points and the facets created for the boundary (note: the output does erase the third dimension, but this is fine for now).
- 4) This .poly file is triangularized (filled with triangles) using a software called Triangle (Shewchuk, 1996). The usage of Triangle in the command line is given in Appendix A, and the switches used for all surfaces in this thesis is the following:

```
triangle.exe -pqADjPNS0CV surface.poly
```

- 5) The output from Triangle is a .ele file which describes the elements (facets) of the 2D triangular mesh.
- 6) The .ele file from Triangle and the original XYZ points file (note: must be in .node format) can be inputted as a pair into a 3D FacetModeller session to finally have the 3D topographical surface in the model.

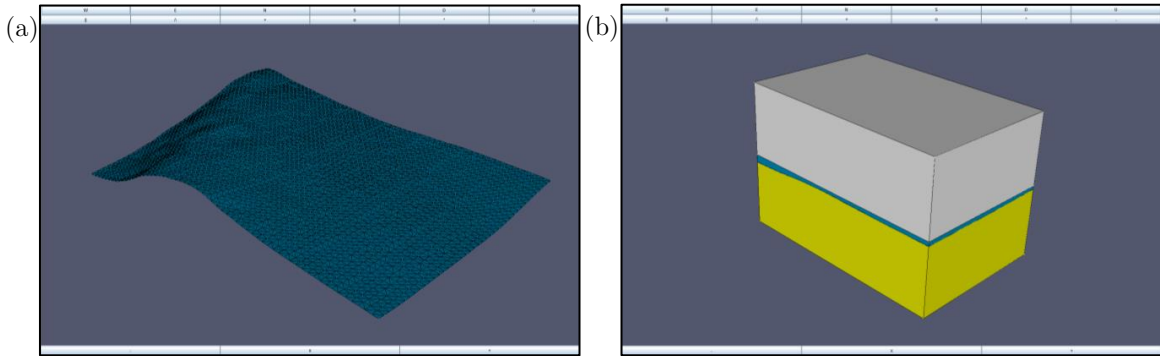


Figure 3.4: The surface (a) from Figure 3.3 once it has been imported into a 3D FacetModeller session and (b) the full model with the boundary facets added enclosing each region.

This process describes how a surface in Petrel (Figure 3.3) is imported into a 3D FacetModeller session. Figure 3.4(a) shows what the same surface in Figure 3.3 appears as once it is imported into FacetModeller. Some surfaces did not always have topography (ex. the synthetic models), so obviously this whole process was not needed for those instances. A flat surface could easily be made within FacetModeller by simply adding four nodes at equal depth and connecting them all with a single rectangular facet.

Importing and establishing the surfaces is one stage of building the model, but the entire VOI must be enclosed with no holes. This is accomplished by adding boundary facets on the edges of the model and this ensures that the regions of the model are enclosed. An example of the model once the boundary facets are added is shown in Figure 3.4(b). This example model contains three regions: the air, the seawater, and the sub-seafloor sediments. Once the VOI is enclosed, a .poly file containing all the nodes and facets can be exported which is used to generate the

*mesh*. An XYZ point lying inside each region of the model (three for this example) must be added to the end of the .poly file prior to meshing.

### 3.1.3 Step III: Generating the Unstructured Mesh

An *unstructured mesh* is simply the 3D model from FacetModeller filled in with *tetrahedral cells*. A mesh is needed because it serves as the computational domain for the forward modeling code as the vector and scalar potentials are solved for on the tetrahedral edges and nodes respectively (see Section 2.2.5).

The .poly file output from FacetModeller is tetrahedralized using public-domain software called TetGen (Si, 2007). This piece of software is quite involved and there are many different switches and input files that can be used to create, modify, and refine a mesh (see Appendix B). The command line syntax commonly used to generate meshes throughout this entire thesis is the following,

```
tetgen.exe -pq1.414/16AmfenCV 3Dmodel.poly
```

All the switches here are discussed in Appendix B. The only portion of the switches that changed the most throughout the thesis are the **-q** and **-m** switches. The two numbers that follow the **-q** switch are the general refinement constraints for the maximum radius-edge ratio and the minimum dihedral angle. These constraints have a strong correlation to the amount of cells generated for the mesh, so at times these numbers were modified either to improve mesh quality or reduce the number of cells. The **-m** switch is used in conjunction with a .mtr file which contains a file specifying the desired edge lengths in the resulting mesh by

assigning values to input nodes. This .mtr file changed depending on the input model and the desired outcome.

The output from TetGen is obviously the files needed to represent the mesh (mesh.1.ele, mesh.1.node, mesh.1.face, mesh.1.edge, mesh.1.neigh), but the command prompt also outputs some useful statistics about the mesh. Figure 3.5 shows the TetGen command line statistics of the output mesh from the input model shown in Figure 3.4(b). This output served as a useful debugging tool and provided useful information regarding the resulting mesh. The output gives the number of tetrahedra (e.g. 754,950) and the number of points added to the model in order to achieve the desired level of refinement (e.g.  $86,878 + 25,001 + 8,181$ ). More importantly, the output gives statistics on mesh quality which was one tool used to assess the quality of the mesh and determine if changes needed to be made.

A valid question to ask is what distinguishes a poor quality from a good quality mesh? A poor quality mesh is considered to be one that contains many cells with large aspect ratios and really small, *or* really large dihedral angles. These types of poor quality cells translate to long, skinny tetrahedra. Solving for the vector and scalar potentials around these cells causes inaccuracies and poor convergence for the iterative solver in CSEM3DFWD. Consequently, good quality meshes are sought, and the statistics output from TetGen, like the one shown in Figure 3.5, can help determine if a mesh is of good quality, or not. One goal is to have the smallest and largest dihedral angles be large and small respectively (the same can be said for face angles). Another goal is to have the fewest amounts of cells with

```

Statistics:

Input points: 3407
Input facets: 6015
Input segments: 4823
Input holes: 0
Input regions: 3

Mesh points: 123467
Mesh tetrahedra: 745950
Mesh faces: 1496469
Mesh faces on facets: 73467
Mesh edges on segments: 13004
Steiner points inside domain: 86878
Steiner points on facets: 25001
Steiner points on segments: 8181

Mesh quality statistics:

Smallest volume:          13.762 | Largest volume:          6.7245e+10
Shortest edge:           4.8998 | Longest edge:            12019
Smallest asp.ratio:      1.2247 | Largest asp.ratio:       14.64
Smallest facangle:       15.865 | Largest facangle:       136.9381
Smallest dihedral:       6.1343 | Largest dihedral:       164.9566

Aspect ratio histogram:
  < 1.5      : 24405 | 6 - 10      : 1414
  1.5 - 2    : 230848 | 10 - 15     : 46
  2 - 2.5    : 257909 | 15 - 25     : 0
  2.5 - 3    : 129285 | 25 - 50     : 0
  3 - 4      : 78985  | 50 - 100    : 0
  4 - 6      : 23058  | 100 -       : 0
(A tetrahedron's aspect ratio is its longest edge length divided by its
smallest side height)

Face angle histogram:
  0 - 10 degrees: 0 | 90 - 100 degrees: 190044
  10 - 20 degrees: 94 | 100 - 110 degrees: 71873
  20 - 30 degrees: 89421 | 110 - 120 degrees: 21260
  30 - 40 degrees: 476977 | 120 - 130 degrees: 2990
  40 - 50 degrees: 885881 | 130 - 140 degrees: 159
  50 - 60 degrees: 967435 | 140 - 150 degrees: 0
  60 - 70 degrees: 843486 | 150 - 160 degrees: 0
  70 - 80 degrees: 575073 | 160 - 170 degrees: 0
  80 - 90 degrees: 364714 | 170 - 180 degrees: 0

Dihedral angle histogram:
  0 - 5 degrees: 0 | 80 - 110 degrees: 1043228
  5 - 10 degrees: 169 | 110 - 120 degrees: 162998
  10 - 20 degrees: 21170 | 120 - 130 degrees: 98874
  20 - 30 degrees: 131507 | 130 - 140 degrees: 56714
  30 - 40 degrees: 327146 | 140 - 150 degrees: 33750
  40 - 50 degrees: 584423 | 150 - 160 degrees: 7058
  50 - 60 degrees: 731613 | 160 - 170 degrees: 305
  60 - 70 degrees: 708527 | 170 - 175 degrees: 0
  70 - 80 degrees: 568218 | 175 - 180 degrees: 0

Memory usage statistics:

Maximum number of tetrahedra: 756501
Maximum number of tet blocks (blocksize = 8188): 93
Approximate memory for tetrahedral mesh (bytes): 120,900,160
Approximate memory for extra pointers (bytes): 7,449,792
Approximate memory for algorithms (bytes): 3,422,480
Approximate memory for working arrays (bytes): 18,860,148
Approximate total used memory (bytes): 150,632,580

```

Figure 3.5: The TetGen command line statistics of the mesh created from the input model shown in Figure 3.4(b). Inspection of the mesh quality statistics can be used to help determine if the quality of a mesh is satisfactory for numerical simulation. This example mesh was good quality.

large aspect ratios. This thesis considered any cell with an aspect ratio  $> 6$  to be a poor quality cell (the second column). Numerical data can be helpful in assessing mesh quality, but an alternative or supplemental method is to actually visualize the mesh itself.

### 3.1.4 Step IV: Visualization

TetGen outputs a number of files that can be used to visualize the mesh. One of Peter Lelièvre's utility programs written in Fortran, `mest2vtu.exe`, combines all the mesh outputs from Tetgen into a `.vtu` file which is used to input into a program called Paraview. This mesh visualization software allows the freedom for one to view the mesh through cuts, slices, thresholds, etc. All figures of unstructured meshes shown in this thesis were made using Paraview. An example of the unstructured mesh from the statistics given in Figure 3.5 is shown in Figure 3.6. Thresholds and cuts of this nature allow one to see the *inside* of the mesh and also the behavior of the cells on surface interfaces.

In many cases, any significant number of poor quality cells noted in the statistics will be evident in the mesh itself. However, there can be instances (many times in this thesis) where the quality statistics would indicate a reasonable amount of poor cells, but they would not be evident (or easily visible) in the mesh itself. So, it is important to consider both pieces of information. Upon inspecting the mesh and reading the statistics, a decision must be made if the mesh is acceptable. If the mesh is not acceptable, as the process in Figure 3.2 indicates, then the process

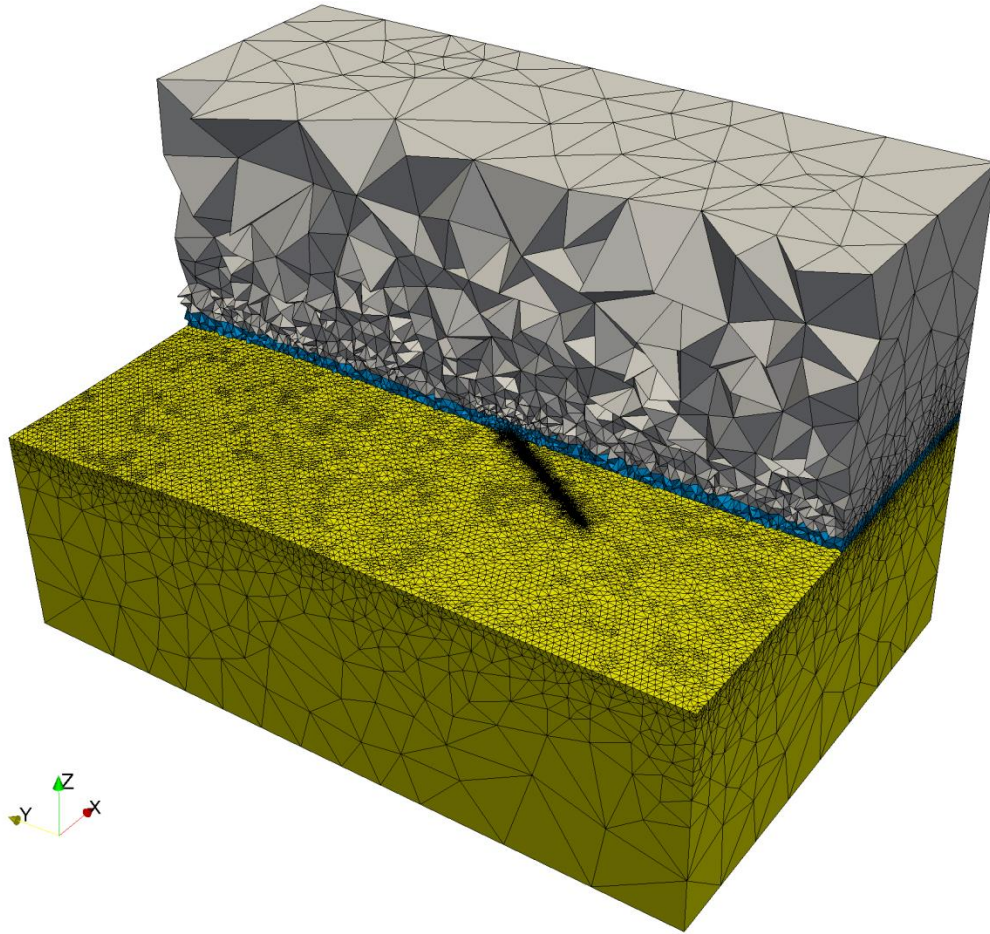


Figure 3.6: The unstructured mesh as a result of tetrahedralization of the input model from Figure 3.4. The same three regions are shown and this unstructured mesh exhibits the benefit of local refinement (at observation locations) while containing larger cells nearby in the mesh.

cycles back to regenerating the mesh, or making changes at the model building stage. If the mesh quality is acceptable, then the next stage is data simulation.

### 3.1.5 Step V: Data Simulation

Once the mesh is deemed acceptable, it is ready for marine CSEM data simulation using the CSEM3DFWD code. The first sets of inputs are the mesh output files from TetGen (mesh.1.ele, mesh.1.edge, mesh.1.node, mesh.1.neigh, mesh.1.node).

The second set of inputs is two files: one that specifies the resistivities of the regions and a second that specifies the dimensions of the VOI, source geometry, receiver locations, and the GMRES parameters (number of iterations and size of the Krylov subspace).

There are two main outputs when the code finishes: (1) the residual norm of the iterative solver versus the number of iterations, and (2) the solutions for the real and imaginary components of the in-line electric field. Figure 3.7 shows the decay of the residual norm and in-line amplitude for the mesh shown in Figure 3.6. No change in the residual norm (beyond 750 iterations in Figure 3.7) indicates the solution has reached convergence. However, just because a solution has converged does not necessarily mean the results are accurate. The relative decrease in the residual norm is an indication of *how well* the solution converged. A greater reduction is a good indicator that the iterative solver converged to a more accurate solution (this claim is based on the many simulations performed for this study). The data itself is the other output and the in-line electric field amplitude and phase are determined simply by,

$$E_{amplitude} = \sqrt{E_{real}^2 + E_{imaginary}^2} \quad (3.1)$$

$$\varphi = \text{atan}\left(\frac{E_{imaginary}}{E_{real}}\right) \quad (3.2)$$

At this stage, the quality of the data needs to be checked and this can be done by visually inspecting the data and convergence. The data is possibly not accurate enough if the curves are not *smooth* (i.e. bumps/jumps in the data). If this is the case, as Figure 3.2 indicates, the modeling process cycles back to make changes to

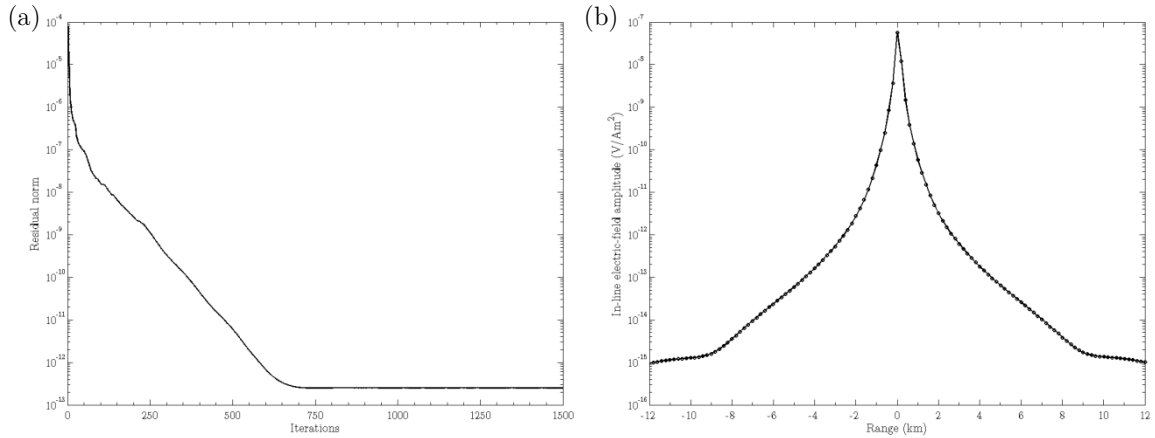


Figure 3.7: (a) The residual norm of the iterative solver versus the number of iterations, and (b) the in-line electric field amplitude for the mesh shown in Figure 3.6. The convergence is adequate as it levels off and the residual norm reduces by many orders of magnitude. The in-line electric field amplitude is smooth and the data is therefore deemed accurate.

the initial model and/or modify the mesh. However, if the curves appear smooth (and either match published results, or measured data in the upcoming chapters) and the convergence is satisfactory, then the forward data is likely acceptable.

These five steps show the high-level modeling process used for the proceeding chapters of this thesis. The three upcoming chapters apply this modeling methodology to two synthetic examples, and two real exploration examples at the Mizzen and Bay du Nord fields in the Flemish Pass Basin.

# Chapter 4

## Synthetic Forward Models

### 4.1 Marine Halfspace Model

The important starting place for this thesis was to begin by synthesizing marine CSEM data from a *simple synthetic model* in order to become familiar with the modeling process and the software involved. A logical choice for the starting model was a marine halfspace. The dimensions of the model were  $x = [-10 \text{ km}, 10 \text{ km}]$ ,  $y = [-10 \text{ km}, 10 \text{ km}]$ ,  $z = [-10 \text{ km}, 5 \text{ km}]$ . A horizontal interface was placed at  $z = 0 \text{ km}$  to serve as the boundary between seawater and sediments (the two layers). The conductivity of the seawater and sediments were set to  $3.3 \text{ S/m}$  and  $1.0 \text{ S/m}$  respectively. The transmitter was chosen to be an x-directed HED with a frequency of  $1.0 \text{ Hz}$  and was placed  $50\text{m}$  above the origin at  $(x, y, z) = (0, 0, 50\text{m})$ . The skin depth in the seawater and sediments are approximately  $275\text{m}$  and  $500\text{m}$  respectively, therefore, the boundary of the model is enough skin depths away to satisfy the zero boundary condition. The observation locations (receivers) were chosen to range from  $x = [-2 \text{ km}, 2 \text{ km}]$  at  $y = 0\text{m}$  and  $z = 0.01\text{m}$  with a  $10\text{m}$

spacing. There were four individual tests performed on this halfspace model, each with incremental changes, in order to recover accurate results. All the amplitude and phase responses were compared to a semi-analytic response based on a 1D Hankel transform computed by the code, DIPOLE1D, provided by Key (2009).

### 4.1.1 Test I

The first test was an initial attempt to try and create a mesh suitable for numerical simulation. No complex strategies for refinement were employed here, however, nodes were placed on the seafloor 40m apart. It was prior knowledge that the tetrahedra needed to be *smaller* around the observation locations, so this was the initial attempt for refinement. The mesh was generated with the following,

```
tetgen.exe -pq1.4/16AfnCV test1.poly
```

which resulted in 27,985 cells and a minimum dihedral angle of 16°. Figure 4.1 shows a threshold cut of the mesh and the cluster of cells at the interface is a result of the refinement scheme. A zoomed-in view of refinement on the surface is shown in Figure 4.2(a) where the nodes spaced at 40m are clearly observed. A Krylov subspace of 500 and the resulting amplitude and phase are shown in Figure 4.2(b) and Figure 4.2(d). The match to the analytic response for amplitude and phase is surprisingly satisfactory. However, the responses themselves appear to be noisy and not well resolved and this is clearly indicated by the calculated residuals in Figure 4.2(c) and Figure 4.2(e). The total percent errors for the amplitude and phase are 14.2% and 8.7% which would not be acceptable coming from a real model, therefore, improvements are needed.

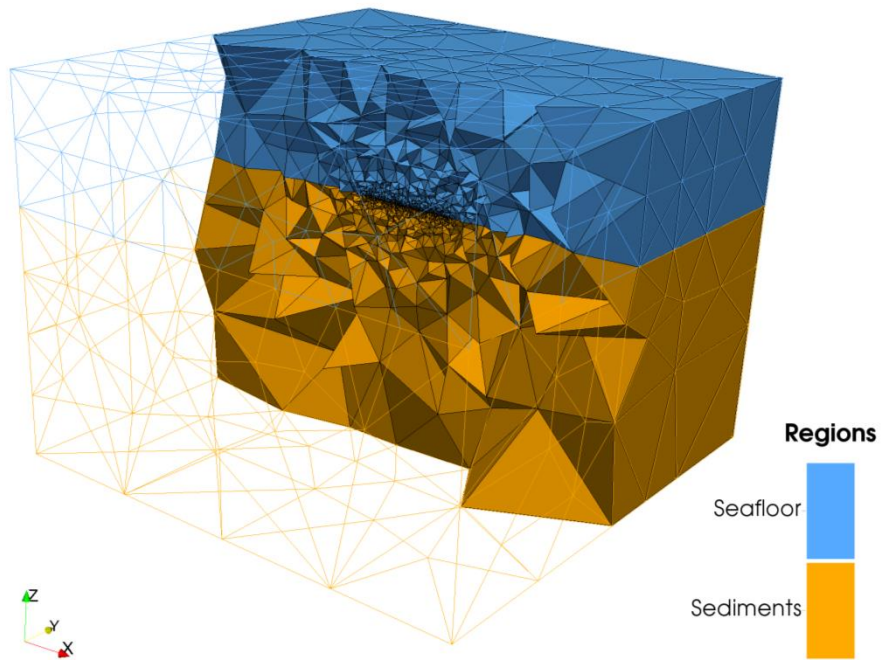


Figure 4.1: A threshold cut of the halfspace mesh from Test I. This mesh contains 27,985 cells and the dihedral angle constraint of  $16^\circ$  was satisfied.

### 4.1.2 Test II

A different refinement scheme was implemented in order to improve the level of noise observed in the recovered data. Nodes were placed on the seafloor 20m apart to add further refinement. Also, a .mtr file was included to impose a 10m constraint on the nodes placed on the seafloor. The intended result was to have tetrahedra with edge lengths of 10m surrounding the observation locations, while giving TetGen some freedom on where it adds extra nodes. The mesh was generated using the same command line prompt in Test I, but this test included the `-m` switch. The resulting number of tetrahedra was 126,600 and the minimum dihedral constraint of  $16^\circ$  was maintained.

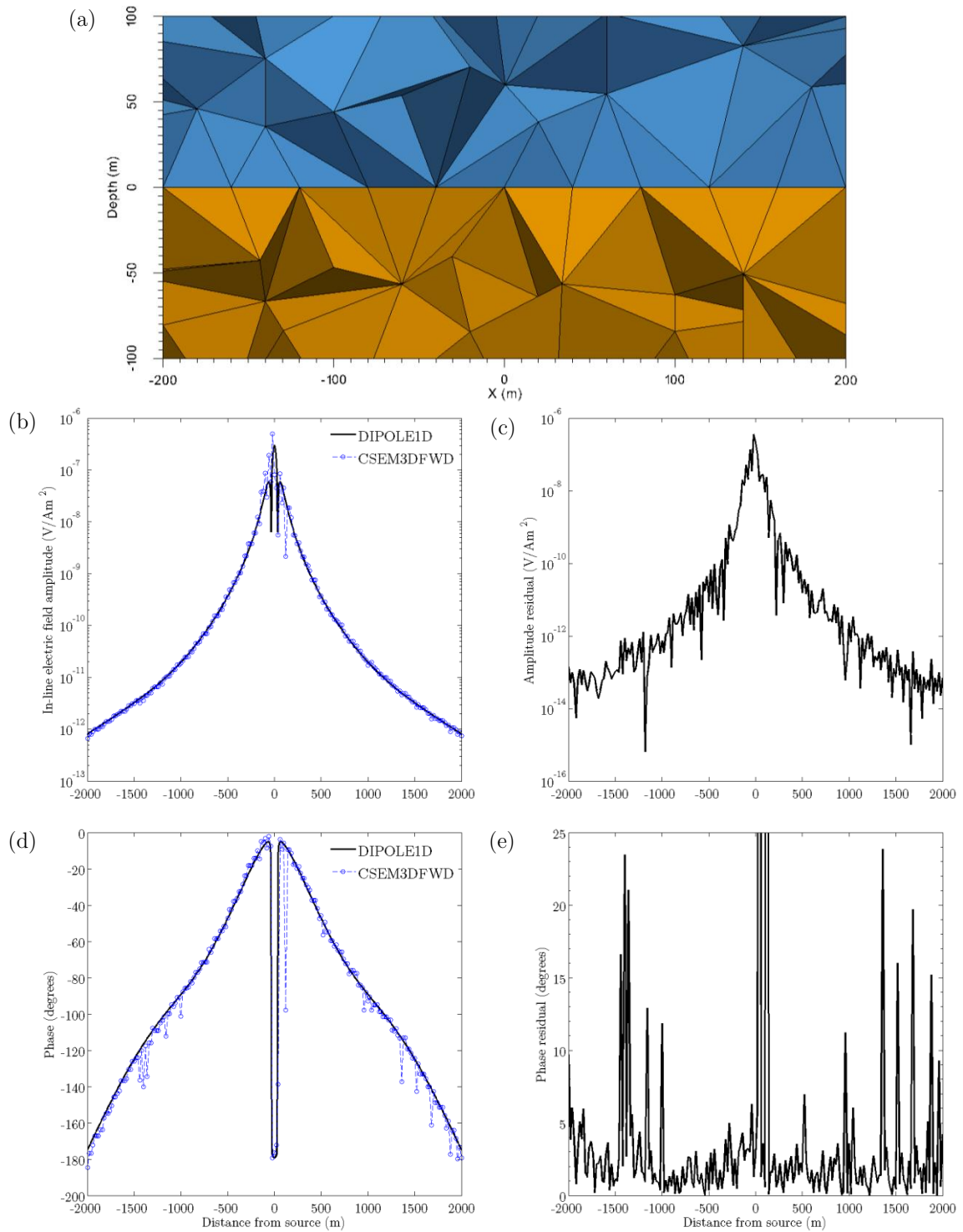


Figure 4.2: The Test I (a) mesh slice zoomed to the origin to observe the 40m node spacing refinement on the surface, (b) in-line electric field amplitude, and (d) phase compared to DIPOLE1D (Key, 2009). The residuals for the amplitude and phase are shown in panels (c) and (e) respectively with total percent errors of 14.2% and 8.7%.

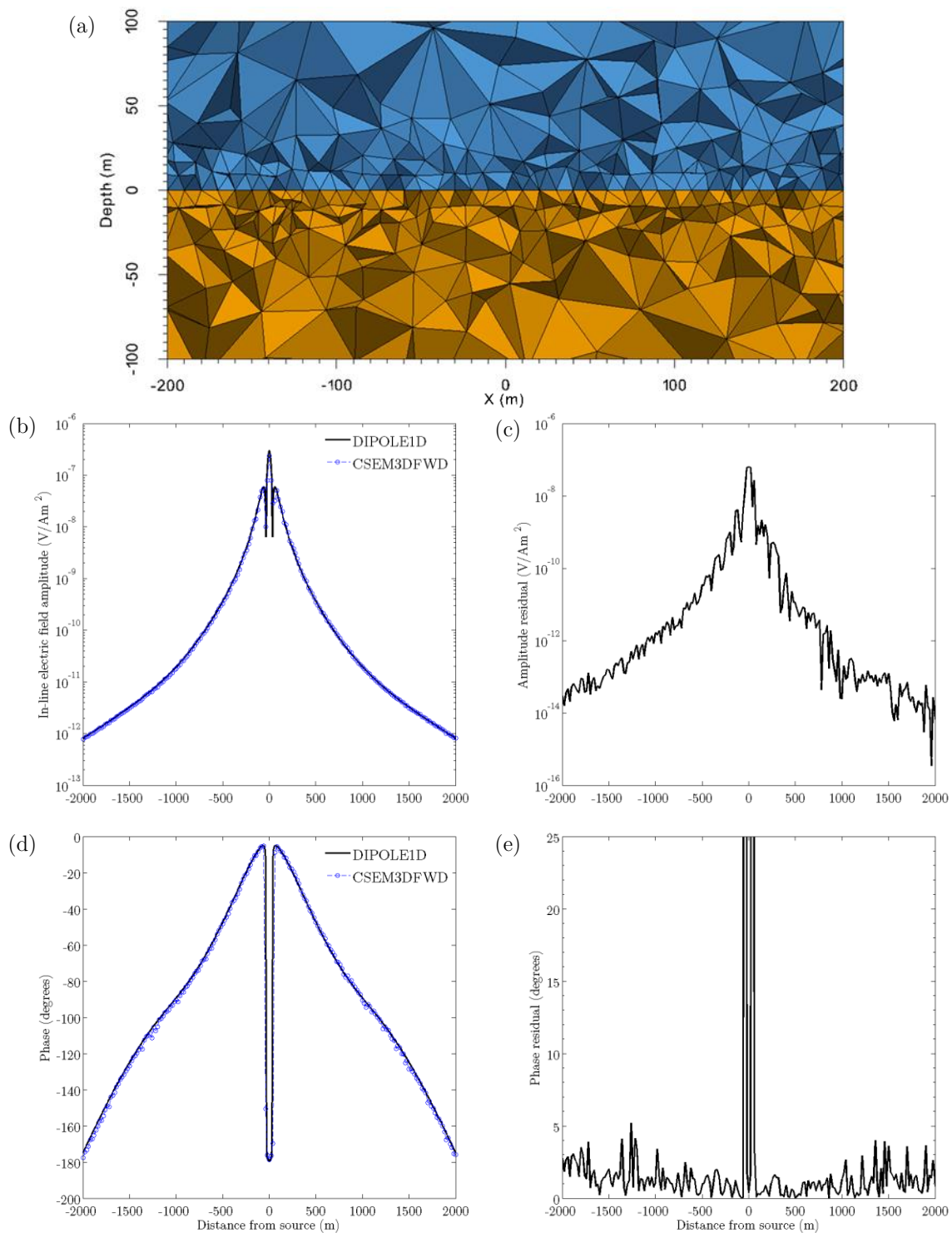


Figure 4.3: The Test II (a) mesh slice zoomed to the origin to observe the 20m node spacing, 10m edge-length refinement on the surface, (b) in-line electric field amplitude, and (c) phase compared to DIPOLE1D (Key, 2009). The residuals for the amplitude and phase are shown in panels (c) and (e) respectively with total percent errors of 5.6% and 4.4%.

A zoomed-in view of the refinement on the surface is shown in Figure 4.3(a) where tetrahedra with edge lengths of approximately 10m are observed. It appears this level of refinement added 100,000 cells which are a majority of the cells for the whole mesh. The amplitude and phase results in Figure 4.3(b) and Figure 4.3(d) do show improvement over the previous test and the residuals are certainly lower. The match to the analytic responses remained to be satisfactory and the total percent errors for the amplitude and phase reduced to 5.6% and 4.4%. However, the element of computational noise did not diminish entirely as there is still a degree of *jitteriness* in the data. The intent is to recover amplitude and phase values that are as *smooth* as the analytic response; therefore, improvements are still needed.

### 4.1.3 Test III

The previous two tests were focused on observation location refinement, but another consideration was refining at the transmitter. Everything in Test II was repeated here, except one node was added at the location of the transmitter. A 0.5m constraint on this node was added to the .mtr file as well. The same expression was used to generate the mesh which resulted in 124,166 cells and the minimum dihedral constraint of  $16^\circ$  was met. A zoomed-in view of the mesh slice is shown in Figure 4.4(a) where the *pulse* of refinement for the transmitter is observed. Upon inspection of the amplitude and phase and their respective residuals in Figure 4.4, it appeared that *refining around the transmitter had no noticeable impact on the results*. Consequently, changes had to be made to the receiver refinement in order to remove the jitteriness in the data.

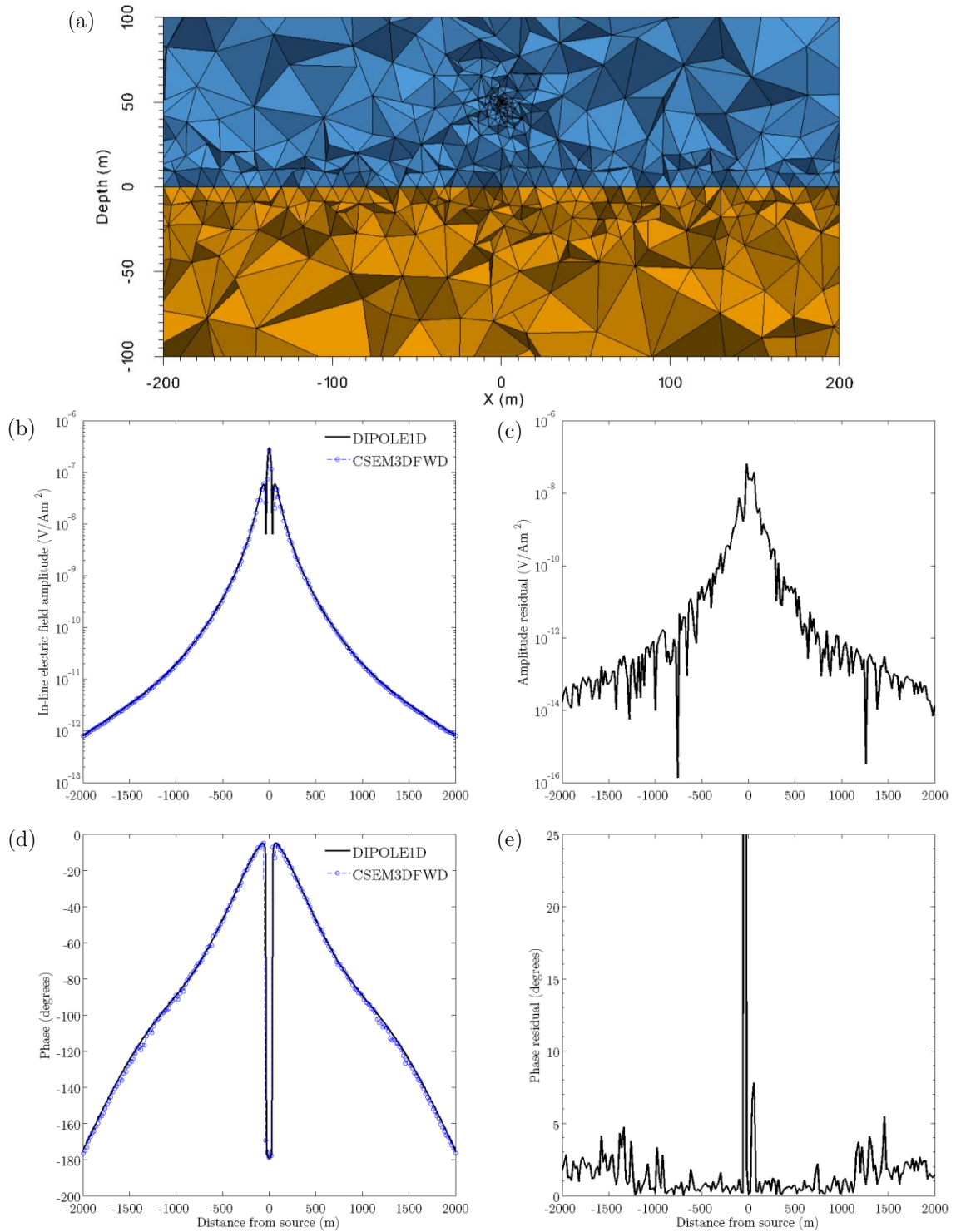


Figure 4.4: The Test III (a) mesh slice zoomed in to observe the refinement at the transmitter and the 20m node spacing, 10m edge-length refinement on the surface, (b) in-line electric field amplitude, and (d) phase compared to DIPOLE1D (Key, 2009). The residuals for the amplitude and phase are shown in panels (c) and (e) respectively with total percent errors of 4.6% and 4.5%.

#### 4.1.4 Test IV

The previous tests have shown that the results are dependent on the size of the tetrahedra surrounding the observation locations, but a factor not yet considered is the *quality* of these tetrahedra. The .mtr method of refinement at the observation locations puts a constraint on the edge lengths of the tetrahedra, but TetGen still has freedom regarding the quality of those cells. A potential solution is to put an additional constraint on the *quality* of the cells surrounding the observation locations. This can be achieved by adding points to the model that, when meshed, will create *regular tetrahedra* that enclose the observation locations. A regular tetrahedron contains four equivalent equilateral triangular faces, and the four points needed to construct a regular tetrahedron are given by (via <http://mathworld.wolfram.com/RegularTetrahedron.html>),

$$\begin{aligned}(x_1, y_1, z_1)_i &= (x(i) + \frac{\sqrt{3}}{3}a, y(i), z(i)) \\(x_2, y_2, z_2)_i &= (x(i) - \frac{\sqrt{3}}{6}a, y(i) + \frac{1}{2}a, z(i)) \\(x_3, y_3, z_3)_i &= (x(i) - \frac{\sqrt{3}}{6}a, y(i) - \frac{1}{2}a, z(i)) \\(x_4, y_4, z_4)_i &= (x(i), y(i), z(i) + \frac{\sqrt{6}}{3}a)\end{aligned}\tag{4.1}$$

where  $a$  is the desired edge length of the tetrahedron and  $i$  refers to the  $i^{th}$  observation location. These formulas were used to add three nodes on the surface, one above, and one below to create a regular tetrahedron on both sides of the surface for each receiver location. The mesh was once again created using the same command line switches as before which resulted in a mesh of 175,655 cells. The .mtr file *only* had a constraint on the transmitter node; TetGen was smart enough

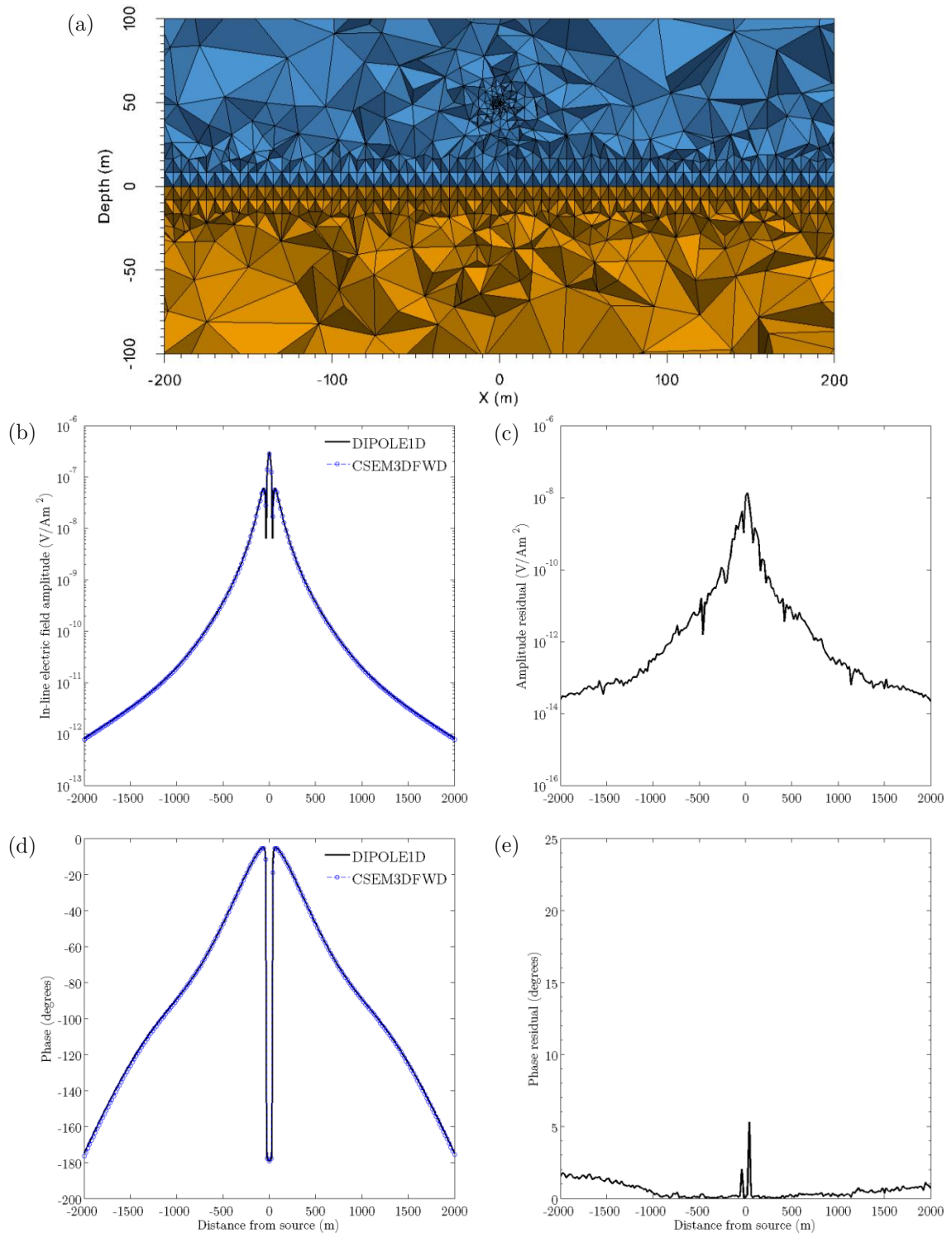


Figure 4.5: The Test IV (a) mesh slice zoomed in to the origin to observe the refinement at the transmitter and *regular tetrahedra* on the surface with edge lengths of 10m, (b) in-line electric field amplitude, and (c) phase compared to DIPOLE 1D (Key, 2009). The residuals for the amplitude and phase are shown in panels (c) and (e) respectively with total percent errors of 2.3% and 1.9%.

to form the regular tetrahedra from the added nodes alone. Figure 4.5(a) shows these regular tetrahedra on a zoomed-in mesh slice. Notice the improved uniformity and quality of these cells compared to the meshes from the previous three tests. Most importantly, the amplitude and phase results in Figure 4.5(b) and Figure 4.5(d) show a monumental improvement as they are just as smooth as the analytical response. A positive impact is also seen in the residuals for both amplitude and phase as the percent errors reduced to 2.3% and 1.9%.

#### **4.1.5 Remarks**

This simple halfspace modeling study was useful in helping develop expertise with the modeling process and software. Each of the tests included incremental changes/improvements, but with each test, the number of cells increased. The impact of increasing the number of cells in the mesh is shown by the convergence curves for each test shown in Figure 4.6. Notice that for each consecutive test it takes more iterations for the solution to reach convergence. However, the results from Test 4 were smooth and of good quality despite the larger mesh.

There were also three main learning outcomes that helped shape the modeling approach for upcoming studies in this thesis. First, decreasing the size of the tetrahedra around the observation locations appears to improve the results. Intuitively, this makes sense because the fields are changing rapidly at these locations and to accurately capture the change of the EM fields at these points in space requires smaller cells. However, there are diminishing returns to decreasing

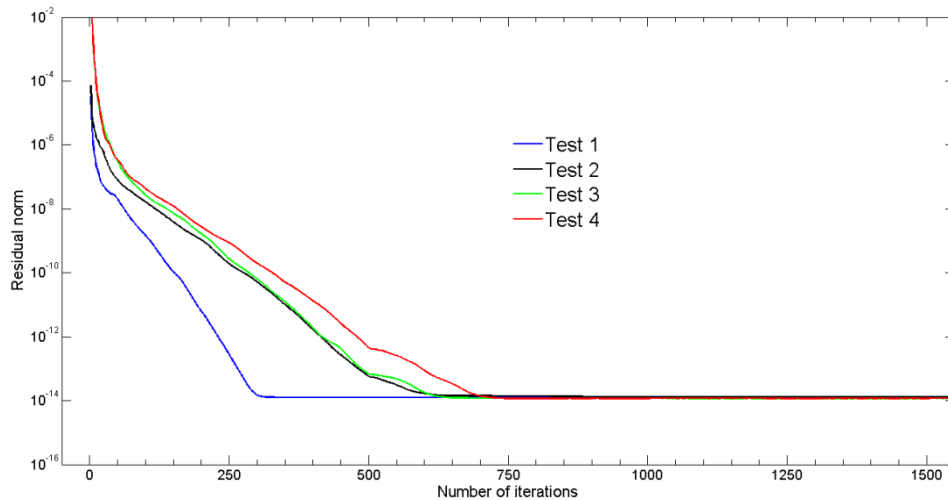


Figure 4.6: The convergence curves for each of the halfspace tests. The larger a mesh was for a given test, the more iterations were needed in order to reach convergence.

the size of these cells because at some point the fields will no longer change/improve with decreasing cell size. Second, it appeared that refinement around the transmitter had no impact on the results and should be disregarded altogether (however, this was not done until Chapter 5). Most importantly, constraining the shape of the tetrahedra around the observation locations to be *regular* drastically improved the results. All upcoming studies in this thesis used this technique of enclosing observation locations in regular tetrahedra.

## 4.2 Marine Layered Earth Reservoir Model

The second synthetic model considered for this thesis was a marine layered earth reservoir model. This model has an added level of complexity over the marine halfspace due to the inclusion of an air layer and a reservoir layer. A model of this nature is one step closer to what would be a realistic model.

The dimensions of this model were  $x = [-20 \text{ km}, 20 \text{ km}]$ ,  $y = [-20 \text{ km}, 20 \text{ km}]$ , and  $z = [-10 \text{ km}, 10 \text{ km}]$ . The interface between seawater and sediments remained at  $z = 0 \text{ km}$  and another surface was added at  $z = 1.0 \text{ km}$  to be the interface between air and seawater as shown in Figure 4.7. The top of the reservoir is at  $z = -1.0 \text{ km}$  and is 100m thick, but the lateral extent was dealt with carefully. Since the computed results were going to be compared to *1D analytic responses*, this meant the 3D model needed to be as close to 1D as possible. The solution was to make the reservoir slab large enough around the observation locations to maintain the 1D approximation, but keep the extent limited in such a way that it did not reach the boundaries of the mesh to reduce the number of cells. As shown in Figure 4.7, the resistivities of the air, seawater, sediment, and hydrocarbon layers were  $1.0 \times 10^8 \Omega\text{m}$ ,  $0.3 \Omega\text{m}$ ,  $1.0 \Omega\text{m}$ , and  $100 \Omega\text{m}$  respectively. The observation locations were chosen to range from  $x = [-5.0 \text{ km}, 5.0 \text{ km}]$  at  $y = 0\text{m}$  and  $z = 0.01\text{m}$  with a 40m spacing. The transmitter was again chosen to be an x-directed HED with a frequency of 1.0 Hz and was placed 100m above the seafloor and the first observation location  $(x, y, z) = (-5000\text{m}, 0, 100\text{m})$ .

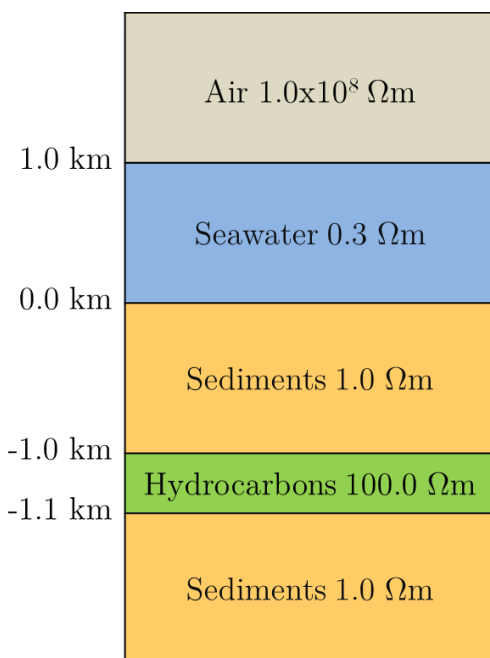


Figure 4.7: The 1D representation of the marine layered earth reservoir. The top of the reservoir is placed at  $z = -1.0$  km and is 100m thick.

There were four separate simulations performed on this model: in-line and broadside simulations with and without the hydrocarbon layer. The responses with hydrocarbons (reservoir model) were normalized to those without hydrocarbons (halfspace model) and the differences between in-line and broadside were evident. Ultimately, the goal of this modeling study was to simulate the response of a basic marine reservoir, analyze the sensitivity to the reservoir, and compare all results to the semi-analytic 1D response provided by Key (2009).

#### 4.2.1 In-line halfspace

The first of the four different simulations used the in-line transmitter configuration over the halfspace model (the inline configuration is where the transmitter is

*parallel* with the axis of the observation locations). This halfspace model was similar to the one in Section 4.1, except there is an air layer in this model. The refinement at the observation locations was again implemented by inserting nodes into the model which would create regular tetrahedra after the meshing process. The regular tetrahedra were still meshed to have 10m edge lengths despite the observation locations having 40m spacing. Recall the sizes of the tetrahedra need to be small around the observation locations (a result of Section 4.1.2) to achieve an accurate result, therefore, using an edge length that is the same size as the spacing (40m in this case) may not be feasible.

The mesh was generated with the following,

```
tetgen.exe -pq1.4/16AmfnCV layered_Ex_noReservoir.poly
```

which resulted in 435,625 cells and the minimum dihedral angle of  $16^\circ$  was met. Figure 4.8 shows various zoomed-in slices of the mesh and Figure 4.8(c) shows a close up of the observation refinement. The numerical simulation of this mesh was performed with a Krylov subspace of 600 and the resulting amplitude and phase are shown in Figure 4.9. Notice how both the amplitude and the phase are both smooth and appear to have a solid match with the analytical responses. However, there is some deviation in the computed results starting around 5.0km when the airwave begins to influence the data. The only explanation for this minor mismatch is that DIPOLE1D operates under the quasi-static approximation, whereas CSEM3DFWD uses the full wave equation. The airwave is indeed a wave, so the oscillatory contribution of the airwave to the total field calculated via DIPOLE1D is ignored, which is a possible explanation for the minor mismatch.

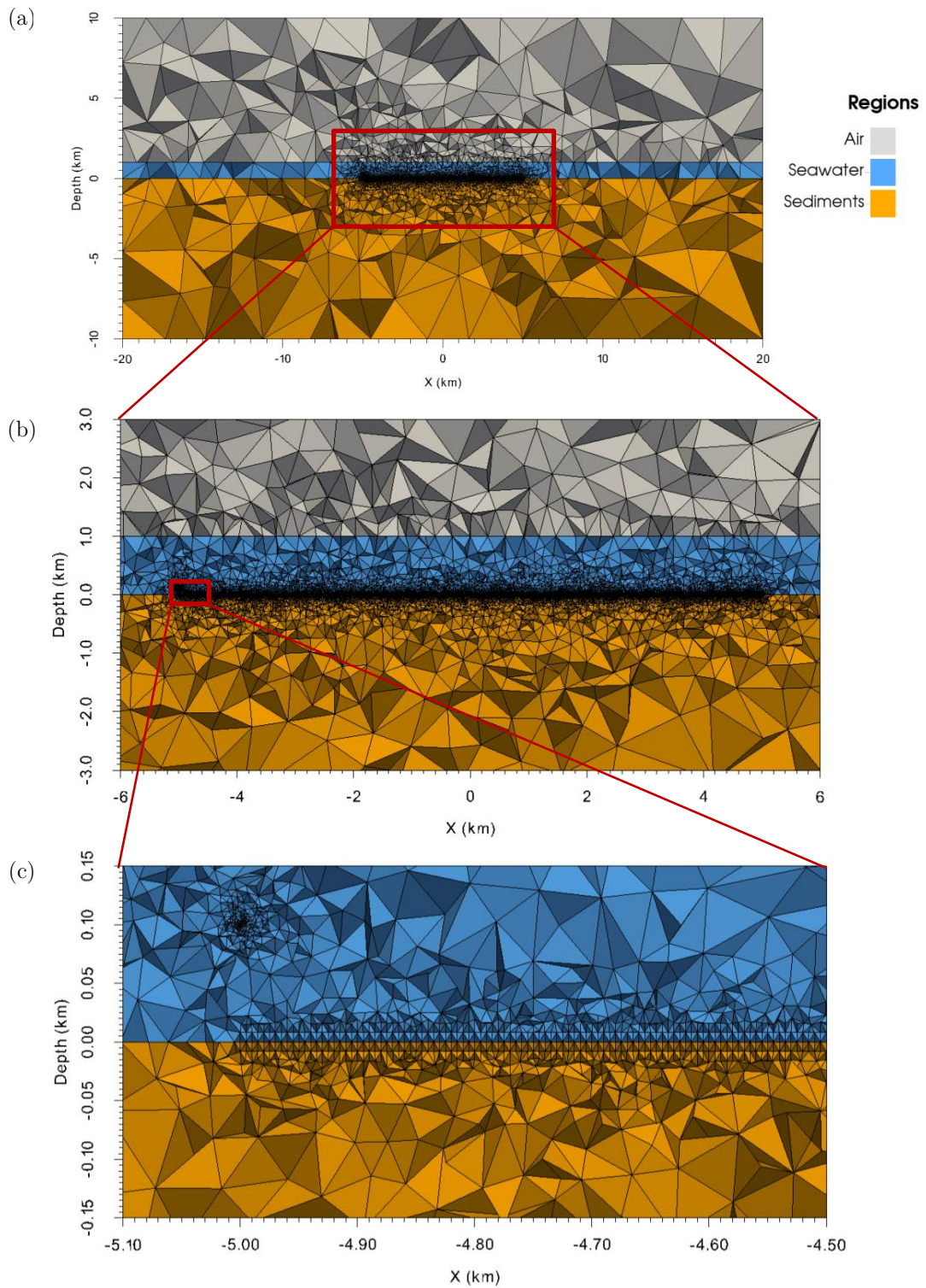


Figure 4.8: Various 2D slices of the halfspace mesh (with air) at  $y = 0$  km. (a) The entire x-z range, (b) x ranging from -6 km to 6 km, and (c) a zoom-in showing the observation location refinement.

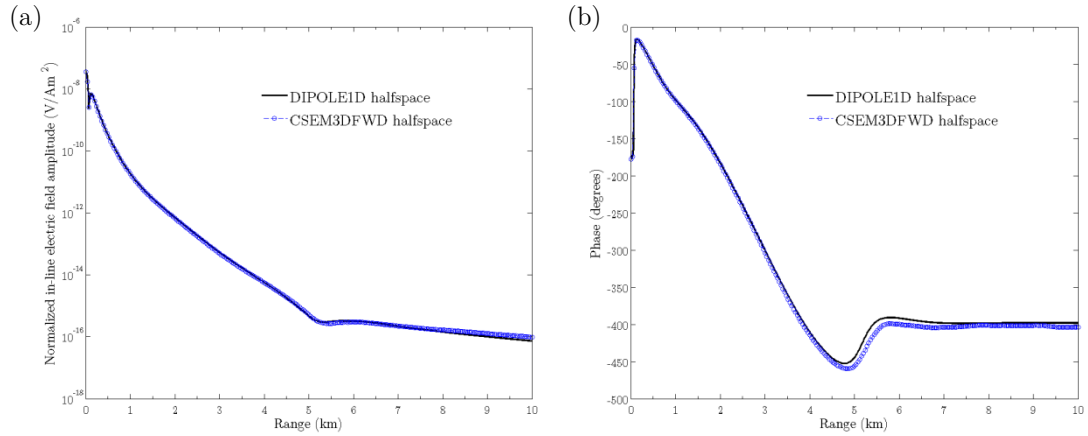


Figure 4.9: The computed (a) amplitude and (b) phase results from the halfspace model (with air) using an in-line transmitter orientation. Both are compared to a 1D semi-analytic solution (Key, 2009).

## 4.2.2 Broadside halfspace

The second of the four simulations was the broadside transmitter configuration over the halfspace model (the broadside configuration simply orients the transmitter *perpendicular* to the axis of the observation locations). The exact same mesh used for the in-line halfspace was used again here (435,625 cells) and the only change was rotating the transmitter 90° in the input file for the broadside configuration. Results for the amplitude and phase are shown in Figure 4.10. Again, the results are smooth and there are only minor mismatches at ranges dominated by the airwave because DIPOLE1D operates in the quasi-static regime.

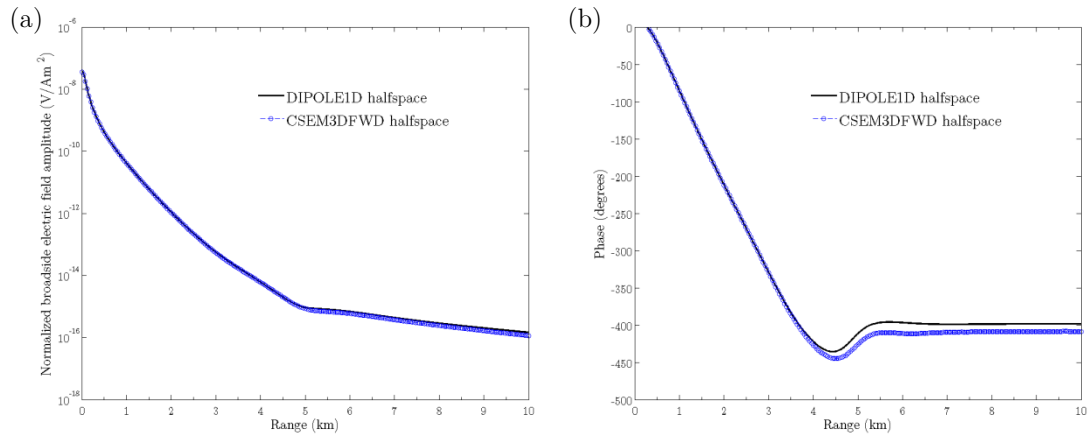


Figure 4.10: The computed (a) amplitude and (b) phase results from the halfspace model (with air) using a broadside transmitter orientation. Both are compared to a 1D semi-analytic solution (Key, 2009).

### 4.2.3 In-line reservoir

The third of the four simulations was the in-line transmitter configuration over the reservoir model. As mentioned previously, the dimensions of the reservoir layer were chosen carefully to maintain the 1D approximation while also reducing the number of cells. The extent of the hydrocarbon layer was chosen to be 14 km x 10 km and the superposition of this layer on the meshed seafloor surface is shown Figure 4.11. Notice that the boundaries of the reservoir slab extend beyond the start/end of the observation locations, but do not extend to the boundary of the whole model. It was theorized that the size of this slab was large enough to achieve the necessary 1D approximation.

The refinement at the observation locations and the TetGen switches were the same as the previous two simulations, and the reservoir slab was represented simply with eight nodes and six boundary facets. The resulting mesh consisted of

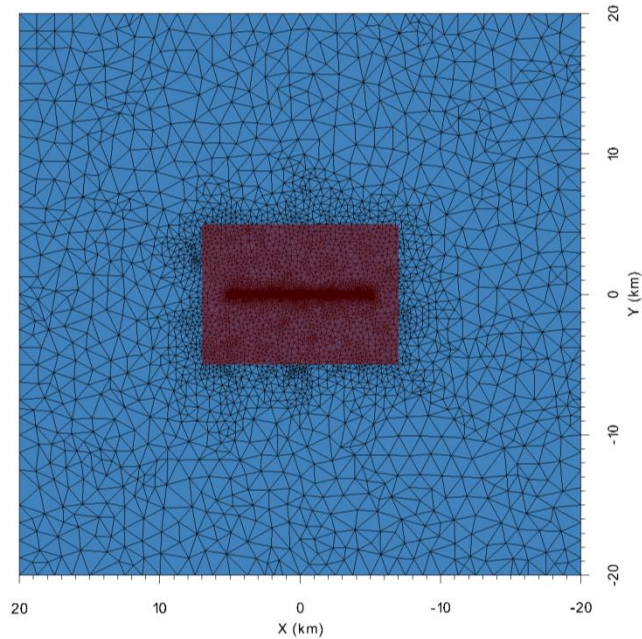


Figure 4.11: The dimensions of the reservoir slab (14 km x 10 km) and its superposition on the meshed seafloor surface for the in-line reservoir model. The boundaries of the reservoir slab extend beyond the start/end of the observation locations to maintain the 1D assumption.

778,405 cells and the minimum dihedral angle  $16^\circ$  was still maintained. Figure 4.12 shows a 3D threshold cut and a 2D slice of this in-line reservoir mesh. Including the reservoir in the model added  $\approx 400,000$  cells. Therefore, if the reservoir slab was extended to the boundaries of the model, then the resulting mesh could have had onwards of 3-4 million cells which would make solving the system of equations inefficient and impractical.

The numerical simulation of this mesh was performed with a Krylov subspace of 300 and the resulting amplitude and phase are shown in Figure 4.13. Notice how both the amplitude and the phase are both smooth and there appears to be no mismatch to the analytical response associated with the airwave. The presence of

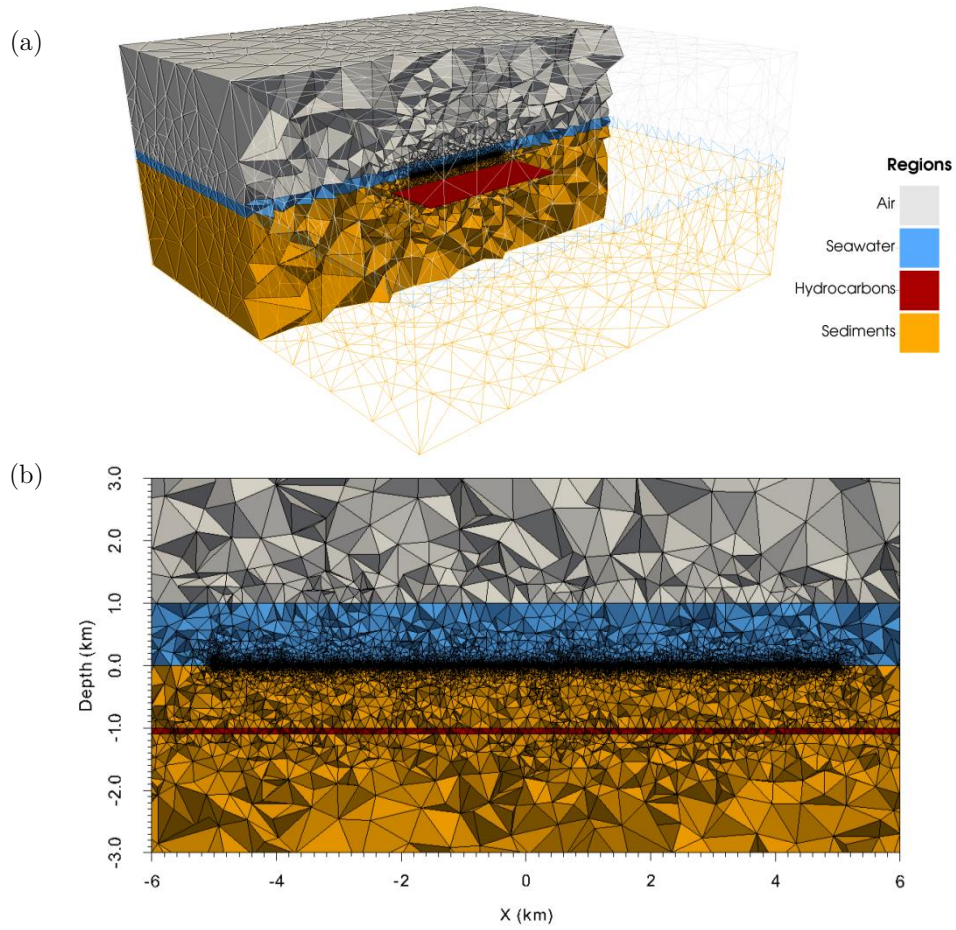


Figure 4.12: The (a) threshold cut of the entire 3D in-line reservoir mesh, and (b) a 2D slice at  $y = 0$  km zoomed into the reservoir.

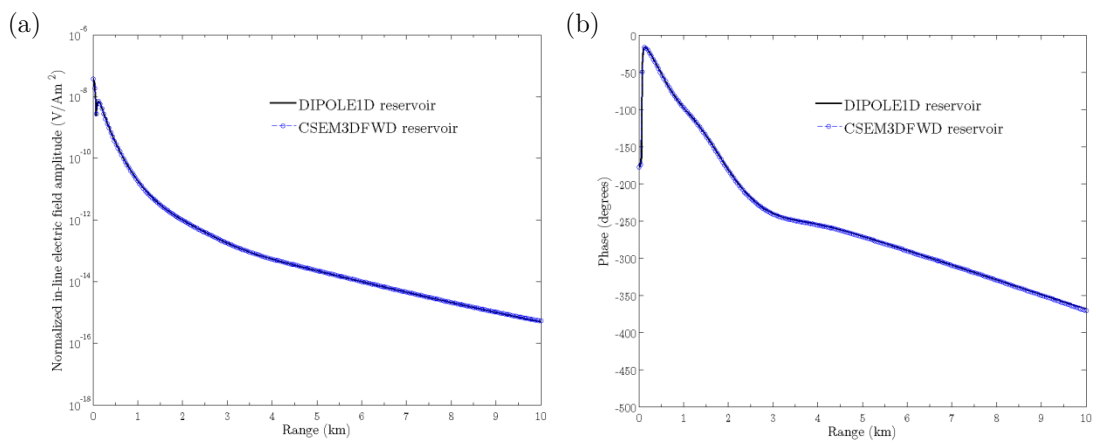


Figure 4.13: The computed (a) amplitude and (b) phase results from the reservoir model using an in-line transmitter orientation. Both are compared to a 1D semi-analytic solution (Key, 2009).

the hydrocarbon layer has increased the value of the electric field to a point where the airwave contribution to the total field is minimal allowing for a better match.

#### 4.2.4 Broadside reservoir

The fourth and final simulation was the broadside transmitter configuration over the reservoir model. For the in-line reservoir model, the dimensions of the reservoir slab were 14 km x 10 km, but after some testing those dimensions had to be modified for the broadside configuration. Initially, the exact same mesh from the in-line reservoir model (778,405 cells) was used for this simulation, but the results had a higher mismatch than expected (not shown for brevity). The amplitude of the 1D analytical response was visibly higher than the response from CSEM3DFWD and the problem appeared to be the size of the reservoir.

The transmitter for the broadside configuration is oriented along the y-axis and in hindsight, it seemed intuitive that this configuration would be more sensitive to resistivity changes *in that dimension*. It appeared that having the reservoir slab extend to only 5km along the y-axis in either direction was not sufficient to achieve a 1D approximation because the CSEM3DFWD results seemed to be picking up signal from beyond the edge of the slab. So, the extent of the reservoir slab was extended to 14 km x 14 km as shown in Figure 4.14. This was a 40% increase in the size of the reservoir slab, which subsequently increased the size of the mesh from 778,405 cells to a predictable 925,781 cells. The numerical simulation of this mesh was performed with a Krylov subspace of 100 and the resulting amplitude

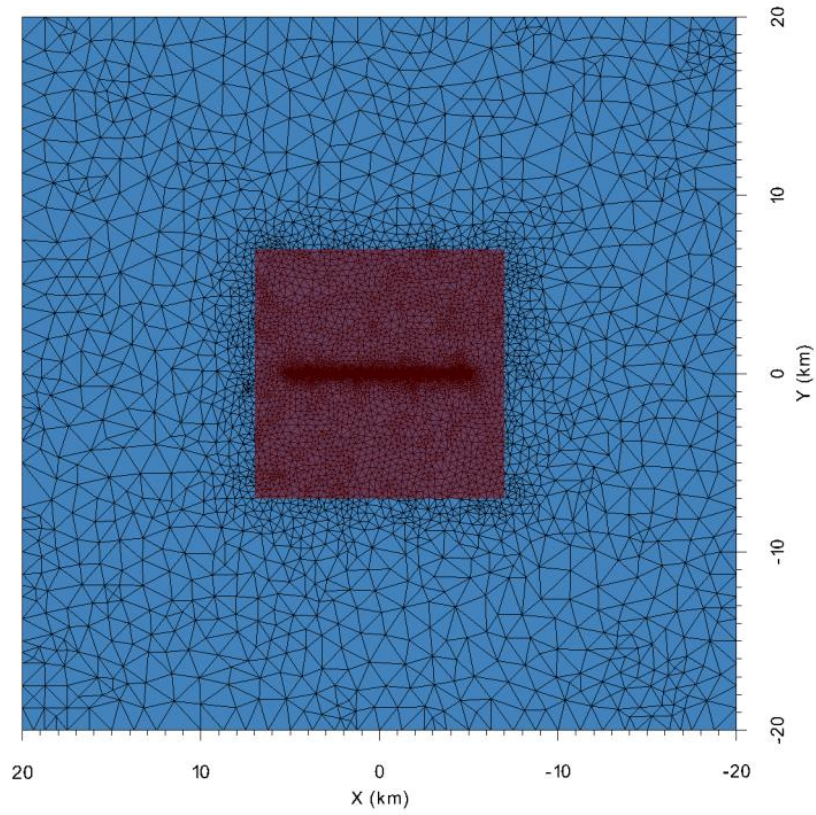


Figure 4.14: The dimensions of the reservoir slab (14 km x 14 km) and its superposition on the meshed seafloor surface for the broadside reservoir model. The boundary of the reservoir slab had to extend further along the y-axis in order to obtain a better match with the 1D analytical results.

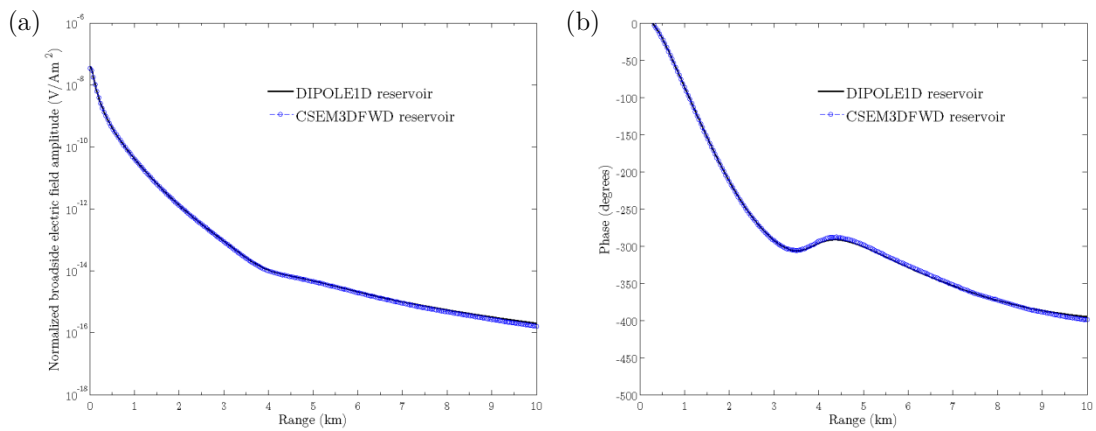


Figure 4.15: The computed (a) amplitude and (b) phase results from the reservoir model using a broadside transmitter orientation. Both are compared to a 1D analytic solution (Key, 2009).

and phase are shown in Figure 4.15. The amplitude and phase are again smooth with a good match, but there is a slight mismatch at the far offsets. Recall from Section 3.1 that broadside fields are not as sensitive to resistors, so the increase in the electric field due to the reservoir will be less. This allows the contribution of the airwave to the total field to be greater, and due to the limitation of DIPOLE1D, there appears to be a minor mismatch at the far offsets.

#### 4.2.5 Remarks

The results from these four simulations are easier to visualize, interpret, and make comparisons when plotted together. The first four panels in Figure 4.16 show the (a) in-line amplitudes, (b) broadside amplitudes, (c) in-line phase, and (d) broadside phase. In regard to the reservoir responses, notice how there is a much higher increase in the electric field for the in-line component than the broadside component, as predicted. However, the halfspace amplitude and phase curves are quite similar, which is intuitive because under wholespace conditions the response will be the same regardless of transmitter orientation.

One technique used to understand marine CSEM *sensitivity* to a reservoir is through normalization. For this example, the reservoir response is normalized to the halfspace response for both in-line and broadside transmitter configurations as shown in Figure 4.16(e). Even after the normalization of these curves there is still a good match to the 1D analytical sensitivities. There is a drastic difference in the maximum sensitivity between the two configurations as the maximum sensitivity

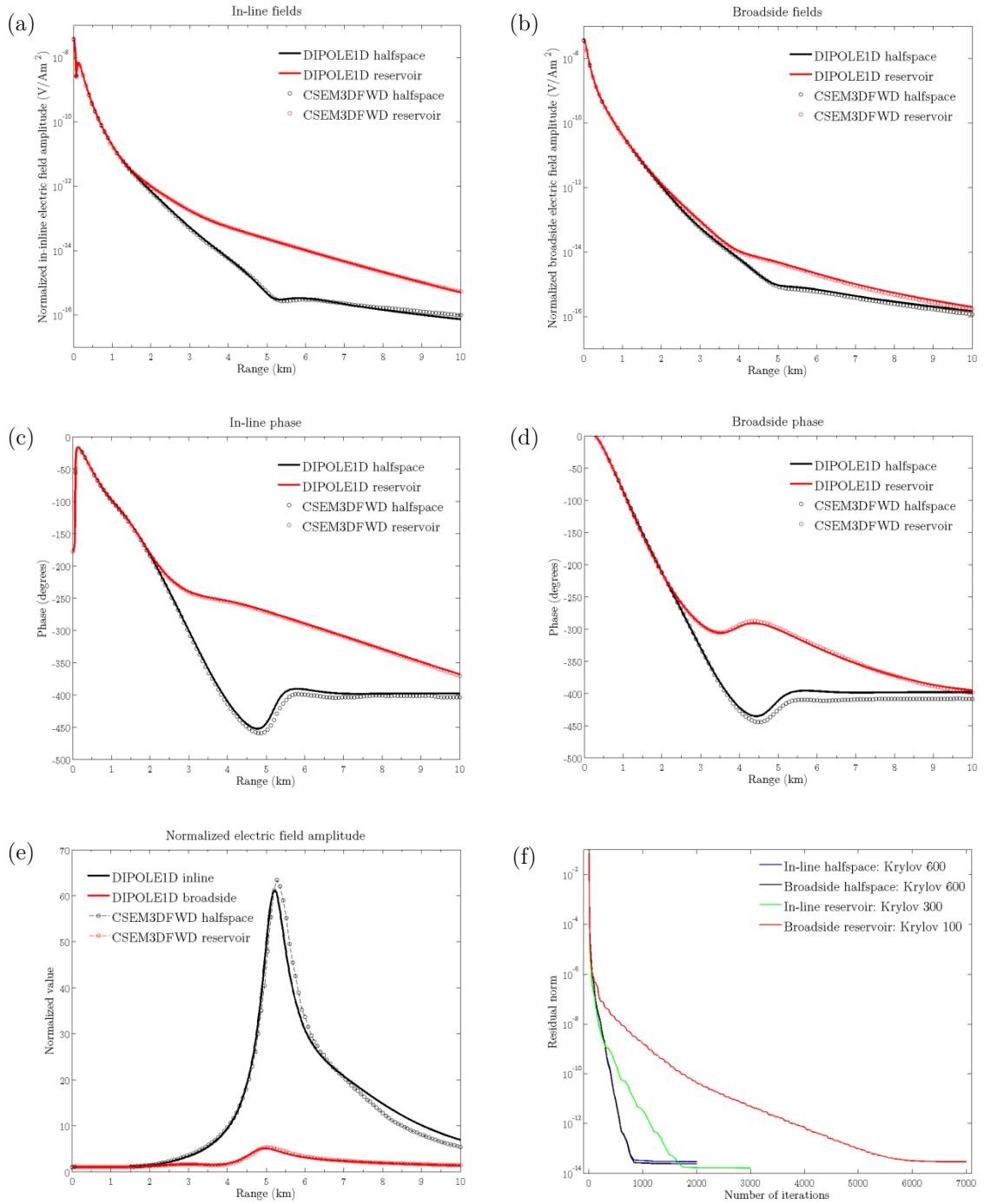


Figure 4.16: The (a) in-line amplitude, (b) broadside amplitude, (c) in-line phase, and (d) broadside phase for both the halfspace and reservoir models. All have a transmission frequency of 1.0 Hz, and the amplitude and phase plots are compared to a 1D semi-analytic solution (Key, 2009). (e) The normalization of the reservoir to the halfspace response for both in-line and broadside configurations. (f) The residual norm of the iterative solver for each of the four simulations.

for in-line and broadside is 60x and 5x respectively. This shows that there is a strong sensitivity of the in-line fields to this reservoir.

The final panel in Figure 4.16 shows the convergence of the iterative solver for each simulation. All of these simulations were performed on a Dell Optiplex 9020 desktop computer (3.2 GHz Intel Core i5 processor, 16GB RAM). Notice how the halfspace models reached convergence the quickest due to the smaller mesh size and higher Krylov subspace. The reservoir models were much larger and in order to solve for the system of equations, a lower dimension for the Krylov subspace was required to maintain the memory usage under 16 GB. Using smaller dimensions requires more iterations and longer computation times to reach convergence as the in-line and broadside reservoir convergence curves show. However, the simplicity of these meshes still allowed for the solution to converge despite the usage of small dimensions.

In summation, the simulations of the marine layered earth reservoir model were a success. The matches to the 1D analytical results were adequate, but a limitation of the code was causing some mismatch in areas of the data dominated by the airwave. This study further validated the theory that in-line marine CSEM transmitter orientations are more sensitive to resistors than broadside orientations. The meshes for this study were synthetic and quite simple, but they served as useful starting points on learning how to create models and synthesize marine CSEM results.

## Chapter 5

# The Mizzen Study in the Flemish Pass Basin

The previous chapter reported the synthesizing of marine CSEM data from relatively simple, synthetic models. This chapter seeks to apply the same methodology of simulating marine CSEM data, but instead from *real complex models* created from *real data* in the Flemish Pass Basin offshore Newfoundland, Canada. The main challenges were maintaining quality results and convergence of the iterative solver with increasing complexity of the model.

### 5.1 Geology of the Mizzen field

The Flemish Pass Basin is located 450 km east offshore St. John's, Newfoundland, Canada (see Figure 5.1) and has seen an increase in exploration activity over the past decade. The geological history of the Flemish Pass is given by Foster and Robinson (1993) and an interpretation of the lithostratigraphy is provided by Nalcor Energy in Figure 5.2.

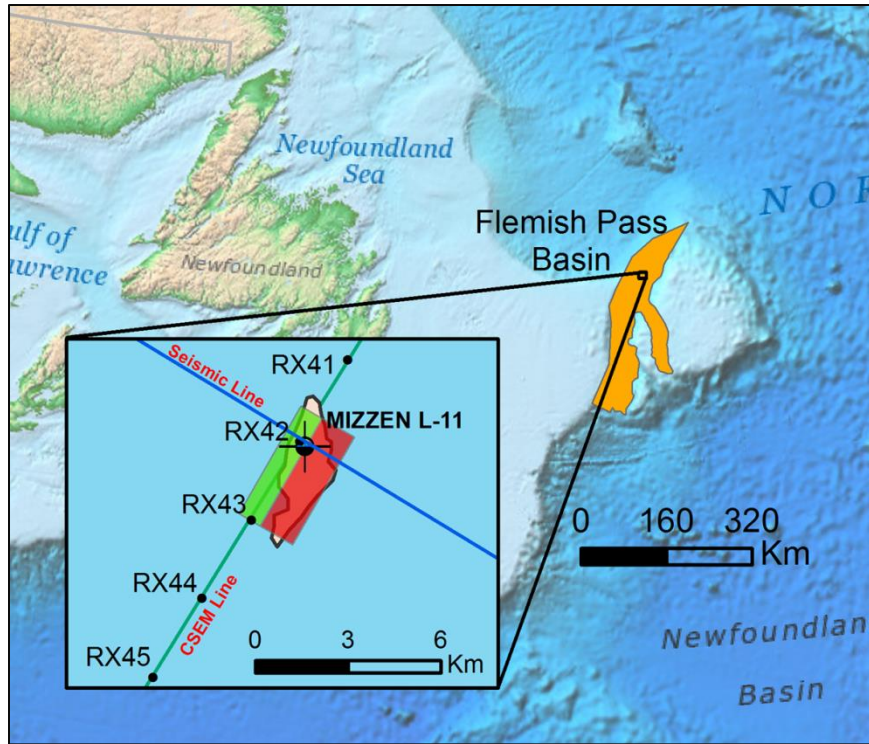


Figure 5.1: A seafloor bathymetry map of offshore Newfoundland indicating the location of: the Flemish Pass Basin, a 2D seismic line passing over L-11, a tan polygon depicting the L-11 reservoir extents (courtesy Statoil quarterly website update 2014) which is overlain by a plan view of the reservoir slab approximation used for this study (green is brine, red is hydrocarbons), and one of the transmitter lines and five receivers of a marine CSEM survey (acquired by EMGS).

The Flemish Pass Basin is an extensional rift basin with a strong potential for the formation of petroleum systems. There are three elements needed for a successful petroleum system – a reservoir, source, and seal – and many fields with these three elements have been discovered in this region. The potential reservoir considered for this study is located in the Mizzen field of the Flemish Pass Basin (see Figure 5.1) and they are Tithonian (or late Jurassic) aged. A widely known and accepted source rock for the region is the Egret Member which is slightly older in the Kimmeridgian (Foster and Robinson, 1993). Lastly, the base Cretaceous unconformity serves as a seal for the system. The Egret Member (Kimmeridgian) is

quite close to the Tithonian aged sands in geologic age, so in theory, the migration from source to reservoir rock could be easily achievable.

## Orphan & Flemish Pass Basins

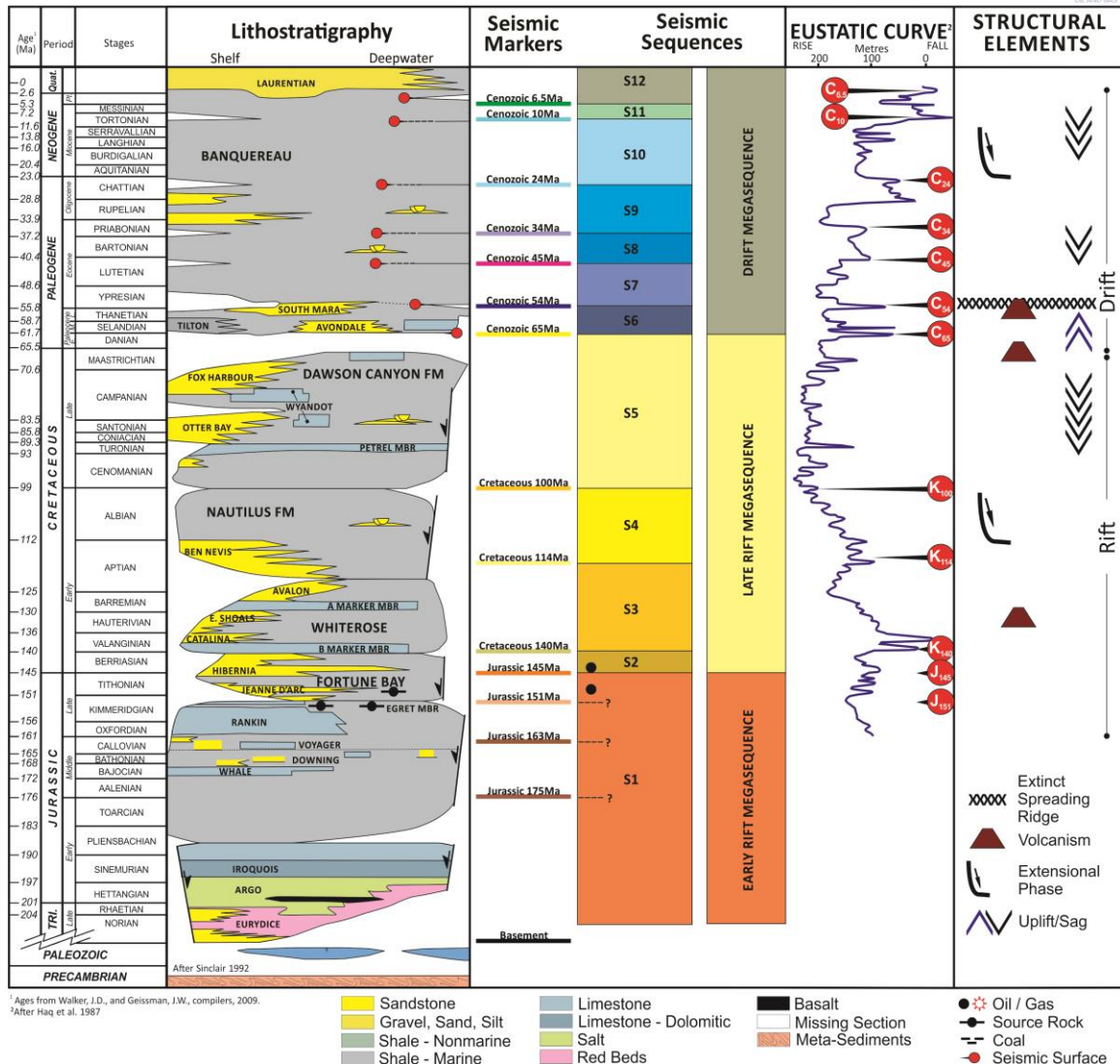


Figure 5.2: An interpretation of the lithostratigraphic geology in the Flemish Pass Basin from Nalcor Energy. The areas of particular interest for this chapter are the Tithonian aged sands, the base Cretaceous unconformity, and the Egret member source rock in the Kimmeridgian.

## 5.2 Motivation

The first well drilled in the Mizzen area in 2003, L-11, hit minor oil in one of three Tithonian aged sands, with the underlying sands encountering brine. A schematic of the gamma ray, resistivity, density, and sonic logs associated with L-11 are shown in Figure 5.3. Many of the seismic markers in Figure 5.2 are indicated by the labeled horizontal lines in Figure 5.3. These three sands that lie below the base Cretaceous/top Jurassic marker (J\_145 in Figure 5.3) are quite obvious upon inspection of the logs. 2D seismic data (via TGS/PGS) and 3D marine CSEM data (via EMGS) have both been recently acquired in the Flemish Pass Basin, and in particular, over the Mizzen prospect (Wu et al., 2015). Marine CSEM data acquisition was possible in the Flemish Pass because of the deep water column with an average thickness over 1 km (whereas the nearby Jeanne D'Arc basin is on the shelf with a water column  $< 100\text{m}$ , and marine CSEM data is practically useless due to airwave issues).

Seismic interpretation has long been successful at delineating structure from reflector shapes and positions, but not all bright spots (high amplitudes on seismic sections) are indicative of hydrocarbons, as high amplitudes can also be a result of lithology changes as opposed to fluid changes. However, amplitude-versus-offset (AVO) analysis can sometimes reveal the nature of the pore fluid within a reservoir body (Chiburis et al., 1993). A summary of the four different AVO classes is given in Figure 5.4. One 2D seismic line (geographically shown in Figure 5.1) passed over the L-11 well and the near and far angle stacks for this line zoomed into the late Jurassic/early Cretaceous are both shown in Figure 5.5. Up-dip from where the L-

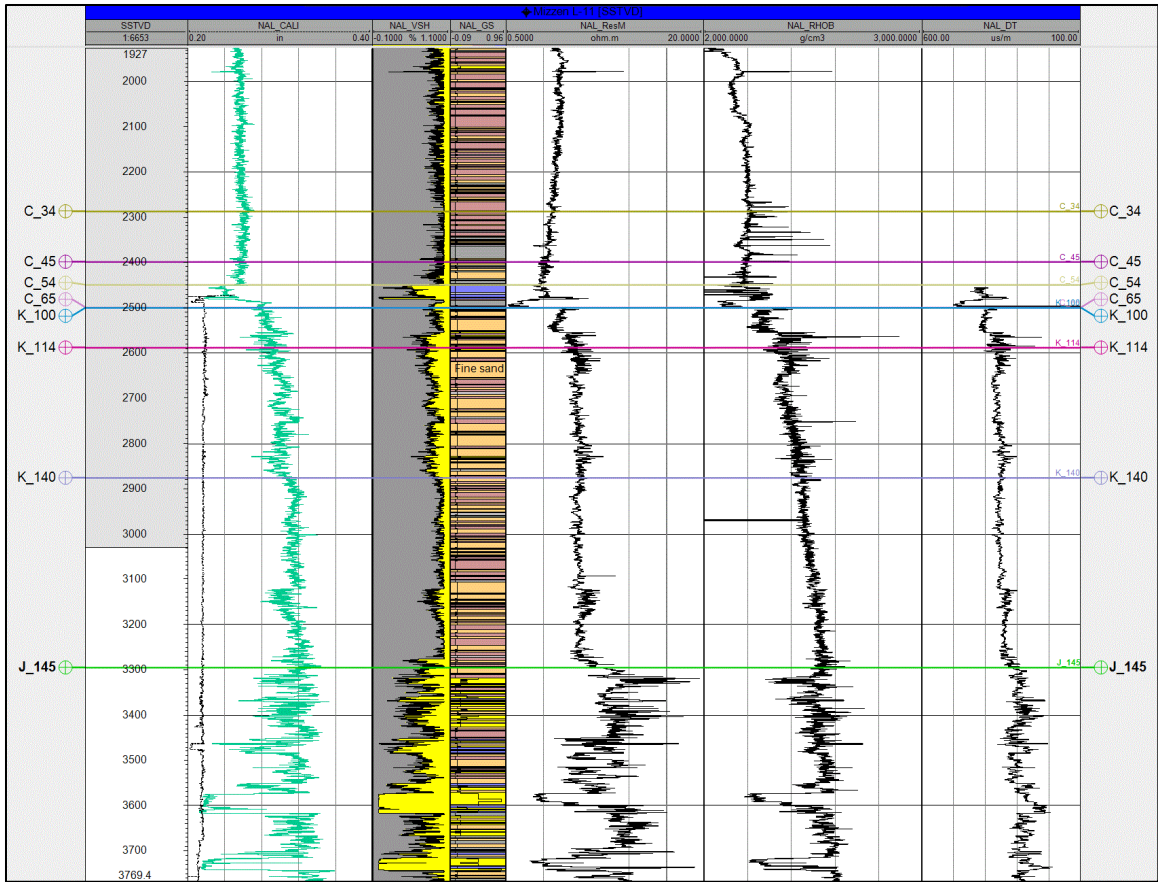


Figure 5.3: A well-section viewer from Petrel showing the (left to right) gamma ray, Vshale, grain size, resistivity, density, and sonic logs from Mizzen L-11. The seismic markers are also indicated (permission given by Nalcor Energy).

11 well was drilled (well path not shown for confidentiality reasons) there are class II and III AVO anomalies. Although the well only hit minor oil in the top sand and brine in the lower two sands, these AVO anomalies suggest the potential for hydrocarbons up-dip in structure from where the well was drilled.

In the exploration industry, the hydrocarbon potential in these three sands would likely be assessed with fluid substitution techniques using Gassmann's equations (Gassmann, 1951). However, this thesis considers an alternative, supplemental

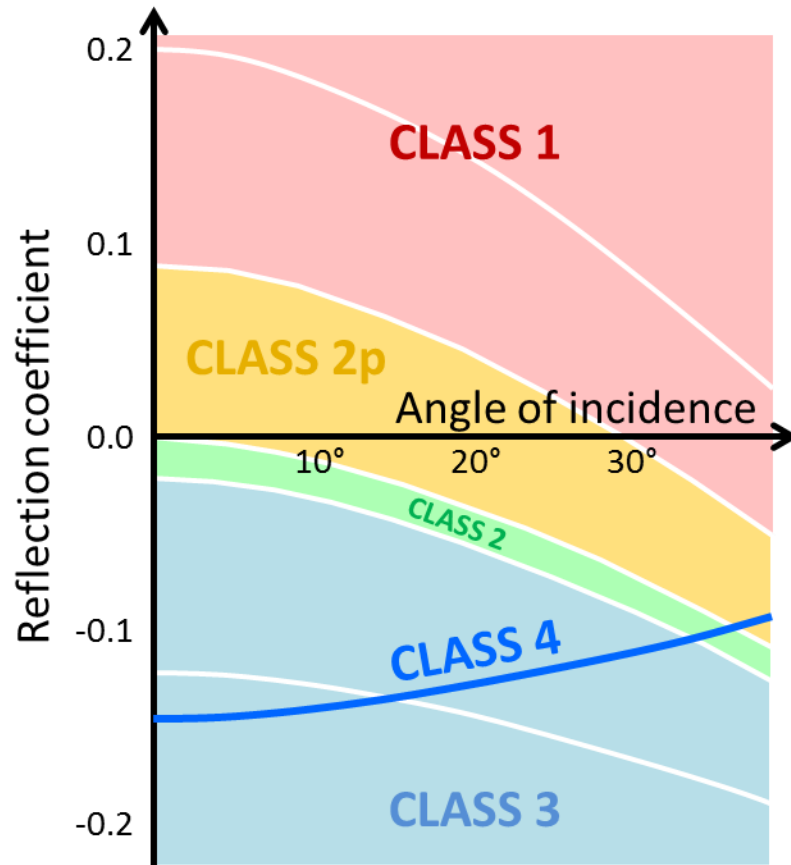


Figure 5.4: The four different P-wave seismic amplitude-versus-offset (AVO) classes for a shale to gas-sand interface (similar to Figure 2 in Rutherford and Williams, 1989).

interpretation approach which is 3D marine CSEM finite-element forward modeling *with comparisons to measured CSEM data*. The data acquired by EMGS is paramount to this study because it provides a necessary basis for comparison. It is difficult, or almost impossible, to establish the *accuracy* of forward modeling data without something to compare the result to (i.e. data misfit cannot be established if either the predicted or observed data is absent). The synthetic models had a 1D analytic result to compare against, but complicated models have no analytic solution, so measured data is the only alternative.

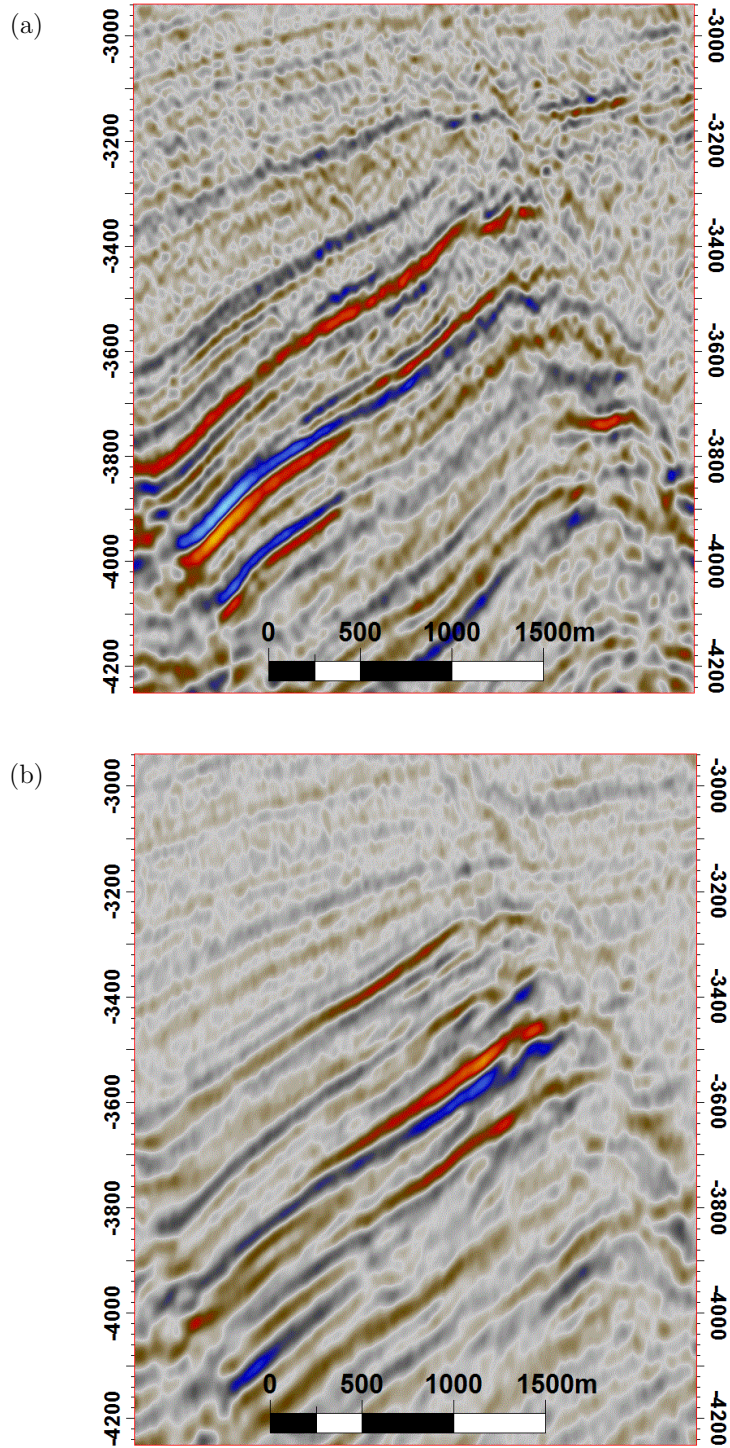


Figure 5.5: The near angle stack (a) and far angle stack (b) from the seismic line that passes over Mizzen L-11 in the Flemish Pass Basin (data courtesy TGS/PGS). Class II and III AVO anomalies in the three Tithonian aged sands are observed up-dip in structure from where the well was drilled.

The models representing the Mizzen L-11 field in the Flemish Pass were built by incrementally adding surfaces, observation locations, and refinement, and simulations were made along the way. The measured CSEM data served as a *target* for the simulated data to try and match. Ultimately, the prospectivity of the three reservoir sands was determined by using a similar normalization process used in Section 4.2 to calculate sensitivity. The two desired outcomes of this study were to show that this finite-element forward modeling technique can successfully simulate data from a complex model, but also that this technique can be used to supplement interpretation for a real offshore exploration problem.

### 5.3 Preliminary 1D modeling

Before any true 3D modeling was performed, it was important to revisit 1D modeling in order to understand how the sensitivities of the Mizzen sands would be different than the synthetic layered earth study. The 1D modeling in Section 4.2 showed a large sensitivity to the reservoir (e.g. 60×), but that was for one 100m reservoir buried 1.0 km below mudline with the surrounding sediments containing a resistivity of 1.0  $\Omega\text{m}$ ; the geology at Mizzen is quite different. First, the three Tithonian sands are separated by Jurassic sediments and are buried over 2.0 km below mudline. Second, the resistivities of the sub-seafloor sediments are all larger than 1.0  $\Omega\text{m}$ . Lastly, the crystalline basement rock that is undoubtedly present is highly resistive and was also not considered in the synthetic studies. All of these factors are predicted to *reduce* the sensitivity to the Tithonian reservoirs, and the question remains if marine CSEM will continue to have a measurable sensitivity under these vastly different conditions.

The 1D sensitivity analysis at Mizzen was performed by *blocking* (assigning constant values for depth intervals) the L-11 resistivity log and then simulating marine CSEM data from that corresponding 1D model at multiple frequencies using DIPOLE1D (Key, 2009). Blocking the resistivity log (Figure 5.3) was straightforward because each geochronologic interval (i.e. Tertiary, Cretaceous, and Jurassic) had a distinct resistivity. The Tertiary and Cretaceous were quite clean (mostly shale) with blocked resistivities of 1.4  $\Omega\text{m}$  and 2.0  $\Omega\text{m}$  respectively. A blocked resistivity for the Jurassic was much more difficult because of the frequent

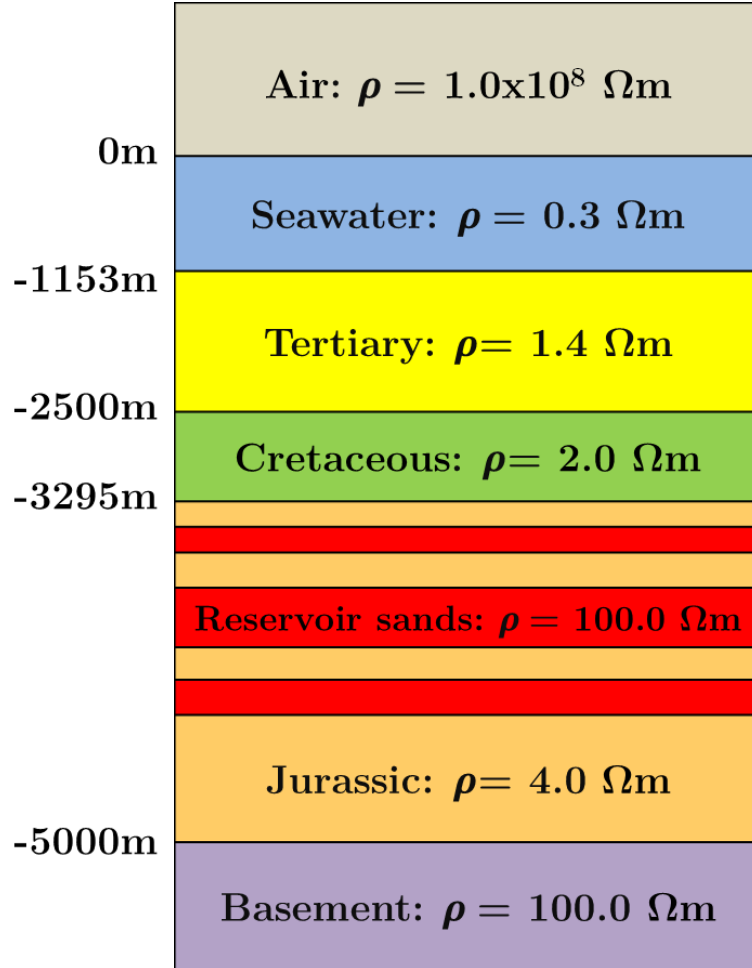


Figure 5.6: The 1D resistivity model as a result of blocking the Mizzen L-11 resistivity log and assigning resistivity values to each region.

changes in the resistivity; however, the best average was chosen to be  $4.0 \Omega\text{m}$ . The logging stopped mid-Jurassic so there are no logged resistivities for the basement, but the depth to the basement was based on seismic interpretation and a generic value of  $100 \Omega\text{m}$  was used for the resistivity. The L-11 well did not hit hydrocarbons in the Tithonian sands (two of three sands were wet), but the AVO analysis suggested hydrocarbon potential up-dip. Therefore, for the 1D study, the sands were *assumed* to be hydrocarbon bearing and a value of  $100 \Omega\text{m}$  was used. Figure 5.6 shows the final result after blocking the L-11 resistivity log and assigning values to various regions.

1D in-line marine CSEM data was simulated from the model shown in Figure 5.6 at four different frequencies with the transmitter placed 30m above the seafloor (-1123m). Data was simulated with the three Tithonian sands assumed to be filled with hydrocarbons (“reservoir response”), and also with the three sands completely removed (“layered earth response”). The reservoir response was normalized to the layered earth response to recover a rough quantitative measure of the sensitivity to these Tithonian sands. Figure 5.7(a) shows the eight in-line amplitude responses for the four frequencies considered and Figure 5.7(b) shows the normalized values for each of the four frequencies.

A high frequency would be best from a resolution standpoint, so 1.0 Hz seemed to be the most favorable frequency at first. However, the maximum sensitivity for 1.0Hz, which occurs at 7 km offset (Figure 5.7b), lies below the approximate noise level of  $10^{-16} \text{ V/Am}^2$  (Figure 5.7a) and may not be detectable. This necessitated the

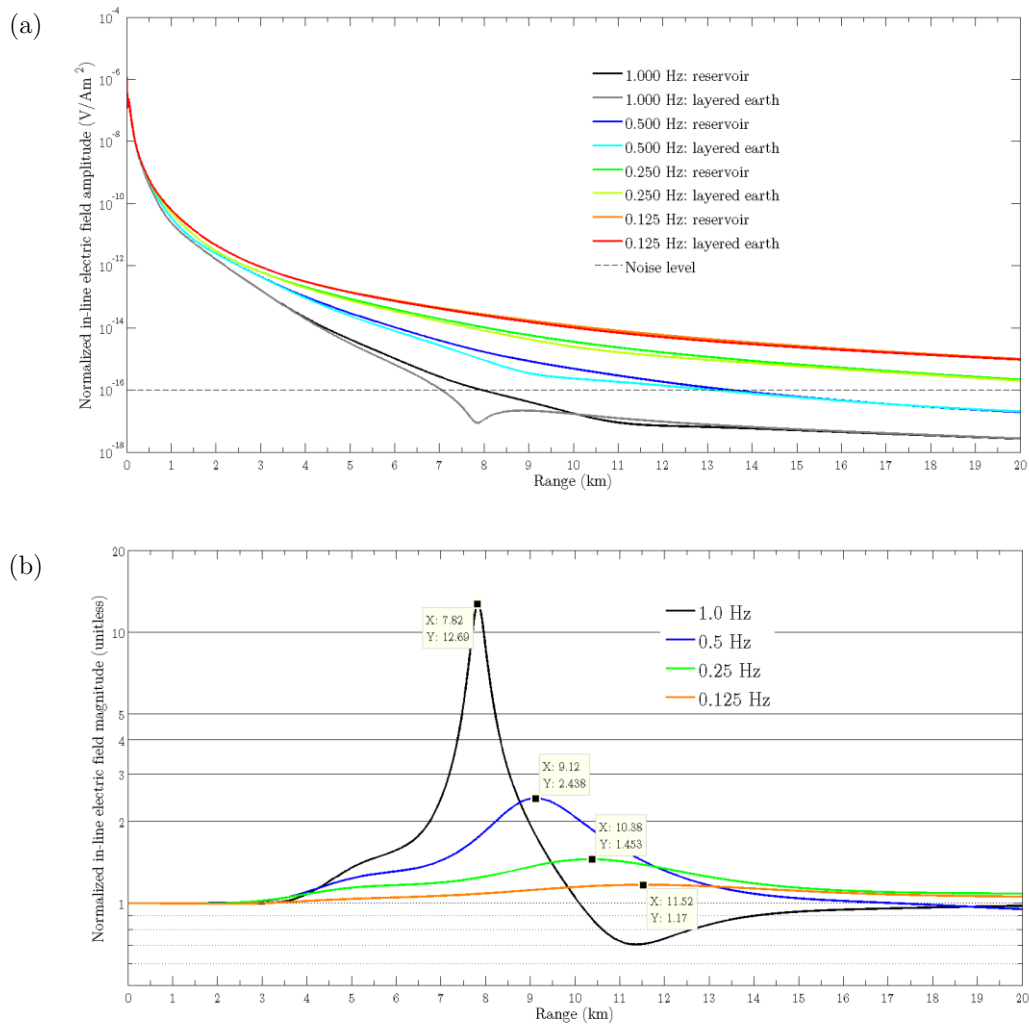


Figure 5.7: The (a) 1D in-line amplitude simulations for four frequencies via DIPOLE1D (Key, 2009) from the 1D model given in Figure 5.6, and the (b) sensitivity curves for each frequency calculated by normalizing the reservoir response to the layered earth response.

consideration of lower frequencies. Notice how the other three frequencies (0.5 Hz, 0.25 Hz, and 0.125 Hz) all have a maximum sensitivity at an offset where the computed in-line electric fields lie above the noise level. The most favorable frequency appears to be 0.5 Hz because it achieves the highest sensitivity while the fields remain above the noise level.

The purpose of this section is to predict if marine CSEM will be sensitive to these Tithonian reservoirs, and which frequencies to consider for the 3D forward modeling phase. It seems that despite the presence of a basement layer, the higher background resistivities, and the sands being buried much deeper, significant sensitivity to the reservoirs considered for this study still exists. The sensitivities are undoubtedly lower than the scenario considered in the previous synthetic example (Section 4.2), but they still lie above the generic noise level. Furthermore, an outcome of the 1D forward modeling showed that the most favorable frequency was 0.50 Hz. Other frequencies will still be considered for numerical simulation, but 0.50 Hz will likely be the primary frequency of interest.

It is critical to realize, however, that this entire analysis contains a 1D assumption which is not realistic and is overestimating the truth. The 1D simulations assume the reservoirs are infinitely laterally extensive, whereas in reality the reservoirs are 3D isolated bodies. This 1D study was helpful in determining how the additional factors mentioned above would influence the sensitivity, but the outcomes themselves cannot be directly used to understand the 3D sensitivity. In summation, this 1D analysis is certainly overestimating the true 3D sensitivity of the Tithonian reservoirs and the real test is to determine if marine CSEM remains sensitive to these reservoirs in three dimensions using 3D finite-element forward modeling.

## 5.4 3D Model Building at Mizzen

The first step of building the 3D model (as discussed in Section 3.1) surrounding the Mizzen prospect was obtaining information and establishing various parameters of the model. The EMGS marine CSEM survey components used for this study are indicated by the transmitter line and five receivers shown in Figure 5.1. There was only one transmitter line that passed over the theorized extent of the Mizzen L-11 reservoir, so only one was considered. The transmitter and receivers have a SSW to NNE trend which was a factor in considering the size of the VOI.

The VOI was established such that the L-11 well was situated near the center and the lateral extent was large enough to satisfy the EM modeling boundary conditions. The skin depth formula depends on a homogeneous conductivity and one frequency which is not the case for this scenario because the resistivity increases with depth and multiple frequencies are being considered. However, an average resistivity of the Jurassic ( $4.0 \Omega m$ ) was used to calculate skin depths as it is the most resistive geochronologic interval. The resistivity value of the basement was not used because the basement is quite deep in the model and its influence on the data was predicted to only influence the far offsets. Skin depths were calculated using Equation 2.11 for three different frequencies (0.25Hz, 0.50Hz, 1.00Hz),

$$z_{0.25Hz} \approx \frac{500}{\sqrt{(0.25)(0.25)}} = 2000m$$

$$z_{0.50Hz} \approx \frac{500}{\sqrt{(0.25)(0.50)}} = 1414m$$

$$z_{1.00Hz} \approx \frac{500}{\sqrt{(0.25)(1.00)}} = 1000m$$

If only one frequency was considered, then the lateral extent of the model could be based on the skin depth from that single frequency alone, however, that is not the case here. In order to ensure good results for *all three frequencies*, the largest skin depth (2000m) was used to make a model large enough to satisfy the boundary conditions for all three frequencies. The boundaries for the x-axis were made such that they extended roughly 20 km in either direction from the L-11 well (recall from Section 3.1.1 that the boundaries of the model should be 8-10 skin depths away from the transmitter). The boundaries for the y-axis were made larger for a particular reason. The marine CSEM survey parameters have a more northerly trend than they do easterly (see Figure 5.1). This is important because the transmitters/receivers would be closer to the y-axis boundary on either end. Therefore, the y-axis boundary was made larger to extend roughly 30 km in either dimension from the L-11 well. The z-axis was chosen to extend 20 km above sea level because of personal experience, and below sea level by 20 km to ensure the basement would be accurately represented. In summary, the VOI of the model was determined to be  $x = [0 \text{ km}, 40 \text{ km}]$ ,  $y = [0 \text{ km}, 60 \text{ km}]$ ,  $z = [-20 \text{ km}, 20 \text{ km}]$ .

Four surfaces – the seafloor, base Tertiary, base Cretaceous, and base Jurassic – were created at Nalcor Energy by the process discussed in Section 3.1.1. Each of the surfaces was created with 1000m node spacing and the lateral extents matched those of the VOI. These surfaces were added to the model *incrementally* in order to ensure any issues or errors could be identified.

### 5.4.1 Seafloor model

The first topographical surface to be included in the model was the seafloor surface. A topographic map of the seafloor surface is shown in Figure 5.8 with the black dots representing the 1000m spaced nodes. The northwestern portion of the surface drops off quickly as this leads to the Orphan Basin, but the seafloor is relatively flat in the area of the Flemish Pass.

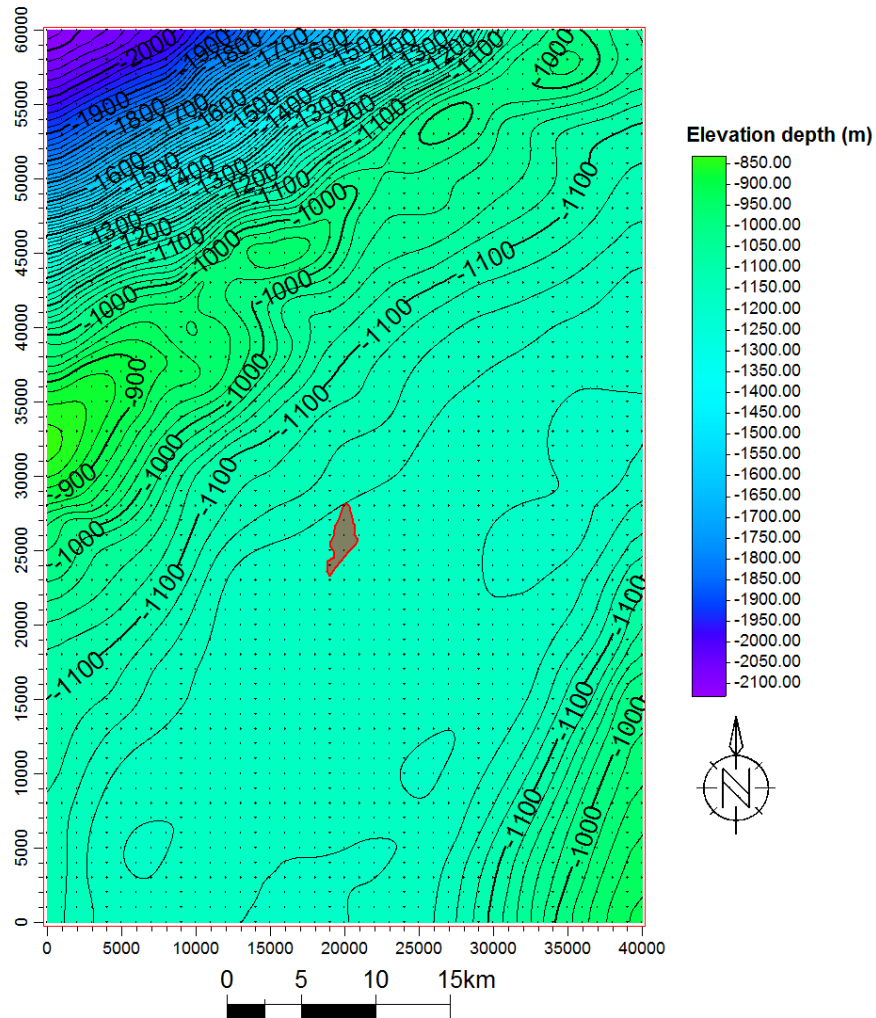


Figure 5.8: A topographical map of the seafloor surface where the black dots are the 1000m spaced nodes used to represent the surface for modeling purposes. The polygon from Statoil depicting the L-11 reservoir extent is shown for reference. Mean sea level is  $z = 0\text{m}$ . Contour interval = 20m.

This surface was imported into FacetModeller using the process described in Section 3.1.2 and was meshed using the following command line switches in TetGen,

```
tetgen.exe -pq1.4/16AfenCV seafloor_model.poly
```

which resulted in a mesh with 737,255 cells. The relevant mesh statistics are given in Figure 5.9. Notice how the smallest dihedral angle is  $5.41^\circ$  despite the minimum dihedral constraint of  $16^\circ$  being used. This implies that the nature, quality, and/or constraints of the model make it impossible to achieve this constraint. The seafloor of the layered earth models was flat which resulted in quality meshes, but this scenario contains a seafloor surface with only a little topography and there is already degradation in the quality of the mesh. However, the percentage of poor quality cells is only 0.249% (1838/737,255 cells).

Another interesting statistic is the shortest edge being 0.00095m which means there are some *very* small cells in the mesh. These small cells are undesirable because they likely add more cells to the mesh than needed. Figure 5.10 shows a 3D view of the mesh with various pieces removed to show the internal structure. The Tertiary region extends to the base of the mesh because there are not yet any other surfaces below the seafloor. Small *pulses* of nodes, which likely correlate to these tetrahedra reported with small edge lengths, are observed across the entire seafloor surface and these can be seen in Figure 5.10. An easier way to observe these pulses is to zoom into the seafloor surface as shown in Figure 5.11. Notice how these pulses lie right on the seafloor surface. This appears to be an artifact of the meshing process when TetGen has too much freedom. An .mtr file was introduced to help constrain

Mesh quality statistics:			
Smallest volume:	8.155e-11	Largest volume:	1.2156e+11
Shortest edge:	0.00095367	Longest edge:	12342
Smallest asp.ratio:	1.2331	Largest asp.ratio:	17.522
Smallest facangle:	12.362	Largest facangle:	138.6835
Smallest dihedral:	5.4118	Largest dihedral:	167.4759
Aspect ratio histogram:			
< 1.5	: 18729	6 - 10	: 1752
1.5 - 2	: 213227	10 - 15	: 81
2 - 2.5	: 256257	15 - 25	: 5
2.5 - 3	: 134670	25 - 50	: 0
3 - 4	: 86138	50 - 100	: 0
4 - 6	: 26396	100 -	: 0
(A tetrahedron's aspect ratio is its longest edge length divided by its smallest side height)			

Figure 5.9: The statistics of the seafloor mesh (737,255 cells) without the use of the `-m` switch and a corresponding `.mtr` file.

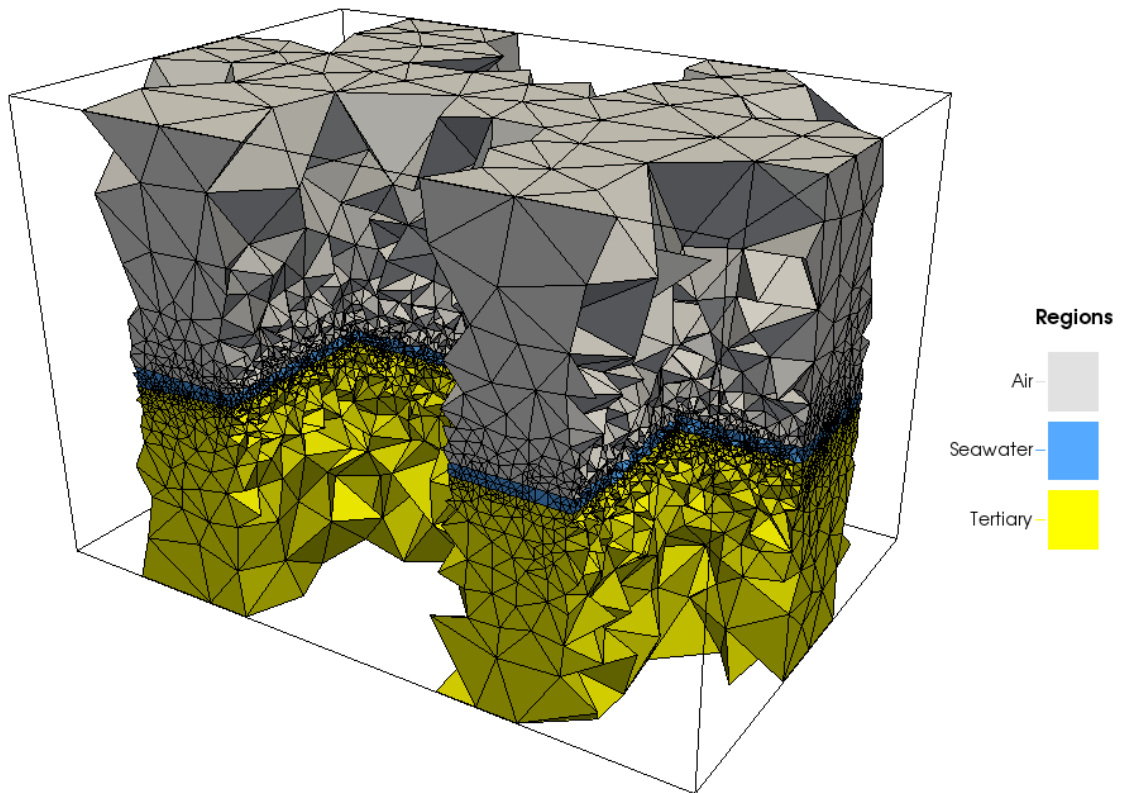


Figure 5.10: A 3D view of the seafloor mesh (created without the use of an `.mtr` file) with various pieces removed to show the internal structure.

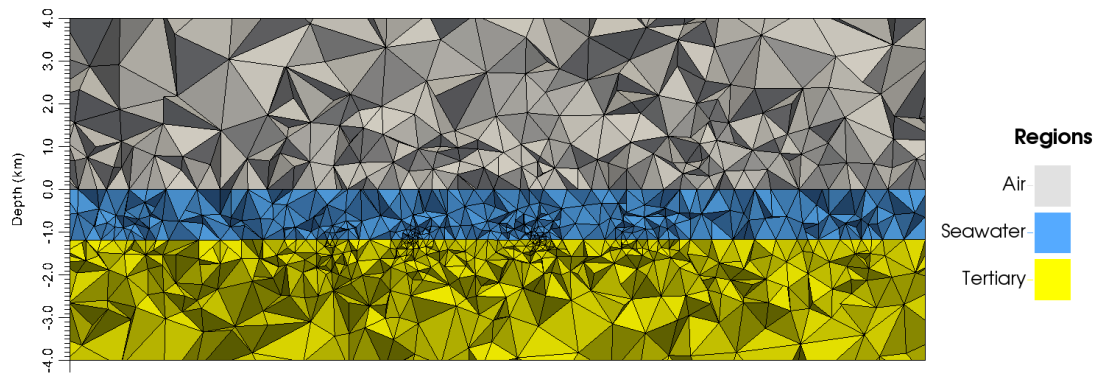


Figure 5.11: A 2D slice of the seafloor mesh (without the use of a .mtr file) zoomed in to show the pulses of nodes created on the seafloor surface.

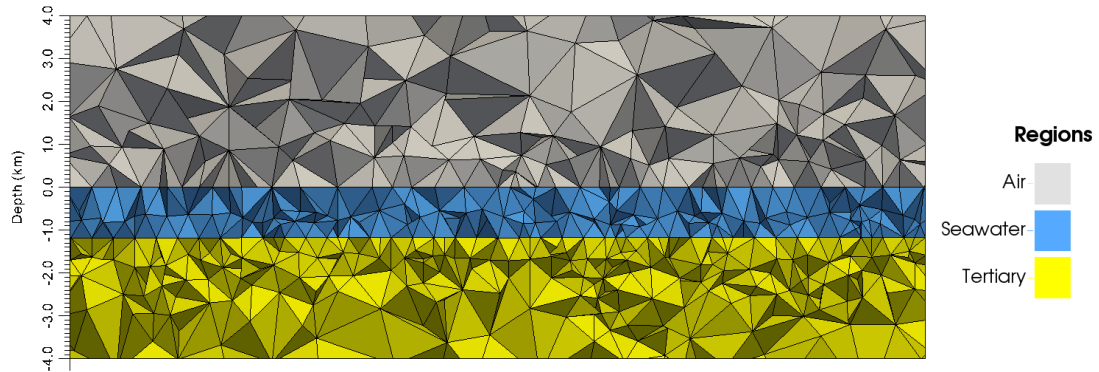


Figure 5.12: A 2D slice of the seafloor mesh with a 500m edge-length constraint imposed on the seafloor nodes. The constraint clearly removed the pulses of small nodes.

Mesh quality statistics:						
Smallest volume:	9.1244e+05	Largest volume:	6.291e+10			
Shortest edge:	207.31	Longest edge:	10886			
Smallest asp.ratio:	1.2252	Largest asp.ratio:	15.702			
Smallest facangle:	5.4164	Largest facangle:	169.1672			
Smallest dihedral:	5.9061	Largest dihedral:	168.8331			
Aspect ratio histogram:						
< 1.5	:	14292		6 - 10	:	782
1.5 - 2	:	133461		10 - 15	:	37
2 - 2.5	:	143646		15 - 25	:	1
2.5 - 3	:	67942		25 - 50	:	0
3 - 4	:	41416		50 - 100	:	0
4 - 6	:	12010		100 -	:	0
(A tetrahedron's aspect ratio is its longest edge length divided by its smallest side height)						

Figure 5.13: The statistics of the seafloor mesh (413,587 cells) created with the use of a 500m edge-length constraint on the seafloor surface nodes.

the meshing process. The nodes on the seafloor surface are spaced at 1000m and a 500m edge-length constraint was placed on every seafloor node. This constraint implies TetGen cannot add additional nodes within a 500m radius of the 1000m spaced input nodes on the seafloor surface. Consequently, this still allowed TetGen to have some freedom in adding nodes to the surface, but this constraint prevented small cells from being made on the surface. A new mesh was made using the same switches as before, but with the inclusion of the `-m` switch (the `.mtr` file). Figure 5.12 shows the exact same mesh slice as Figure 5.11 and notice how the inclusion of the 500m edge length constraint improved the tetrahedra along the boundary of the seafloor surface. The new mesh contained 413,587 cells which was a reduction of over 300,000 tetrahedral cells. This was a monumental reduction in the number of cells and the impact on the quality of cells is also shown by the statistics in Figure 5.13. The dihedral angle constraint of  $16^\circ$  still could not be maintained which must be a result of the complexity of the topographical surface. However, the shortest edge was increased to 207m which is easily seen in Figure 5.12, and the percentage of poor quality cells was reduced to 0.198% (820/413587 cells) which was a minor improvement.

The quality of this mesh appeared sufficient based on visual inspection of the mesh and the statistics, but the only concrete way to know if the quality was good enough was to actually run a simulation using the mesh. The purpose of this was not initially to recover any quality results, but rather to observe how well the residual norm of the iterative solver decays. To do so, only one observation location was used. A y-directed transmitter was arbitrarily placed 30 m above the

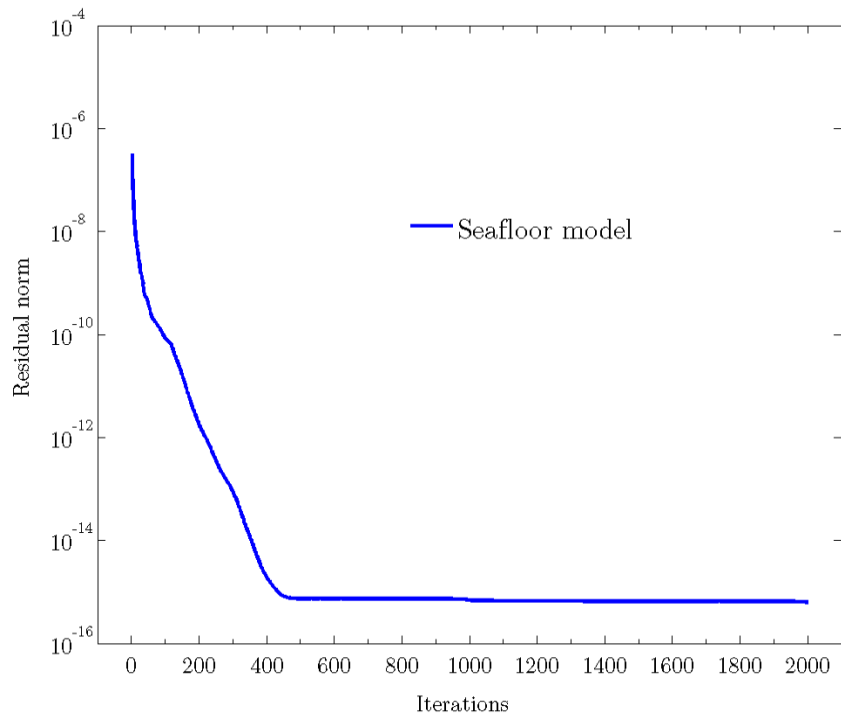


Figure 5.14: The convergence of the residual norm for the seafloor model containing the 500m edge-length constraint on the seafloor surface nodes. A Krylov subspace of 500 was used.

seafloor surface at  $(x, y, z) = (20 \text{ km}, 26 \text{ km}, -1140 \text{ m})$  and the one observation location was placed 8 km north of the transmitter just above the seafloor surface at  $(x, y, z) = (20 \text{ km}, 34 \text{ km}, -1128 \text{ m})$ . The resistivities for the air, seawater, and Tertiary were taken directly from those shown in the 1D modeling section (see Figure 5.6). A Krylov subspace of 500 was used and the resulting convergence from the seafloor model is shown in Figure 5.14. It can be seen that the residual norm did indeed decrease sufficiently for the computed fields to be accurate. The next step was adding the base Tertiary surface to the model.

## 5.4.2 Base Tertiary model

The second topographical surface included in the model was the base Tertiary surface. A topographic map of the base Tertiary is shown in Figure 5.15 with the black dots representing the 1000m spaced nodes. This surface is actually quite simple as it almost appears to be a tilted plane dipping towards the northwest. This surface was added to the seafloor model and was meshed similarly to the

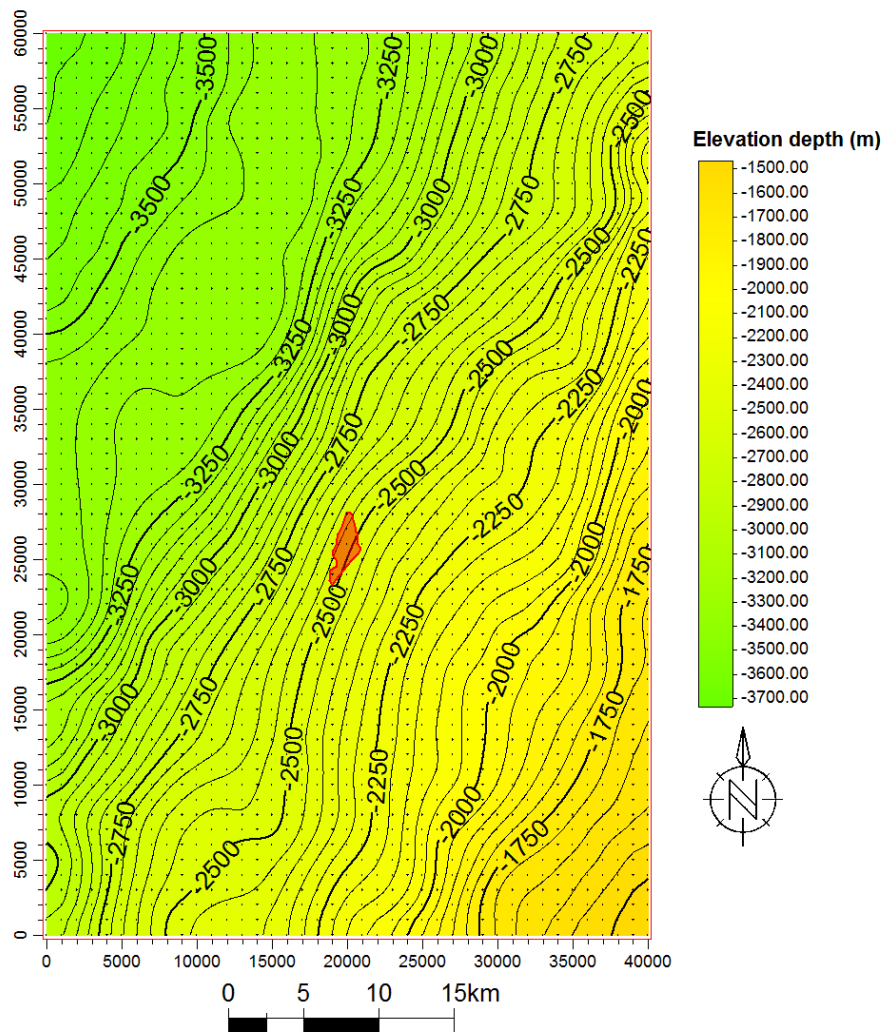


Figure 5.15: A topographical map of the base Tertiary surface where the black dots are the 1000m spaced nodes used to represent the surface for modeling purposes. The polygon from Statoil depicting the L-11 reservoir extent is shown for reference. Contour interval = 50m.

seafloor model with the .mtr constraint. The 500m constraint on the seafloor nodes was imposed again, and this constraint was extended to the base Tertiary nodes to prevent any small pulses of nodes from forming on the base Tertiary surface as well. The base Tertiary model was meshed with the following command line switches in TetGen,

```
tetgen.exe -pq1.4/16AmfenCV baseTertiary_model.poly
```

which resulted in a mesh with 651,667 cells. The relevant mesh statistics are given in Figure 5.16. The smallest dihedral angle is 6.12°, the shortest edge is 135m, and the percentage of poor quality cells is 0.259% (1685/651667 cells). In summation, it appears the inclusion of the base Tertiary surface did not further degrade the quality of the mesh. Figure 5.17 shows a 3D view of the mesh with the north-east quadrant removed to show the internal structure. The Cretaceous region extends to the base of the mesh because there are not yet any other surfaces below the base Tertiary.

Mesh quality statistics:						
Smallest volume:	2.7408e+05		Largest volume:	7.4362e+10		
Shortest edge:	135.2		Longest edge:	10814		
Smallest asp.ratio:	1.2253		Largest asp.ratio:	14.616		
Smallest facangle:	15.509		Largest facangle:	136.7152		
Smallest dihedral:	6.1262		Largest dihedral:	164.9923		
Aspect ratio histogram:						
< 1.5	:	24374		6 - 10	:	1558
1.5 - 2	:	213597		10 - 15	:	127
2 - 2.5	:	224415		15 - 25	:	0
2.5 - 3	:	104027		25 - 50	:	0
3 - 4	:	64785		50 - 100	:	0
4 - 6	:	18784		100 -	:	0
(A tetrahedron's aspect ratio is its longest edge length divided by its smallest side height)						

Figure 5.16: The statistics of the base Tertiary mesh (651,667 cells) with the use of a 500m edge-length constraint on the seafloor and base Tertiary surface nodes in the .mtr file.

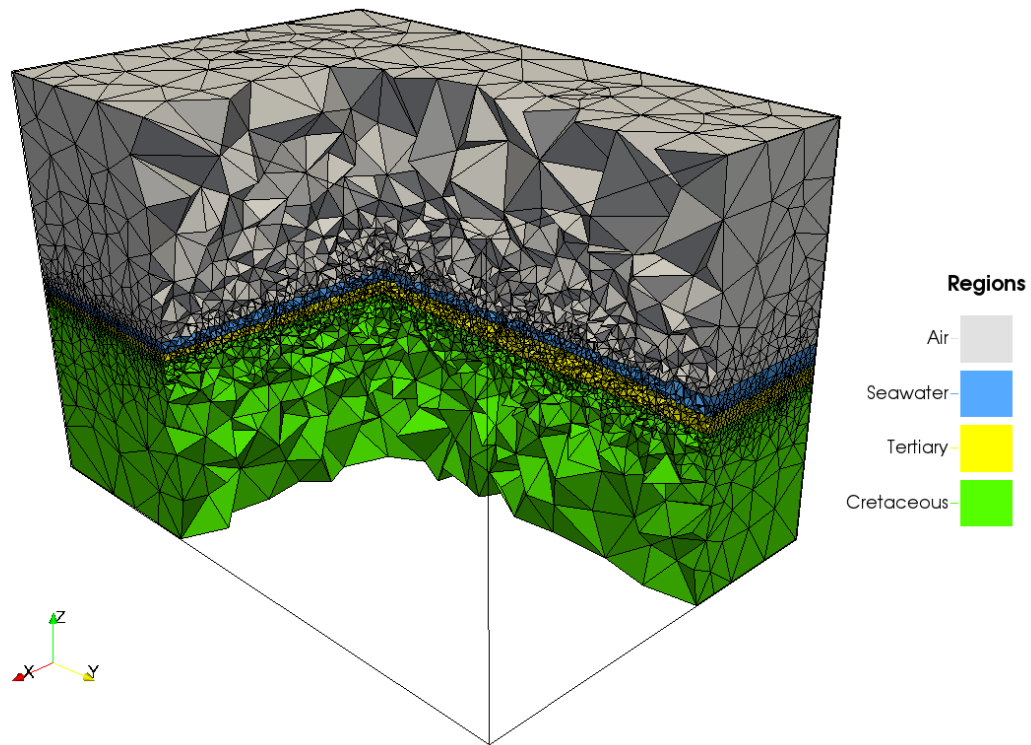


Figure 5.17: A 3D view of the base Tertiary mesh with the 500m edge-length constraints placed on both the seafloor and base Tertiary nodes. This mesh contains 651,667 cells and a piece has been removed to show the internal structure of the mesh.

The quality of this mesh appeared sufficient based on visual inspection and the mesh statistics, so it was appropriate to again see how well the residual norm of the iterative solver converged for this model. The same transmitter and single receiver from the seafloor model were used here and a Krylov subspace of 500 was used. Figure 5.18 shows the residual norm of the base Tertiary model and it appears to have decreased similarly as the seafloor model. The only change is it took the base Tertiary model slightly longer to reach its minimum residual norm, as expected due to the increased number of cells in the mesh.

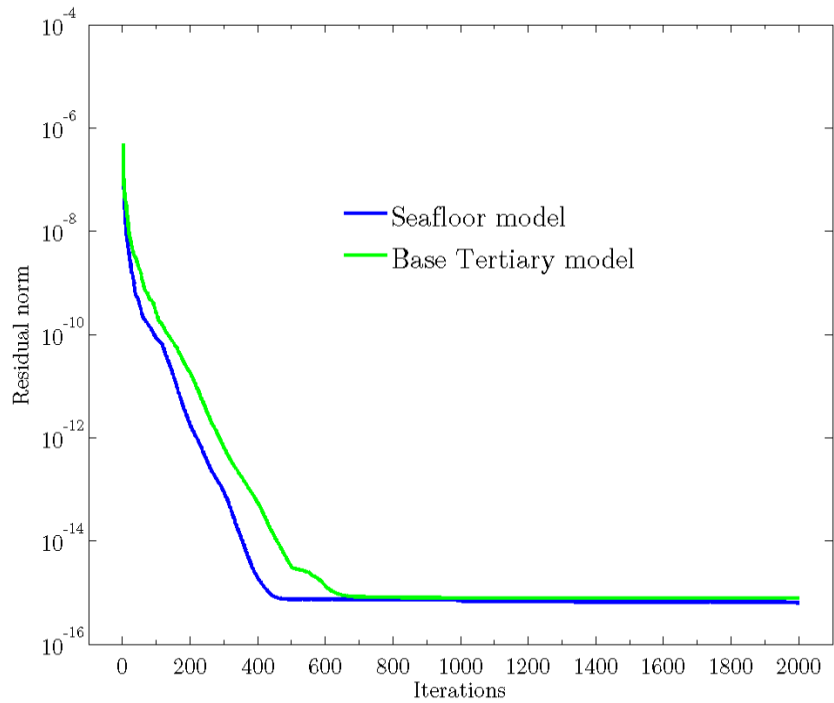


Figure 5.18: The decay of the residual norm for the base Tertiary model compared to the seafloor model. A Krylov subspace of 500 was used.

Upon final inspection of the mesh, there appears to be no place *where the thickness of the Tertiary is thin*. Consider a situation where the thickness of the Tertiary is small (e.g. 50m) and the nodes on the surfaces above and below have 1000m spacing and a 500m .mtr constraint. TetGen is going to try to make tetrahedra in that small region with edge lengths of 500m and this would result in poor quality (long, skinny) cells. In situations like these, either the node spacing on the surface needs to be refined, or TetGen needs the *freedom* to add nodes where needed. At this stage, this is not an issue, but this becomes relevant with the base Cretaceous surface in the next section.

### 5.4.3 Base Cretaceous model

#### 5.4.3.1 Attempt I

The third topographical surface for which an attempt was made to include it in the model was the base Cretaceous surface. A topographic map of the base Cretaceous is shown in Figure 5.19. Notice how this surface is far more complex than the previous two with much larger isolated elevation changes. The black symbols indicate where two wells were drilled (L-11 and O-16). Notice that these wells were drilled in *Jurassic highs* as many of the fields are located just below these highs. The area enclosed by the pink rectangle is the Mizzen area of interest (AOI) and the southern-most well within this rectangle is Mizzen L-11.

This surface is predicted to make meshing complicated because recall that the Mizzen sands are situated right beneath this surface (see Figure 5.3) and the top-most sand is only about 15m thick. When the Mizzen reservoirs are included in the model, their impact on the mesh will likely cause the cells around them to be small and will influence the surface above. Foreseeing this potential issue, the base Cretaceous surface was refined with more nodes in the area of interest (the pink rectangle). The surface was represented with 1000m spaced nodes outside the pink rectangle (with a 500m edge-length constraint in the .mtr file), but the area of interest contained 200m spaced nodes (with a 100m edge-length constraint). The same 500m constraints on the base Tertiary and seafloor surface were kept, and the base Cretaceous model was meshed with the following command line switches in TetGen,

```
tetgen.exe -pq1.4/16AmfenCV baseCretaceous_model.poly
```

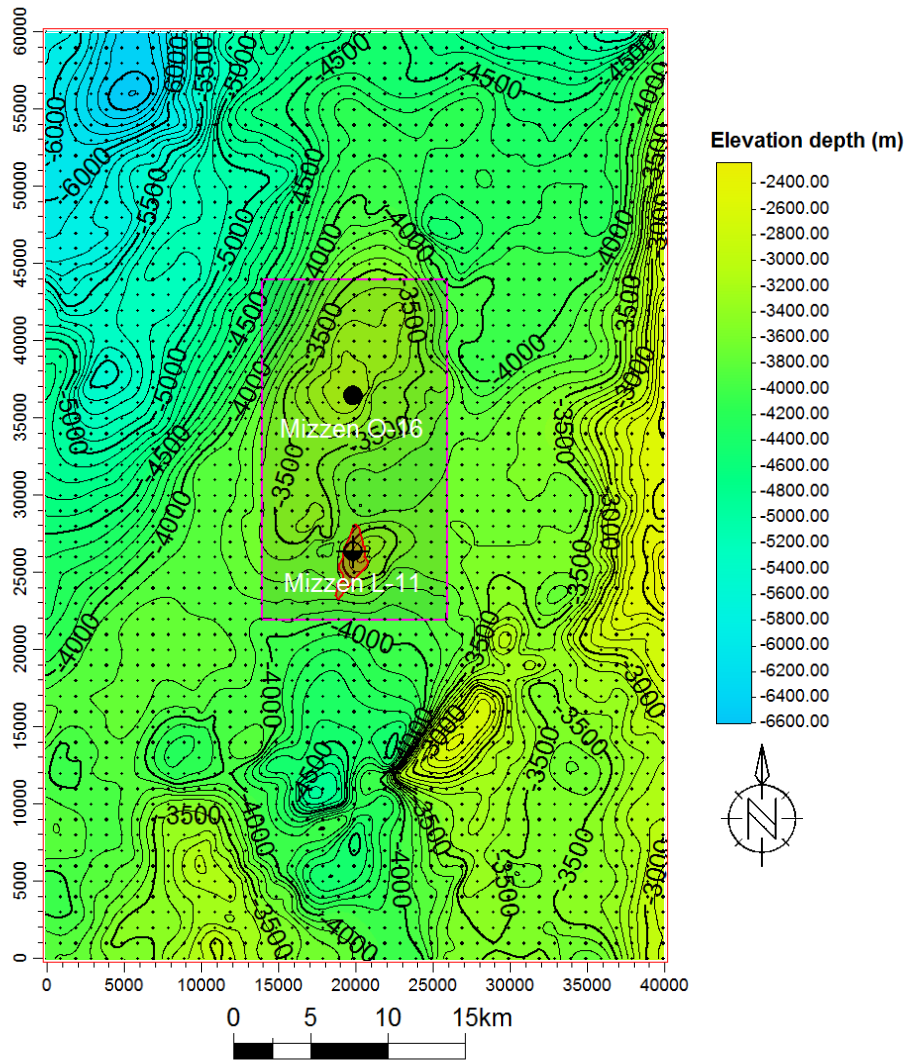


Figure 5.19: A topographical map of the base Cretaceous surface. The pink rectangle represents the Mizzen area of interest (the nodes spaced at 200m are not shown) and the polygon from Statoil depicting the L-11 reservoir extent is shown for reference. Contour interval = 100m.

which resulted in a mesh with 1,863,175 cells. The relevant mesh statistics are given in Figure 5.20. The smallest dihedral angle is  $1.67^\circ$ , the shortest edge is 39m, and the percentage of poor cells is 0.507% (9449/1863175) which seems to be a decline in quality compared to the base Tertiary mesh. The refinement patch on the surface added an astronomical amount of cells to the mesh as shown in Figure

Mesh quality statistics:						
Smallest volume:	5084.7		Largest volume:	6.311e+10		
Shortest edge:	39.072		Longest edge:	10399		
Smallest asp.ratio:	1.2248		Largest asp.ratio:	43.984		
Smallest facangle:	4.9559		Largest facangle:	157.2888		
Smallest dihedral:	1.6748		Largest dihedral:	174.4057		
Aspect ratio histogram:						
< 1.5	:	74084		6 - 10	:	8600
1.5 - 2	:	605782		10 - 15	:	791
2 - 2.5	:	625368		15 - 25	:	50
2.5 - 3	:	294951		25 - 50	:	8
3 - 4	:	191523		50 - 100	:	0
4 - 6	:	62018		100 -	:	0
(A tetrahedron's aspect ratio is its longest edge length divided by its smallest side height)						

Figure 5.20: The statistics of the base Cretaceous mesh – attempt I – (1,863,175 cells) with the use of a 500m edge-length constraint on the seafloor and base Tertiary nodes, and a variable constraint on the base Cretaceous nodes.

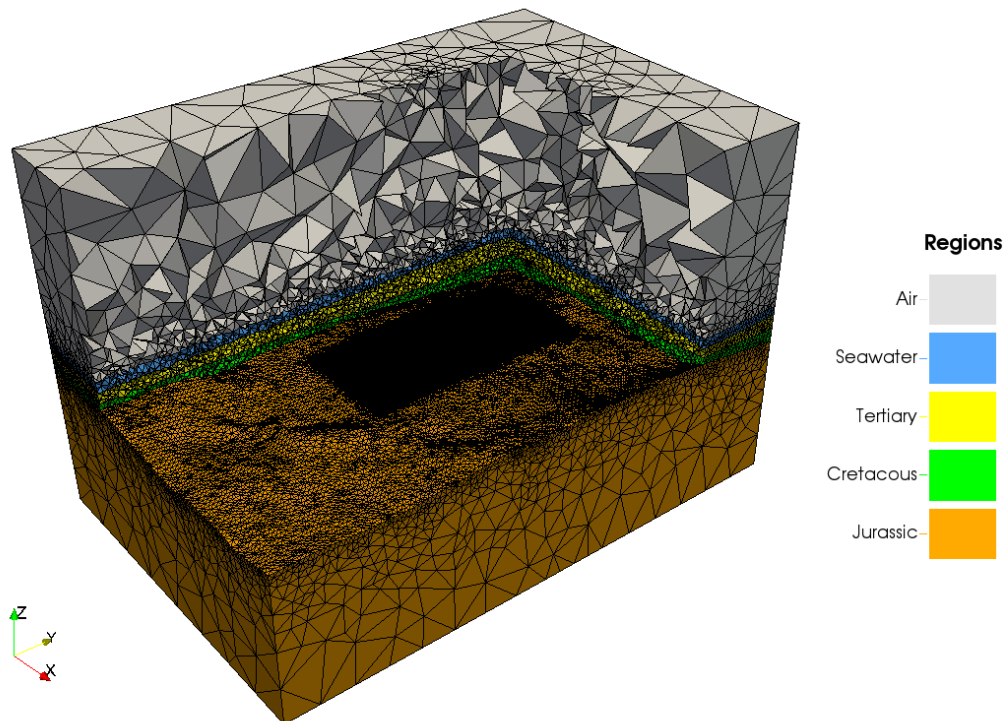


Figure 5.21: A 3D view of the base Cretaceous mesh (attempt I). This mesh contains 1,863,175 cells. A portion is removed to show the refinement match on the base Cretaceous surface.

5.21. Another issue is the thickness of the Cretaceous is quite thin in the northern section of the Mizzen AOI (shown by the Cretaceous thickness map in Figure 5.22). Edge-length constraints of 500m were placed on the base Tertiary and base Cretaceous nodes which resulted in poor quality tetrahedra (long, thin cells) where the Cretaceous is thin. This is clearly shown by the 2D slice in Figure 5.23.

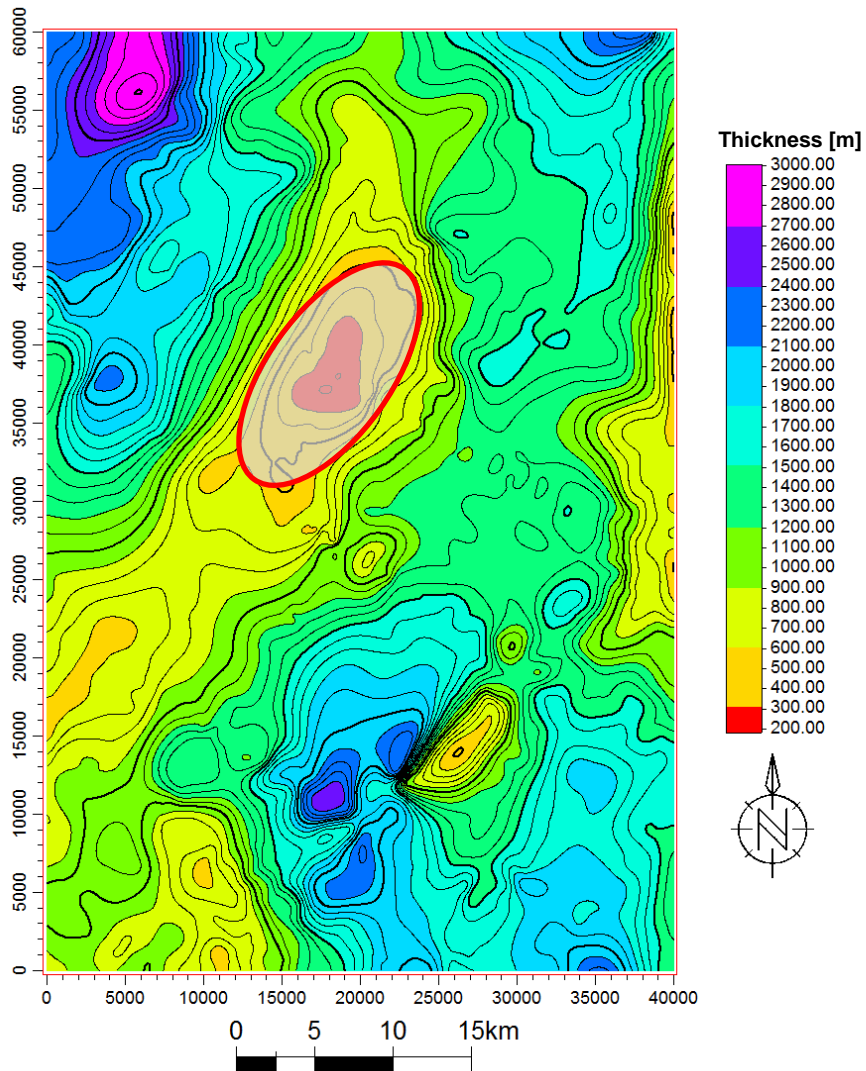


Figure 5.22: A topographical thickness map of the Cretaceous. The red circle indicates an area with a thin Cretaceous thickness causing meshing issues. Contour interval = 100m.

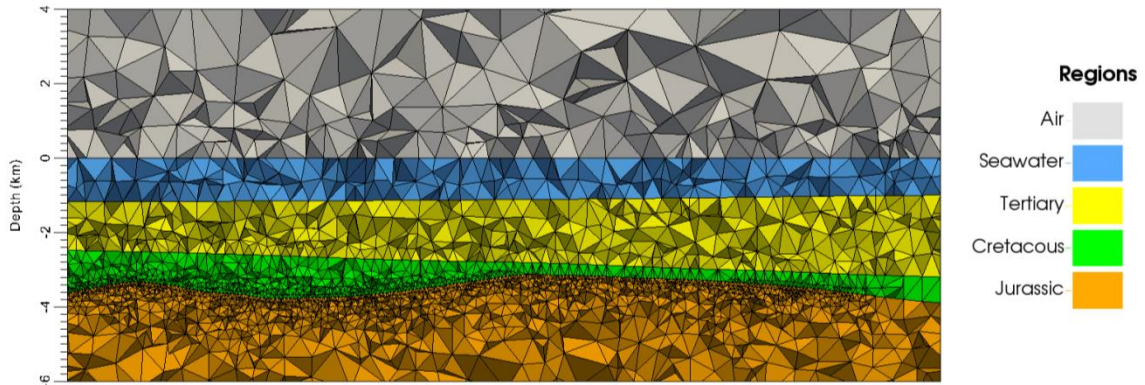


Figure 5.23: A 2D slice of the base Cretaceous mesh (attempt I) cutting through the center of the Mizzzen AOI. Poorly shaped cells are observed where the Cretaceous is thin.

A simulation was still performed despite the issues with the base Cretaceous mesh (attempt I). A Krylov subspace of 300 was used due to the increased number of cells, and hence memory requirements. The convergence for this mesh is shown in Figure 5.24. Not surprisingly, the residual norm for this model did not decrease sufficiently, and thus this mesh was not acceptable for moving forward. The poor convergence could be attributed to many factors and the issue cannot be pinpointed because there were too many changes from the base Tertiary mesh. Some examples may include poor quality cells from the thin Cretaceous area, the sheer number of cells, and/or too much refinement on the base Cretaceous surface. A second meshing attempt tried to address these issues.

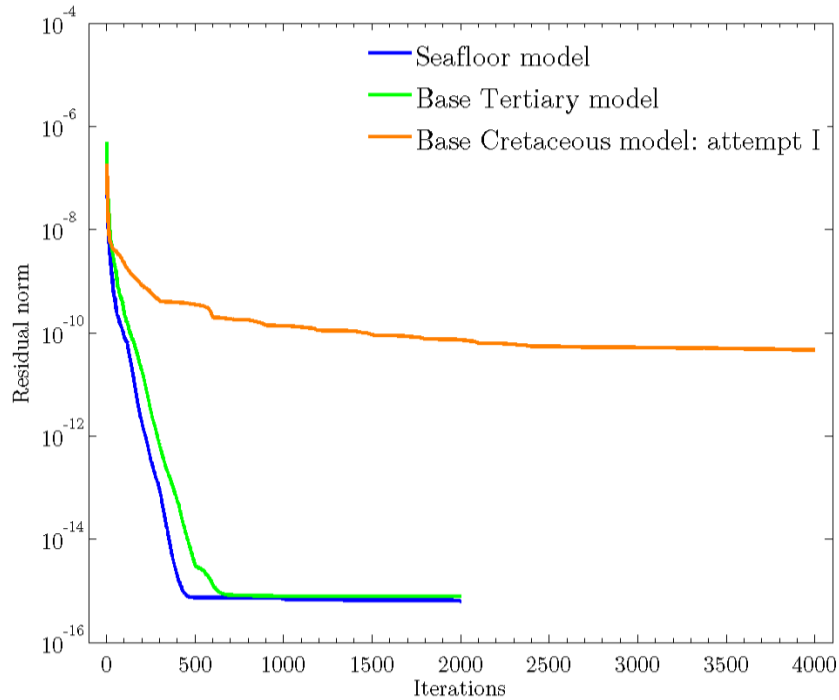


Figure 5.24: The decay of the residual norm for the base Cretaceous model (attempt I) compared to the previous two examples. The residual norm does not decrease sufficiently and thus the mesh is not acceptable. A Krylov subspace of 300 was used.

### 5.4.3.2 Attempt II

The base Cretaceous surface was created very differently in the second attempt in an effort to improve some of the issues that may have been causing poor convergence. In hindsight, the *entire* Mizzen AOI did not need to be refined because the area of thin Cretaceous thickness is isolated. However, it seemed appropriate to maintain refinement on the surface directly above the Mizzen prospect in anticipation of the reservoir sands being included later. So, the entire base Cretaceous surface was modified such that all the nodes were spaced 1000m apart except for a small region around Mizzen L-11 (see Figure 5.25) with 100m

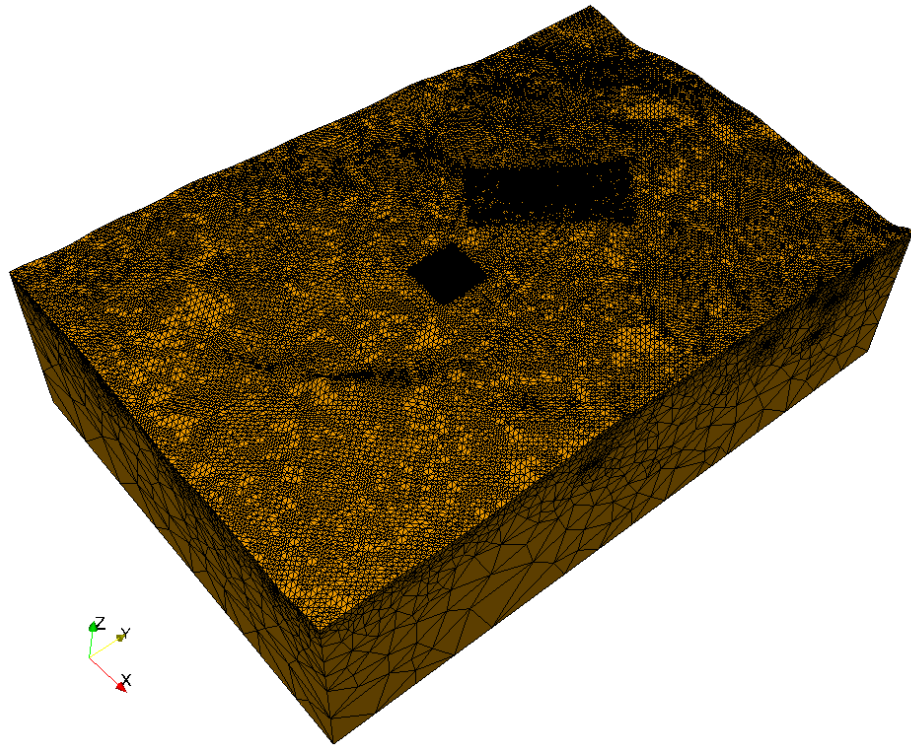


Figure 5.25: A 3D view of the base Cretaceous surface after meshing (attempt II). The small square patch is refinement on the surface in the area of the Mizzen L-11 well, in anticipation of the reservoir sands being included later. The rectangular patch is a result of *removing* the edge-length constraint on the base Tertiary and base Cretaceous nodes surrounding the thin Cretaceous thickness area.

spaced nodes. In order to address the thin Cretaceous thickness problem, the base Tertiary and base Cretaceous nodes surrounding the area circled in Figure 5.22 simply had their constraint in the .mtr file *removed* to give TetGen freedom to add tetrahedra as necessary. The same TetGen switches were used from the first attempt and the resulting mesh from this attempt contained 1,803,145 cells with similar mesh statistics – the percentage of poor cells was 0.537% (9679/1803145) – of the first attempt. It was a surprise to see that the number of tetrahedra for the second attempt was comparable to that of the first attempt when the refined region on the surface was reduced. However, the area surrounding the Mizzen

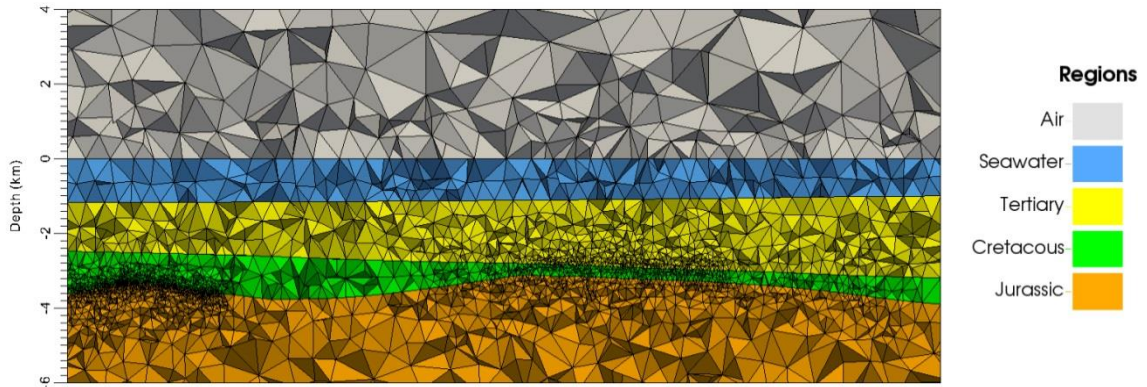


Figure 5.26: A 2D slice of the base Cretaceous mesh (attempt II) cutting through the center of the Mizzen AOI. The cells over the Mizzen prospect (left) are refined and the cells in the area of the thin Cretaceous thickness (right) are greatly improved.

prospect was refined with 100m spacing (as opposed to 200m in the first attempt) which is likely where the additional tetrahedra came from. These two modifications to the base Cretaceous surface are easily observed by the 2D slice in Figure 5.26. Notice the refinement on the base Cretaceous surface above the area of the Mizzen prospect (left) and also the cells in the area of the thin Cretaceous thickness (right) are greatly improved.

A numerical simulation test of this updated mesh was performed in the hope that the changes made would improve the convergence. A Krylov subspace of 1000 was also used with the expectation that a higher subspace dimension could further improve the convergence. The residual norm for this second meshing attempt of the base Cretaceous model is shown in Figure 5.27, and to some surprise, the decay of the residual norm had no improvement. However, it seems that the residual norm did not fully level off (i.e. flat line), and if given enough iterations it could have reached a more acceptable value. It appears that the residual norm for this

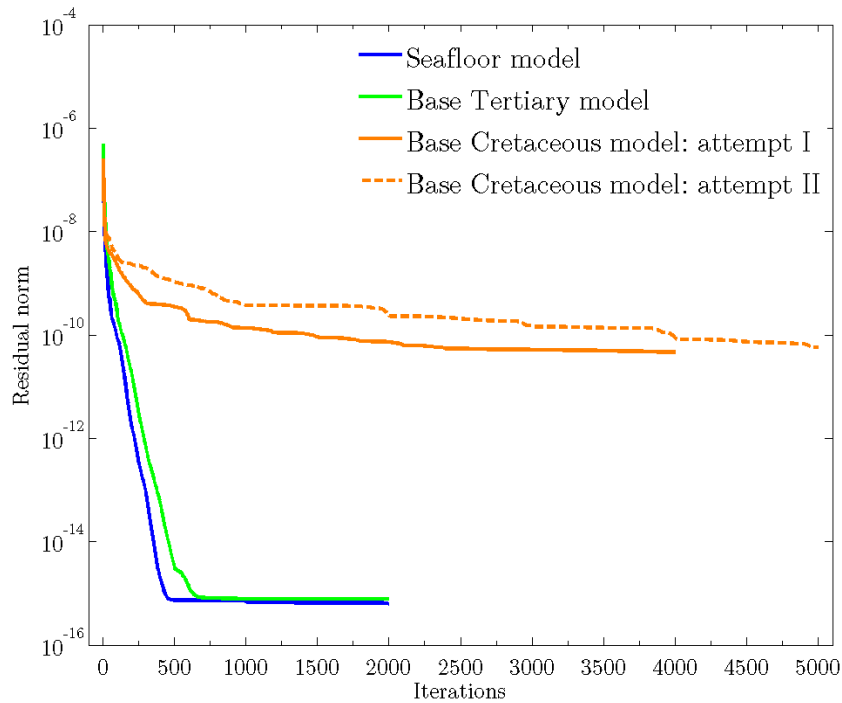


Figure 5.27: The decay of the residual norm for the base Cretaceous model (attempt II) compared to previous models. A Krylov subspace of 1000 was used.

mesh requires  $\sim 5000$  iterations to reduce by one order of magnitude. By simple extrapolation it seems that it would take approximately 30,000 iterations for the residual norm to reach the final residual norm achieved by the seafloor or base Tertiary model. This is undesirable from a practical point of view because 30,000 iterations would require *a few days* to recover this one result using this code on a mesh of this size.

At the time, including the base Cretaceous surface in this model seemed very difficult due to the challenges it brought. So, in the interest of time, it was decided that the *base Cretaceous surface would not be included in the Mizzen model*. This essentially combined the Cretaceous and Jurassic into one layer. The Cretaceous is

relatively thin (<1000m) compared to the other regions in the Mizzen area, so removing it may not be as big a sacrifice as it may seem. Another advantage with removing this surface is when the Mizzen reservoirs are eventually included, they will no longer have a surface lying right above which will alleviate potential meshing issues. In fact, with the removal of the base Cretaceous, the Mizzen reservoirs would lie in the *middle* of the combined Cretaceous-Jurassic layer – a less challenging scenario for meshing purposes. The base Cretaceous surface was only disregarded for this Mizzen model as it was successfully included in the Bay du Nord model later in Chapter 6.

#### **5.4.4 Base Jurassic (basement) model**

The last topographical surface included in the model was the base Jurassic surface (also referred to as the *basement surface*). A topographic map of the base Jurassic is shown in Figure 5.28. The base Jurassic has a very similar level of complexity as the base Cretaceous with sharp elevation changes and high reliefs. In the Mizzen area, there appears to be a basement high, and there is also another basement high towards the east which is approaching the Flemish Cap. The basement high in the Mizzen area is important to remember later on because the basement acts as a strong resistor, and the shallower it is, the more it could adversely impact the sensitivity to the potential reservoirs. The meshing process was quite simple with the base Cretaceous surface excluded. The nodes for all three surfaces were given a 500m edge-length constraint in the .mtr file. There were no areas in the mesh where a given layer had a small thickness, so no special refinement schemes were

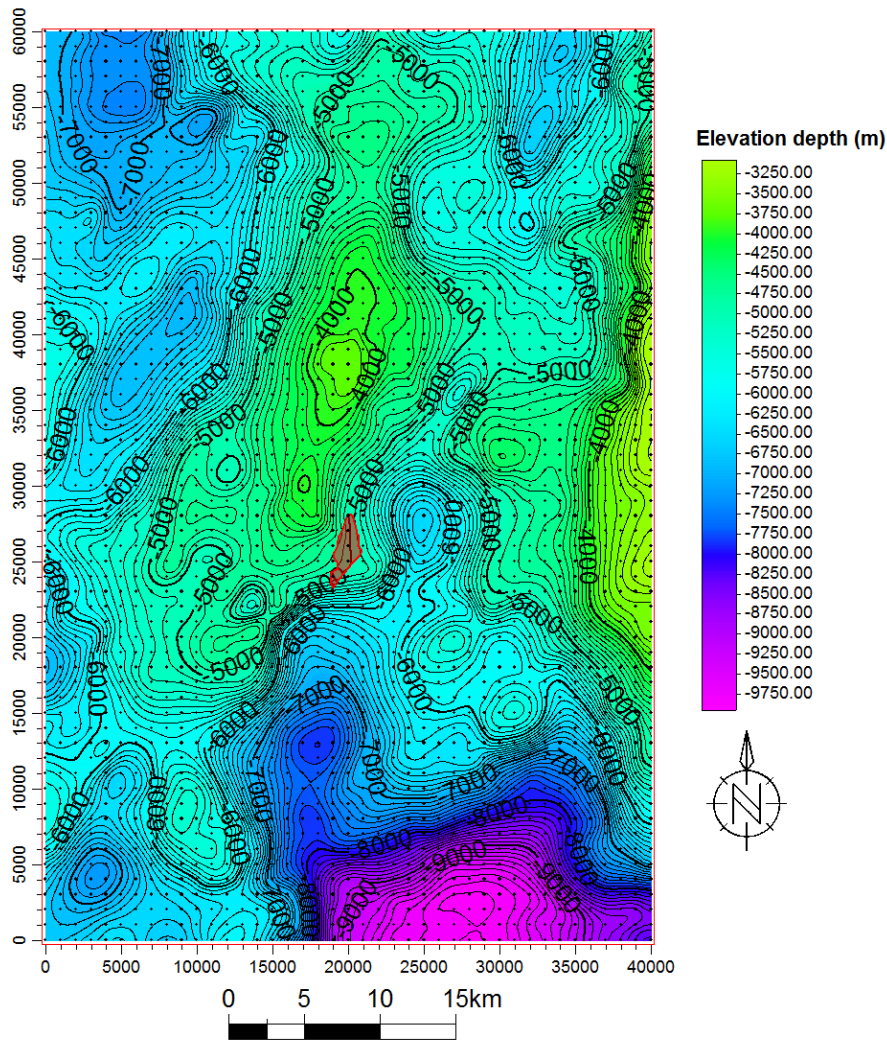


Figure 5.28: A topographical map of the base Jurassic (basement) surface with a basement high in the Mizzen area of interest and a basement high towards the Flemish Cap in the east. The polygon from Statoil depicting the L-11 reservoir extent is shown for reference. Contour interval = 100m.

necessary. The three-layer model was meshed with the following switches in TetGen,

```
tetgen.exe -pq1.4/16AmfenCV basement_model.poly
```

which resulted in a mesh with 1,079,930 cells. The relevant mesh statistics are given in Figure 5.29. The smallest dihedral angle is  $2.90^\circ$ , the shortest edge is 97m, and the percentage of poor cells is 0.223% (2413/1079930) which is a great

Mesh quality statistics:				
Smallest volume:	1.9246e+05		Largest volume:	5.9963e+10
Shortest edge:	96.728		Longest edge:	10085
Smallest asp.ratio:	1.2258		Largest asp.ratio:	39.055
Smallest facangle:	8.5316		Largest facangle:	160.6598
Smallest dihedral:	2.8972		Largest dihedral:	174.4451
Aspect ratio histogram:				
< 1.5	: 45345		6 - 10	: 2247
1.5 - 2	: 382984		10 - 15	: 159
2 - 2.5	: 361575		15 - 25	: 4
2.5 - 3	: 159800		25 - 50	: 1
3 - 4	: 98437		50 - 100	: 0
4 - 6	: 29378		100 -	: 0
(A tetrahedron's aspect ratio is its longest edge length divided by its smallest side height)				

Figure 5.29: The statistics of the base Jurassic mesh (1,079,930 cells) with the use of a 500m edge-length constraint on the nodes for all three surfaces.

improvement over the base Cretaceous meshes and is similar to the seafloor and base Tertiary meshes. In fact, it appears the inclusion of the base Jurassic surface did not further degrade the quality of mesh from the base Tertiary model despite the complexity of the basement surface. Figure 5.30 shows a 3D view of the mesh with a piece removed to show this complexity of the basement surface. The basement region extends to the base of the mesh because this is the final surface.

A numerical simulation test was performed on the base Jurassic mesh to once again observe the quality of convergence. A Krylov subspace of 500 was used and the decay of the residual norm for the base Jurassic mesh, as well as the previous meshes, is shown in Figure 5.31. The base Jurassic mesh is relatively simpler than the base Cretaceous meshes (i.e. no refined regions on the surfaces) and this is clearly shown by the absolute and relative decay of the residual norm for the base

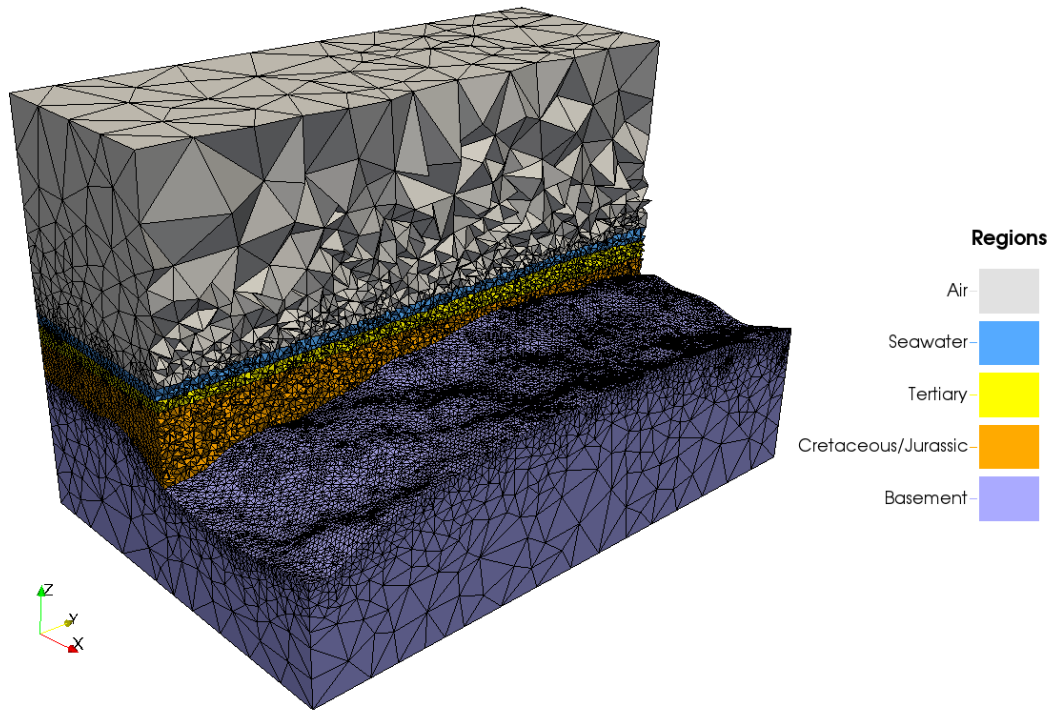


Figure 5.30: A 3D view of the base Jurassic mesh. This mesh contains 1,079,930 cells. A portion has been removed to show the complexity of the basement surface.

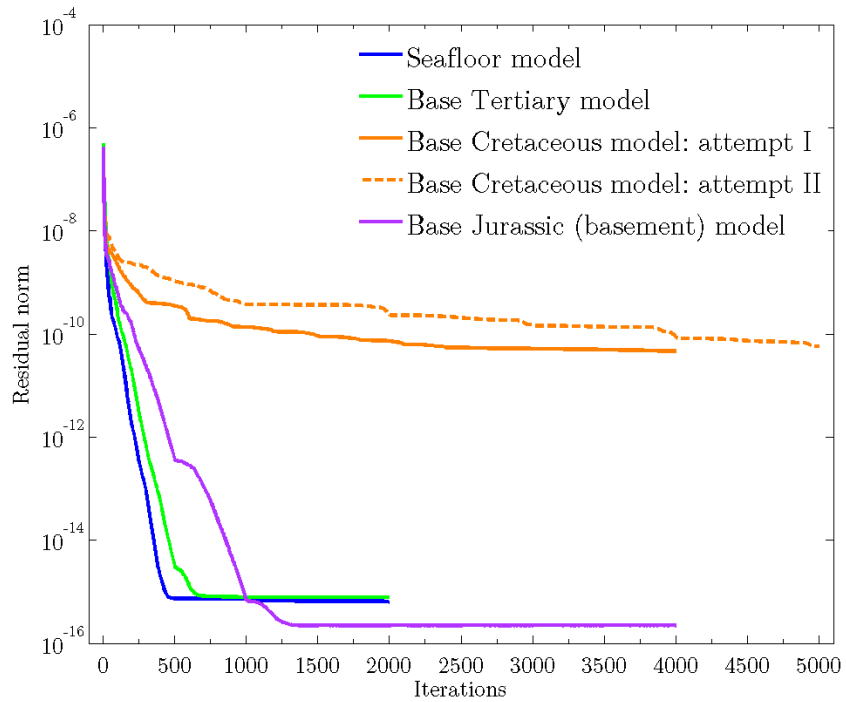


Figure 5.31: The decay of the residual norm for the base Jurassic model compared to the previous meshes. A Krylov subspace of 500 was used.

Jurassic mesh. The inclusion of these three surfaces to the model meant the skeleton of the model was complete and the next task was incorporating the observation locations into the model.

## 5.5 Observation Location Refinement

The need for refinement of tetrahedra around the computational observation locations was established as a critical necessity in Section 4.14. In Chapter 4, the placement of the observation locations was predetermined in order to match the 1D analytic responses. The same idea was extended to this scenario containing real, measured marine CSEM data. In order for the results simulated by CSEM3DFWD to have any chance at establishing a good comparison (i.e. low data misfit) to the measured data, the observation locations in the model and the transmitter established in the CSEM3DFWD code need to match those of the measured CSEM data. This was one of the most critical stages in the model building process because establishing good comparisons to the measured data also helped validate the resistivities chosen for the regions in the model.

### 5.5.1 Transmitter parameters

The HED transmitter used by EMGS to acquire marine CSEM data had a dipole length of  $\approx 280\text{m}$  and a current of 1500 Amps. At first, one may think that the transmitter established in CSEM3DFWD would need to mimic this, but this is not necessary. The current and dipole length of the transmitter impacts the response measured in any CSEM receiver by only a mere scaling factor. Therefore, the

receiver response is normalized by the current and dipole length which is why any and all electric field amplitude plots have a y-axis in units of  $V/Am^2$  instead of the traditional electric field units of  $V/m$ . So, the transmitter in CSEM3DFWD can use a transmitter with 1 Amp and a length of 1m (unit dipole moment).

### 5.5.2 Electromagnetic reciprocity

The challenge faced with the measured marine CSEM data is it was acquired with a *multi-source* scheme. EMGS used a setup where they deployed limited amounts of receivers onto the seafloor and then towed the HED transmitter – which is emitting a continuous pulse – above the receivers. From a practical perspective, this method is logistically easier to obtain data for than the reciprocal case. A small schematic illustrating the multi-source acquisition method is given in Figure 5.32(a). This example has just one receiver on the seafloor (red circle) with five transmitter pulse locations above the receiver. The underlying issue from a 3D forward modeling perspective is each transmitter source requires a separate solution of Maxwell’s equations in order to compute the fields. Five separate simulations would be required for the example given in Figure 5.32(a). It is still possible for CSEM3DFWD to recover the response in one receiver from multiple sources, albeit cumbersome, but there is a far better solution to address this issue.

Chen et al. (2005) had a similar problem when trying to perform 3D forward modeling of marine magnetometric resistivity data. However, they simplified their problem by employing *electromagnetic reciprocity* (see Harrington, 1961). Chen et

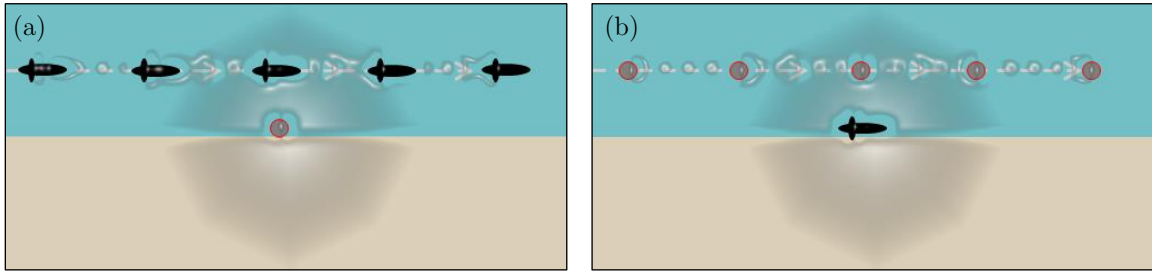


Figure 5.32: (a) A small example of the standard multi-source marine CSEM data acquisition set-up with five transmitter pulses and one receiver. (b) The same example, but after reciprocity is applied, changing the set-up to contain one transmitter and five receivers.

al. (2005) showed that the measured response from the multi-source scenario was identical to a response where the *transmitter locations from the multi-source scenario were replaced with receivers and the receiver from the multi-source scenario was replaced with an artificial transmitter*. In short, the transmitter and receiver locations can be swapped, as shown in Figure 5.32(b), and the measured response will be the same. Reciprocity can be applied to this scenario and change the problem from a multi-source to a single source problem that CSEM3DFWD can support. Therefore, the XYZ locations of the EMGS transmitter pulses became the XYZ points for observation locations in the model, and the XYZ locations of the receivers were replaced with artificial transmitters that mimicked the parameters of the real transmitter. Each EMGS transmitter pulse occurred every 10 seconds which translated to a pulse every 10m on average. Up until this point, the focus has been on the *convergence* of the model and not the quality (e.g. smoothness) of the results themselves. The logical next step was to use reciprocity and perform test simulations on the Mizzen model to see if smooth results could be obtained.

### 5.5.3 Seafloor model simulation I

The seafloor model in Section 5.4.1 was used here to test the quality/smoothness of the results from the inclusion of a transmitter and receivers that mimic the EMGS data acquisition over Mizzen L-11. The receiver that was chosen was RX42, shown in Figure 5.1, and after using reciprocity, the location of RX42 became the location of the artificial computational transmitter. There is only the one EMGS transmitter line considered for this study (shown in Figure 5.1), and all the transmitter points  $\pm 12$  km from RX42 became the computation receivers (e.g. 2401 receivers at 10m spacing). However, one simplification had to be made. The EMGS transmitter had a nominal in-line bearing of  $36.35^\circ$ , but for obvious reasons it was impossible for the boat to stay perfectly straight. As a result, the bearing of the transmitter has minor oscillations and may not be perfectly in-line with the receiver at all locations. After reciprocity, there is only one transmitter, but the question became, what bearing should be used for the in-line measurements? The bearing used for the computational transmitter was taken by finding the angle between the first and last of the computational receivers. So, for this particular example, that was a bearing of  $32.02^\circ$ .

The first simulation used the exact same mesh from the seafloor model in Section 5.4.1, but simply changed the transmitter and receiver locations to reflect the information above. No refinement was added around the receiver locations for this first test, which is why a new mesh did not have to be made. The in-line amplitude result is given in Figure 5.33 and the value of the amplitudes seems reasonable. However, notice how the response has a stair-step-like appearance. This was

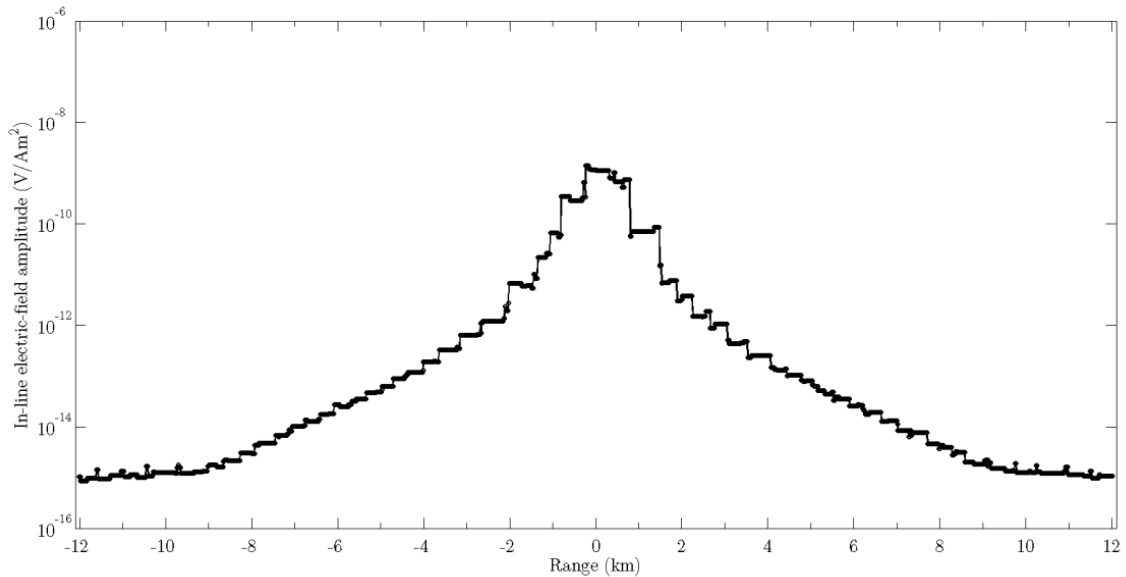


Figure 5.33: The in-line amplitude results for the first test of using the real transmitter/receiver locations surrounding RX42 after employing reciprocity. The small regular tetrahedra were *not* included to refine the mesh around the receiver locations, but the results clearly show that this is needed.

expected because the receiver locations were not enclosed by small, regular tetrahedra.

#### 5.5.4 Seafloor model simulation II

The XYZ points of the observation locations have been established through the reciprocity scheme, and, as the first simulation suggested, regular tetrahedra needed to be formed around the observation locations to recover quality results. The space between each observation location was  $\approx 10\text{m}$  on average, so the edge lengths of the tetrahedra were bounded to  $10\text{m}$ . The formulas given in Equation 4.1 were modified slightly to generate the nodes for these observation locations. The difference for this scenario, as opposed to the synthetic examples in Chapter 4, is the observation locations are no longer lying on the seafloor, and instead are

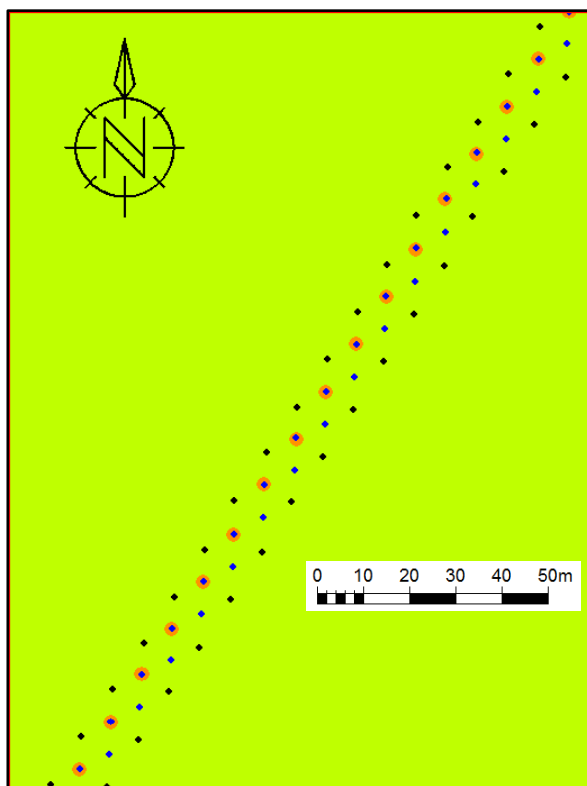


Figure 5.34: A segment of the connected chain of nodes required for enclosing the receiver locations surrounding RX42 (after employing reciprocity) in regular tetrahedra. See text for a description of the different nodes in this figure.

roughly 30m above the seafloor. The synthetic examples had to have two joining tetrahedra, above and below the seafloor, to enclose the observation locations. However, for this scenario, only one tetrahedron is needed for each observation location and it is positioned such that the observation location is situated in the center of that tetrahedron.

The result is a long connected chain of nodes (and what would become cells after meshing) and Figure 5.34 shows a plan-view segment of these nodes. The black nodes are the three points that make up the base face for a tetrahedron, the blue nodes are the *elevated* points that the three remaining faces connect to, and the

orange points represent the observation locations (imagine a pyramid and the observation location is located in the center). These nodes were added to the model and meshed using the following switches in TetGen,

```
tetgen.exe -pq1.6/16AmfenCV seafloor_model_OBS_II.poly.
```

The result is a mesh containing 554,949 cells, a minimum dihedral angle of  $0.245^\circ$ , and a percentage of poor cells equating to 8.26% (45846/554949). It seemed this mesh contained an unusual amount of poor quality cells, and after inspection of the mesh it became apparent as to why. All the seafloor nodes still contained the 500m edge-length constraint in the .mtr file. Recall that the nodes added for the observation location refinement were only  $\approx 30\text{m}$  above the seafloor. The nodes surrounding the observation locations want edge lengths of 10m, but the nearby seafloor nodes want edge lengths of 500m. The result was TetGen created many skinny cells in this area and this accounted for the significant percentage increase in poor quality cells. An illustration of this issue is given in Figure 5.35.

To fix this problem, the seafloor nodes closest to the observation locations (within 1 km) were hand-picked, and had the edge-length constraint removed so TetGen would have more freedom in these areas. The resulting mesh contained 1,022,890 cells, a minimum dihedral angle of  $6.0^\circ$ , and a percentage of poor cells equating to 0.271% (2773/1022890). Figure 5.36 shows the same plan views as Figure 5.35 and the improvement is evident. There was a significant increase in the amount of cells, which was expected, but the poor quality cells have vanished as a result.

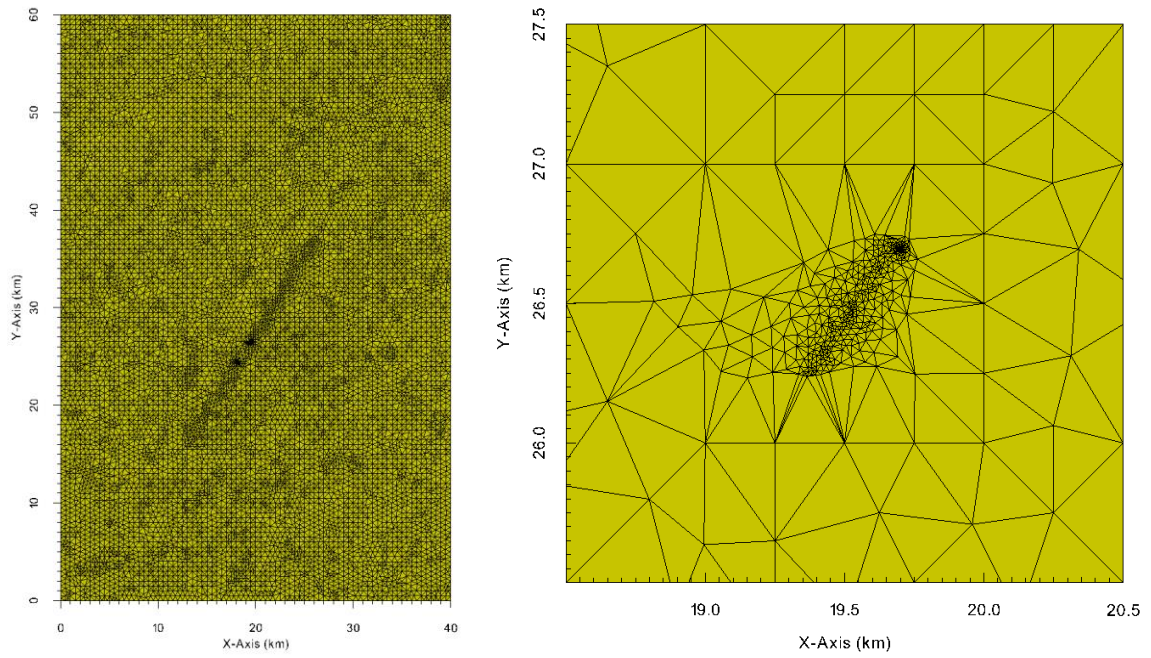


Figure 5.35: Two plan view images of the seafloor mesh that includes the nodes for refinement around the observation locations. The 500m edge-length constraint imposed on the seafloor nodes surrounding the observation locations results in poorly shaped tetrahedra.

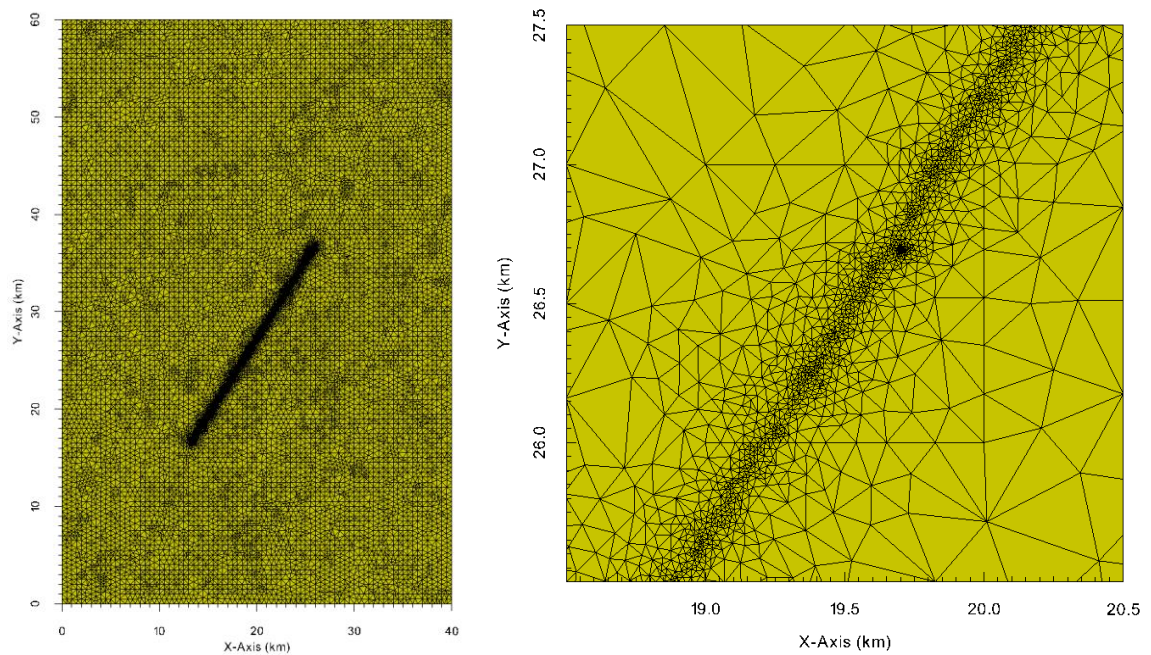


Figure 5.36: Two plan view images of the seafloor mesh when the 500m edge-length constraint is removed from the seafloor nodes surrounding the refinement for the observation locations. A drastic improvement of the mesh is observed.

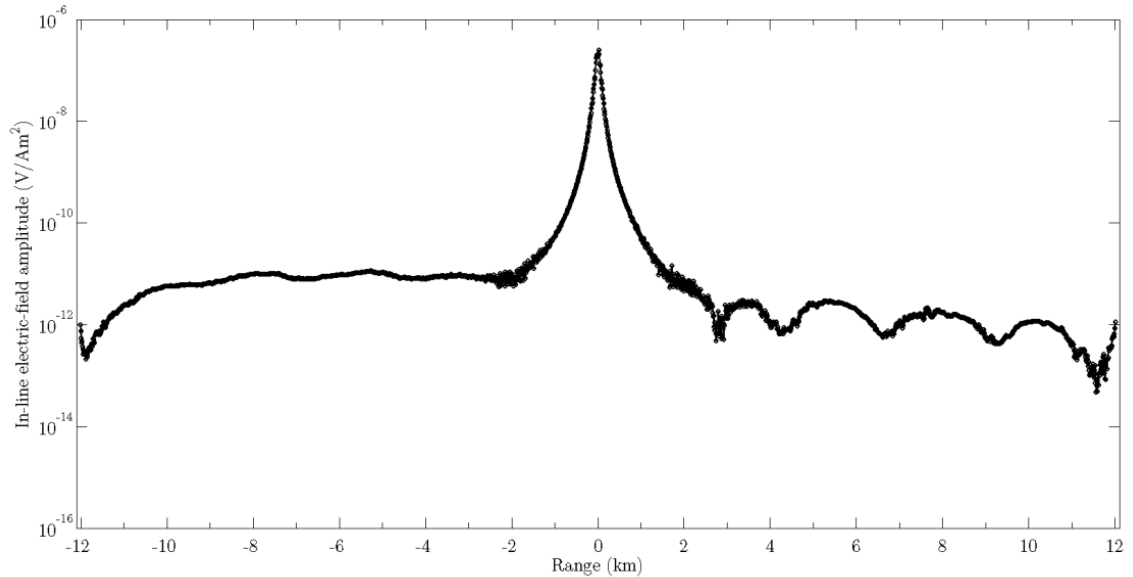


Figure 5.37: The in-line amplitude results from the second test of using the real transmitter/receiver locations surrounding RX42 after employing reciprocity. Regular tetrahedra are formed around 2401 observation locations (10m spacing) and the results still appear inaccurate.

A simulation of the good quality mesh (1,022,800 cells) was performed and the in-line amplitude result is given in Figure 5.37. To some surprise, the amplitude is highly inaccurate. Marine CSEM results are always traditionally smooth until the noise threshold is reached, but this result contains bumps in the data that are artificial and not anticipated.

### 5.5.5 Seafloor model simulation III

The mesh from the previous simulation appeared to be of high quality, so the poor results must have had something to do with the observation locations. It was a possibility that too many observation locations were used. Marine CSEM fields are slowly varying in logspace, so 2401 observation points with 10m spacing was certainly oversampling. Instead, an arbitrary spacing of 200m was chosen which

resulted in 121 observation locations. In short, 95% of the observation locations were removed, but the remaining 5% were still identically the same as before.

Before refinement nodes were added for these 121 observation locations, it was theorized that an additional source of inaccuracy from a forward modeling perspective could have been that the observation locations were not always perfectly in-line with the artificial transmitter bearing. So this issue was fixed through a series of processing steps. The angle in the horizontal plane between the start and end observation points was used to rotate all the observation points clockwise. The result of this processing step is shown in Figure 5.38. The x-axis is the distance along the observation locations and the y-axis is the deviation from the line connecting the start and end points. This shows the oscillations in the observation location path, which is actually a result of the vessel not being able to keep perfectly straight and the transmitter would subsequently deviate off course slightly as well. The next processing step was *flattening* all the observation locations by setting their  $y = 0\text{m}$  to make them perfectly straight. The third processing step was shifting all the points vertically by the average deviation (blue dotted line in Figure 5.38). Lastly, all the points were rotated counter-clockwise by the same angle between the start and end points. The final result is a *slightly different* version of the observation location points that are now perfectly in-line with the transmitter. Additional tests (not given) showed that simulating data using the true observation locations compared to the flattened observation locations improved the smoothness of the recovered in-line electric field amplitude.

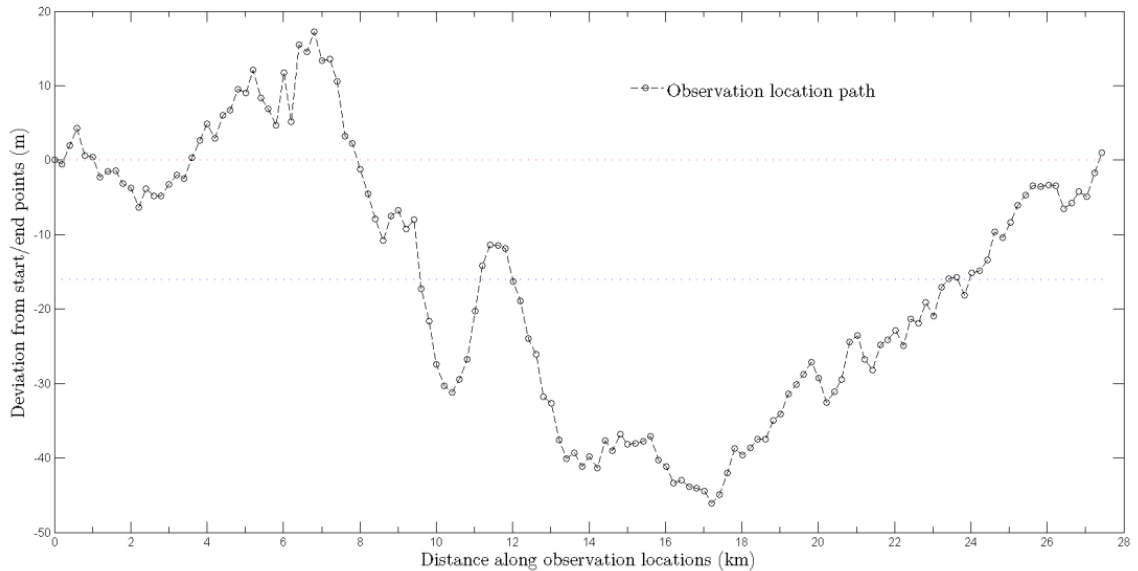


Figure 5.38: The deviation of the observation locations from the line connecting the start and end points. This clearly shows the oscillations which are a result of the vessel not being able to keep perfectly straight and the transmitter subsequently deviated off course slightly.

Creating nodes to surround the (flattened) observation locations was much simpler with this scenario because the observation locations were spaced far enough apart that the tetrahedra did not have to *connect* to one another. So, instead of having a long connected chain of tetrahedra for observation location refinement, each individual observation location was encased in one isolated tetrahedron. The same formulas in Equation 4.1 were used here and the nodes were designed to have tetrahedra (after meshing) with 10m edge lengths (see Appendix C for a copy of the MATLAB script that calculates the locations of these nodes). The seafloor nodes surrounding the observation location nodes still had their edge length constraints removed to give TetGen freedom, and the following switches were used to generate the mesh,

```
tetgen.exe -pq1.414/16AmfenCV seafloor_model_OBS_III.poly.
```

The result was a mesh containing 687,417 cells, a minimum dihedral angle of  $6.281^\circ$ , and a percentage of poor cells equating to 0.180% (1240/687417). A simulation of this mesh was performed and the in-line amplitude results are given in Figure 5.39. These amplitudes appear better than those in the first (Figure 5.33) and the second (Figure 5.37) tests, but are still noisy. However, this amplitude is behaving much better than the amplitude from the second test. The noise improvement of the amplitude from Test II to Test III in Section 4.1 was simply achieved by reducing the size of the tetrahedra surrounding the observation locations. Perhaps all that is required is something similar performed here.

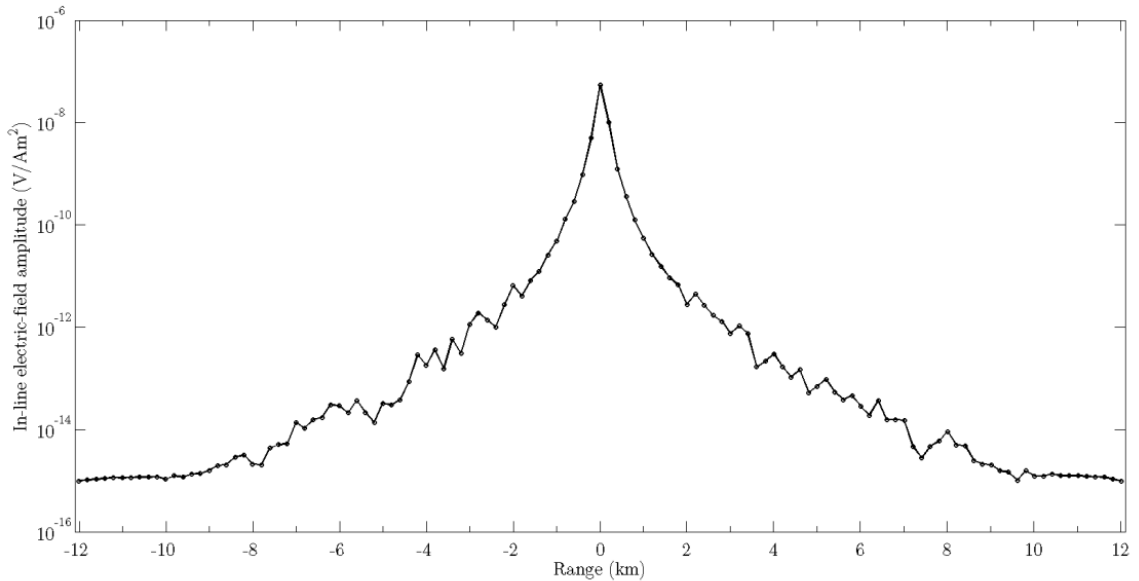


Figure 5.39: The in-line amplitude results from the third test of using the flattened observation line surrounding RX42 after employing reciprocity. Regular tetrahedra with 10m edge lengths are formed around 121 isolated observation locations (200m spacing). The amplitude is improved, but still noisy.

### 5.5.6 Seafloor model simulation IV

The fourth and final observation location refinement test was the exact same as the previous test, except the nodes were designed to have tetrahedra (after meshing) with *5m edge lengths*. The mesh was generated with the same switches and resulted in 802,032 cells, a minimum dihedral angle of  $3.27^\circ$ , and a percentage of poor cells equating to 0.203% (1625/802032). The in-line amplitude result is shown in Figure 5.40 and the amplitude is smooth is much improved. Notice how a reduction in the size of the tetrahedra around the observation locations can have such a significant impact on the computed results. This result is acceptable and contains the degree of data quality sought after for all simulations. Consequently, this exact scheme for refinement around the observation locations is *used for the remainder of this thesis*.

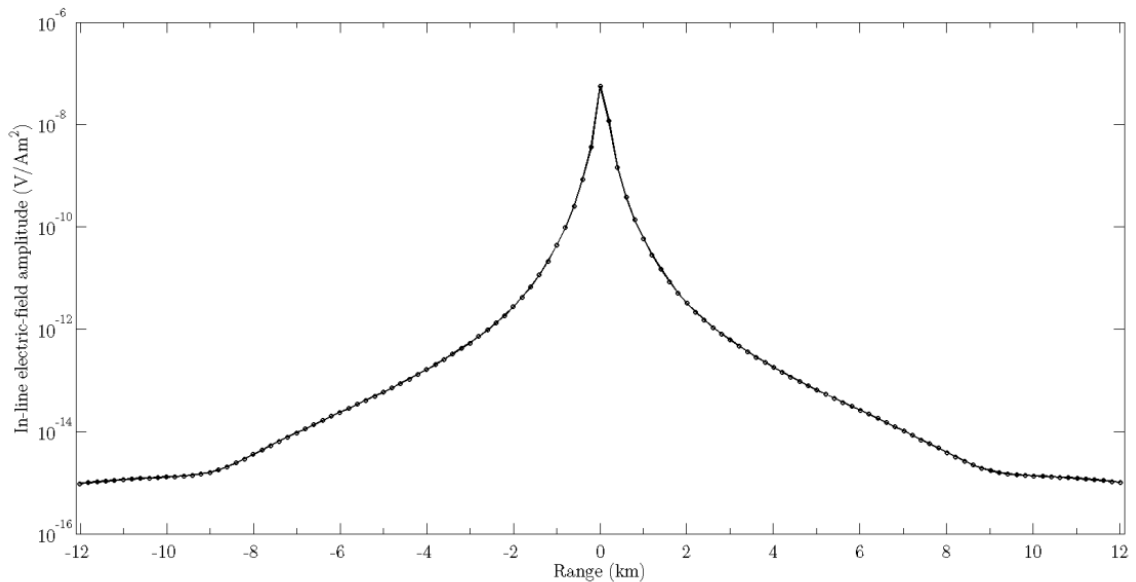


Figure 5.40: The in-line amplitude results for the fourth and final test of using the flattened observation line surrounding RX42 after employing reciprocity. Regular tetrahedra with 5m edge lengths are formed around 121 isolated observation locations (200m spacing). The amplitude is smooth and much improved.

## 5.6 The Mizzen Reservoir

The final component for the model building stage was including the Mizzen reservoir sands. The data coverage around Mizzen L-11 is limited, but there were three pieces of data that aided in building the reservoirs: the L-11 well log, the 2D seismic line passing over the prospect, and a lateral extent polygon created by Statoil.

The L-11 well log (Figure 5.3) was the first piece of vital information needed for constructing a representation of the three Mizzen sands. The well log was able to give the *thickness* of each of the sands and these were rounded to the nearest decade (20m, 40m, and 30m for the top, middle, and base sands respectively). Establishing the thickness of each sand was important because doing so with the seismic data would likely not be as accurate.

Only one seismic line passes over the L-11 prospect (see Figure 5.1), but this was enough information to help constrain the reservoir extent in *two dimensions*. Based on the amplitudes in the seismic data (see Figure 5.5), the three potential reservoirs could be represented as dipping slabs as indicated by the superimposed slabs on the far angle stack in Figure 5.41. Since the well essentially hit brine in these sands (only minor oil in the top sand), the most likely scenario is that brine must fill these sands as far down-dip as the sand extends in the fault block. This is shown by the green portion of the slabs in Figure 5.41. However, the up-dip portions of the sands were theorized to contain hydrocarbons – based on the AVO anomalies – and subsequently these areas were filled with hydrocarbons for the

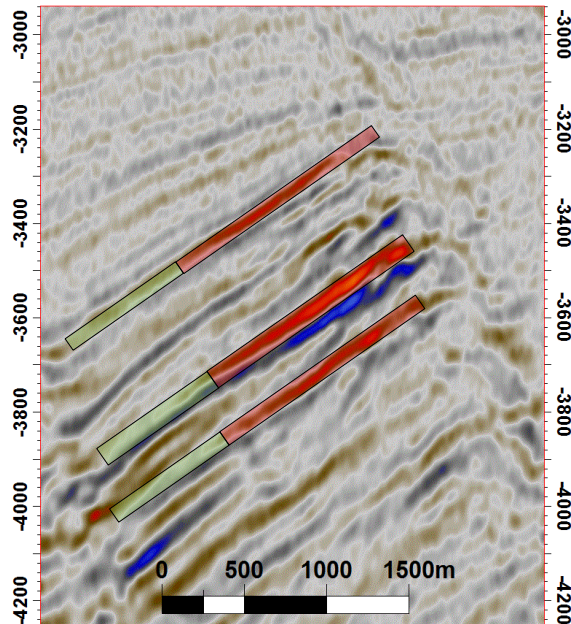


Figure 5.41: The same far angle stack from Figure 5.5(b), but with the cross-section of the dipping slab approximation for the three sand reservoirs superimposed on the image (data courtesy TGS/PGS). The red portions signify the hydrocarbon saturations in the slabs up-dip based on AVO, and the green portions signify the brine saturations down-dip in the slabs.

model. The hydrocarbon bearing portions of the slabs are shown as red in Figure 5.41. In two dimensions, the sand bodies were fairly well constrained with the slab thicknesses coming from the well log and the sand extents coming from the 2D seismic data. The challenge arose when trying to determine the 3D nature of these sands.

EMGS did perform an inversion (on a rectilinear grid using a finite-difference forward solver) of their marine CSEM data set in the Flemish Pass Basin, so any resistive anomaly over L-11 could have helped constrain the extent of the Mizzen sands. However, personal inspection of the inversion from EMGS showed the anomaly was faint and broad around L-11 which made it difficult to use in this

context; so it was not considered. Therefore, the only information available that gave some indication of the lateral extent of these sands was the polygon available from Statoil in a quarterly website update in 2014 (see Figure 5.1). This polygon was likely derived from 3D seismic data exclusively licensed by Statoil, and it did not seem appropriate to base the shape and extent of the Mizzen reservoir sands used in this thesis harshly on data that was not accessible to this study. To keep the reservoir simple, the slab representation in 2D (Figure 5.41) was simply extended in/out of the plane of the seismic line. The Statoil polygon was used only to help guide the starting and ending positions of the slab. None of these pieces of information gave any indication of the plunge of these reservoir slabs, so they were assumed to have no plunge. The result was three  $2.0 \times 4.0$  km slabs with about a  $13^\circ$  dip and a  $210^\circ$  strike (dipping towards the northwest). The brine portions of the slabs were  $0.8 \times 4.0$  km and the hydrocarbon portions of the slabs were  $1.2 \times 4.0$  km. A plan view of the lateral extent of these slabs is shown in Figure 5.1.

These three pieces of information were the basis for constructing the framework for the Mizzen sands, but more importantly, the slabs had to be incorporated into the model. The simplest way to represent the slabs in the model was using eight nodes and six facets (i.e. a dipping rectangular prism) for each slab. However, it was predicted that only having nodes on the corners of the rectangular prism would give TetGen too much freedom to add undesirable nodes on the six faces. This same issue was discussed in Section 5.4.1 where having no constraints on the seafloor surface resulted in TetGen adding unnecessary *pulses* of small nodes on the surface; avoiding this same phenomenon was desirable when meshing the slabs.

Consequently, the Mizzen slabs were made in a similar fashion to the surfaces. A grid of nodes was created to represent the top and base of each slab. These nodes were spaced at  $2\times$  the thickness of each corresponding slab (i.e. cells with an aspect ratio of 2.0). The nodes were not spaced the same as the thickness in an effort to reduce the amount cells at a minimal expense of cell quality. All of these grids of nodes were meshed in Triangle to create a surface. These surfaces for the top and base of each sand were imported into FacetModeller and each slab was subsequently *enclosed* by including the four boundary facets on the sides. The nodes used to represent each sand are shown in Figure 5.42. Notice how the thicker the slab is, the larger the spacing of the nodes.

The model could be meshed once the sands were constructed using Facetmodeller. This model, however, was constructed to be centered around RX44 instead of RX42, therefore, the refinement nodes for the observation locations were in slightly different areas. RX44 lies southwest of Mizzen L-11 and unlike RX42, the observation locations needed to only trend northeast from the receiver to pass over the prospect. RX42 lies directly above the prospect, so it was theorized observation locations should trend in both directions because it was not known which side would be most sensitive to the reservoir.

The observation locations were chosen to extend from 0 to 14 km offset at the traditional 200m spacing established in Section 5.5.6. Once the observation locations for RX44 and the three slabs were included, the corresponding model was meshed using the following switches in TetGen,

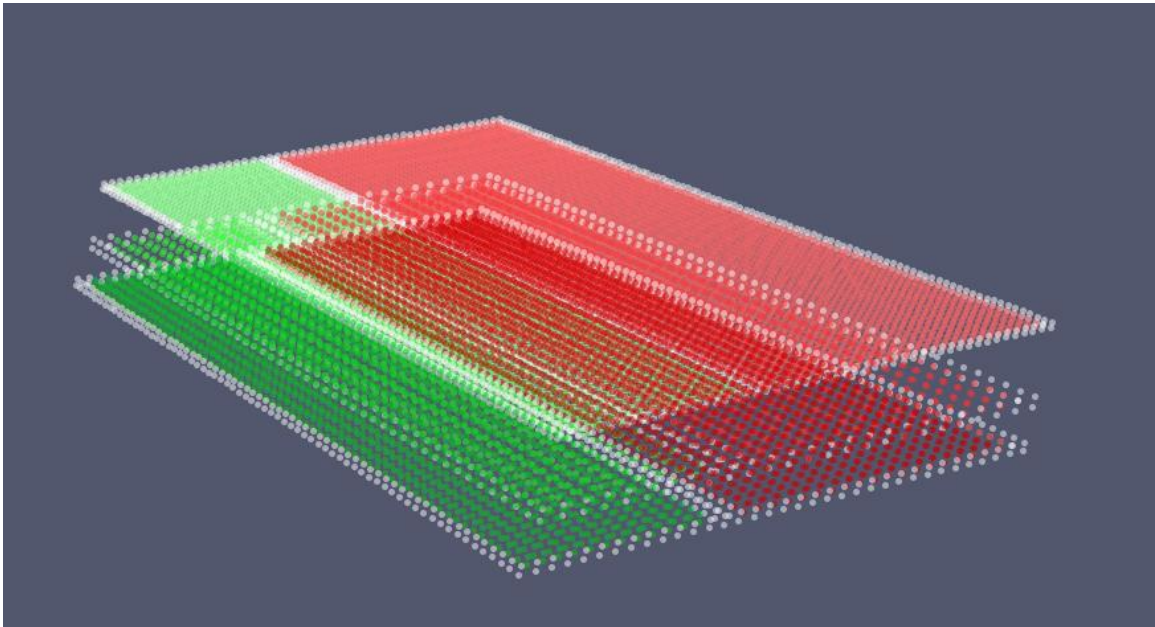


Figure 5.42: The nodes used to create the three Mizzen sands. The nodes shown represent the top and base of each of the sands which were used to create individual surfaces using Triangle.

**`tetgen.exe -pq1.48/16AmfenCV mizzen_reservoir_model.poly.`**

The result was a mesh containing 1,750,072 cells, a minimum dihedral angle of  $4.62^\circ$ , and a percentage of poor cells equating to 0.218% (3819/1750072). These statistics suggest that the mesh continued to exhibit good quality even after the inclusion of the Mizzen slabs. It is worth mentioning that no edge length constraints were needed on the nodes representing the three slabs (or the observation locations). Using many nodes to represent the slab surfaces was enough to constrain the slab bodies such that TetGen did not add any undesirable nodes/cells. So, the only constraints used in the .mtr file were the 500m edge length constraints on the nodes representing the three geochronologic surfaces. A view showing the entire mesh is given in Figure 5.43. This figure shows the various regions of the mesh and shows the size of the Mizzen slab reservoirs in the context of the whole model. Figure 5.44 shows two perspective views of the Mizzen slabs

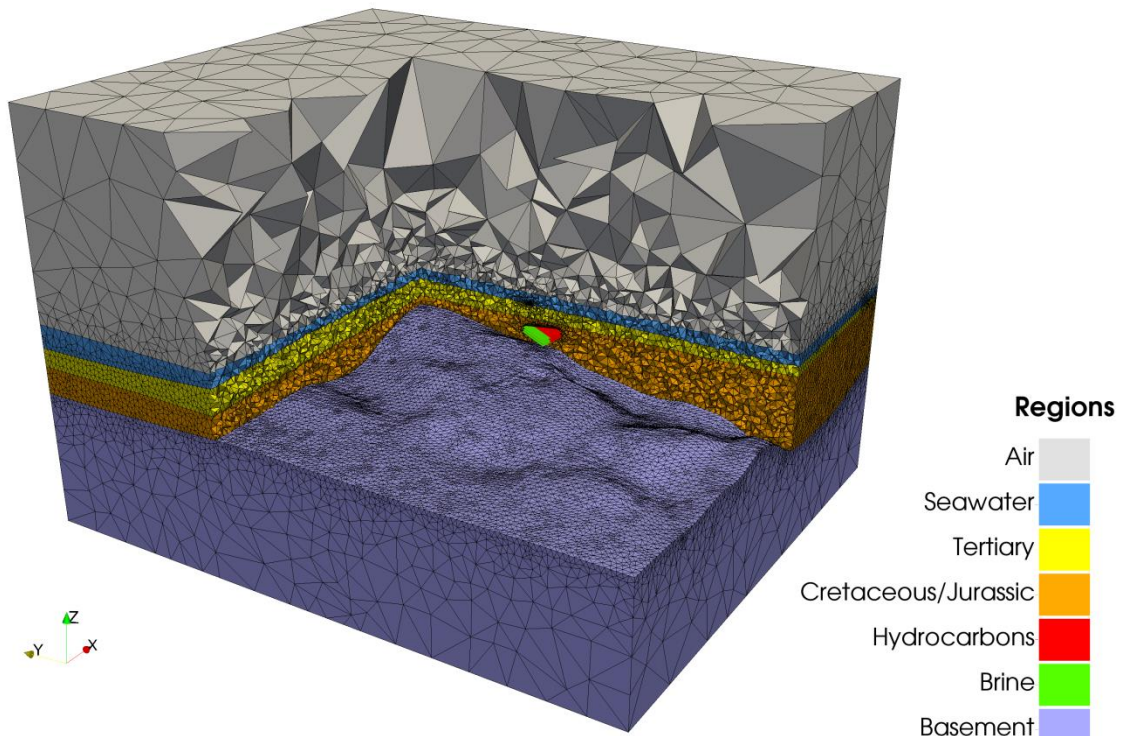


Figure 5.43: The entire mesh including the three Mizzen slabs and observation location refinement around RX44. A portion of the mesh is removed so the slabs are visible.

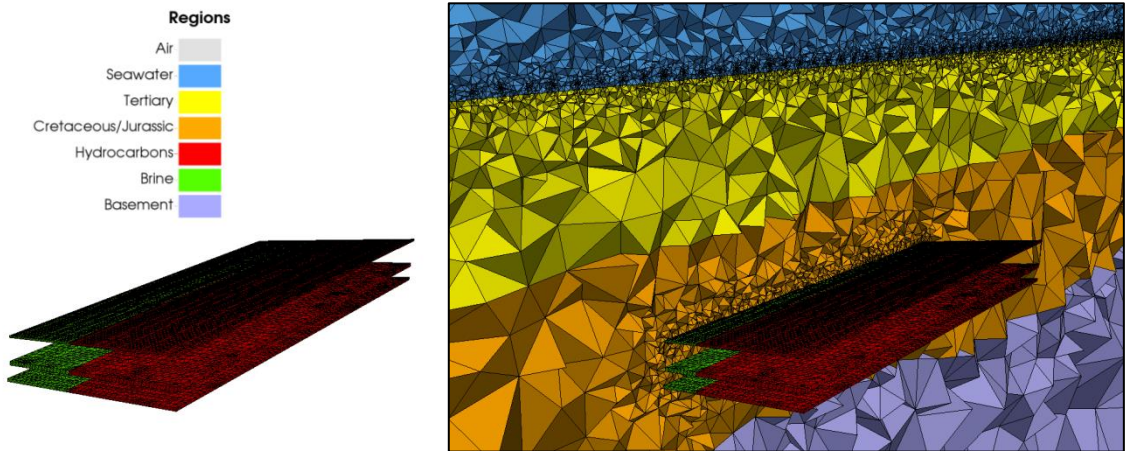


Figure 5.44: Two perspective views of the Mizzen slabs along the EMGS transmitter line (shown in Figure 5.1). The small pulses of nodes above the seafloor represent the refinement for the observation locations spaced 200m apart.

along the EMGS transmitter line (see Figure 5.1). The small pulses of cells slightly above the seafloor are the refined areas for the observation locations spaced 200m apart. Figure 5.45 shows a 2D slice along the EMGS transmitter line. Notice how the refinement begins about 3.0 km to the left of the edge of the slabs; this is the location of RX44 and this is consistent with the map given in Figure 5.1. A final image of the mesh is given in Figure 5.46 which is another 2D slice, but along the seismic line. Notice the similarities between this slice and what is shown by the far angle stack of the seismic data in Figure 5.5. After all, it is intuitive that the seismic data and the slabs in the mesh should look similar because the 2D extent of the slabs was *derived* from the seismic data.

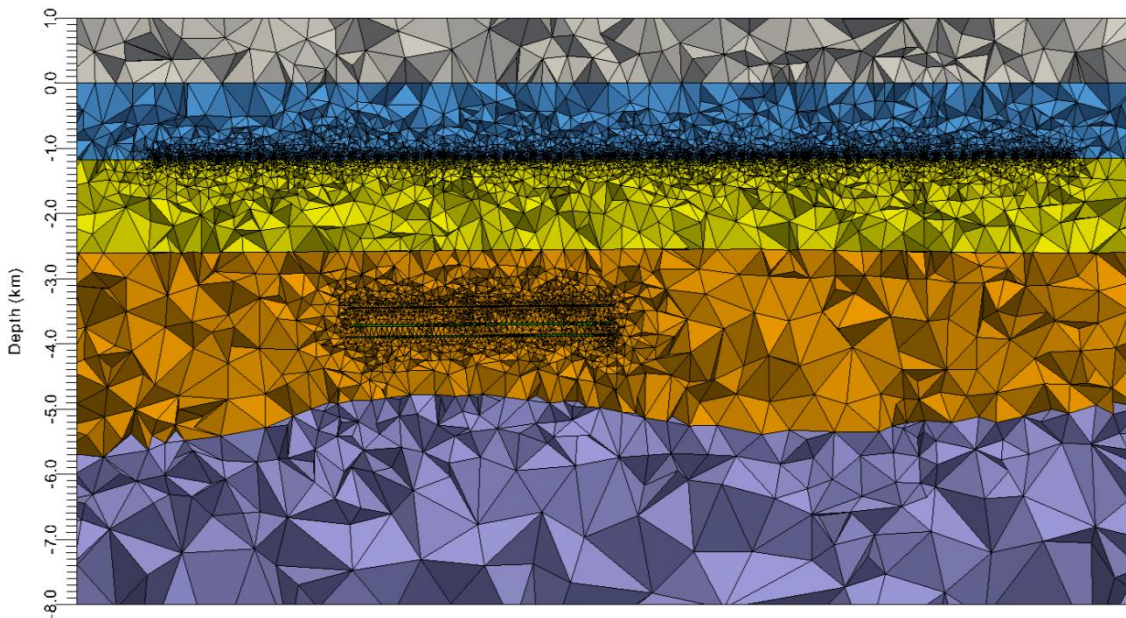


Figure 5.45: A zoomed-out 2D slice along the EMGS transmitter line. This figure indicates the 14 km range of the refinement for the observation locations specific to RX44 starting at the left and ending at the right.

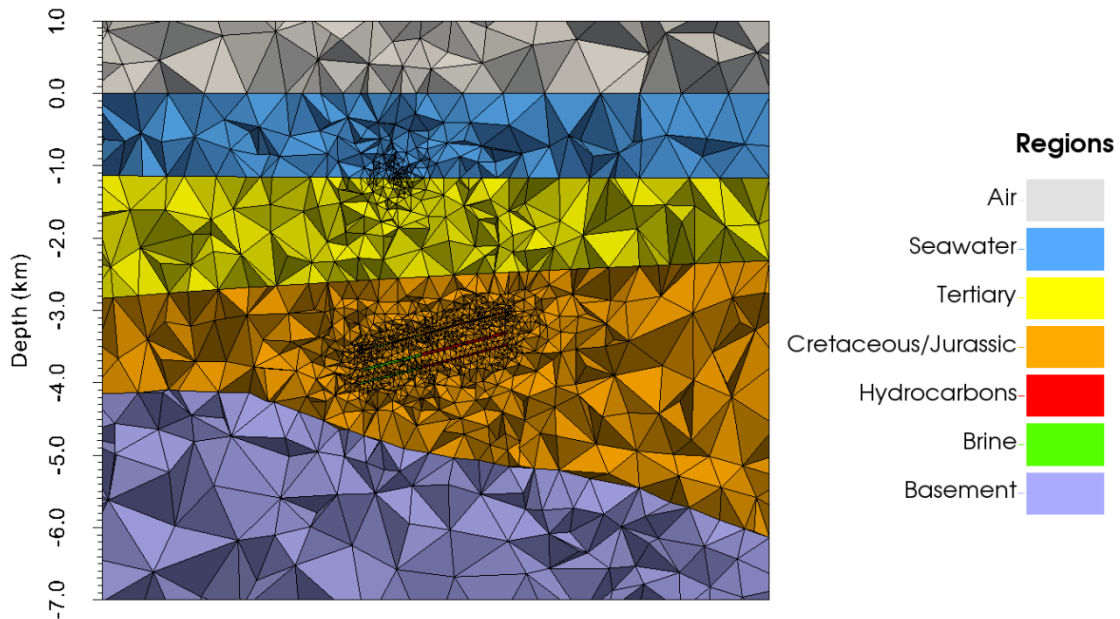


Figure 5.46: Another 2D slice of the mesh created for RX44, but along the seismic line. This slice has similarities to the far angle stack (Figure 5.5b and Figure 5.41) which is anticipated because the 2D extents of the Mizzen slabs were derived from the AVO data.

### 5.6.1 Verification of hydrocarbon volumes

At this stage, the model (and mesh) was complete, but there was one final component that needed to be verified before moving on to numerical simulations. There were various assumptions taken when creating the Mizzen reservoirs and it was important to ensure that the size of these reservoirs was somewhat consistent with the truth *if a measure of the truth exists*. Since the Flemish Pass Basin is still in an *exploration phase* the amount of data available is quite limited. If the basin had been in a production phase (typically there is 3D seismic acquisition and more wells drilled) there would be far more data available that could give information about the size of the reservoir. However, the only information that was available to this thesis was estimations on the amount of recoverable oil in the Mizzen field given by Statoil. An announcement was made by Statoil in 2013

(<http://www.statoil.com/>) where they predicted an estimated 100-200 million barrels of *recoverable oil* the Mizzen field. First of all, this was an estimate that encompassed the entire Mizzen field which included the field under Mizzen L-11, but also a much larger field under another well, Mizzen O-16 (the solid black dot within the pink rectangle in Figure 5.19). Secondly, a few equations had to be used to arrive at a value that can be compared to the *recoverable oil* estimate given by Statoil. The first equation is a calculation of the original oil in place (OOIP), or essentially how much oil is contained in the reservoir. The formula for OOIP is given by,

$$OOIP = BRV \times \Phi \times (1 - S_W) \times \left(\frac{1}{FVF}\right) \times 6.29 \quad (5.1)$$

$$BRV = area \times thickness \times net/gross \text{ ratio}$$

where BRV is the bulk rock volume,  $\Phi$  is the porosity,  $S_W$  is the water saturation,  $FVF$  is the formation volume factor, and the 6.29 scaling factor is used to convert the volume units from  $m^3$  to barrels of oil (see <http://wiki.aapg.org/>). The bulk rock volume quantifies the volume of the reservoir, but a reservoir is not always 100% sand (e.g. carbonate streaks, silty zones, etc.) which facilitates the need for a net/gross ratio. The formation value factor simply accounts for the change in hydrocarbons volumes when the oil is pumped from pressurized zones at depth to STP at the surface. Equation 5.1 was used to calculate the OOIP for the hydrocarbon portions of the three slabs in model:

$$OOIP = (1.2 \text{ km} * 4.0 \text{ km} * 90\text{m} * 0.75) \times 0.2 \times$$

$$(1 - 0.25) \times \left(\frac{1}{1.4}\right) \times 6.29 \approx \mathbf{218M} \text{ barrels of oil.}$$

It is worth mentioning there was no information available to know an exact or refined value for some of the variables, but the best estimates were used. A net-to-

gross ratio of 0.75 was used because in the well log the sands contain some carbonate streaks and silty zones. The porosity of the sands (20%) was loosely taken from the empirically derived porosity log at L-11. Nalcor suggested values of 25% for water saturation and 1.4 for the formation value factor as these were common values they used to perform their own estimates. The second formula applies a recovery factor (RF) to the OOIP formula to report an estimate in barrels of recoverable oil:

$$\text{Recoverable Oil} = \text{OOIP} \times \text{RF}. \quad (5.2)$$

An unfortunate reality of drilling is the amount of oil that is able to be recovered out of the ground is much less than what is typically in place. For these calculations at Mizzen L-11, a conservative, yet not unreasonable recovery factor of 20% was used resulting in  $\approx$  **44M** barrels of recoverable oil. However recall that the estimate Statoil gave included L-11, but also a field under another well, Mizzen O-16. This study did not focus on Mizzen O-16 so the amount of data available to determine a recoverable oil estimate for this field was limited. However, in Statoil's quarterly website update in 2014, they not only gave an indication of the lateral extent of the reservoir under L-11, but also under O-16. A rough approximation determined that the lateral extent of O-16 was  $4\times$  larger than Mizzen L-11. Assuming there are the same three sands with the same thickness under O-16, then the recoverable oil estimate at O-16 is simply  $4\times$  that of L-11 giving **176M** barrels of recoverable oil. Therefore, this study estimates a total of 220M barrels of recoverable oil in the Mizzen field. This is obviously an overestimate compared to the 100-200M barrels of recoverable oil estimate given by Statoil. However, a significant amount of assumptions were made in determining this estimate. It is

possible that the estimate recovered for L-11 is close to the truth and the overestimate came from O-16. In summation, it seems 44M barrels of recoverable oil at Mizzen L-11 is within an acceptable range of what may be the truth implying the extent/size of the slabs was acceptable. Based on the recoverable oil estimate, quality mesh statistics, and the consistencies observed in the mesh, it appeared this mesh containing the Mizzen slabs was suitable for numerical simulation.

## 5.7 Preliminary Numerical Results

The steps building up to this point have established the necessary components for the simulation of marine CSEM results over the Mizzen prospect. Using only one mesh (the one containing the Mizzen slabs) seemed dangerous because there are so many components to the final mesh and it would be difficult to isolate which components were causing changes to the numerical results (important for the upcoming section, Section 5.8).

Consequently, five distinct models/meshes were made with incremental additions to go from the most basic model to the most complicated model containing the Mizzen sands. Mesh slices from these five models are shown in Figure 5.47. The first model contained only the seafloor surface which gave the *seafloor model* and this was obviously the most basic one. The base Tertiary surface was added to the seafloor model giving the *tertiary model* in Figure 5.47(b). The base Jurassic (basement) surface added to the tertiary model gave the *basement model*. Lastly, the three reservoir slabs added to the basement model gave the final model that was constructed in the previous section. However, it was desired to synthesize

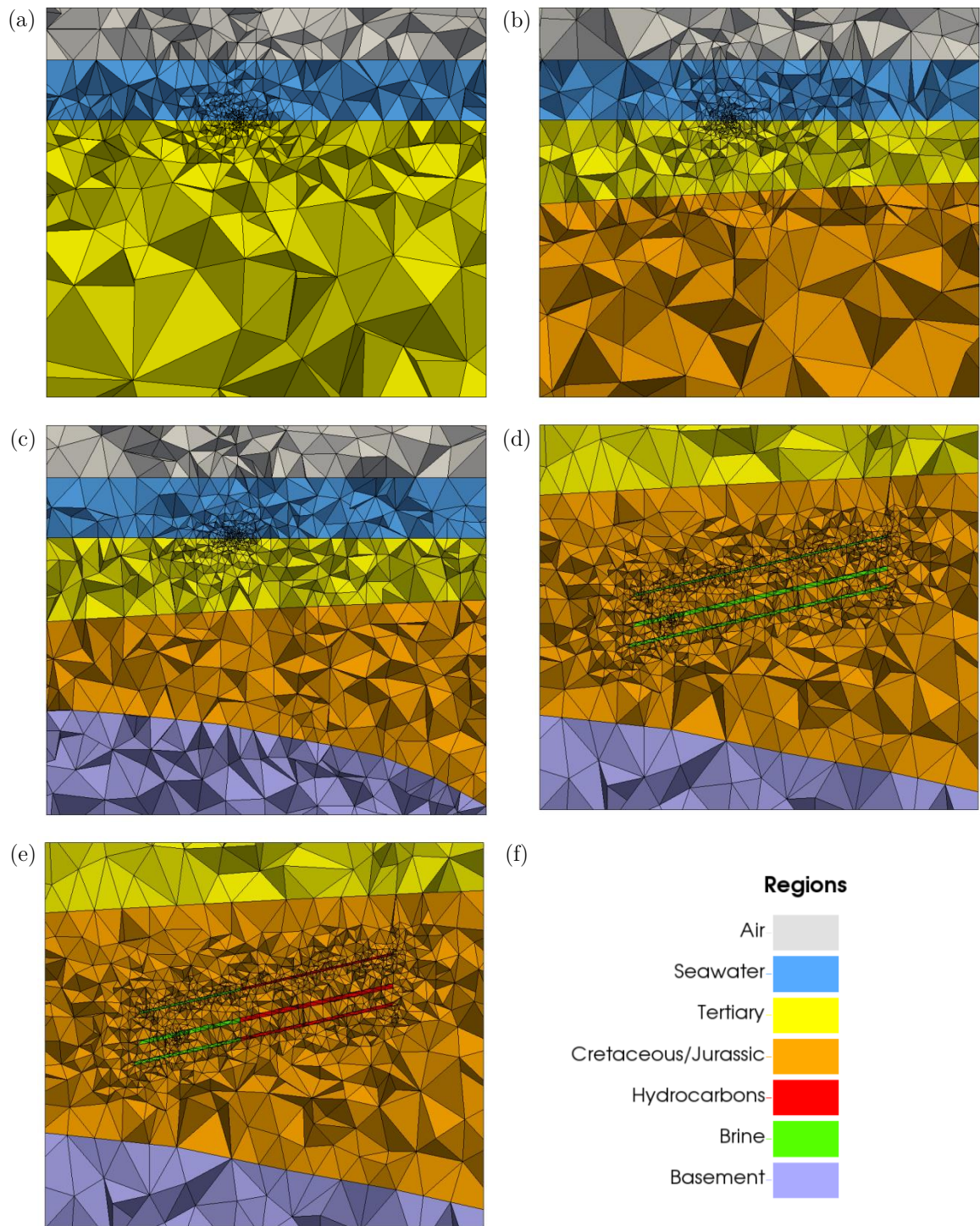


Figure 5.47: Mesh slices for the (a) seafloor model, (b) tertiary model, (c) basement model, (d) brine slab model, and (e) the hydrocarbon slab model, illustrating the subsequent incremental changes between each model. Panel (f) provides a color key for the corresponding regions of the model.

results from two different variants of the reservoir model. The first assumed the entire volume of the slabs was brine (including the up-dip portions) and this is shown in Figure 5.47(d). The second was the predicted scenario with the up-dip portions of the slabs containing hydrocarbons as depicted in Figure 5.47(e). The reason for generating a brine response was if in the unlikely scenario there were no hydrocarbons up-dip in the three sands as indicated by the AVO, these portions of the sands would likely be saturated with brine. This brine slab model also seemed most appropriate to serve as the *background model* for the hydrocarbon slab model to normalize against for sensitivity calculations. Each of these models contained refinement at the observation locations appropriate for RX44, and were all subsequently meshed taking this into account. Table 5-1 summarizes mesh information for each of the five models. Notice that the percentage of poor cells was maintained through the course of building each of these models and this shows that the method used to add surfaces to the model did not degrade the quality of the mesh.

These five meshes were all used for simulations, but the resistivities of the regions had to first be established. A good starting point for the resistivities was using those directly from the L-11 well log. Figure 5.48 shows a schematic of the resistivities derived from L-11. Since the base Cretaceous surface was not included, the Cretaceous and Jurassic regions were combined into one. So the issue arose as to what resistivity to use for that combined region. The two individual regions given in Figure 5.6 were depth averaged to give a resistivity of 3.36  $\Omega\text{m}$  for the combined region in Figure 5.48. The two lower sands were brine filled, so a

Table 5-1: A summary of mesh information for the seafloor, tertiary, basement, brine slab, and hydrocarbon slab models with observation location refinement appropriate for RX44.

<b>Mesh Statistics</b>	Mesh tetrahedra	Smallest dihedral angle	Largest aspect ratio	Percentage of poor cells
Seafloor model	749943	4.87	15.34	0.194%
Tertiary model	1065979	6.09	16.24	0.232%
Basement model	1578222	5.25	16.56	0.220%
Brine slab model	1750072	4.62	19.17	0.218%
Hydrocarbon slab model	1750072	4.62	19.17	0.218%

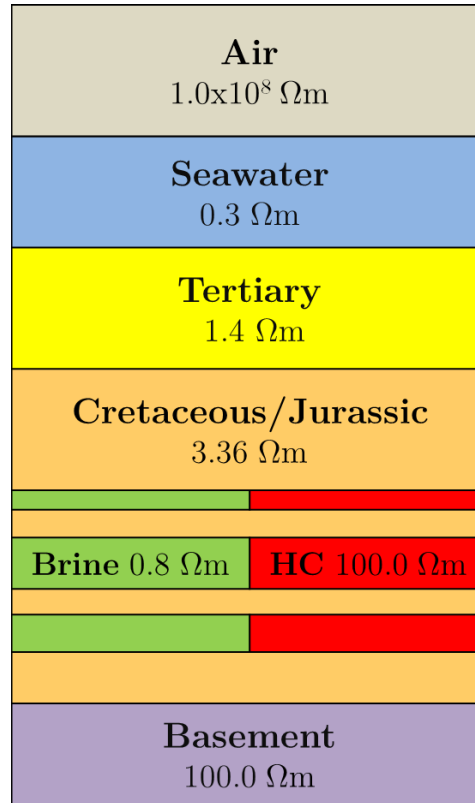


Figure 5.48: The starting resistivities derived from the L-11 well log for forward modeling purposes. The resistivity of the combined Cretaceous/Jurassic layer was found by taking a depth average of the resistivities from the two regions.

resistivity for the brine portions of the slabs was easily determined. However, none of the slabs had significant concentrations of hydrocarbons (topmost sand hit minor oil, but likely still contained high water saturations), so a generic hydrocarbon resistivity of  $100.0 \text{ } \Omega\text{m}$  was used. The region with the most uncertainty was the basement because the well did not extend that deep. The crystalline, low porosity nature of basement rock gives it an inherently high resistivity, but there was no data to help guide a specific value. Therefore, a resistive value of  $100.0 \text{ } \Omega\text{m}$  was used which seemed sufficient in representing the resistive basement.

With these resistivities, simulations on all five meshes at  $0.50 \text{ Hz}$  were performed and the convergence for each model is shown in Figure 5.49. The seafloor and tertiary models were simulated with a Krylov subspace of 500 and the remaining

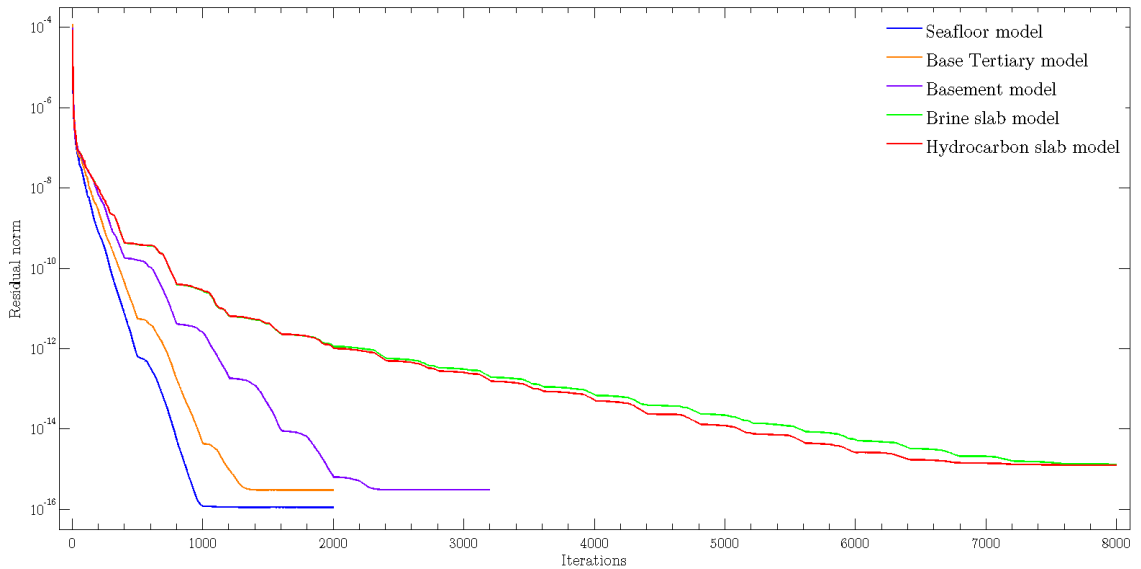


Figure 5.49: The value of the residual norm from the GMRES iterative solver for the various models at RX44 and a frequency of  $0.50 \text{ Hz}$ . The seafloor and tertiary models had a Krylov subspace of 500 and the three remaining models had a Krylov subspace of 400.

three models were simulated with a Krylov subspace of 400. Notice how the three models without the Mizzen slabs converged quite quickly, but the inclusion of the slabs appeared to slow down convergence considerably. This poor convergence was surprising given the good quality of the Mizzen slab meshes, but it seems the *complexity* of the model has an adverse effect on the convergence despite the quality of the mesh. The in-line amplitude results from all five meshes are shown in Figure 5.50 with a zoomed-in version given in Figure 5.51. What is also shown in these figures is the measured mCSEM data and noise from EMGS for comparison purposes. At first glance, it is clear that the measured mCSEM data from EMGS does not match the final hydrocarbon model. There is a logical explanation for this mismatch. Recall from Sections 2.1.4 and 2.1.5 that in-line fields from mCSEM are sensitive to the *vertical resistivity* ( $\rho_v$ ). However, the resistivity log from L-11 gives a measure of the *horizontal resistivity* ( $\rho_h$ ). So, it appears the background resistivities are exhibiting electrical anisotropy and this would explain the mismatch. The measured in-line mCSEM data is sensitive to  $\rho_v$ , and in the presence of electrical anisotropy,  $\rho_v$  is always larger than  $\rho_h$  which explains why the measured mCSEM data lies above the computed result for the hydrocarbon slab model.

Putting the mismatch to the measured mCSEM data aside, there are still important observations regarding the computed results. The results from each model show *predictable* changes in the in-line amplitude results. For instance, there is a distinguishable increase in the electric field going from the Tertiary model to the basement model. This change is expected because the basement model includes

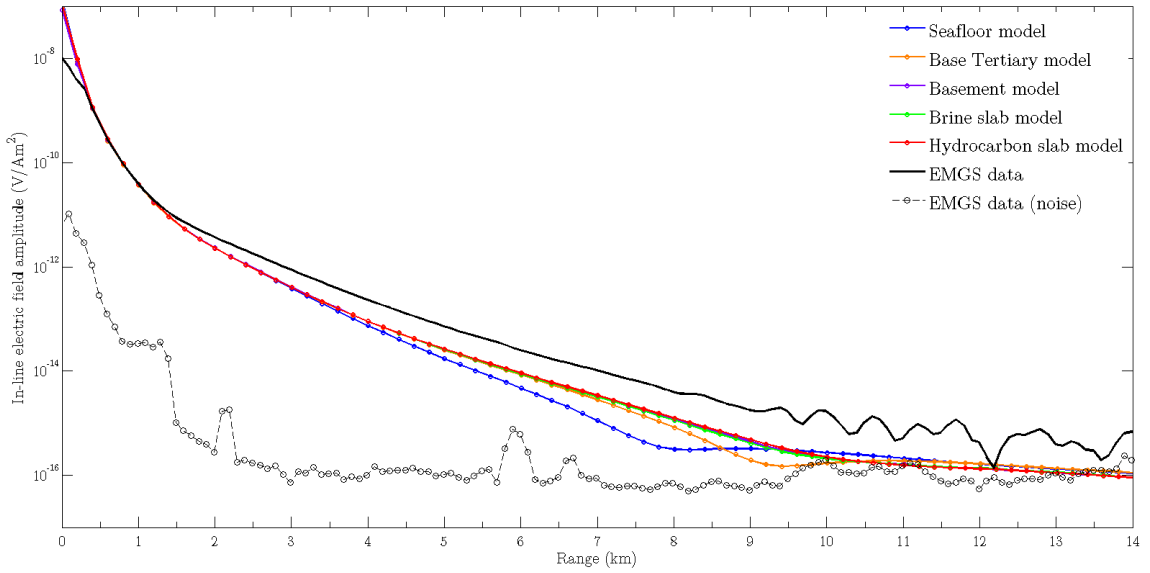


Figure 5.50: The preliminary synthesized in-line electric field amplitudes for each of the five models at RX44 for a frequency of 0.50 Hz. The measured mCSEM data and noise from EMGS for the same receiver and frequency is plotted for comparison.

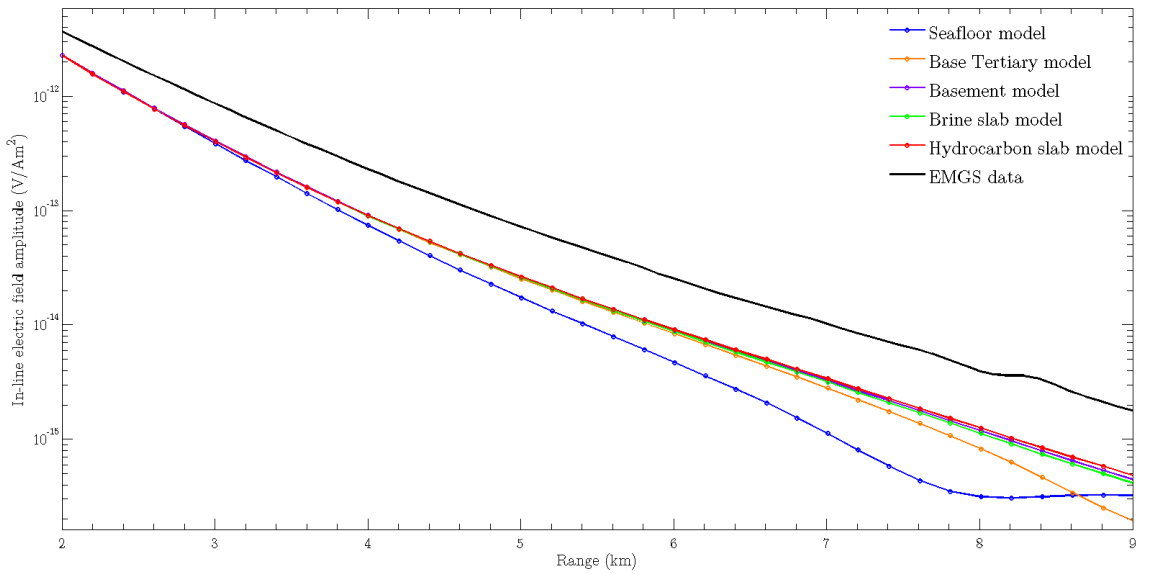


Figure 5.51: The preliminary synthesized in-line electric field amplitudes for each of the five models at RX44 for a frequency of 0.50 Hz (Figure 5.50) zoomed in to show detail.

a strong resistive layer at depth and its presence should increase the electric field amplitude. However, since the basement surface is buried quite deep, its influence on the data does not show up until 5.5 - 6.0 km offset.

The most important changes, if they exist, are between the brine model (background) and the hydrocarbon model. In Figure 5.50 the amplitudes for these two models seem to lie right on top of one another, but a closer inspection in Figure 5.51 shows a minor deviation between the brine model and the hydrocarbon model. The minimal change in amplitude between these two models implies a low sensitivity, but the sensitivity is difficult to quantify based solely on inspection. The hydrocarbon model response was normalized to the brine model response and the corresponding sensitivity curve is shown in Figure 5.52. From a computational perspective, the maximum sensitivity of mCSEM to the hydrocarbon bearing portions of the slabs is about 17%. This means that 17% of the signal at a range of 9.2 km can be attributed to the hydrocarbons. However, this sensitivity needs to be interpreted in the context of the noise level in the measured data to determine if this sensitivity is *detectable* or not. So, the measured noise plotted in Figure 5.50 was normalized to the measured in-line amplitude to give a percent noise level in the measured data and this is shown as the solid black line in Figure 5.52. Notice how the noise escalates after 9.5km and this is also easily observed by just looking at the data itself in Figure 5.50. It appears the sensitivity curve lies above the noise level (17% sensitivity versus 4% noise), but not by much. Moreover, this 17% sensitivity is likely not the true sensitivity of the frequency at this receiver because the reservoir slab model data does not yet match the measured mCSEM data.

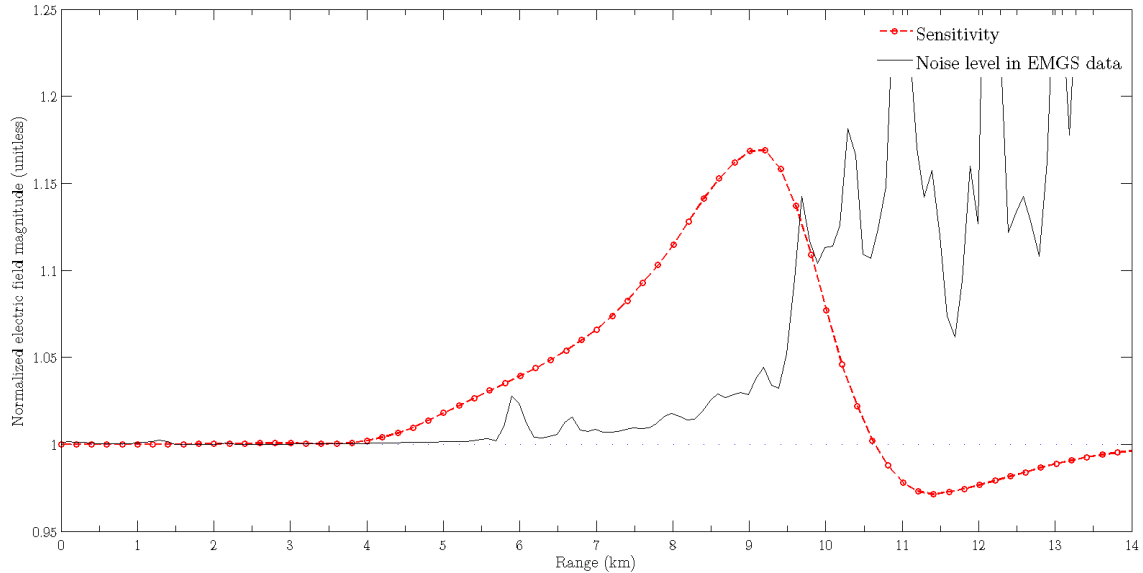


Figure 5.52: The computed sensitivity to the hydrocarbons contained up-dip in the three sands at RX44 for a frequency of 0.50 Hz. The percent noise level in the measured mCSEM data is also plotted to help determine the detectability of the computed sensitivity.

The last piece of data to interpret is the phase, which is given in Figure 5.53. Again, the computed phase results do not match the measured phase due to the discrepancy between  $\rho_h$  and  $\rho_v$ . However, some interesting observations of the computed phase are still found. The influence of the airwave begins to dominate the seafloor model response at 8km offset, the tertiary model response at 9.5km offset, and the remaining three model responses at 11km offset. This clearly illustrates that the inclusion of more resistive layers in the model shifts the range at which the airwave begins to dominate.

In summation, the simulated results from CSEM3DFWD were of good quality, but did not match with the measured mCSEM data from EMGS. The mismatch was ultimately linked to electrical anisotropy. It seemed the background resistivities

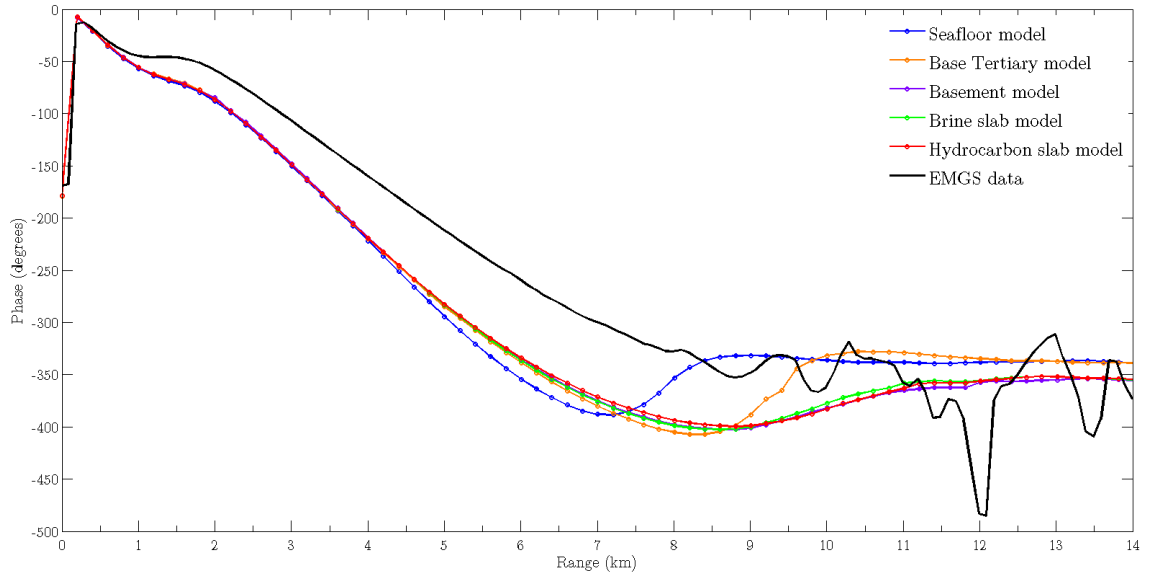


Figure 5.53: The preliminary synthesized phase for each of the five models at RX44 for a frequency of 0.50 Hz. The measured mCSEM data from EMGS for the same receiver and frequency is plotted for comparison.

needed to be modified from  $\rho_h$  to reflect  $\rho_v$  in order to achieve a satisfactory match with the measured mCSEM data.

## 5.8 Modifying Resistivities

In order to match the measured mCSEM data, the starting resistivities from the L-11 well log ( $\rho_h$ ) needed to be modified to reflect the vertical resistivity that in-line mCSEM fields are sensitive to. The air and seawater are considered isotropic and did not have to be modified from the previous section (Figure 5.48). All the resistivities for the subsurface regions were likely candidates for modification. However, the resistivities of the reservoir slabs (both brine and hydrocarbon portions) were not modified. Only the background resistivities were chosen to be modified (i.e. Tertiary, Cretaceous, Jurassic, and basement). *Incremental simulations* were used to try and match the data and what allowed this to be possible was having several different models. The incremental changes between the five models shown in Figure 5.47 were critical to modifying the background resistivities to match the measured data because the contributions from each layer could be *isolated* to see how they influenced the mCSEM data.

Figure 5.51 was helpful in determining how and why resistivities of certain regions needed to change because it was zoomed into a key area. Notice how the other models do not start deviating from the *seafloor model* until about 3.0 km offset (beyond 3 km the presence of the Cretaceous/Jurassic layer starts to influence the data). The seafloor model has a significant mismatch between 1-3 km and this suggested that the resistivity of the Tertiary region must have been underestimated. So, the first step was starting with the seafloor model and simulating multiple responses with changes in the resistivity for the Tertiary. Figure 5.54 shows the computed amplitude and phase results for seafloor models

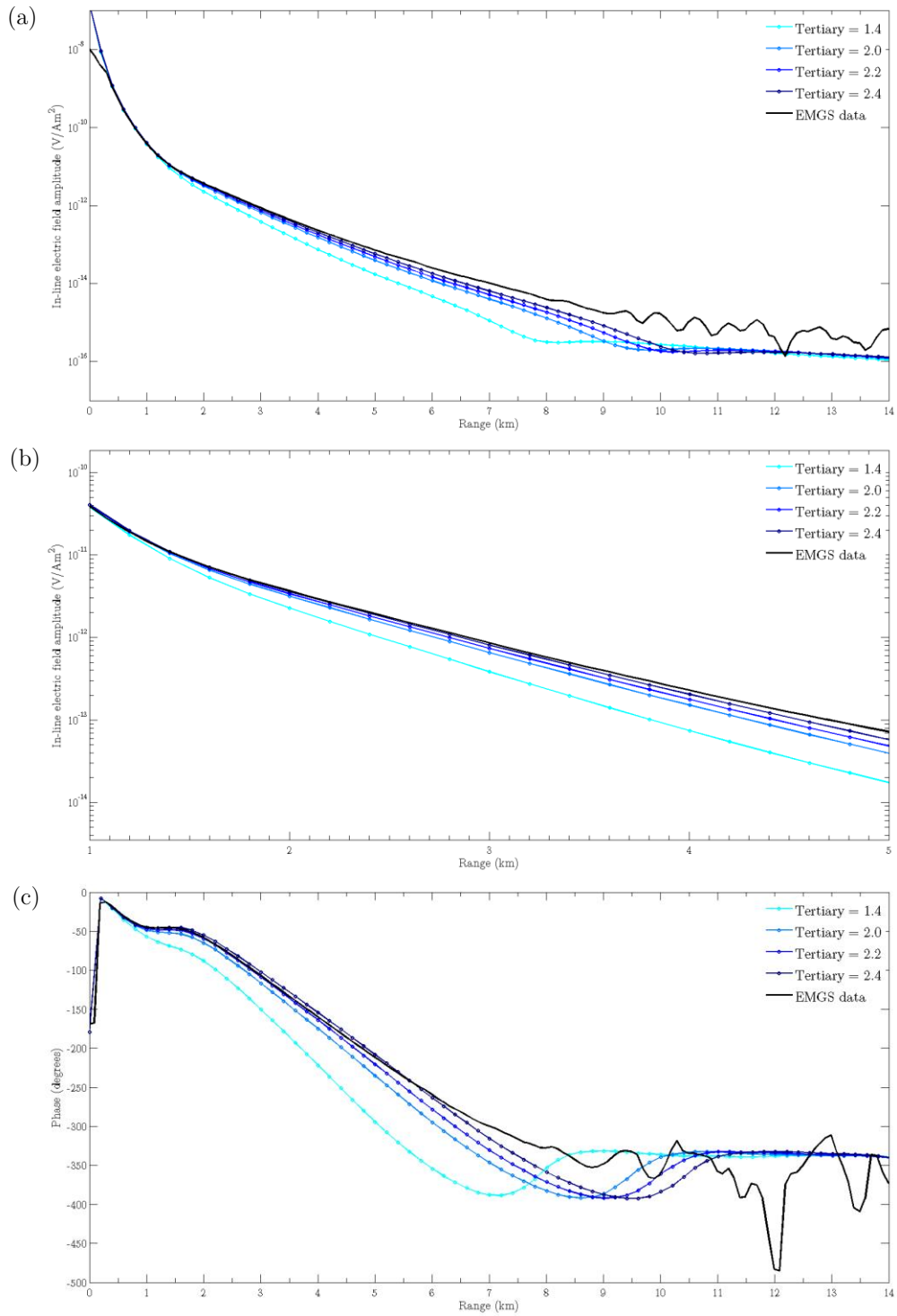


Figure 5.54: The computed (a) in-line amplitude, (b) in-line amplitude zoomed in, and (c) phase responses for varying the value of the Tertiary region in the seafloor model at RX44 for  $f = 0.50$  Hz. The measured mCSEM data and the preliminary seafloor model response with the Tertiary = 1.4  $\Omega\text{m}$  are shown for reference.

with different resistivity values for the Tertiary. The starting Tertiary resistivity of  $1.4 \Omega\text{m}$  is plotted for comparison. Notice how higher values for the Tertiary achieve a much better match with the data. However, it is worth mentioning that a value of resistivity for the Tertiary should not be chosen such that it matches the measured data for all offsets. Matching the measured data too closely with this model is unsuitable because there are other regions that have yet to be accounted for. From the preliminary results, the influence of the Cretaceous/Jurassic region to the in-line amplitude starts around 3.0 km. However, if a higher value for the Tertiary is used, the influence of the Cretaceous/Jurassic region would likely be pushed to a further offset. Therefore, a value for the Tertiary was chosen such that the simulated in-line amplitudes matched the measured in-line amplitudes to 3.0 km and slightly beyond. A value for the Tertiary equal to  $2.4 \Omega\text{m}$  appeared to match the in-line amplitude well until about 3.5km offset (see Figure 5.54b).

Up until this point, the comparisons to the phase have been neglected. Achieving matches to the phase was considered *secondary*, whereas matches to the in-line amplitude were primary because the amplitudes were ultimately used to calculate sensitivities. Another contributing factor is the data files from EMGS do not contain a measure for the amount of noise in the phase. The EMGS data files only report standard deviations for the electric field amplitude and not its real/imaginary components, so the noise in the phase could not be determined. So, matches were made based primarily on the in-line amplitude. Comparisons to the phase were deemed auxiliary and were only used to ensure the simulated phase was not *drifting* considerably from the measured phase. With this in mind, the

simulated phase with the Tertiary = 2.4  $\Omega\text{m}$  matched reasonably well with the measured phase. In summary, it appeared modifying the Tertiary to 2.4  $\Omega\text{m}$  was suitable and this was a sufficient starting point for including the next layer, the combined Cretaceous/Jurassic layer (e.g. Tertiary model).

The second step in this curve matching process was fixing the Tertiary resistivity to 2.4  $\Omega\text{m}$  and varying the Cretaceous/Jurassic resistivity in the tertiary model. As mentioned previously, the value of the Tertiary was not chosen to match the measured amplitude beyond 3.5  $\Omega\text{m}$  in anticipation of the remaining regions causing changes to the amplitude. However, after inspection of the in-line amplitudes in Figure 5.54(a) it still seemed as if there was a reasonably small gap between the predicted and the measured data beyond 3.5 km, so the resistivity of the Cretaceous/Jurassic layer may not need significant modifications.

Three resistivities for the Cretaceous/Jurassic layer are shown in Figure 5.55, one of which is the starting resistivity of 3.36  $\Omega\text{m}$  and the other two are 3.60  $\Omega\text{m}$  and 4.00  $\Omega\text{m}$ . The seafloor model with the Tertiary = 2.4  $\Omega\text{m}$  is shown for reference. First off, notice that the influence of the Cretaceous/Jurassic region begins to influence the amplitudes starting around 3.5 km offset, which is close to the original prediction. Again, a resistivity value for the Cretaceous/Jurassic region was not chosen such that it matched the measured data at all offsets. Figure 5.51 indicated that the basement started to influence the amplitudes starting around 5.5 km, which may be pushed to 6.0 km now with the value of the Tertiary increased. Also, the response from the reservoir slabs needed to be taken into account.

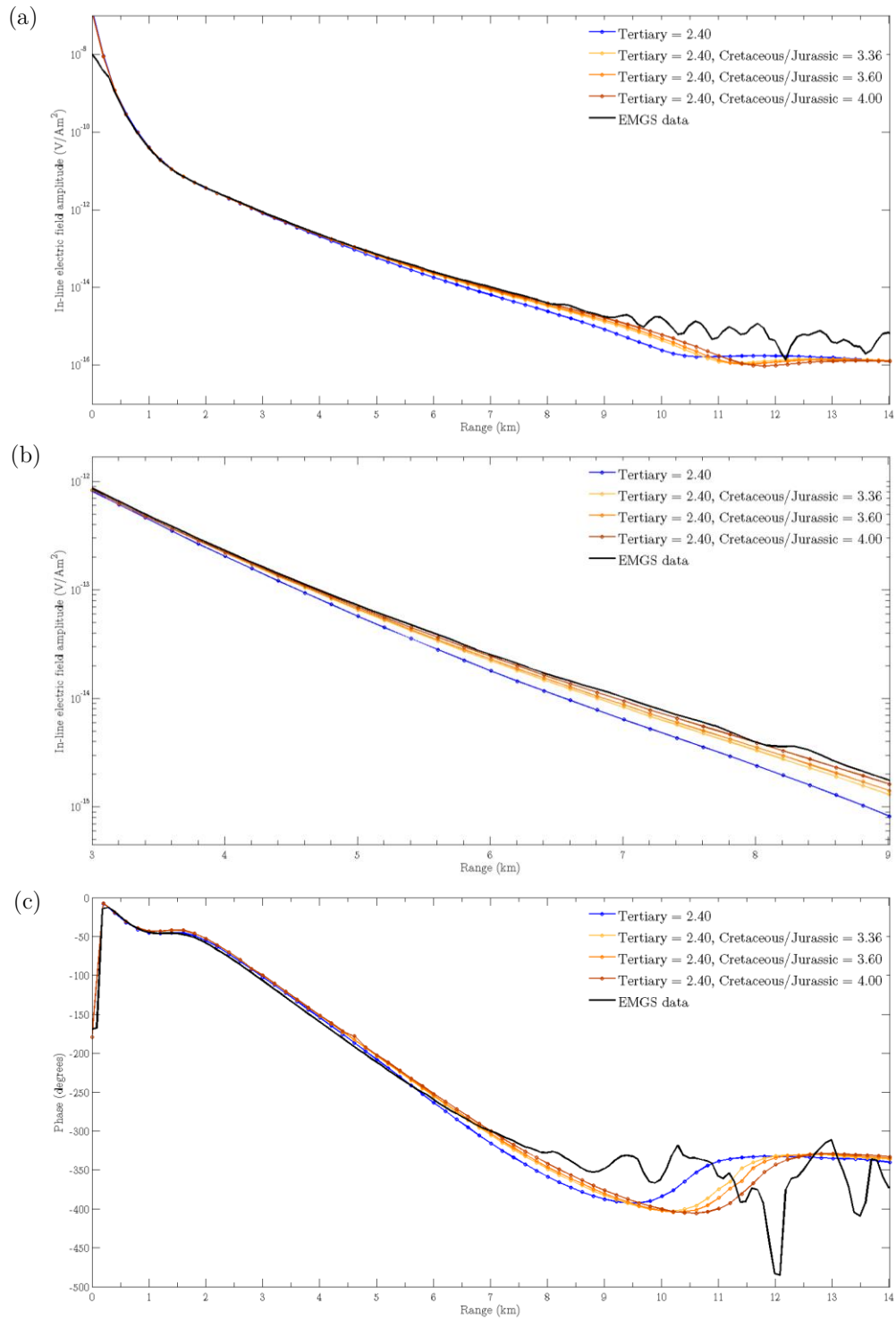


Figure 5.55: The computed (a) in-line amplitude, (b) in-line amplitude zoomed in, and (c) phase responses for varying the value of the Cretaceous/Jurassic region in the tertiary model at RX44 for  $f = 0.50$  Hz. The measured mCSEM data and the previous seafloor model response with the Tertiary = 2.4  $\Omega\text{m}$  are shown for reference.

Figure 5.52 shows that the amplitude anomaly coming from the hydrocarbons in the slabs begins around 4 km, albeit the sensitivity is quite small. Therefore, for the region between 3.5 km and 6 km, it is predicted that the response from the Tertiary model should lie *close* to the measured amplitude, and later, the response from the basement will focus on matching the amplitude after 6 km. The three in-line amplitude curves are shown in Figure 5.55(b) and they all seem to lie close to the measured data. However, the curve for Cretaceous/Jurassic = 4.0  $\Omega\text{m}$  seemed a bit too high as it nearly matched the in-line amplitude beyond 6.0 km and the influence of the basement layer would likely increase the value of the computed amplitude above the measured data. So, the curve for the Cretaceous/Jurassic = 3.6  $\Omega\text{m}$  was the most favorable. In the range between 4-6 km the amplitude lies close to the measured data, and beyond 6.0 km there is a minor gap between the observed and predicted amplitudes allowing some ‘space’ for the influence of the upcoming basement layer. Again, the matches to the phase in Figure 5.55(c) were satisfactory.

The third step in this curve matching process was fixing the Tertiary resistivity to 2.4  $\Omega\text{m}$  and the Cretaceous/Jurassic resistivity to 3.6  $\Omega\text{m}$  and varying the basement resistivity in the basement model. Since there was no data suggesting an appropriate value of the basement, a range of values were considered: 30.0  $\Omega\text{m}$ , 50.0  $\Omega\text{m}$ , 100.0  $\Omega\text{m}$ , and 500.0  $\Omega\text{m}$ . The inline amplitude responses for each of the basement resistivities are shown in Figure 5.56(a) and Figure 5.56(b) with the amplitude of the previous tertiary model plotted for reference. First off, notice that the influence of the basement region begins to influence the amplitudes starting

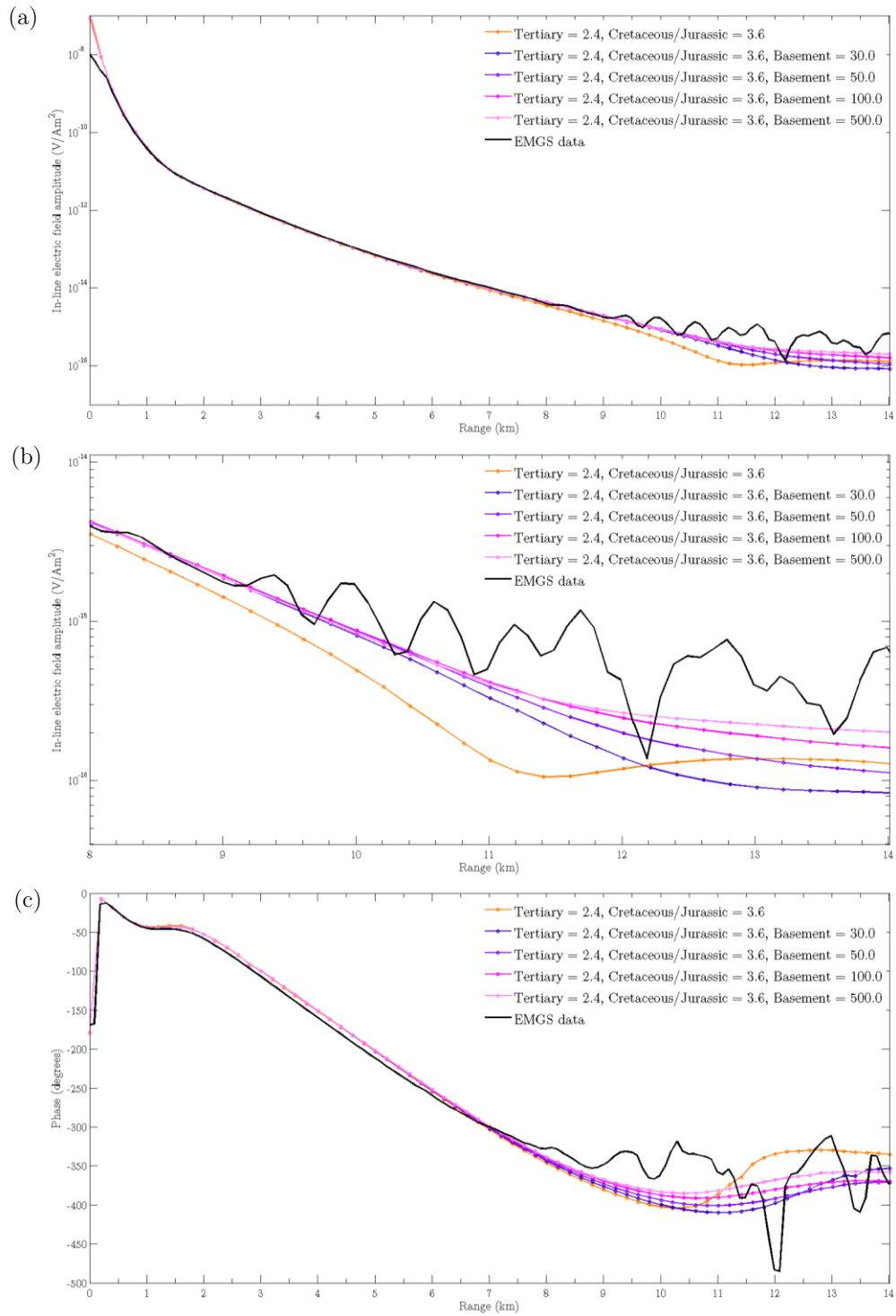


Figure 5.56: The computed (a) in-line amplitude, (b) in-line amplitude zoomed in, and (c) phase responses for varying the value of the basement region in the basement model at RX44 for  $f = 0.50$  Hz. The measured mCSEM data and the previous tertiary model response (Tertiary = 2.4  $\Omega\text{m}$ , Cretaceous/Jurassic = 3.6  $\Omega\text{m}$ ) are shown for reference.

around 6.0 km offset, which is close to the original prediction. An interesting observation is that the four different basement model simulations all show the same increase in the amplitude above the tertiary model until about 10.0 km offset. This suggests that up to 10.0 km offset, the only thing that matters is a deep-buried resistor exists, and the resistivity of the basement appears to not be critical. Beyond 10.0 km offset each of the curves show deviation based on the resistivity value of the basement. However, recall that the noise level in the measured data for RX44 escalates starting at 9.5km (see Figure 5.52), so a reasonable assertion is it does not seem feasible to match the measured data beyond 10.0 km for this frequency. Since all basement model simulations were practically identical up to 10.0 km offset, it seemed most logical to pick the *simplest basement resistivity* of 30.0  $\Omega\text{m}$ .

If the basement resistivity in reality is higher than 30.0  $\Omega\text{m}$ , the most impact it would have is increasing the in-line electric field amplitude at far offsets which appear to already be dominated by noise. However, a minor consequence from the choice of basement resistivity may exist. At far offsets, the maximum sensitivity to the hydrocarbons contained in the Mizzen slabs is observed (Figure 5.52). A higher basement resistivity would *mask* the response from the Mizzen hydrocarbons slightly (this was observed through 1D modeling sensitivity analysis, but not shown for brevity), and subsequently decrease the maximum sensitivity anomaly because these phenomena occur at similar offset ranges. Although, if the maximum sensitivity does not lie above the measured noise level, then the issue regarding the choice of basement resistivity is once again not a problem. Consequently, the curve

for the basement = 30.0  $\Omega\text{m}$  was chosen to move forward with. The amplitude for the basement = 30.0  $\Omega\text{m}$  curve matches well with the measured amplitude. Recall that the sensitivity to the Mizzen hydrocarbons was quite small using the preliminary resistivities. So, if the basement response matches the measured amplitude closely using the modified resistivities, chances are the hydrocarbon slab response will continue to match as well.

At this stage, the resistivity modification process was complete because appropriate values for the background resistivities were chosen that best fit the data (this determined  $\rho_v$ ). The final step in this process was including the updated background resistivities in simulations including the reservoir slabs in the model. Therefore, the resistivities for the Tertiary, Cretaceous/Jurassic, and basement regions were assigned values of 2.4  $\Omega\text{m}$ , 3.6  $\Omega\text{m}$ , and 30.0  $\Omega\text{m}$  for simulations of the Mizzen slab model. As mentioned in the beginning of this section, the resistivities of the brine and hydrocarbons were kept the same. The results for each of the five models are shown in Figure 5.57. The in-line amplitudes of the last three models match well with the measured in-line amplitudes from EMGS up until the matching cutoff of 10.0 km. Also, the match to the phase is adequate as the simulated phase appears to not be drifting from the measured data. There is a slight phase mismatch between offsets of 8-10 km, but the noise here seems to be a contributing factor even though it is not shown directly.

Some interesting observations can be made regarding the sensitivities shown in Figure 5.57(c). The sensitivity to the hydrocarbons in the Mizzen slabs using the

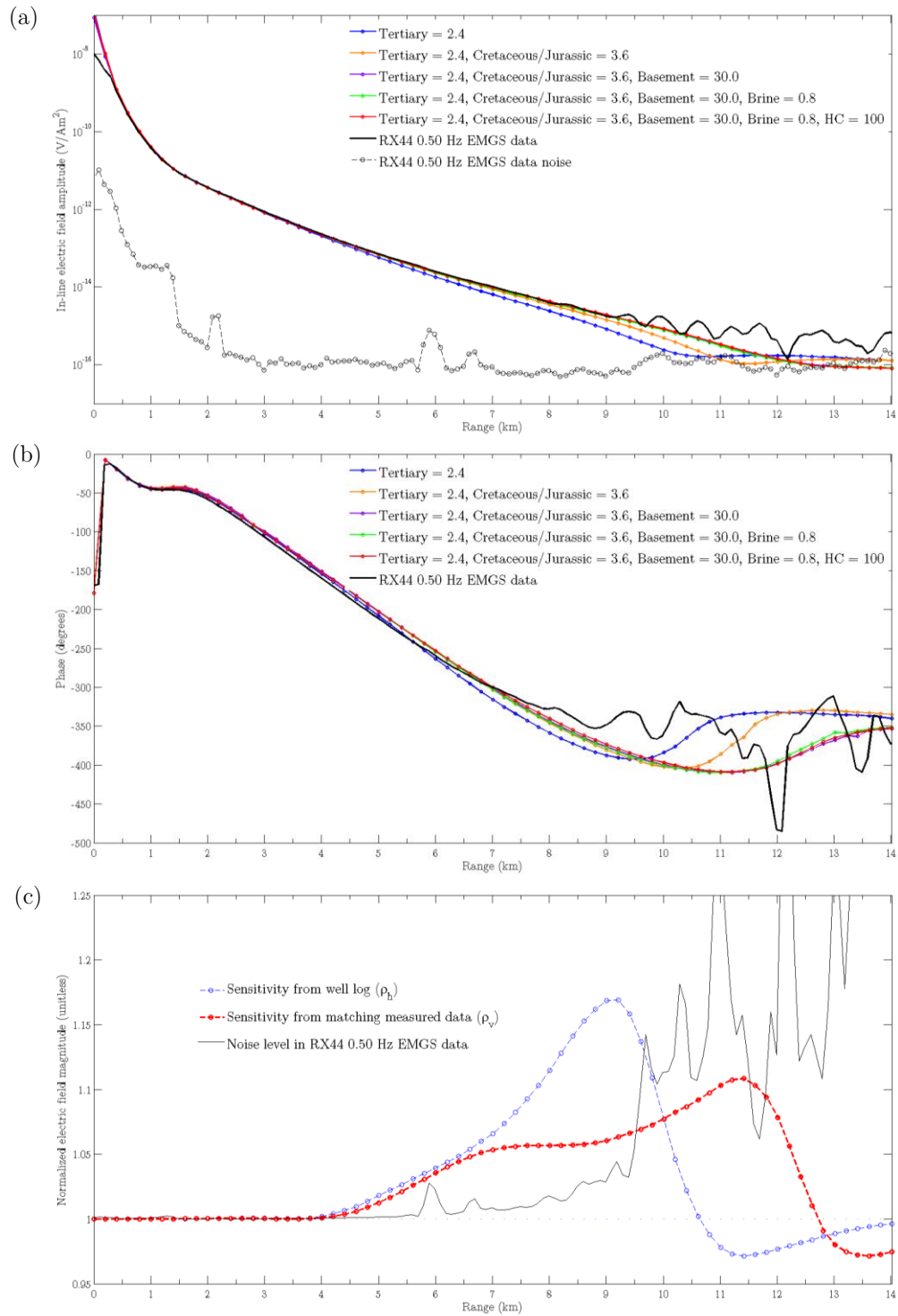


Figure 5.57: The computed (a) in-line amplitude, and (b) phase responses for each of the five models at RX44 for  $f = 0.50$  Hz using the final resistivities established through the incremental simulation approach. Panel (c) compares the sensitivity to the Mizzen slab hydrocarbons using the resistivities from the well log, and the resistivities found through matching the data.

newly derived background resistivities ( $\rho_v$ ) is shown in red, and the sensitivity using the horizontal resistivities from Figure 5.48 is shown in blue for comparison. Notice how modifying the background resistivities from  $\rho_h$  to  $\rho_v$  shifted the maximum sensitivity from 9.0 to 11.5 km offset and reduced the maximum sensitivity from 17% to 11%. This is an interesting consequence because the maximum sensitivity from using the horizontal background resistivities may have been detectable, but the background resistivity modification from  $\rho_h$  to  $\rho_v$  has rendered the maximum sensitivity undetectable due to the amount of noise at that offset.

### 5.8.1 Updated 1D sensitivities

There is additional analysis that can be performed with the change in background resistivities from  $\rho_h$  to  $\rho_v$ . First of all, the horizontal resistivities used in the preliminary stage and the vertical resistivities derived from matching the measured data are both shown as 1D models in Figure 5.58. With both  $\rho_h$  and  $\rho_v$ , the electrical anisotropy for the background layers can be reported. The anisotropy of the basement cannot be reported, because there was no gauge for the horizontal resistivity of the basement as the L-11 well did not drill that deep. For this study, the anisotropy of the Cretaceous and Jurassic layers could not be calculated individually because both of these regions were grouped together. So, the value for  $\rho_h$  was the depth averaged value from the two regions derived from the L-11 well log. Consequently, the electrical anisotropies of the Tertiary and combined Cretaceous/Jurassic regions are,

$$\lambda_T = \sqrt{\frac{2.40}{1.40}} = 1.309 \quad \lambda_{C/J} = \sqrt{\frac{3.60}{3.36}} = 1.035$$

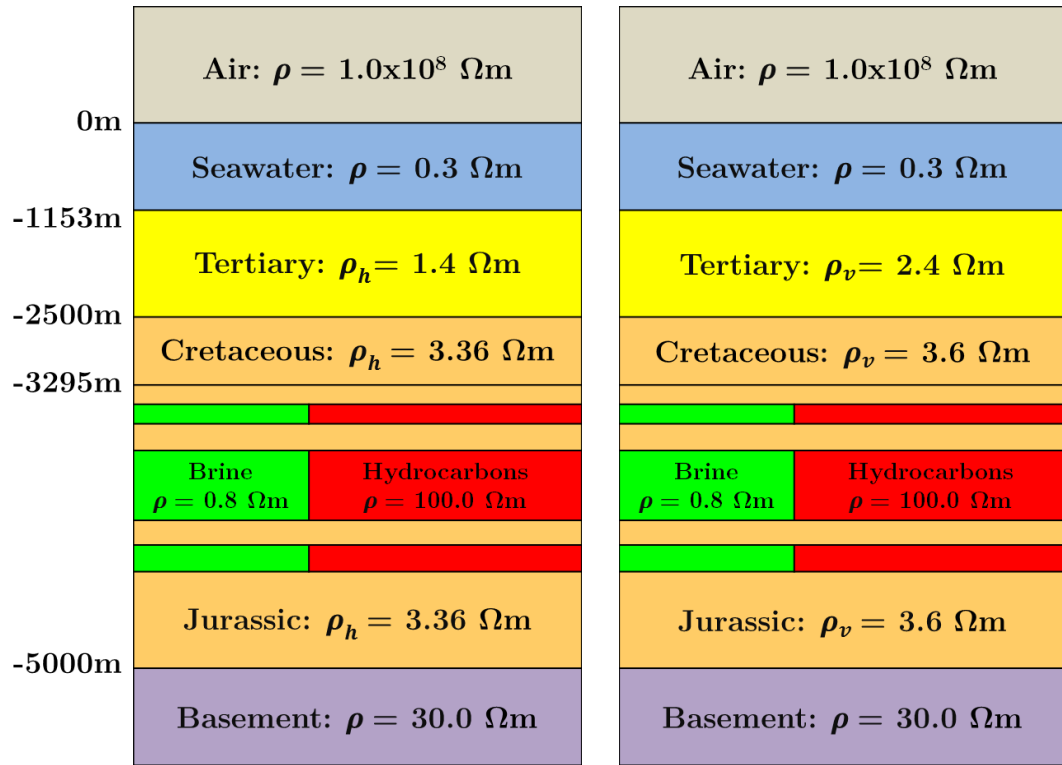


Figure 5.58: 1D models of the horizontal resistivities derived from the L-11 well log that were used in Section 5.7 (left), and the vertical resistivities determined through the incremental simulation approach (right). These 1D models were used for the 1D simulations in Figure 5.59.

These values for electrical anisotropy seem realistic. This accusation is supported by personal communication with Svein Ellingsrud from EMGS where he indicated that these values for electrical anisotropy are similar to what they have encountered in the Flemish Pass Basin. The value for the combined Cretaceous/Jurassic layer seems a bit low compared to the value for the Tertiary, but  $\rho_v = 3.60$  appeared to give the best match to the data.

Another consideration was revisiting 1D sensitivity analysis with the updated vertical resistivities. Similar to the 1D analysis performed in Section 5.3, marine CSEM data was simulated from both of the 1D models shown in Figure 5.58 with

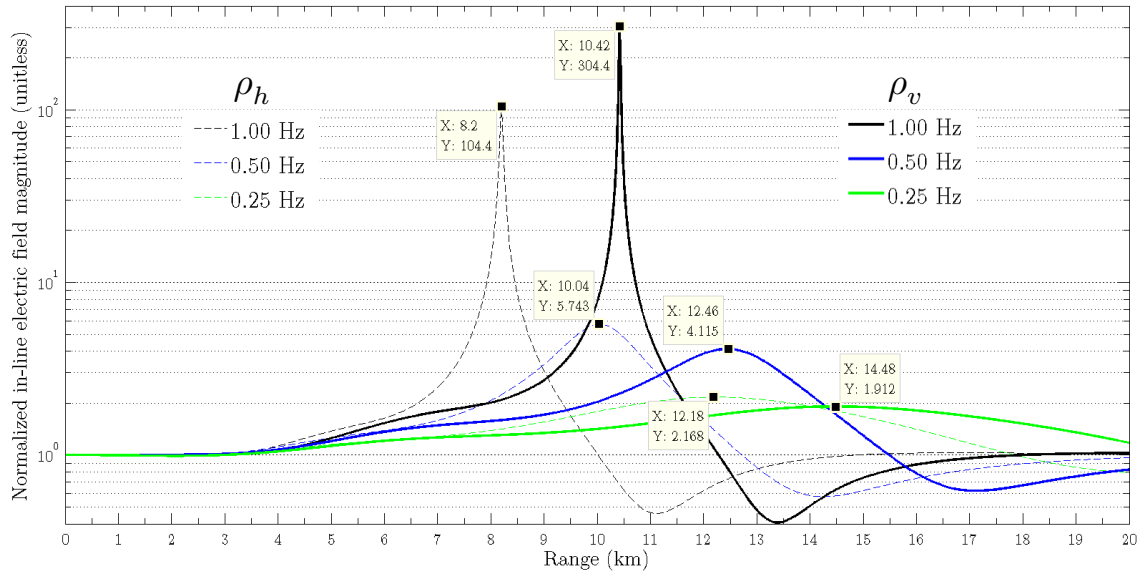


Figure 5.59: The 1D sensitivities to the Mizzen hydrocarbon bearing slabs for the horizontal and vertical resistivity models shown in Figure 5.58 and also for three different frequencies.

DIPOLE1D (Key, 2009). Figure 5.59 shows the corresponding 1D sensitivities to the Mizzen hydrocarbon slabs for various frequencies. An interesting observation is the changes in 1D sensitivity for 0.5 Hz appear to predict and match the sensitivity changes shown in Figure 5.57(c). These 1D sensitivities show the maximum sensitivity is reduced and shifted further in offset when changing from  $\rho_h$  to  $\rho_v$ .

## 5.9 Final Results

The final remaining component of this study was to simulate mCSEM responses at the other receivers and for different frequencies. The previous section established an approach to match the measured mCSEM data accurately through an incremental simulation process involving the layers containing the background resistivities. The background resistivities likely have some degree of lateral variation, so going through the curve matching process for *each receiver location* would be ideal in achieving quality matches at each receiver. However, in the interest of time, the resistivities derived in the previous section (from matching the amplitude at RX44 for 0.50 Hz) were used at the four remaining receivers. This simplification assumed the resistivities of the background regions were laterally *invariant*.

### 5.9.1 Results for RX41

The only results shown here for brevity purposes are the three frequencies (0.25 Hz, 0.50 Hz, and 1.00 Hz) at RX41. Notice that RX41 is on the northeast side of the prospect (see Figure 5.1) and the observation locations were subsequently chosen to extend 14 km southwest in order to pass over the prospect. Figure 5.60 shows the amplitude and sensitivity results at RX41 for 0.50 Hz. Results from all five models were simulated here and the incremental changes between each model are once again observed. Notice that a good match is achieved until 10.0 km offset and Figure 5.60(b) shows that the match to the measured data is exceptionally good. The sensitivity shown in Figure 5.60(c) is similar to the sensitivity for 0.50 Hz at RX44 shown in Figure 5.57 – the maximum sensitivity occurs at an offset

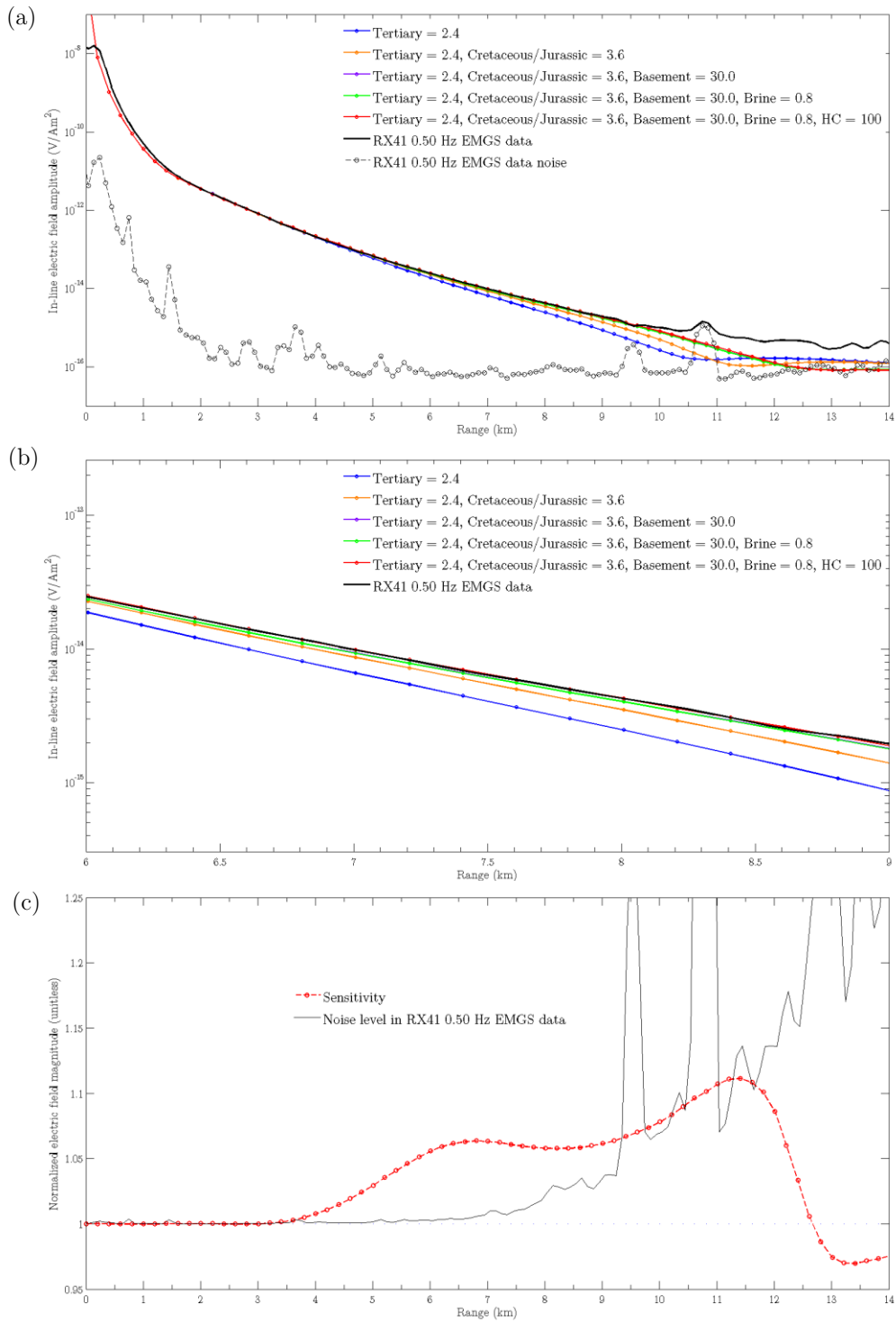


Figure 5.60: The final computed (a) in-line amplitude, and (b) in-line amplitude zoomed in for each of the five models at RX41 for  $f = 0.50$  Hz. A good match is observed. Panel (c) shows the sensitivity to the Mizzen slab hydrocarbons plotted against the noise level in the measured data.

dominated by noise, but there is the 4-8 km offset range that has a sensitivity appearing to lie above the measured noise level.

For the remaining frequencies (and also receivers), data was simulated mostly from the brine slab and hydrocarbon slab models to conserve time and computation resources (i.e. simulations from models without the reservoir slabs, or all layers, were not performed). The next simulation at RX41 was for 0.25 Hz and these results are shown in Figure 5.61. Notice how the computed in-line amplitude responses still match well with the data and the match is better maintained at further offsets compared to 0.50 Hz. As expected, the maximum sensitivity is lower for this frequency and pushed even further in offset. The impact on the sensitivity going from 0.50 Hz to 0.25 Hz is also observed by the 1D sensitivities in Figure 5.59 where similar changes occur. Again, the maximum sensitivity occurs at an offset range dominated by noise, but there is still a small sensitivity in the 4-8 km offset range that lies above the noise level. To some surprise, it was interesting that the noise levels were similar for 0.25 Hz as they were for 0.5 Hz. One would expect that a lower frequency would have lower noise levels at larger offsets due to the skin depth relationship, but that does not appear to be the case here as noise for both 0.25 Hz and 0.50 Hz ramps up at 9.5 km offset and is similar for all offsets. Lastly, the matches to the phase in Figure 5.61(c) seem adequate.

The third and final frequency considered for RX41 was 1.00 Hz and the results are shown in Figure 5.62. Since 1.00 Hz is a higher frequency, the skin depth is higher and therefore the fields will decay more quickly. As a result, the noise began to

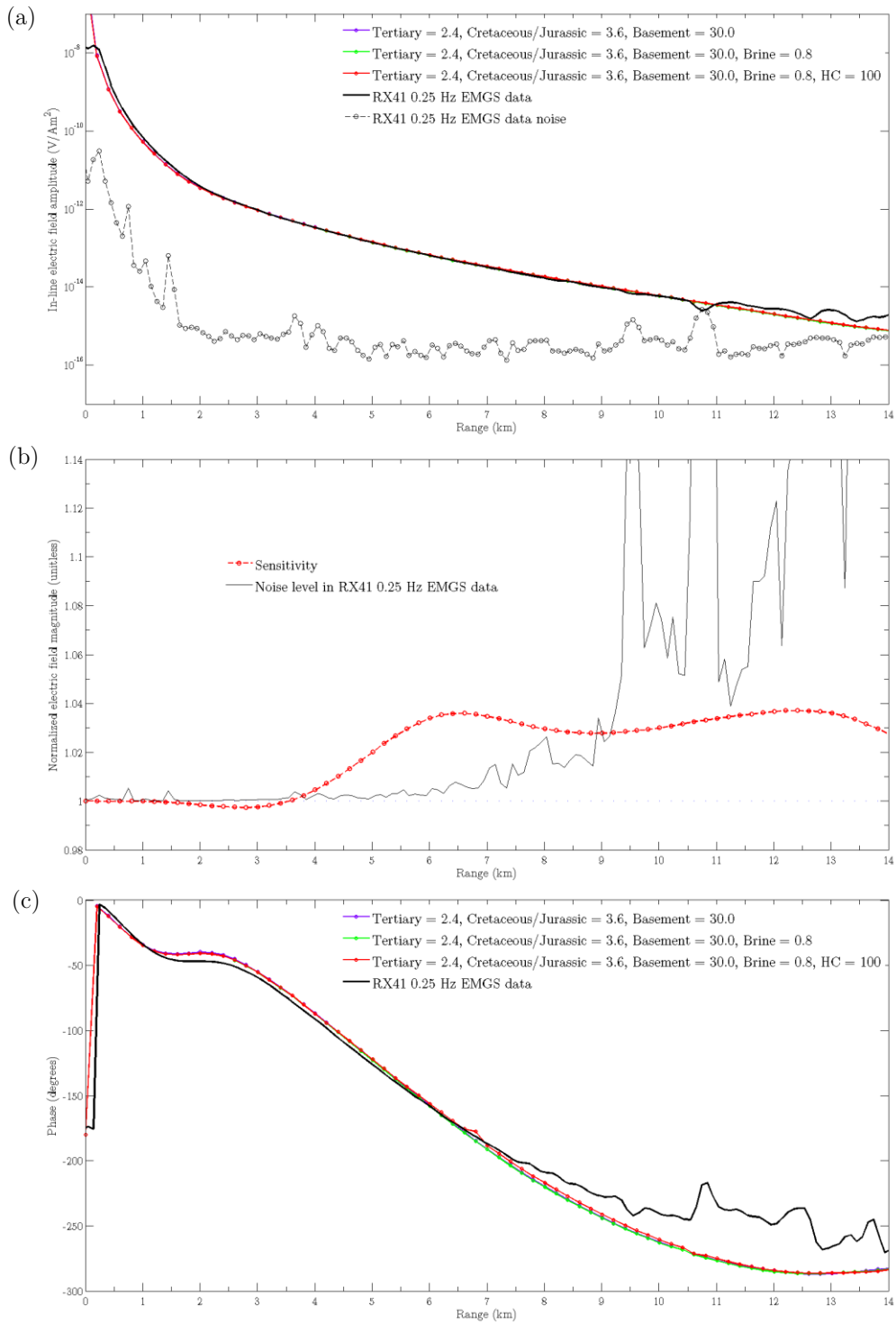


Figure 5.61: The final computed (a) in-line amplitude for three of the models, and the (b) sensitivity to the Mizzen slab hydrocarbons at RX41 for  $f = 0.25$  Hz. The phase (c) is shown for auxiliary comparison purposes.

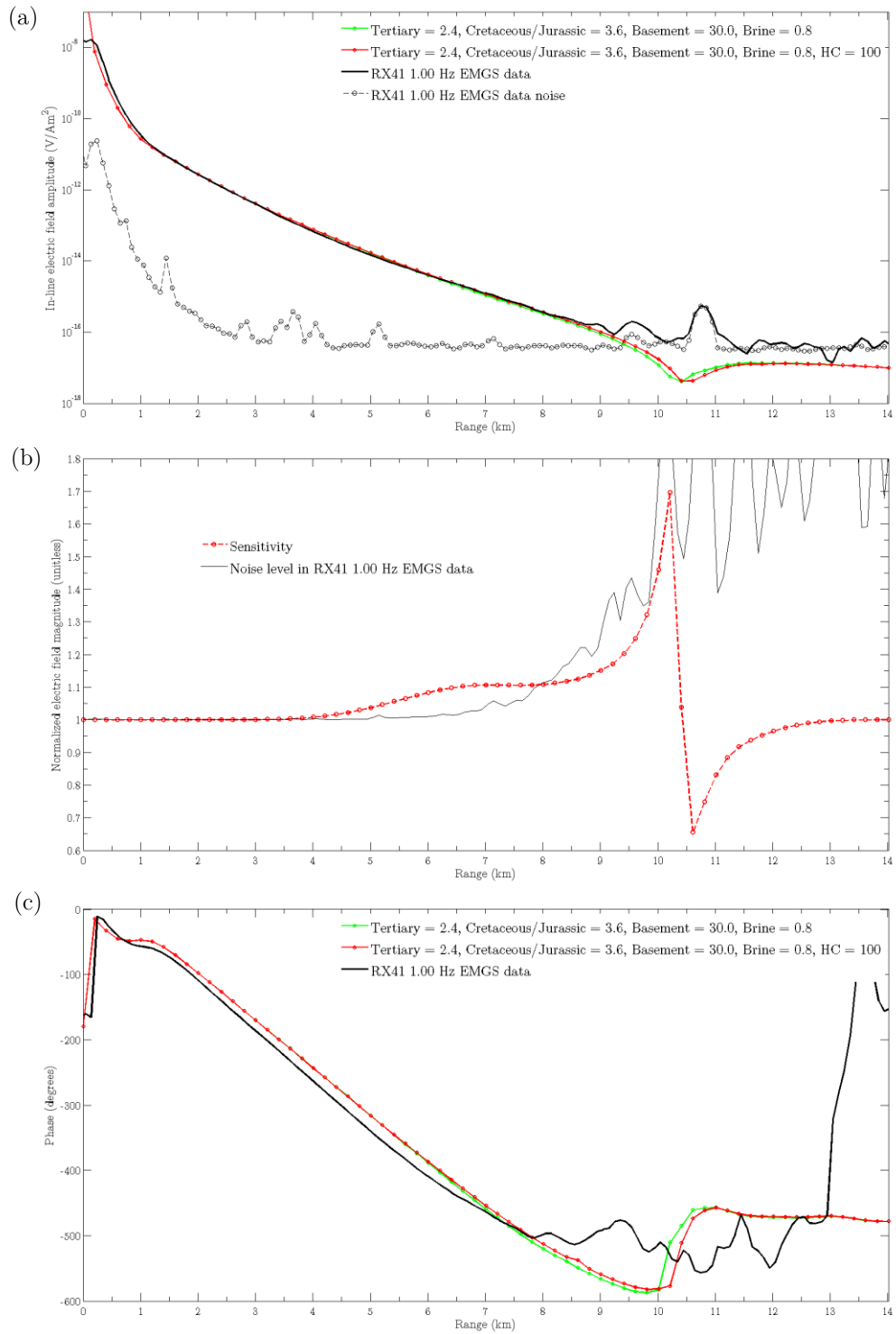


Figure 5.62: The final computed (a) in-line amplitude for two of the models, and the (b) sensitivity to the Mizzen slab hydrocarbons at RX41 for  $f = 1.00$  Hz. The phase (c) is shown for auxiliary comparison purposes.

dominate at an earlier offset and this is observed in the data shown in Figure 5.62. The computed in-line amplitudes were able to achieve a good match with the measured amplitudes up until 9.0 km offset, which is the offset at which the noise begins to escalate as shown in Figure 5.62(b). Again, the maximum sensitivity occurs at an offset dominated by noise in the data, but there is still a small sensitivity that lies above the noise in the 4-8 km range. The computed phase shows a bit of separation/drift from the measured data for nearly all offsets below 9.0 km. This is one of the situations where the match to the amplitude is satisfactory and the match to the phase is mediocre, but for sensitivity calculation reasons more weight is given toward matching the amplitude.

All the remaining receivers and frequencies are given in Appendix D. In summary, a majority of the simulated results continued to have satisfactory matches with the measured EMGS data, while some results had mediocre matches with the measured data. The disadvantage of using the same resistivities derived at RX44 and a frequency of 0.50 Hz led to some less than ideal matches to the measured EMGS data from simulations at *other* receivers and frequencies. However, using only one set of resistivities for the Mizzen models allowed the process to be *streamlined* and more results could be obtained. Many assumptions had already been made, so it seemed most appropriate to pursue *quantity rather than quality*. The convergence curves are not given for any of these simulations with the updated resistivities because all the numerical simulations exhibited similar convergence trends to those shown in Figure 5.49.

### 5.9.2 Sensitivity summaries

An easy way to visualize *all* the data from this study is through the sensitivity curves because it simplifies the important information from the in-line amplitudes into one curve. Figure 5.63 shows all the sensitivity curves for each receiver broken up into one panel for each frequency. Each of the three panels is plotted on the same vertical scale in order to easily see the relative sensitivity changes between each frequency. Panel (a) shows the sensitivities for all receivers at 0.25 Hz. There appears to be a consistency between most of the curves as the maximum sensitivities all equate to 3-4% at an offset of 12-13 km. At the 4-8 km range, the sensitivities equate to 2.0-3.5%. Moving to panel (b) which shows the sensitivities for 0.50 Hz, there is an obvious increase in the sensitivity for all receivers. The maximum sensitivities equate to 7-11% at an offset of 11 km, and for the 4-8 km range, the sensitivities are 3.5-6.0%. Panel (c) shows the sensitivities for 1.00 Hz and there is an even larger increase in the sensitivity of all the receivers. The maximum sensitivities equate to 30-90% (not seen) at an offset of 10 km, and for the 4-8 km, range the sensitivities are 6-11%.

A practical outcome from these sensitivity figures is they show which receivers are the most sensitive to the Mizzen slab hydrocarbons, and there is a *geometrical* explanation for each receiver. Prior to the sensitivity analysis, it was theorized that RX42 would be the most sensitive to the hydrocarbon portions of the slabs because this receiver was the closest in proximity to the L-11 well (see Figure 5.1). However, as Figure 5.63 indicates, *RX42 is actually the least sensitive of the five receivers*. The explanation for this (and all the receivers) is based on the path the

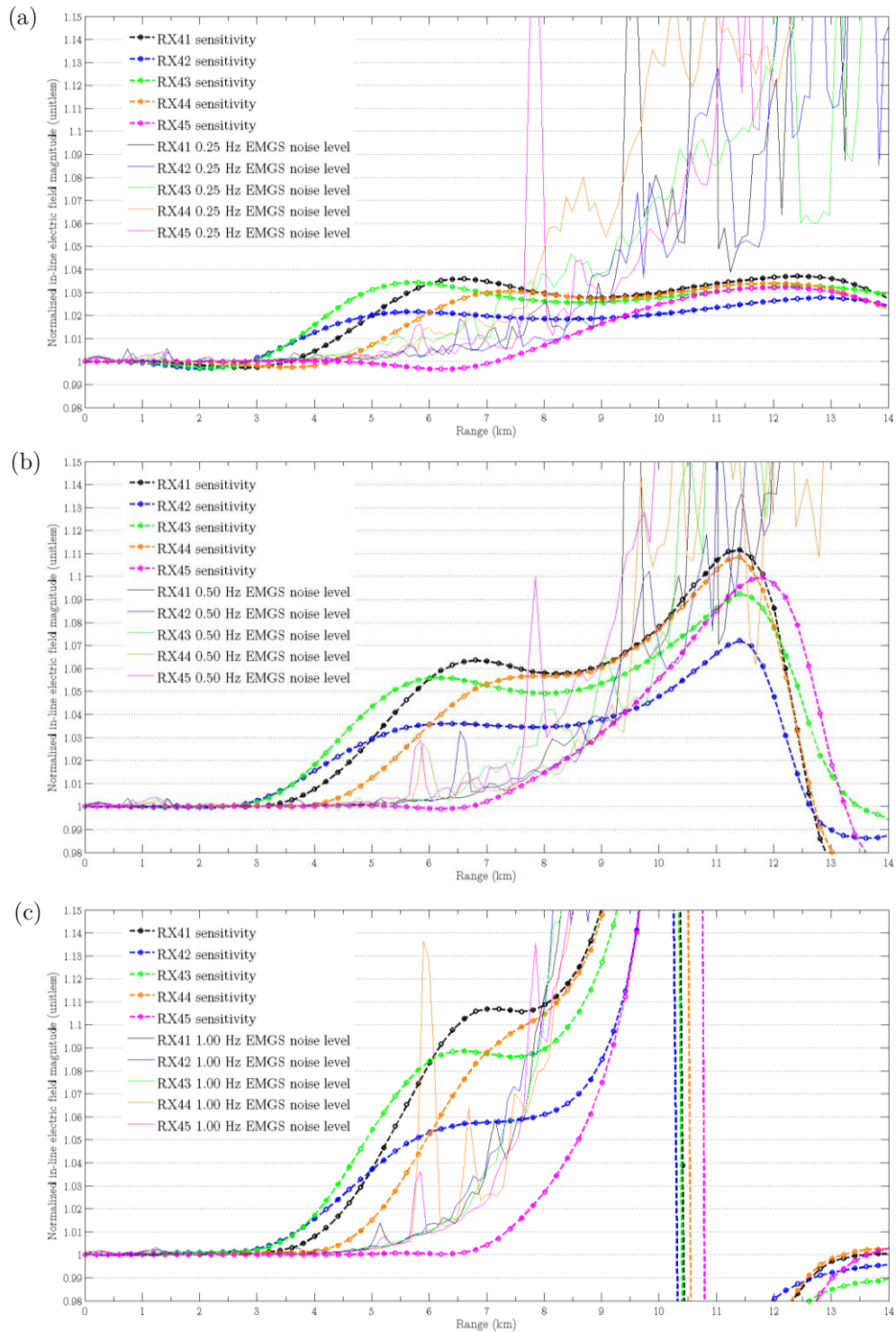


Figure 5.63: The sensitivity summaries to the Mizzen slab hydrocarbons at all receivers for (a) 0.25 Hz, (b) 0.50 Hz, and (c) 1.00 Hz. The noise level at each receiver for each frequency is also shown to help establish if the sensitivities are detectable. All three panels are plotted on the same vertical scale to indicate the relative sensitivity changes between each frequency.

CSEM fields must take to go from transmitter to receiver. As the fields propagate from the computational transmitter at RX42 into the subsurface, the fields will continue propagating downward, reach the reservoir slabs, guide across the reservoir slabs, and refract back up to the seafloor surface where the response is measured. The problem with RX42 is the fields propagating down into the subsurface will only guide across a *fraction* of the reservoir on either side. This explains why RX41 and RX44 have the highest maximum sensitivities because in plan view their locations are situated outside the boundary of the slabs which allows the EM fields to travel and guide across the entire length of the slabs. RX43 also has a good sensitivity, but it appears lower than RX41 and RX44. The logical explanation is RX43 is situated right on the edge of the reservoir slabs and that must be too close for the fields to be able to guide across 100% of the reservoir. However, a benefit of RX43 being the closest to the reservoir is the sensitivity anomaly in the range of 4-8km is seen at a slightly earlier offset. RX45 is an interesting receiver because it is the only receiver that does not have a sensitivity anomaly on the range from 4-8 km. However, this is intuitive because RX45 is 6 km away from the edge of the slabs (see Figure 5.1) and any response from the reservoir would not be expected until after 6 km.

In summary, the overall sensitivity to the Mizzen slab hydrocarbons is small and the maximum sensitivity for all receivers and frequencies occurs at an offset that is dominated by noise in the measured mCSEM data and is conclusively not detectable. However, this sensitivity analysis did show some small sensitivities appear to lie above the noise level in the 4-8 km range.

## 5.10 Mizzen Conclusions

The investigation of mCSEM forward modeling at the Mizzen prospect was performed with two desired outcomes in mind: (1) to show that the finite-element forward modeling technique can successfully simulate data from a complex model, and (2) use this forward modeling technique to help supplement interpretation for a real offshore exploration problem.

Building the Mizzen model was challenging and consisted of many steps and attempts to achieve a model that was acceptable for numerical simulation (i.e. many cycles of the modeling process depicted in Figure 3.2 were needed). The final model consisted of three topographic surfaces derived from 2D seismic data and three dipping slabs that were approximations to the three reservoir sands under Mizzen L-11. The full benefits of an unstructured grid were utilized in this mesh in numerous ways. Generating the mesh with tetrahedra instead of hexahedra allowed for the topography of the surfaces in the model to be more accurately represented than what could be achieved on a structured mesh. Furthermore, using an unstructured grid allowed the mesh to have constraints (e.g. on the surfaces) and refinement at critical locations (e.g. observation locations) while maintaining larger cells elsewhere in the mesh. These factors were important in reducing the number of cells in the mesh. This was important from a computation perspective because a mesh that was too large would require (1) more memory than the available computational resources could allow, and (2) longer computation times.

As a result, the final model was able to reflect the scale and complexity of the Flemish Pass Basin and this was accomplished despite the data limitations of the basin being in an exploration phase. Had the basin been in a production phase, there would have been far more data (e.g. 3D seismic data and more wells) and the various components of the model could have had improved detail. Indeed, more data would have been useful, but the outcome of this study showed that *a complex model could still be built with limited amounts of data* and that is seen as an accomplishment. Despite the complexity of the models, the 3D finite-element forward modeling software (CSEM3DFWD) was still successful at simulating mCSEM results. Even going from the simplest model (seafloor model) to the most complex model (Mizzen hydrocarbon slab model) the numerical results did not suffer and the models with more complexity were still able to achieve convergence (see Figure 5.49). In summary, the first desired outcome was met as this study showed that the finite-element forward modeling method was successful in simulating mCSEM data from the complex models created to reflect the Mizzen prospect.

The second desired outcome of this study was to apply this technique to supplement seismic interpretation at the Mizzen L-11 prospect. The seismic data acquired over Mizzen L-11 contained three AVO anomalies up-dip from where the well was drilled and this finite-element forward modeling technique was used to help determine the prospectivity of these three potential reservoirs. Marine CSEM data was acquired by EMGS over the Mizzen prospect and this data served as a target for the simulated data to try and match. The starting resistivities in the

model were taken from the L-11 well log, but due to electrical anisotropy, these resistivities were underestimated as the predicted data did not match the measured data. However, through an incremental simulation process, the resistivities were modified such that the simulated mCSEM data matched the measured mCSEM data from EMGS. Upon matching the measured data, the prospectivity of the Mizzen hydrocarbon reservoirs was determined through a normalization process used to calculate sensitivity.

Forward modeling results were computed at five different receivers and for three different frequencies. From a forward modeling perspective alone, sensitivity to the Mizzen reservoirs was found at these various locations and receivers. However, when these sensitivities were interpreted in the context of the noise level in the measured mCSEM data, it appeared the maximum sensitivity was not detectable. However, there is a segment of the sensitivities for all frequencies that occurs above the noise level at 4-8 km offsets, but these sensitivities are quite small and may be on the border of being detectable in the measured mCSEM data. Although, all these small sensitivities in the 4-8 km range occur in multiple receivers at each frequency. From an inversion perspective, if all these data sets were collectively used in an inversion, all these small sensitivities in the 4-8 km range could combine to give a small resistive anomaly. EMGS did perform an inversion of the entire Flemish Pass data set (including much more than the five receivers shown) using their 3D finite-difference time-domain modeling code and they did recover a small resistivity anomaly under Mizzen L-11 (not shown).

In summary, when interpreting the computed sensitivities in the context of the noise level in the measured data, the Mizzen reservoirs appear to be borderline detectable. The lack of a strong sensitivity thereof translates to mCSEM struggling to distinguish between brine and hydrocarbon saturations in these three reservoirs. Additionally, the lack of strong, *detectable* sensitivities leads to inconclusive evidence in supporting the hypothesis that hydrocarbons are contained up-dip from where the L-11 well was drilled as suggested by the AVO. In retrospect, the Mizzen reservoir is quite small and likely contains uneconomic volumes of hydrocarbons as the estimated recoverable oil was only 44M barrels. Had the reservoir been larger, the prediction is mCSEM would be far more sensitive and this forward modeling technique would be able to offer a more conclusive verdict regarding detectability.

### **5.10.1 Assumptions**

The outcomes of this study showed this finite-element forward modeling technique can successfully simulate mCSEM data from complex models, and also provided a practical conclusion stating the mCSEM responses may be below the detectability threshold. However, it is necessary to not overlook the assumptions and simplifications required to achieve these outcomes.

One of the most significant simplifications during the model building stage was deciding to exclude the base Cretaceous surface. The L-11 well log clearly indicated there was a different resistivity value for the Cretaceous and Jurassic regions, but this simplification combined these two regions into one. As a result, this likely

overestimated the resistivity in the Cretaceous and underestimated the resistivity in the Jurassic. This may provide an explanation as to why most of the phase comparisons show the simulated phase is lying above the measured at earlier offsets and the simulated phase is lying below the measured at later offsets.

Another assumption that was part of model building stage was the process needed to determine the observation locations. CSEM3DFWD could not support a multi-source forward problem, so reciprocity was used to turn the forward problem into a scenario involving only one computational transmitter for each receiver used by EMGS. The problem occurred when trying to establish the orientation of the transmitters after reciprocity. The EMGS vessel was emitting continuous transmitter pulses, and as Figure 5.38 showed, the vessel could not keep perfectly straight which meant each transmitter pulse could have a slight deviation off of the true bearing. The simplification used by this study was *flattening* the transmitter path of the EMGS vessel. This allowed the orientation of the computational transmitters to be easily determined and allowed for the transmitter to be perfectly *in-line* with the computational receivers (the EMGS transmitter pulses before reciprocity). However, by flattening the transmitter path, the physical locations of the EMGS transmitter pulses were moved away from the point where the pulse occurred. After reciprocity, this meant that the receiver locations were in a slightly differently location, and as a result, the computed fields could possibly be different compared to if the receiver locations were in their original position. However, the receiver locations were not moved far from their original locations (a few tens of metres at the most), so it is possible that this simplification could have a minimal

to negligible impact on the computed data. In fact, despite these assumptions, the simulated data was still able to achieve a very good match to the measured in-line amplitudes for many receivers and frequencies.

There were also many simplifications made when building the Mizzen reservoir for the model. In 2D, the three Mizzen sands could be represented quite well as dipping slabs from the seismic line, but the issue was determining the 3D extent of these three sands. There was only one seismic line that passed through the prospect and the only information regarding the lateral extent of the Mizzen reservoir that was available at the time was a polygon published by Statoil. However, this polygon was based on data not available to this study so it did not seem valid to base the extent of the Mizzen reservoirs on this polygon. So, the three dipping slabs in 2D were simply extended in/out of the plane of the seismic line and the extents terminated approximately according to the boundary of the Statoil polygon. In reality, the shape of the Mizzen reservoirs is likely quite different, but a slab approximation was the best representation this study could achieve considering the information available.

One of the last assumptions was during the numerical simulation stage. The CSEM3DFWD code assumes each region in the mesh contains a homogeneous resistivity. Marine sediments likely have some degree of lateral inhomogeneity, so this assumption may not hold. Any lateral changes in resistivity could have been accounted for by determining resistivities through the incremental simulation process at each receiver location, and any changes to the resistivity would be found

in order to match the measured data. However, this was not done due to time constraints.

## Chapter 6

# The Bay du Nord Study in the Flemish Pass Basin

The previous chapter reported the synthesizing of marine CSEM data from complex models surrounding the Mizzen L-11 prospect. The finite-element forward modeling method was successful at synthesizing data from these models. However, the small size of the reservoir slabs led to small sensitivities and inconclusive evidence to support the hypothesis that hydrocarbons are in place up-dip in structure. This chapter describes the work that was done by applying the same finite-element forward modeling method to models built from an entirely different field in the Flemish Pass Basin, the Bay du Nord field. The models built for this field had added levels of complexity in comparison to the Mizzen field, and the challenges again were maintaining quality results and convergence in the presence of increasing model complexity.

## 6.1 Bay du Nord

In 2013, an exploration well (C-78) was drilled by Statoil in the Flemish Pass Basin which led to the discovery of the Bay du Nord field. This discovery received significant media attention because it was the largest discovery to date in the Flemish Pass Basin. Statoil made an announcement in June 2016 reporting an estimated 300-600M barrels of recoverable oil for the field (<http://www.statoil.com/>). This field in particular was chosen for the second forward modeling study of this thesis because of the improved data coverage and the preconceived knowledge Bay du Nord was a much larger reservoir compared to the reservoir built for the Mizzen study in the previous chapter.

The Bay du Nord field is also located in the Flemish Pass Basin, and therefore, the regional geology interpreted at the Mizzen field (Figure 5.2) is still relevant to the geology at Bay du Nord. Figure 6.1 shows the close proximity between the Mizzen L-11 and Bay du Nord C-78 wells. Similar to the L-11 well, the C-78 well was drilled into a Jurassic high to target hydrocarbon bearing sands in the Tithonian (late Jurassic). A schematic of the gamma ray, density, sonic, resistivity, and porosity logs for C-78 is shown in Figure 6.2. Upon inspection of the well logs, there are two sand zones that exhibit clear indications for hydrocarbon reservoirs: strong resistivity anomalies, low densities, and high porosity values. Both of these sand zones appear to roughly be 50m thick and are located in close proximity to the base Cretaceous marker interpreted to be around  $z = -3000\text{m}$ . This is reminiscent of the geological scenario at Mizzen L-11 as the potential reservoir

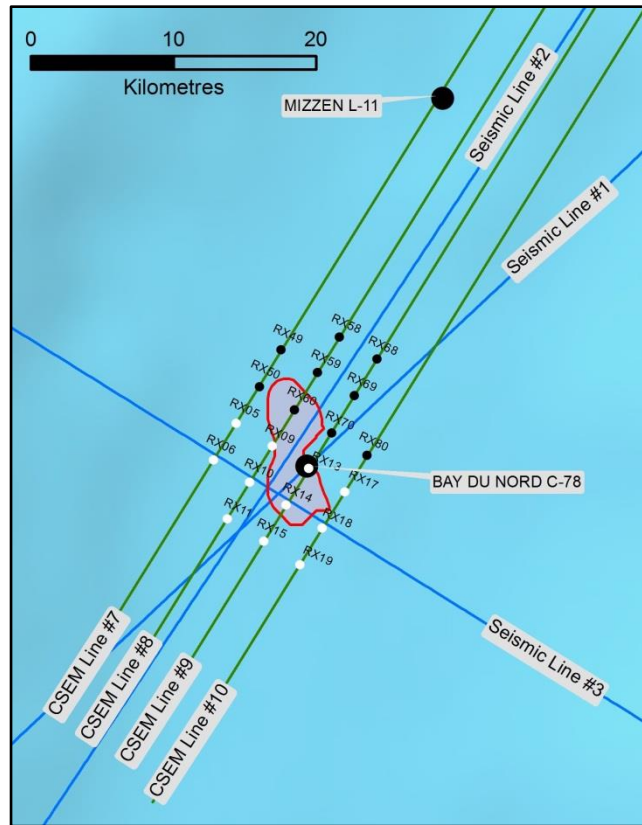


Figure 6.1: A map in the Flemish Pass Basin indicating: the relative locations between Mizzen L-11 and Bay du Nord C-78, the three 2D seismic lines in proximity to Bay du Nord C-78, a polygon estimating the Bay du Nord reservoir extent (shown in red), and four transmitter lines and twenty receivers of a marine CSEM survey (acquired by EMGS) in proximity to the reservoir extent.

sands in that field were also Tithonian aged and were located just below the base Cretaceous.

The data coverage surrounding Bay du Nord C-78 is far more extensive than the data coverage surrounding Mizzen L-11. First, the map in Figure 6.1 shows that there are four mCSEM transmitter lines from EMGS in proximity to the estimated Bay du Nord reservoir extent (this extent is derived in Section 6.4). EMGS acquired their mCSEM data in the Flemish Pass sequentially in three separate survey layouts. As a result, the receivers surrounding the Bay du Nord prospect

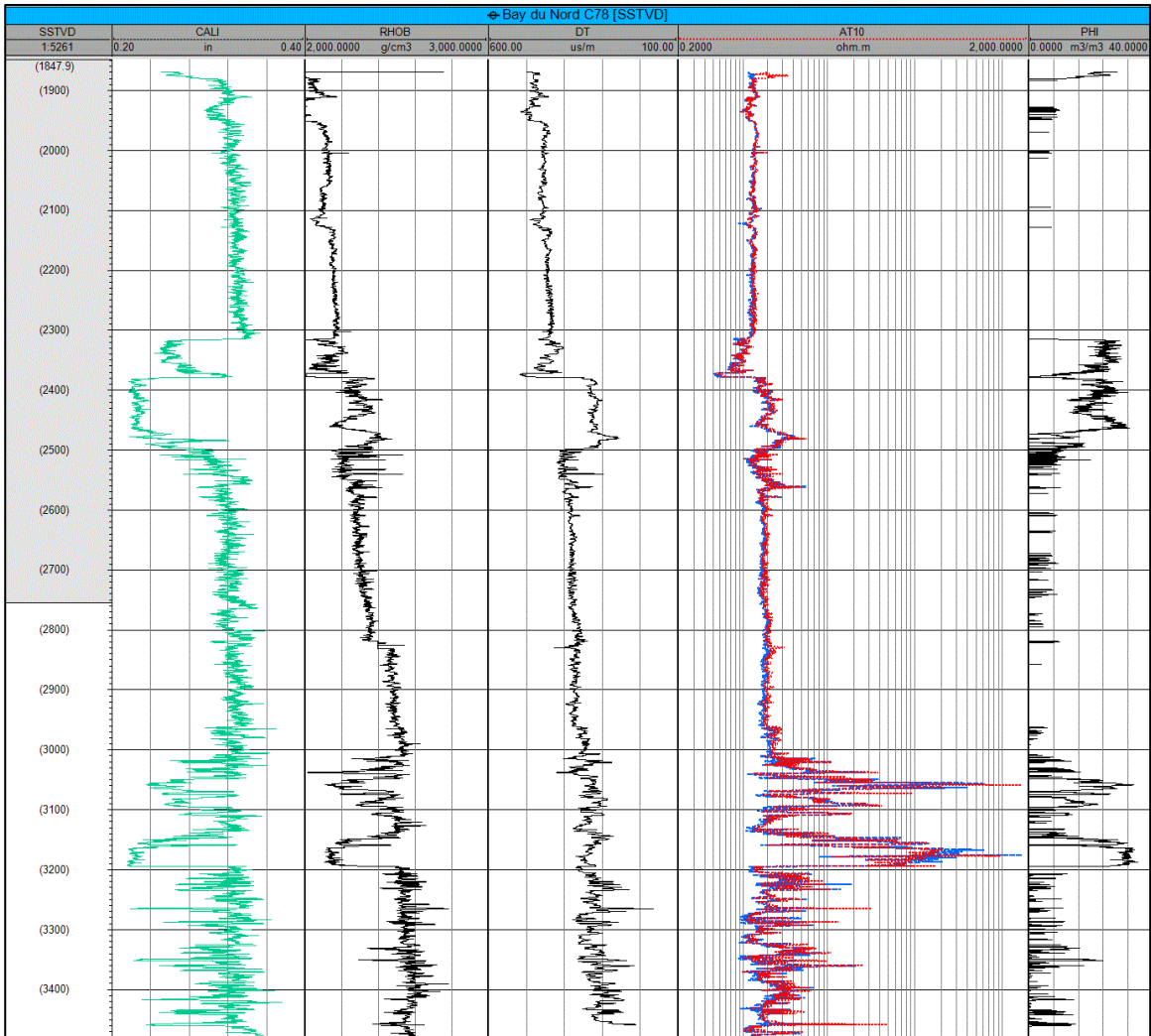


Figure 6.2: A well section viewer from Petrel showing the (left to right) gamma ray, density, sonic, resistivity, and porosity logs for Bay du Nord C-78 (permission given by Nalcor Energy).

were part of *two* separate survey layouts. Since the Bay du Nord reservoir was predicted to have a much larger lateral extent than Mizzen, more CSEM receivers were considered to fully recover the details of any potential anomaly. Figure 6.1 shows the twenty CSEM receivers considered for this study: the nine north-eastern receivers (black circles) were part of survey layout II, and the eleven south-western receivers (white circles) were part of survey layout III. The investigation at Mizzen

showed the largest sensitivities came from receivers closest to the outside boundaries of the reservoir, so all the receivers surrounding the predicted Bay du Nord extent were chosen. Furthermore, in order to observe how the mCSEM sensitivities change the further away a receiver is from the reservoir, additional receivers were considered at greater distances from the reservoir.

In addition to more mCSEM data coverage, there are also more 2D seismic lines surrounding the Bay du Nord prospect. Figure 6.1 shows three seismic lines which pass through the predicted Bay du Nord extent. The near and far angle stacks for seismic line #1, seismic line #2, and seismic line #3 are shown in Figure 6.3, Figure 6.4, and Figure 6.5 respectively. The strong seismic reflection at  $z = -2500\text{m}$  on the near and far angle stacks for each seismic line is the base Tertiary carbonate (also seen by the well-log signatures in Figure 6.2). The orange horizon on each of the seismic panels is the smoothed base Cretaceous surface that was later an input to the model. The light green horizon in the Jurassic highs represents the top of the Bay du Nord sand and this is described later in Section 6.4. Notice in each of the seismic lines there are strong AVO anomalies in the Jurassic highs, but the most noteworthy is the AVO anomaly for seismic line #1 shown in Figure 6.3(b). Figure 6.1 shows that the C-78 well was drilled in close proximity to seismic line #1 and this well actually drilled into the Jurassic high shown in Figure 6.3(b). This gives strong evidence that the observed AVO anomalies correlate to the hydrocarbon saturations in the Tithonian sands shown by the C-78 well log.

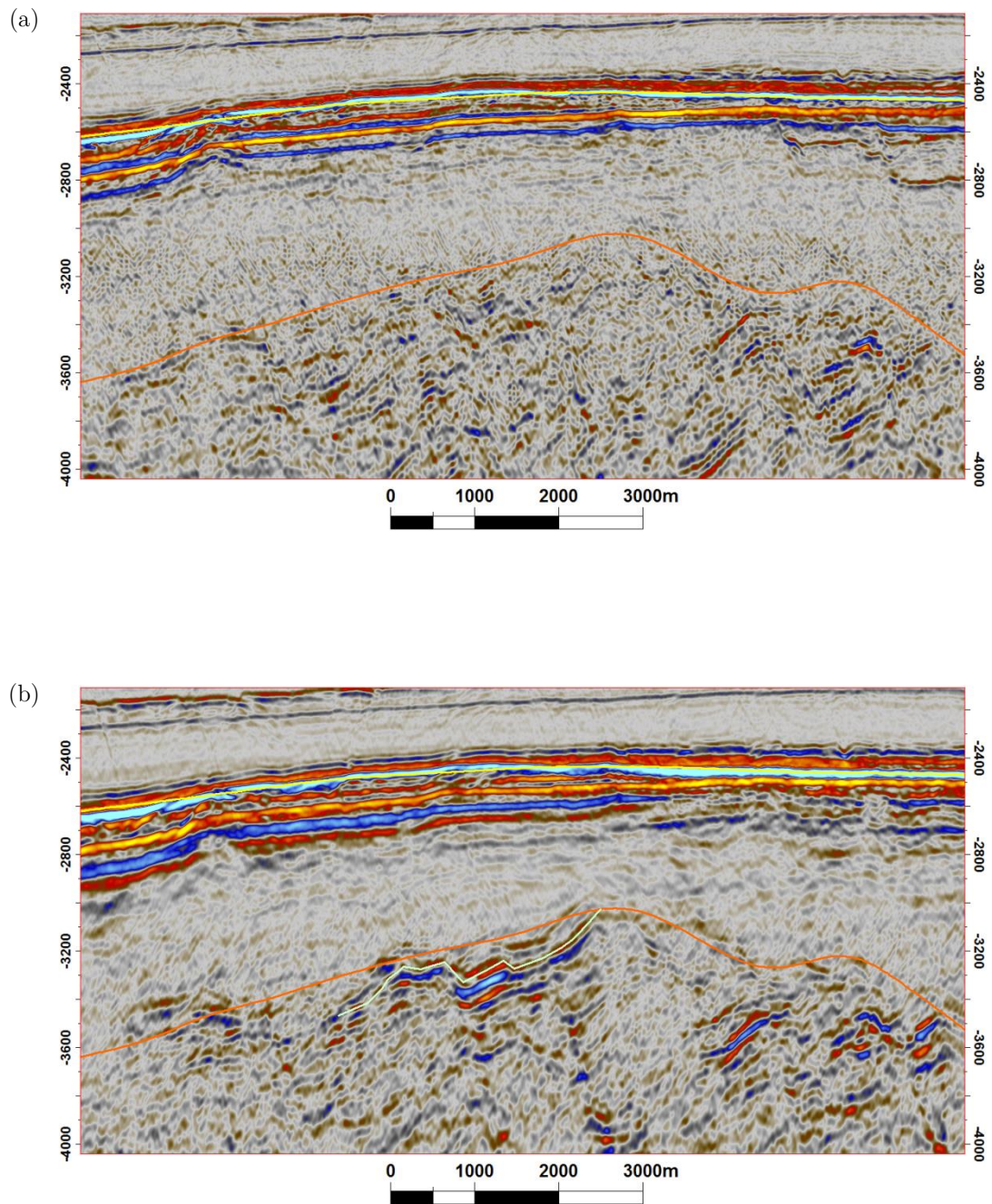


Figure 6.3: The (a) near angle stack and (b) far angle stack from *seismic line #1* in Figure 6.1 (data courtesy TGS and PGS). The yellow horizon is the base Tertiary, the orange horizon is the base Cretaceous, and the light-green horizon is the pick for the top of the Bay du Nord sand.

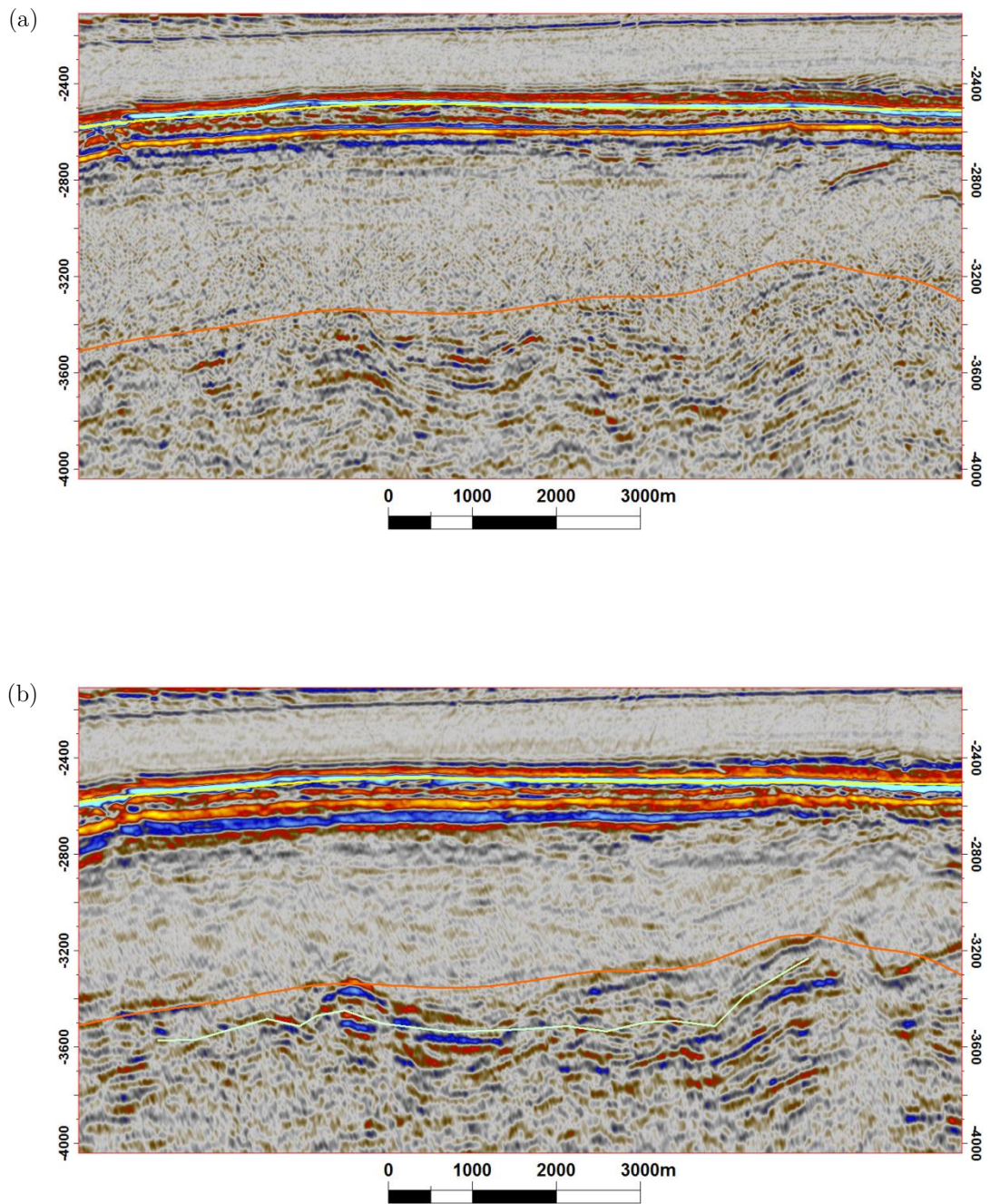


Figure 6.4: The (a) near angle stack and (b) far angle stack from *seismic line #2* in Figure 6.1 (data courtesy TGS and PGS). The yellow horizon is the base Tertiary, the orange horizon is the base Cretaceous, and the light-green horizon is the pick for the top of the Bay du Nord sand.

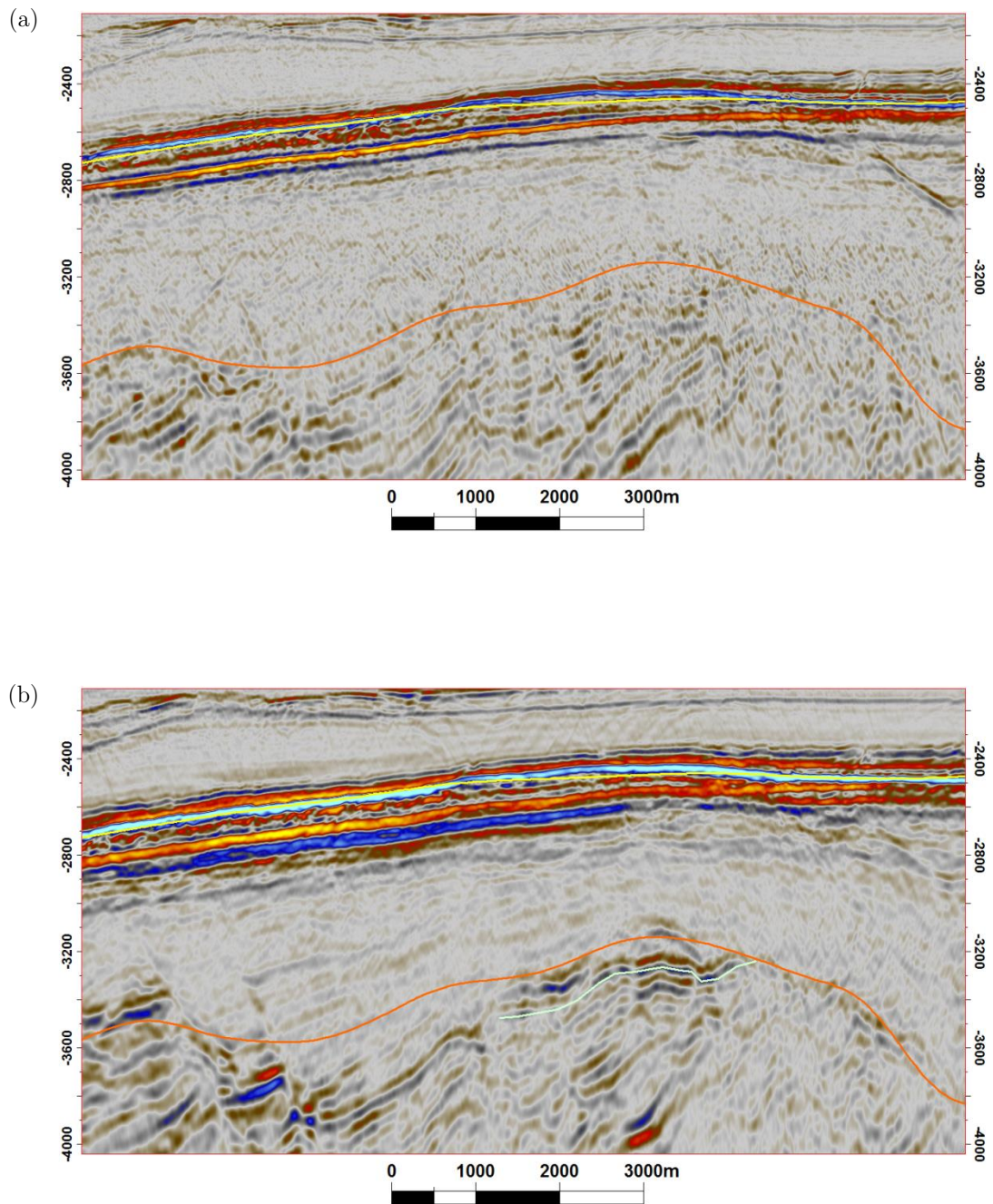


Figure 6.5: The (a) near angle stack and (b) far angle stack from *seismic line #3* in Figure 6.1 (data courtesy TGS and PGS). The yellow horizon is the base Tertiary, the orange horizon is the base Cretaceous, and the light-green horizon is the pick for the top of the Bay du Nord sand.

### 6.1.1 Motivation

The motivation behind this forward modeling study at Bay du Nord was similar to the Mizzen study, but with a slightly different approach. The improvement in data coverage facilitates the construction of a more complex model. More specifically, the seismic data coverage surrounding the Bay du Nord prospect allows the model representation of the reservoir to move far beyond simplistic slab approximations. Consequently, this chapter sought to show that the finite-element forward modeling technique would continue to successfully simulate mCSEM data from a complex model containing a far more complicated representation of the reservoir. The practical purpose of this study, however, contains a far different motive than the Mizzen study. Recall that the reservoir potential at Mizzen L-11 contained a sense of ambiguity because the well log primarily hit wet sands and the only hydrocarbon indicator was the AVO anomalies up-dip from where the well was drilled. The reservoir potential at Bay du Nord is far more certain based on the success of the C-78 well and the supporting evidence from the seismic data. Therefore, a forward modeling study centered on assessing the reservoir potential in the Bay du Nord field is likely *redundant*. Instead, the practical motivation for this study is to show that a *more detectable sensitivity exists* for a more economically sized reservoir.

## 6.2 Preliminary 1D modeling

Again, before any 3D modeling was performed it was important to revisit 1D modeling in order to understand how the sensitivities of the Bay du Nord sands may be different than what was encountered at Mizzen. The well log for C-78 was blocked to determine the resistivities of each region. Again, this was a straightforward process and the Tertiary, Cretaceous, and Jurassic regions were assigned horizontal resistivities of 1.4  $\Omega\text{m}$ , 2.0  $\Omega\text{m}$ , and 3.5  $\Omega\text{m}$  respectively. A higher resistivity of 500.0  $\Omega\text{m}$  was used for the basement (a discussion as to why is given later in Section 6.7). The two reservoir sands in C-78 contained varying degrees of resistivity values, so an average value of 100  $\Omega\text{m}$  was used. The depths to the various horizons could also be interpreted from the C-78 well log. However, what cannot be determined from the well log is depth to the seafloor and the basement. Both of these depths were interpreted off of seismic line #1 because the C-78 well was closest to this seismic line (Figure 6.3 is zoomed in too far to be able to see the horizons for the seafloor and top basement). The resulting 1D resistivity model is shown in Figure 6.6 where the Tertiary, Cretaceous, and Jurassic are indicated as horizontal resistivities because they were determined from the well-log, (a measure of  $\rho_h$ ). 1D in-line marine CSEM data was simulated from the model shown in Figure 6.6 at three different frequencies with the transmitter placed 32m above the seafloor ( $z = -1140\text{m}$ ). Data was simulated with the two reservoirs containing hydrocarbons as indicated in the 1D model, but data was also simulated with the two reservoirs assigned the background resistivity of the Jurassic for normalization purposes. The reservoir sands in the second response were not

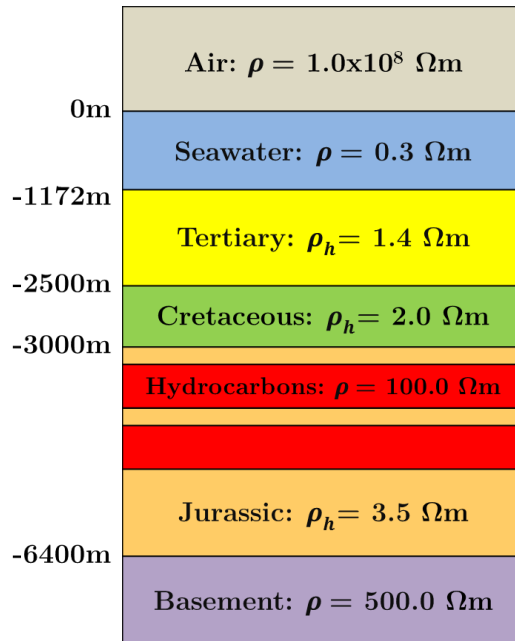


Figure 6.6: The 1D resistivity model from blocking the Bay du Nord C-78 resistivity log and assigning resistivity values to each region. The C-78 well did not reach the basement, so a reasonable value was assumed.

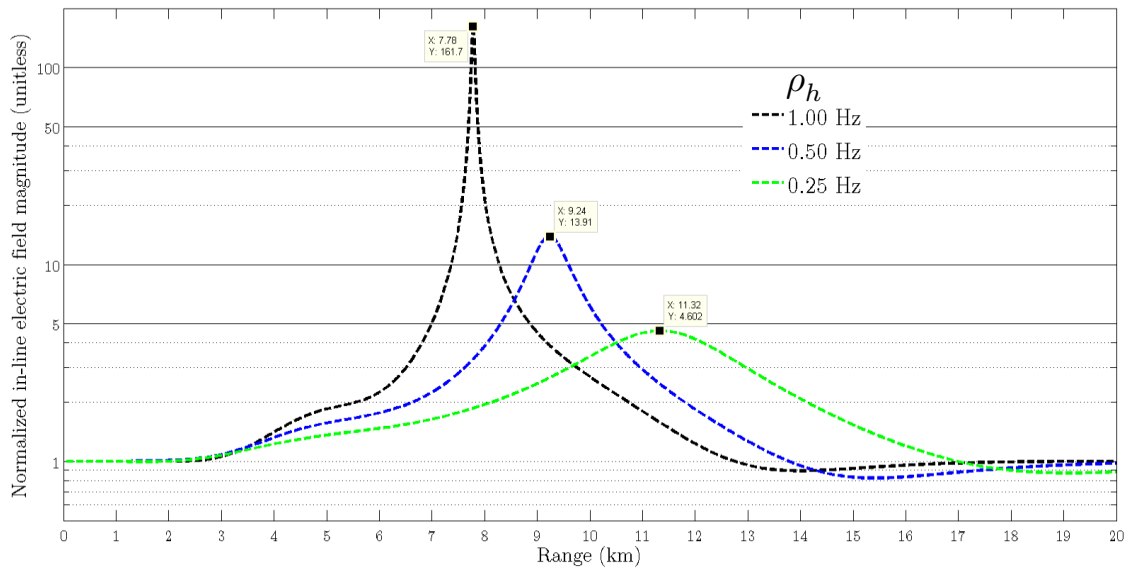


Figure 6.7: The sensitivity curves for the 1D model given in Figure 6.6 at three frequencies. The 1D mCSEM data was synthesized using DIPOLE1D (Key, 2009) and the sensitivities were calculated by normalizing the in-line amplitude reservoir response to the background response.

assigned a value of a brine saturated sand (like what was done for the Mizzen study) because the C-78 well had no evident brine saturations in the sands; therefore, just a background resistivity was used. The reservoir response was normalized to the background response for the three different frequencies and the corresponding sensitivity curves are shown in Figure 6.7.

These sensitivities from the 1D Bay du Nord model show a distinguishable increase over those from the 1D Mizzen model (Figure 5.7b). The maximum sensitivities for the Mizzen model were 12.7, 2.4, and 1.4 for the frequencies of 1.00, 0.50, and 0.25 Hz respectively, whereas the maximum sensitivities from the Bay du Nord model are 161.7, 13.9, and 4.6 for the frequencies of 1.00, 0.50, and 0.25 Hz respectively. This increase in sensitivity is attributed to many factors. First, the reservoirs at Bay du Nord are slightly shallower (the base Cretaceous is nearly 300m shallower) than the reservoir at Mizzen. Secondly, the Bay du Nord reservoirs are thicker and localized to two sand bodies instead of three, and the overall sand thickness is greater at Bay du Nord (100m of sand versus 90m). Lastly, the horizontal resistivity of the Jurassic was determined to be slightly less at Bay du Nord compared to Mizzen (3.5  $\Omega$ m versus 4.0  $\Omega$ m). In summary, all three of these factors seem to account for the relative increase in 1D sensitivity observed at Bay du Nord. However, in reality, the sensitivities in 3D will likely be much less and this was shown by the Mizzen study. The real test is to determine if these different conditions at Bay du Nord cause the finite-element forward modeling technique to detect a larger and more measurable sensitivity in three dimensions than what was seen for the Mizzen study.

## 6.3 3D Model Building at Bay du Nord

### 6.3.1 Establishing the VOI

The first step of building the 3D model (as discussed in Section 3.1) at Bay du Nord was obtaining and creating the necessary *inputs* for the model. The measured data played an important role in building the model and establishing the size of the VOI. Three 2D seismic lines surrounding the Bay du Nord prospect (see Figure 6.1) and the finite-difference inversion of the measured mCSEM data from EMGS were later used to construct the 3D reservoir body.

Similar to the Mizzen model, the VOI of the Bay du Nord model was determined based on the frequencies considered, the background resistivities, and the extent of the measured mCSEM data. The choice for the boundaries of the VOI in the Mizzen study appeared to be sufficient because no evidence of boundary condition issues (i.e. residual norm would not decrease as much and the computed fields would not be as accurate) was found. Consequently, the VOI at Bay du Nord was determined using the same approach.

First, this forward modeling study is considering the same frequencies as the Mizzen study (0.25, 0.50, and 1.00 Hz). The background resistivities increase with depth which complicates the calculation of skin depth, so once again for simplicity, the most resistive background layer (Jurassic) was used. The average longitudinal resistivity of the Jurassic at Bay du Nord is also similar to what was observed at Mizzen. So, using the lowest frequency of 0.25 Hz, the largest skin depth would amount to  $z_{0.25Hz} \approx 2000\text{m}$ . Once again, to satisfy the zero boundary condition the

boundaries of the VOI should be roughly 8-10 skin depths away from the source. However, as Figure 6.1 shows, this study is considering many receivers (or many computational sources after reciprocity is taken into account) and the boundary conditions need to be satisfied at *each one of these locations*. The boundaries for x-axis and y-axis were chosen such that 8-10 skin depths could extend from the western-most, northern-most, eastern-most, and southern-most CSEM receivers. The boundaries for the z-axis were repeated from the Mizzen model. As a result, the VOI of the Bay du Nord model was determined to be  $x = [0 \text{ km}, 50 \text{ km}]$ ,  $y = [0 \text{ km}, 60 \text{ km}]$ , and  $z = [-20 \text{ km}, 20 \text{ km}]$  with Bay du Nord C-78 roughly located in the center. The boundaries for the y-axis were a bit larger than the x-axis because there are more receivers spanning North-South than there are spanning East-West.

### **6.3.2 Geochronologic surfaces**

The next critical component of the model building process was establishing the same geochronologic surfaces used in the Mizzen study. All four surfaces (seafloor, base Tertiary, base Cretaceous, base Jurassic) were created by employees of Nalcor Energy through interpolating horizon picks on many 2D seismic lines (for more information, refer back to Section 3.1.1). The lateral extents of all the surfaces were cropped such that they matched the lateral extents of the VOI. These surfaces were represented in Petrel with a grid spacing of 100m which is too dense for modeling purposes. Therefore, each of the surfaces was down sampled to contain a 1000m node spacing. The choice for 1000m node spacing is verified by observing if the nodes at this spacing can capture the necessary topography changes in each surface.

The first surface is the seafloor and a topographic map of this surface is shown in Figure 6.8. Towards the east of this surface is the Flemish Cap and the deeper valley through the center of the surface is the Flemish Pass. The estimated lateral extent of the Bay du Nord reservoir is superimposed on the surface (red polygon) to show that its lateral location is indeed in the center of the model. Again, the seafloor topography in the Flemish Pass is relatively flat. In fact, as a whole, the topography of the seafloor is slowly varying, so this surface can be easily represented with a 1000m node spacing.

The second surface is the base Tertiary and a topographic map of this surface is shown in Figure 6.9. Towards the east, this surface is becoming shallower because it is approaching the Flemish Cap. Upon inspection, this surface is also quite simple as it appears at some level to be a plane dipping towards to the WNW. A similar observation was seen for the base Tertiary surface surrounding the Mizzen prospect (Figure 5.15) and given the proximity of these two fields, as shown in Figure 6.1, it seems intuitive that the base Tertiary at each field is similar. The simple and slowly varying nature of this surface means it can be easily represented with nodes spaced at 1000m.

The third surface is the base Cretaceous and a topographic map of this surface is shown in Figure 6.10. An important observation of this surface is that the Bay du Nord lateral extent is situated in a *Jurassic high*. This matches the observations of the three seismic lines surrounding Bay du Nord. After all, the base Cretaceous

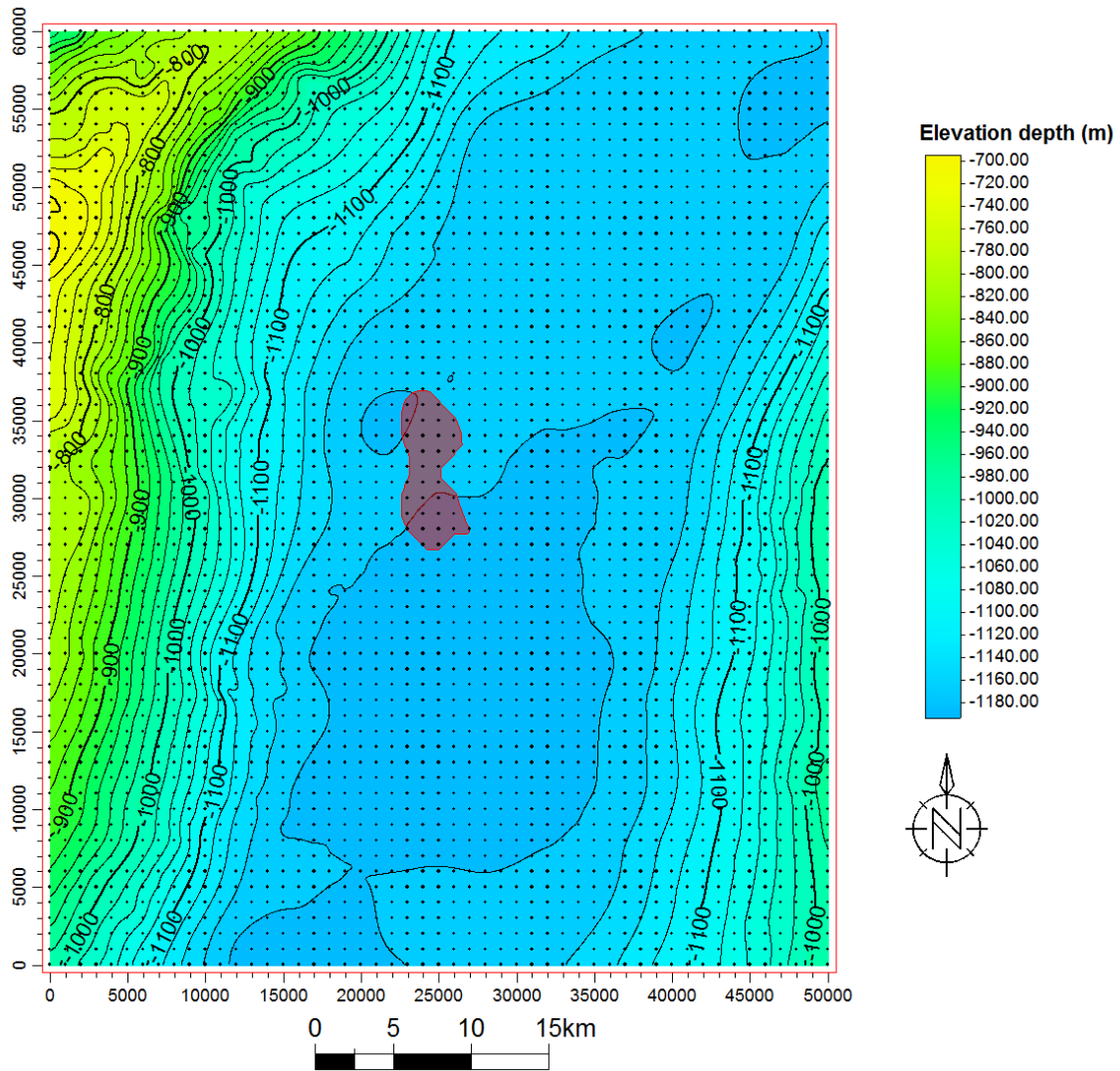


Figure 6.8: The topographical map of the seafloor surrounding Bay du Nord. The black dots are the 1000m spaced nodes used to represent the surface for modeling purposes. The red polygon is the estimated Bay du Nord reservoir extent shown for reference. Contour interval = 20m.

surface is *derived* from the 2D seismic lines so it seems logical that these two pieces of information are consistent. The base Cretaceous is certainly far more complex than the previous two surfaces with isolated topographic highs and lows. Despite the inherent complexity of the base Cretaceous, the superimposed 1000m spaced nodes on the surface appear to still represent the surface well. Even though there

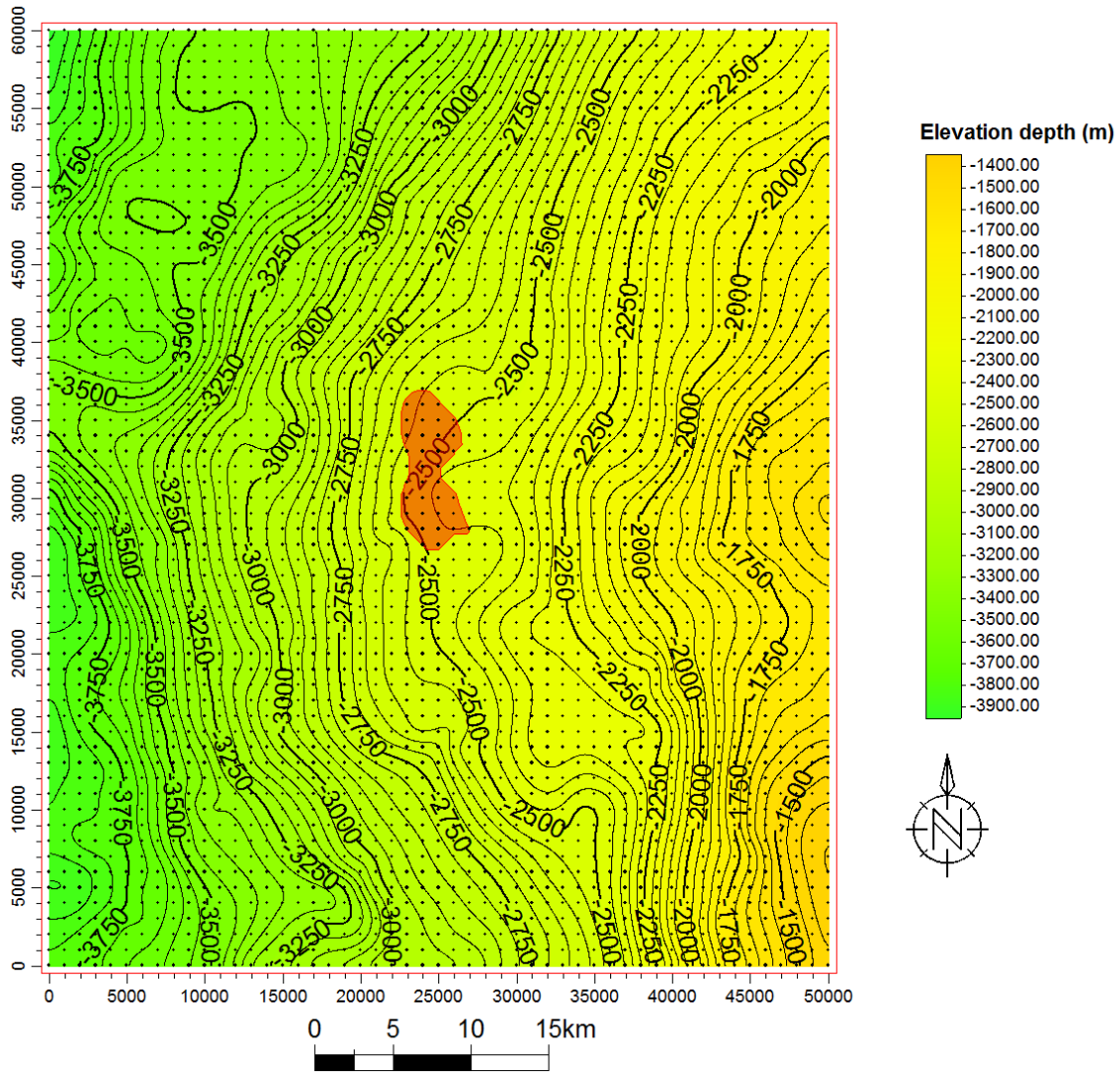


Figure 6.9: The topographical map of the base Tertiary surrounding Bay du Nord. The black dots are the 1000m spaced nodes used to represent the surface for modeling purposes. The red polygon is the estimated Bay du Nord reservoir extent shown for reference. Contour interval = 50m.

are areas with topographic highs and lows, they are formed over distances greater than a few kilometres and multiple nodes will be able to capture the necessary elevation changes. The only place on this surface that the 1000m spaced nodes may fail to represent accurately is the Jurassic high in the north-eastern part of the surface (this is actually where the Harpoon field is located).

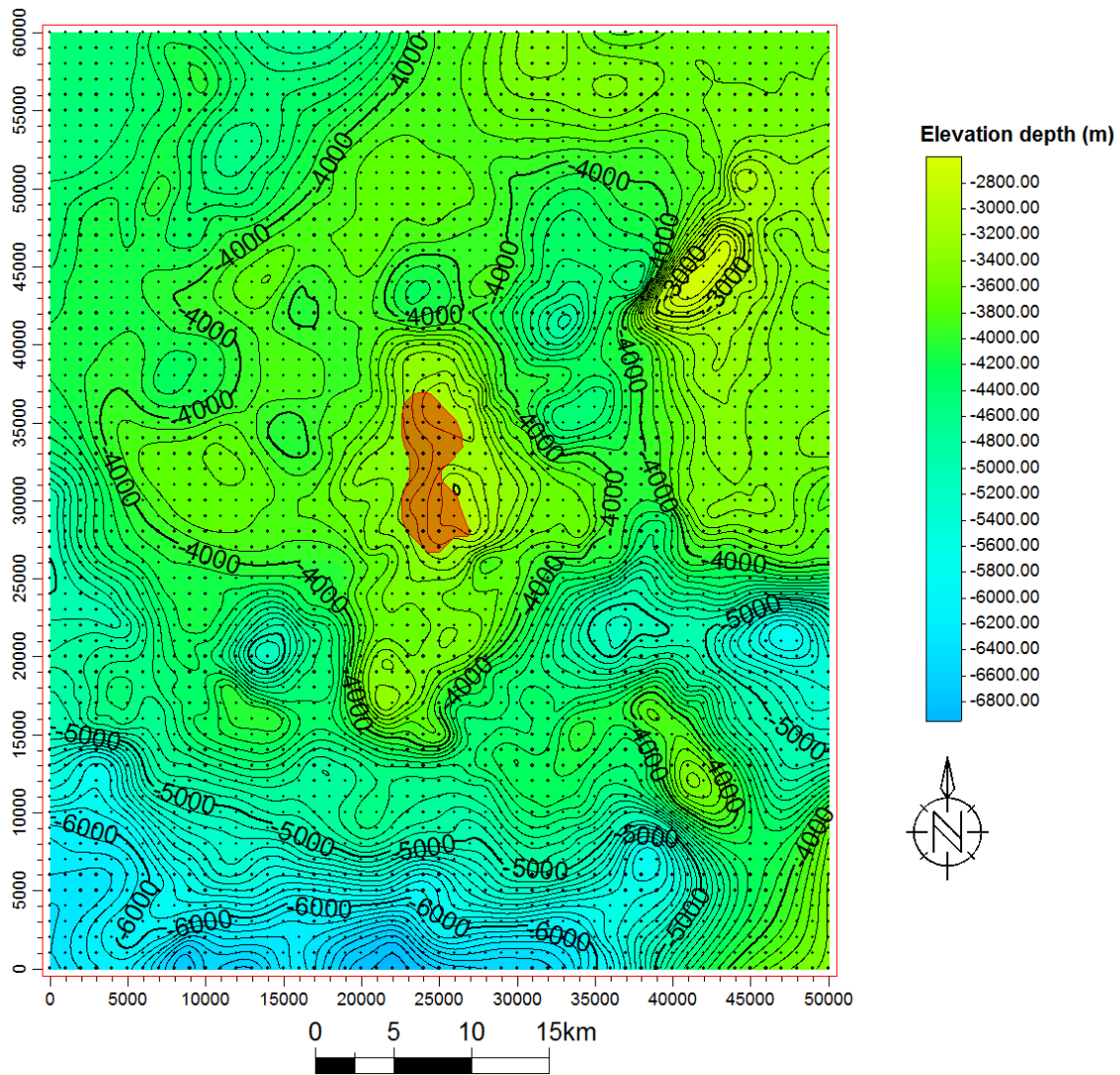


Figure 6.10: The topographical map of the base Cretaceous surrounding Bay du Nord. The black dots are the 1000m spaced nodes used to represent the surface for modeling purposes. The red polygon is the estimated Bay du Nord reservoir extent shown for reference, and the reservoir appears to be situated in a Jurassic high. Contour interval = 100m.

There are areas surrounding this Jurassic high that have very steep grades and nodes 1000m apart will likely not be able to capture this change. However, this Jurassic high is outside the Bay du Nord area of interest, and a small degree of misrepresentation that far away will likely have a negligible effect on the computed results surrounding Bay du Nord.

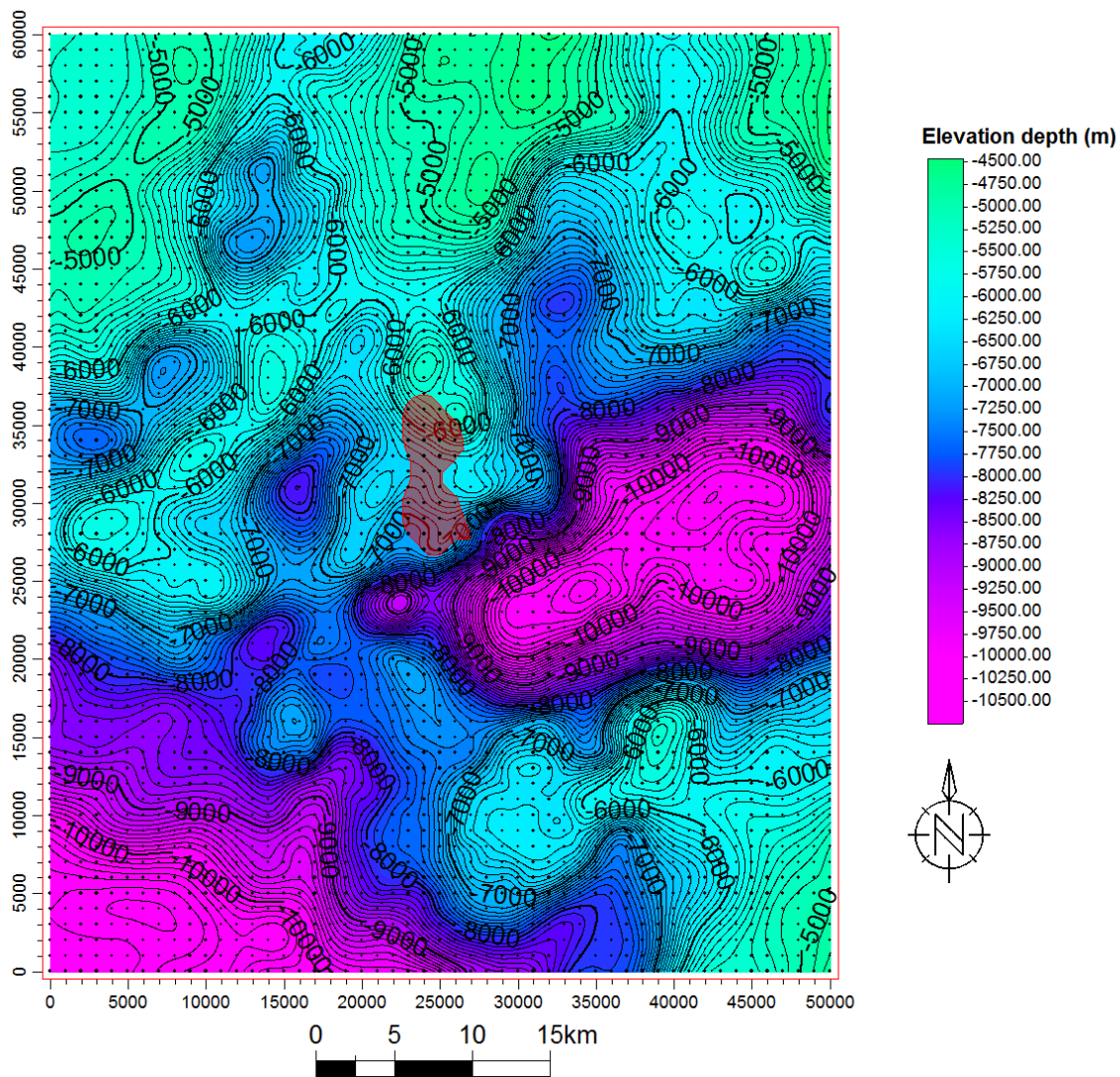


Figure 6.11: The topographical map of the base Jurassic surrounding Bay du Nord. The black dots are the 1000m spaced nodes used to represent the surface for modeling purposes. The red polygon is the estimated Bay du Nord reservoir extent shown for reference. Contour interval = 100m.

The fourth and final surface is the base Jurassic (basement) and a topographic map of this surface is shown in Figure 6.11. It seems that the elevation of the base Jurassic surrounding Bay du Nord is neither high nor low. Recall that there was a basement topographic high surrounding the Mizzen prospect, but the elevation of the basement at Bay du Nord is 1-2 km deeper compared to Mizzen. The two

implications of having a deeper basement at Bay du Nord are (1) that the influence of the basement on the computed results will be pushed to further offsets and (2) its contribution to the total field at those far offsets will likely be smaller as a consequence of skin depth. Even though there are areas with topographic highs and lows, they are formed over distances greater than a few kilometres and multiple nodes will be able to capture the necessary elevation changes. Consequently, using nodes spaced at 1000m should be adequate in representing this surface.

### **6.3.3 Incremental mesh generation**

The next step is taking these four geochronologic surfaces and building models, and subsequently generating meshes from those models. The details of how each incremental model and mesh is made are not discussed because the exact same modeling building (and meshing) processes were repeated from the Mizzen study. Instead, a collective summary is given highlighting the important details.

Similar to the Mizzen study, each of these surfaces is added to the model incrementally with a mesh created at each step in order to isolate the root causes of any meshing errors. As a result, there are four distinct models containing one to four surfaces (seafloor, base Tertiary, base Cretaceous, and base Jurassic models respectively). As the surfaces were incrementally added to the model, they were inspected in FacetModeller and there appeared to be no regions with a small thickness (e.g. like the areas where the Cretaceous was thin for the Mizzen study). Therefore, imposing the meshing constraints on the surfaces in each model and subsequently creating a mesh from each model would be quite simple. The same

500m edge length constraints imposed on the nodes representing the surfaces in the Mizzen study are repeated here.

The surfaces are the primary components of building the model, but the transmitter and observation locations need to be established before any test simulations can be performed. The Mizzen study used one synthetic transmitter-receiver pair in the center of the mesh for testing purposes, but instead, this study went ahead and created observation locations surrounding one of the EMGS receivers near Bay du Nord. Observation location refinement nodes were created to surround RX15 and they trended from the receiver to the northwest so they would pass over the prospect. The observation locations were chosen to have a 200m spacing and span a total range of 14 km. Again, the nodes created for the tetrahedra enclosing the observation locations were chosen so the resulting edge lengths after meshing would be 5m (this was exactly the same process from Section 5.5.6). Similar to what was shown in Section 5.5.4, the edge length constraint on the seafloor nodes surrounding the observation locations in the model was removed to avoid meshing problems.

Each of the models incrementally containing one to four surfaces was meshed and information about each mesh is given in Table 6-1. The switches used to create each mesh were all the same except the quality constraints imposed on the radius-edge ratio. The first two meshes used the generic value of 1.414, but the last two meshes used slightly higher values to reduce the number of cells in the mesh. The information in Table 6-1 shows the number of tetrahedra from each model, and as

Table 6-1: The TetGen switches and mesh statistics for each of the meshes generated from models incrementally containing one (seafloor model) to four (base Jurassic model) surfaces.

<b>Mesh Statistics</b>	TetGen switches	Mesh tetrahedra	Smallest dihedral angle	Largest aspect ratio	Percentage of poor cells
Seafloor model	-pq1.414/16	760,716	6.24	15.203	0.186%
Base Tertiary model	-pq1.414/16	1,065,259	5.51	15.976	0.206%
Base Cretaceous model	-pq1.48/16	1,249,481	3.02	26.819	0.250%
Base Jurassic model	-pq1.50/16	1,702,313	5.06	16.028	0.235%

expected, the number of cells increases when additional surfaces are included. The percentage of poor cells was fairly consistent between all four meshes, but there was a slight increase in the percentage of poor cells with the last two models compared to the first two models and this is likely a consequence of the last two models containing more complicated surfaces. A picture of the 3D mesh from the base Jurassic model is shown in Figure 6.12. The threshold slice is along the CSEM transmitter line #09 (see Figure 6.1) and the topography of the base Jurassic is easily observed. Figure 6.12 also shows that the regions do not contain any small thickness areas.

The information about each mesh (Table 6-1) and the quality of the meshes themselves (only the base Jurassic mesh is shown) indicate the meshes are suitable for test simulations to determine if the residual norm decreases sufficiently for each mesh. Figure 6.13 shows the decay of the residual norm for each of the four

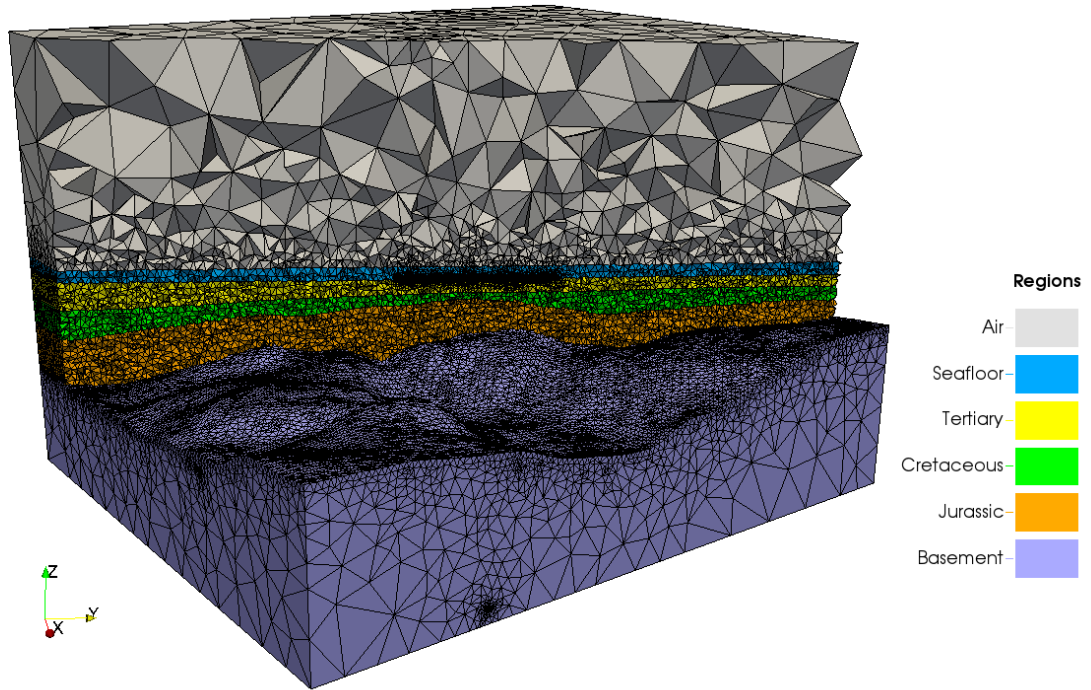


Figure 6.12: The 3D mesh of the base Jurassic model containing 1,702,313 cells. The threshold slice is along the mCSEM transmitter line #09. This slice shows that none of the layer thicknesses (e.g. Cretaceous) are thin, and the topography of the base Jurassic is easily observed.

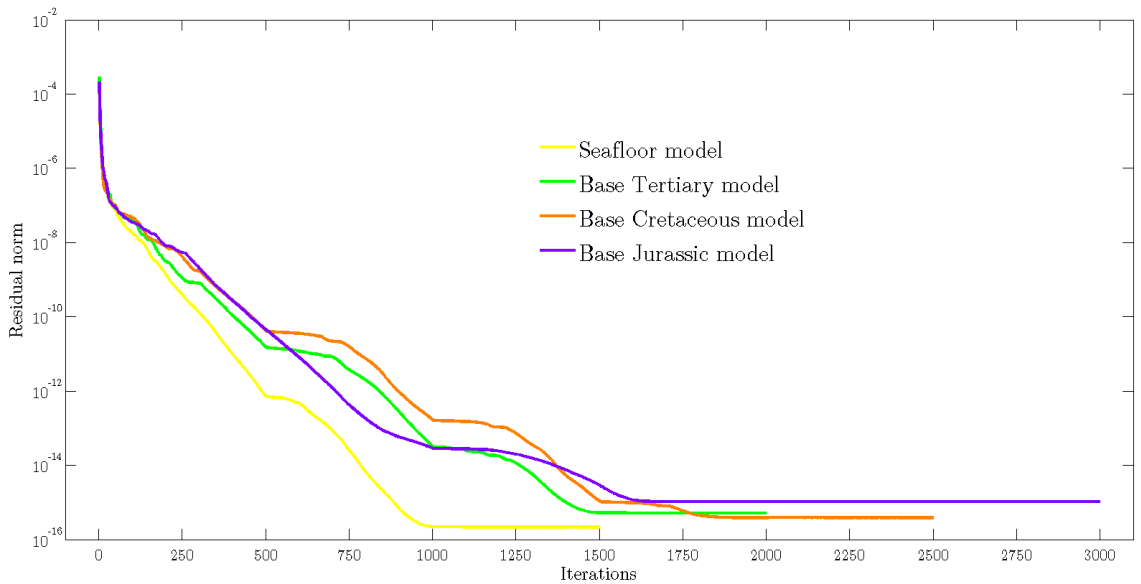


Figure 6.13: The decay of the residual norm for each of the meshes generated from models incrementally containing one (seafloor model) to four (base Jurassic model) surfaces. A Krylov subspace of 500 was used for the first three meshes and a Krylov subspace of 1000 was used for the base Jurassic model.

meshes. The simulations for the first three meshes were performed with a Krylov subspace of 500. However, the base Jurassic mesh used a Krylov subspace of 1000 to offset the increase in mesh size by trying to achieve a reduction of the residual norm in the same number of iterations as the previous meshes. Notice how the decay in the residual norm for each of the models is very good and the inclusion of surfaces only results in minor changes to the residual norm. These test runs show the meshes must be good quality and the final step for the model building process is including the 3D Bay du Nord reservoir body.

## 6.4 Building the Bay du Nord Reservoir Model

### 6.4.1 Creating the Bay du Nord surfaces

The previous section described how the models were incrementally built, eventually leading up to the base Jurassic model, or what would later become the *background model*. The final component of the model building stage is to construct the 3D body representing the Bay du Nord reservoir and include this body in the model. Creating the 3D reservoir body for Bay du Nord was much more involved than the reservoir body for Mizzen because the improvement in seismic data coverage over Bay du Nord permits the construction of a more complex model. The three pieces of data chosen to construct the Bay du Nord reservoir body are the (1) C-78 well log, (2) mCSEM inversion from EMGS, and (3) the three seismic lines surrounding the prospect.

The C-78 well log (Figure 6.2) was used to establish the *thickness* of the Bay du Nord reservoir body. There are two distinct sand bodies that each have a thickness of about 50m, but this chapter assumes there is only one sand body. In other words, the two 50m sand bodies are approximated as one 100m sand body. From a volume perspective, both scenarios are equivalent, except one sand body is easier to model compared to two.

The next stage in building the reservoir body is establishing the *lateral extent*. The only information available to the Mizzen study regarding the lateral extent of the reservoir was the polygon provided by Statoil. However, it did not seem appropriate to build this vital piece of the model on intangible data, and therefore,

a slab approximation was used. Statoil also provided a polygon for the Bay du Nord extent in the same quarterly website update in 2014, but once again it was decided not to use this information.

Luckily for this chapter, there is more data available that is appropriate for constraining the lateral extent. EMGS performed an inversion of their in-line and broadside mCSEM data using a time-domain finite-difference code (Wu et al., 2015). Only the inversion of the *in-line* fields is of interest because the recovered model is a solution for  $\rho_v$ . Their inversion of the broadside fields is a solution for  $\rho_h$  which has little sensitivity to laterally extensive resistors. A depth slice of the  $\rho_v$  inversion in the area of Bay du Nord C-78 is shown in Figure 6.14(a) with the polygon from Statoil given for reference. The color scale is set to red representing high resistivity and blue representing low resistivity. There is clearly a resistive anomaly in the area surrounding the well. The reservoir is not flat, so the resistive anomaly cannot be seen on one slice alone. Multiple depth slices were used to determine the extent of the resistive anomaly and a *new polygon* that collectively represents the extent of these resistive anomalies is shown in Figure 6.14(b). Notice how the red polygon encapsulates the strongest part of the resistivity anomaly. The blue polygon from Statoil is again shown for reference in Figure 6.14(b) and notice that the resistivity anomaly from the inversion does not have a particularly good match to Statoil's polygon.

The previous two pieces of data established the thickness and lateral extent of the Bay du Nord reservoir body, and the final remaining task is to determine the

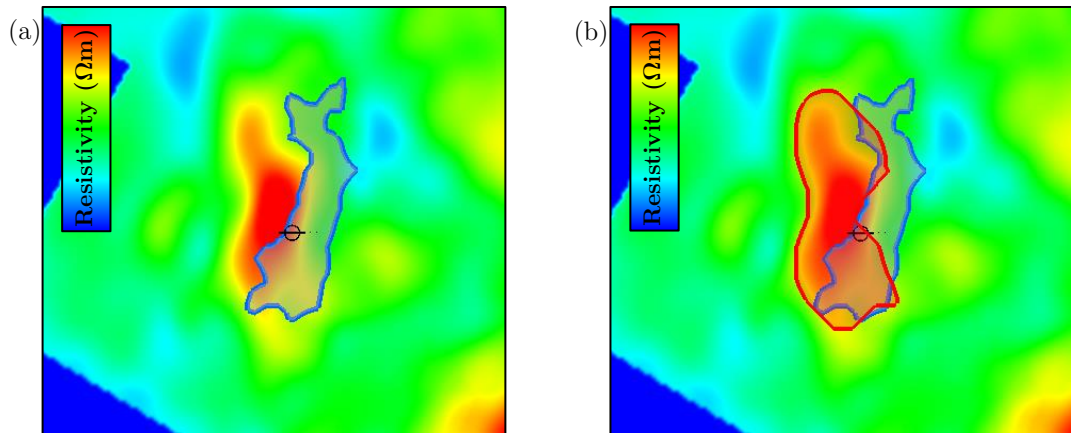


Figure 6.14: (a) A depth slice of the in-line mCSEM inversion from EMGS, and (b) the same depth slice showing the interpretation of the Bay du Nord lateral extent with the red polygon. The blue polygon depicting the Bay du Nord reservoir extent (from Statoil’s quarterly website update in 2014) and the well symbol for Bay du Nord C-78 are shown for reference.

structure, or *topography* of this reservoir body. This was accomplished through seismic data interpretation. The Mizzen study only had one seismic line, so there was not enough information to determine the 3D nature of those reservoir sands. However, there are **three** seismic lines surrounding Bay du Nord C-78 (see Figure 6.1) that lie within the predicted lateral extent of the reservoir determined above.

The topography of the Bay du Nord reservoir was constrained by picking horizons on each of these seismic lines. The oil discoveries in C-78 match well in depth with the bright amplitudes in the far angle stack of seismic line #1 (Figure 6.3b). Therefore, horizons were picked on the far angle stacks for each seismic line to represent *the top of the reservoir sand*. These horizons are shown by the light-green lines in each of the far angle stacks. However, these three horizons only provide topography information for three lines within the Bay du Nord extent; there are obviously many topography points missing throughout the rest of the Bay du Nord extent. To solve this issue, an interpolation was performed in Petrel to *fill the*

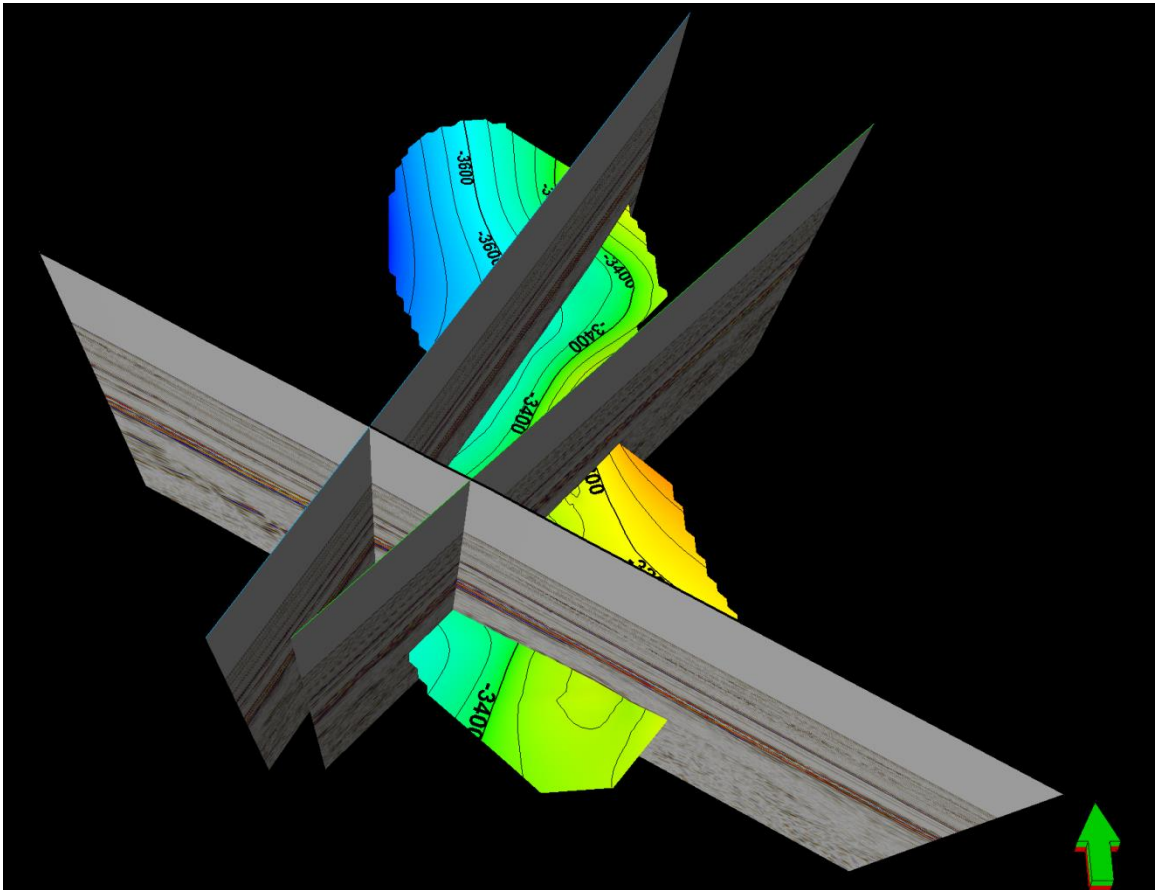


Figure 6.15: The top-of-sand surface for Bay du Nord. The topography of this surface is determined by picking horizons on the three seismic lines shown and interpolating within the Bay du Nord extent given in Figure 6.14.

*voids*. The red polygon in Figure 6.14 was the boundary for interpolation and the horizons from the three seismic lines were the input points. Using a grid spacing of 100m (mainly because the thickness of the resulting sand body will be 100m), an interpolation was performed and the top-of-sand surface is shown in Figure 6.15. This image from Petrel shows the top-of-sand surface passing through all three seismic lines and how it appears to have an element of topography. The *base-of-sand* surface was determined by simply translating the top-of-sand surface down 100m. This does assume, however, that the *thickness is constant* across the entire

sand body. Despite some of the assumptions made, using these three pieces of information permitted the construction of a complex 3D model. The top-of-sand surface shown in Figure 6.15 is far more complex than what was achieved in the Mizzen study (i.e. a dipping plane). The next step in the modeling process (Figure 3.2) is importing this reservoir body information from Petrel into FacetModeller and physically building the model.

#### **6.4.2 Assembling the Bay du Nord reservoir within FacetModeller**

The base-of-sand and top-of-sand surfaces were imported into Facetmodeller using the same process discussed in Section 3.1.2 for the geochronologic surfaces. After the sand surfaces were triangularized (the XYZ points meshed with triangles), they were added to the base Jurassic model (i.e. the background model). The interpolation of the sand surfaces appeared to extend them *beyond* the base Cretaceous surface in two areas. These two areas happen to be in proximity to seismic line #1 and #3 where the reservoir truncates on the base Cretaceous surface (see Figure 6.3 and Figure 6.5 where the green horizon stops at the orange horizon). However, the interpolation of the areas near these seismic lines continued an increasing trend and extended the reservoir surfaces beyond the base Cretaceous. This issue was fixed by simply removing the nodes and triangular facets on the portions of both surfaces that extended beyond the base Cretaceous. The *trimmed* reservoir surfaces within FacetModeller are shown in Figure 6.16 with a 5× vertical exaggeration to show detail. The small areas circled in green and yellow indicate the areas where the surfaces were trimmed in the vicinity of where

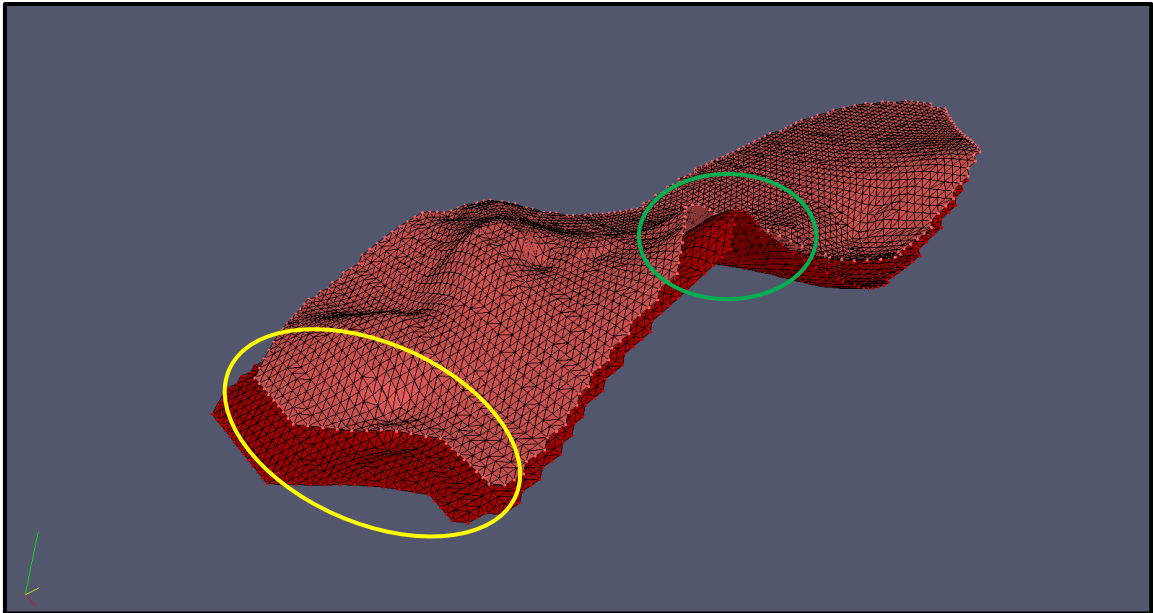


Figure 6.16: The top-of-sand and base-of-sand reservoir surfaces within FacetModeller at 5x vertical exaggeration. The areas circled in green and yellow indicate the areas where the reservoir surfaces are trimmed in the vicinity of where the top-of-sand horizon in seismic line #1 and seismic line #3 truncates on the base Cretaceous.

the top-of-sand horizon in seismic line #1 and seismic line #3 truncates on the base Cretaceous.

The seismic data clearly suggests that the Bay du Nord sand truncates on the base Cretaceous in two areas, but the model itself does not yet reflect this interpretation. Consequently, the sand surfaces should be attached to the base Cretaceous to match the seismic interpretation. At a high level, all that is required is adding facets to connect the nodes at the edge of the reservoir surface to nodes on the base Cretaceous in the two circled areas indicated in Figure 6.16. However, there is a complication because the reservoir surfaces contain 100m spaced nodes and the base Cretaceous contains 1000m spaced nodes. Therefore, connecting the reservoir surfaces to the base Cretaceous (in its current state) would result in

poorly shaped facets. The obvious solution is to modify the base Cretaceous surface to accommodate these areas where both reservoir surfaces would attach.

Attaching the reservoir surfaces to the base Cretaceous would be straightforward if the base Cretaceous surface contained nodes with 100m spacing in the attachment zones. Since the reservoir surfaces contain nodes spaced at 100m as well, this should allow well-shaped facets to connect the two surfaces. Recall from Section 6.3.2 that the surfaces from Petrel were originally created with a 100m node spacing. Nodes and facets surrounding the two attachment zones were removed from the base Cretaceous surface containing the standard 1000m spacing in order to subsequently accommodate the refined areas for attachment purposes. Nodes from the original base Cretaceous surface (spaced at 100m) were isolated in the two areas *precisely* where both reservoir surfaces (top and base) would physically attach to the base Cretaceous. This isolated set of nodes spaced at 100m was added to fill the two gaps on the base Cretaceous surface with 1000m node spacing. Additional nodes were added between the 100m and 1000m spaced nodes to create a *buffer zone*. A buffer zone allows the triangular facets to gradually grow from facets containing edge lengths of 100m to 1000m. This is important to ensure quality shaped facets on the surface.

The result of the new base Cretaceous surface is shown in Figure 6.17. Panel (a) shows the original base Cretaceous surface, and panels (b) and (c) show the modifications made to the surface in order to accommodate the attachment of the reservoir surfaces. The nodes marked in purple are the 100m spaced nodes with

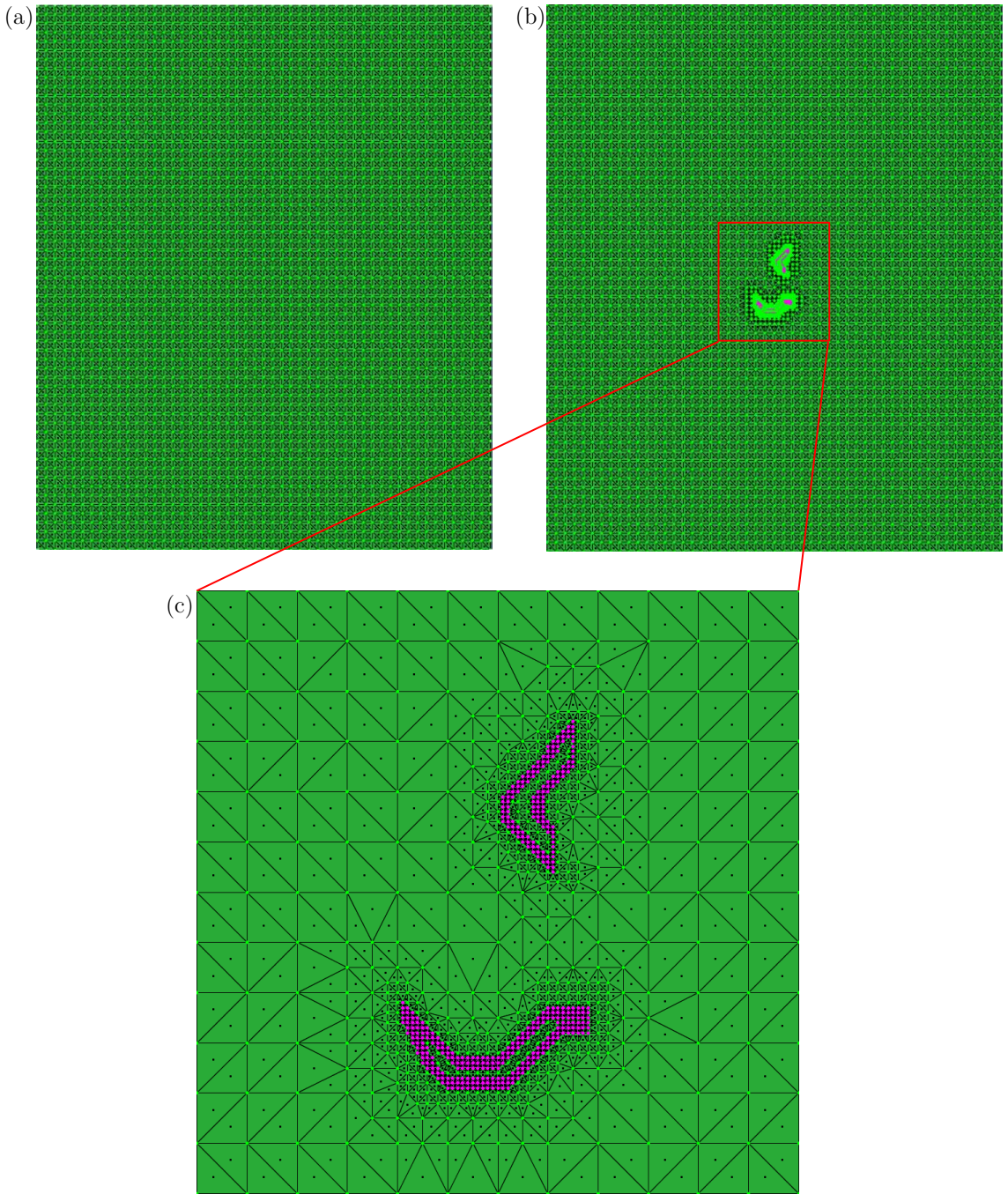


Figure 6.17: (a) The original base Cretaceous surface with no modifications. (b) The base Cretaceous surface with refinement modifications to accommodate the attachment of the two reservoir surfaces. (c) A zoomed in view of the modified base Cretaceous surface showing the attachment zones marked in purple and the buffer zones surrounding these areas. These two attachment regions correlate to the two circled areas in Figure 6.16.

purple facets connecting these nodes. These areas represent the exact regions where the two reservoir surfaces will attach to the base Cretaceous surface. Figure 6.17(c) also shows how the buffer zone allows the quality of the triangular facets surrounding the attachment zones to be maintained. This modified base Cretaceous surface replaced the original surface (Figure 6.17a) and the next step was attaching the reservoir surfaces to these zones marked in purple on the modified surface.

Triangular facets were manually added to attach the boundary nodes on the reservoir surfaces in the two regions circled in Figure 6.16 to the base Cretaceous nodes marked in purple in Figure 6.17. Figure 6.18 shows the facets used to connect the two reservoir surfaces to the base Cretaceous in the green-circled region indicated in Figure 6.16. The reservoir surfaces are marked in red, the base Cretaceous nodes for attachment are again marked in purple, and the facets used to connect each reservoir surface to the base Cretaceous are shown in tan. Notice how the facets marked in tan are well-shaped and had there not been nodes spaced at 100m on the base Cretaceous surface, these facets would be very poorly shaped (i.e. long and skinny). Figure 6.19 shows the facets used to connect the reservoir surfaces to the base Cretaceous in the yellow-circled region indicated in Figure 6.16. Similar observations are seen and the facets are once again well-shaped.

The last step in securely attaching the reservoir surfaces to the base Cretaceous is adding boundary facets between the top-of-sand and base-of-sand reservoir surfaces so the region is *enclosed*. Figure 6.20 shows the rectangular facets added along the boundary of the two sand surfaces to enclose the sand body. A vertical

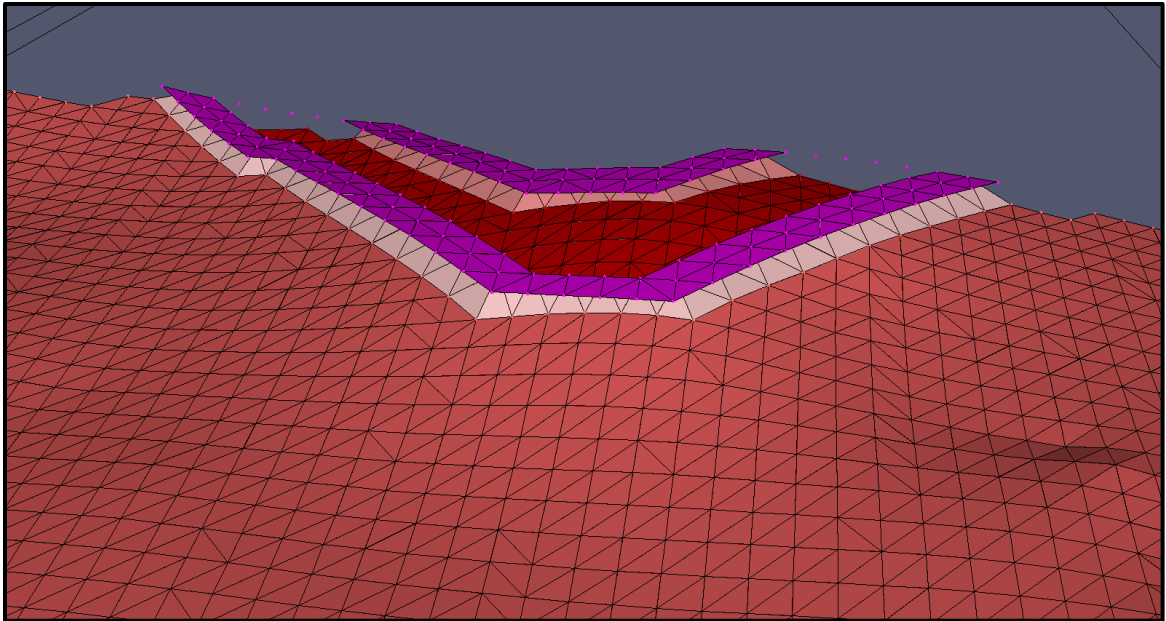


Figure 6.18: A view of the base-of-sand and top-of-sand surfaces in FacetModeller showing the facets used to connect the two reservoir surfaces to the base Cretaceous in the region circled in *green* from Figure 6.16. The connecting facets are colored tan.

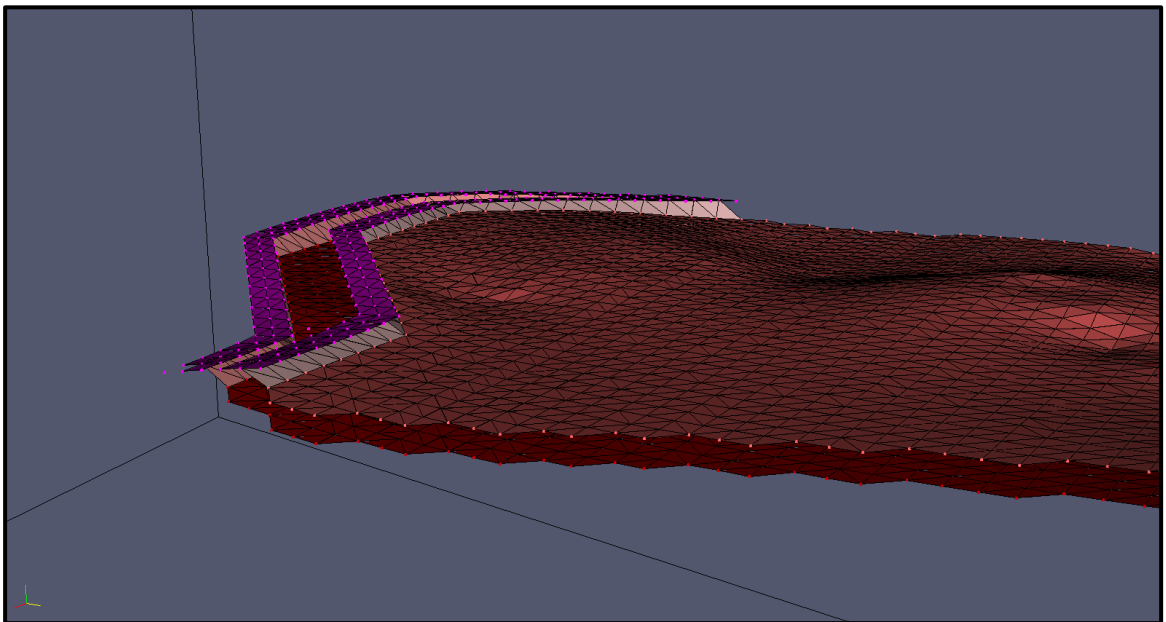


Figure 6.19: A view of the base-of-sand and top-of-sand surfaces in FacetModeller showing the facets used to connect the two reservoir surfaces to the base Cretaceous in the region circled in *yellow* from Figure 6.16. The connecting facets are colored tan.

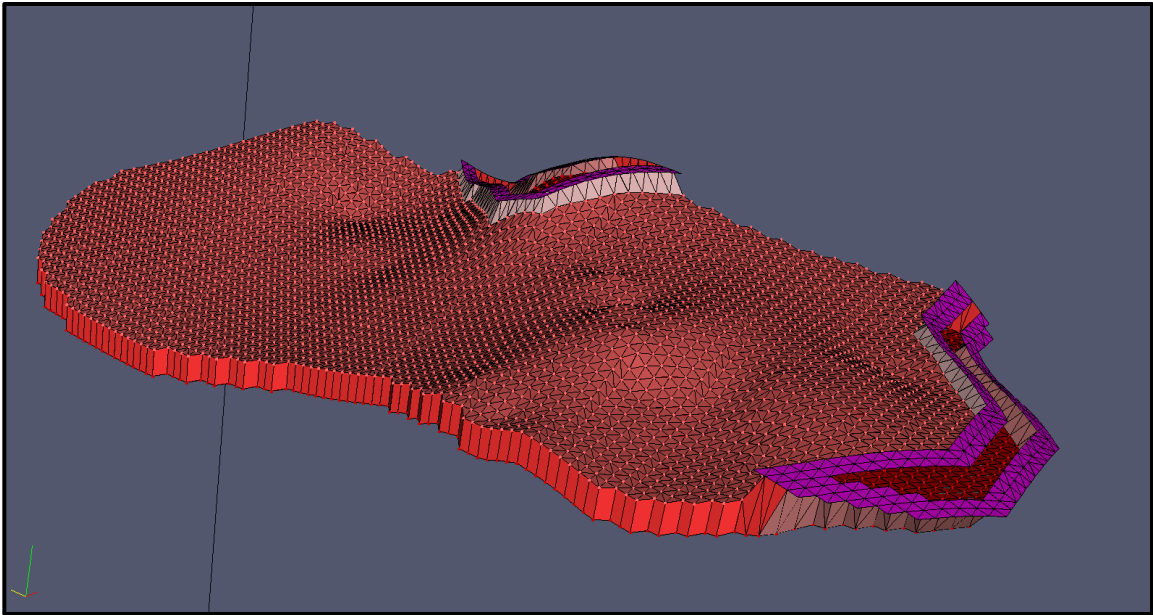


Figure 6.20: A view of Bay du Nord reservoir within FacetModeller. The bright red rectangular facets are the boundary facets enclosing the reservoir body, the tan facets are the connecting facets, and the purple facets are the facets on the base Cretaceous surface. A vertical exaggeration of  $3\times$  is used.

exaggeration of  $3\times$  is used in order to see both the boundary facets and the facets connecting the reservoir surfaces to the base Cretaceous. The facets may appear to be elongated and poorly shaped, but this is simply because the facets are stretched from the vertical exaggeration. In summation, the model shown in Figure 6.20 is able to reflect the interpretation of the seismic lines by truncating on the base Cretaceous and this was achieved through using efficient modifications to the base Cretaceous surface. At this stage, the model is complete and the next step in the modeling process is generating a mesh and performing a test simulation.

### 6.4.3 Bay du Nord reservoir mesh

Before a mesh could be generated from the model in Figure 6.20, the constraints on the model had to first be established. Recall from the previous model, the base Jurassic model, that the nodes on all four geochronologic surfaces contained a 500m edge-length constraint except for the nodes surrounding the observation locations on the seafloor surface. This same idea can be applied to this model containing the Bay du Nord reservoir body, but the constraints on the base Cretaceous surface require special attention. The nodes on the base Cretaceous surface just above the reservoir (i.e. the attachment and buffer zones) cannot have a constraint of 500m because the reservoir is shallow in some areas (actually touching the surface in two areas!) and the resulting mesh would contain poorly shaped cells in these areas. Therefore, the edge-length constraints on the base Cretaceous nodes above the reservoir body were completely removed in order to give TetGen freedom to add any necessary refinement. No constraints were given to the reservoir nodes either.

These edge-length constraints were reflected appropriately in the .mtr file and the Bay du Nord reservoir model was meshed using the following TetGen switches,

```
tetgen.exe -pq1.5/16AmfenCV BdN_reservoir_model.poly.
```

The resulting mesh contained: 2,853,440 cells, a minimum dihedral angle of  $0.86^\circ$ , a largest aspect ratio of 93.95, and a percentage of poor cells equating to 0.406% (11575/2853440). If the information from this mesh is compared to the base Jurassic mesh in Table 6-1, it appears the inclusion of the reservoir body has increased the number of cells in the mesh by over 1 million. This is an obscene

amount of cells coming from the reservoir body. There is also a slight increase in the percentage of poor quality cells (from 0.235% to 0.406%), but that is expected considering the complexity of the reservoir and the attachment regions.

Before any simulation tests are performed on this model, it is important to first inspect the mesh and ensure it is of good quality. Figure 6.21 shows a plan view of the base Cretaceous surface after meshing. The presence of the Bay du Nord reservoir body has created an obvious *imprint* on the base Cretaceous surface.

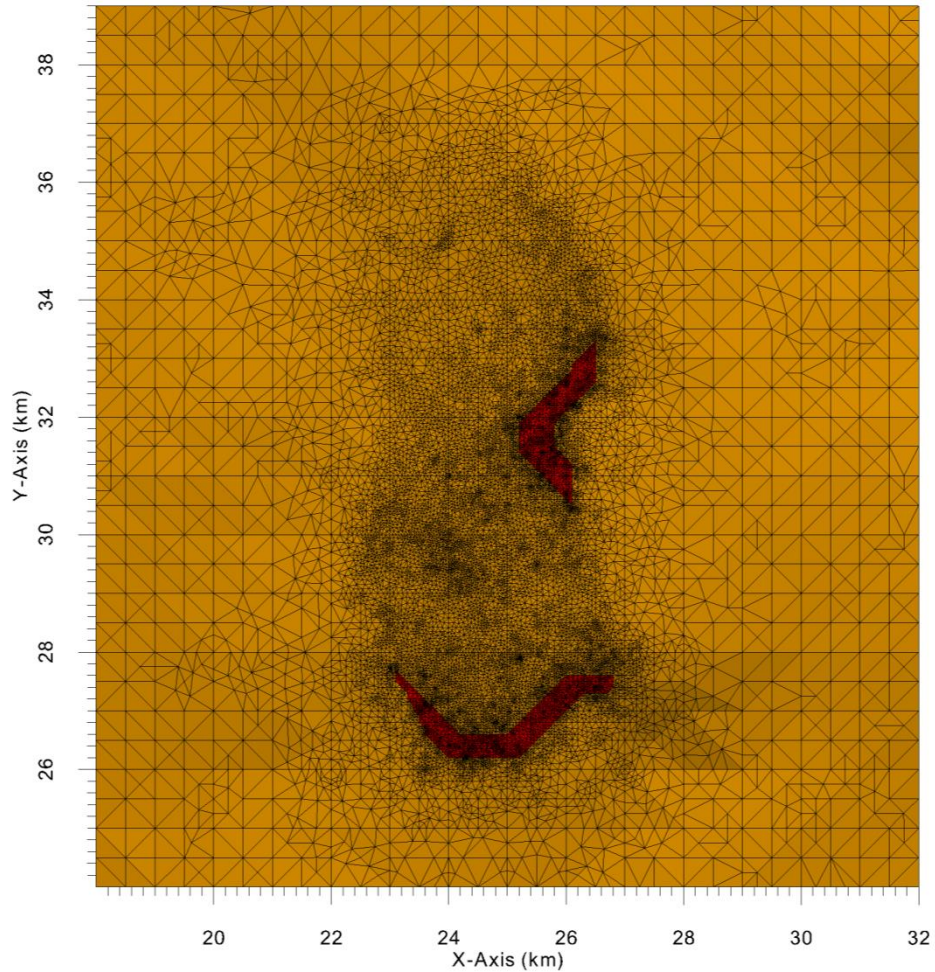


Figure 6.21: A zoomed-in plan view of the modified base Cretaceous surface after meshing. The refinement imprint on the surface appears to mimic the lateral extent of the Bay du Nord reservoir.

There appears to be the strongest degree of refinement in the two attachment regions and that is to be expected. The north-western part of the Bay du Nord reservoir deepens and explains why the refinement is not as dense in that area. As the cells on the surface progress away from the reservoir, the cells increase in size and the edge-length constraint of 500m is reintroduced. Figure 6.22 shows a 3D view of the mesh with a piece removed to show the internal structure of the mesh and the location of the reservoir body. Figure 6.23 is a 2D slice along the CSEM transmitter line #09 (see Figure 6.1). Notice how this slice cuts through both of the attachment regions and observe how the reservoir body attaches to the base Cretaceous in both of these regions. These inspections of the mesh indicate everything is consistent and the mesh appears to be ready for a test simulation.

A numerical simulation test was performed on this Bay du Nord reservoir mesh to determine if the residual norm decays by a sufficient amount to recover an accurate solution. The Krylov subspace has an upper bound of approximately 800 based on the size of this mesh and the available computational resources. The decay of the residual norm is given in Figure 6.24. It is obvious that this mesh did not converge and the residual norm only reduced by about four orders of magnitude. The residual norm for all of the previous meshes, building up to and including the base Jurassic mesh, decayed by over 10 orders of magnitude (see Figure 6.13). Therefore, the decay of the residual norm for the Bay du Nord reservoir mesh is not acceptable and there must be an underlying cause. The following section debugs the potential issues with this mesh and tries to *isolate* the factors causing this poor convergence.

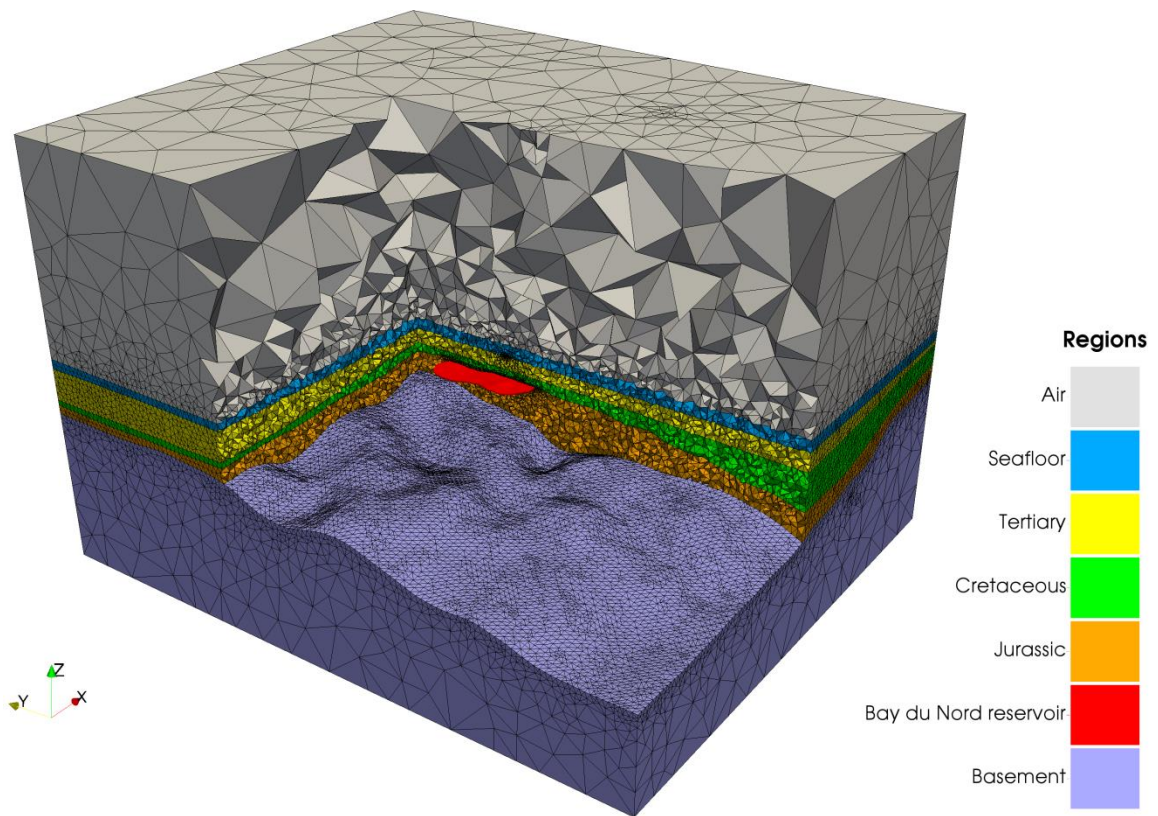


Figure 6.22: The entire 3D Bay du Nord reservoir mesh with a portion removed to show the internal structure of the mesh and the location of the reservoir body.

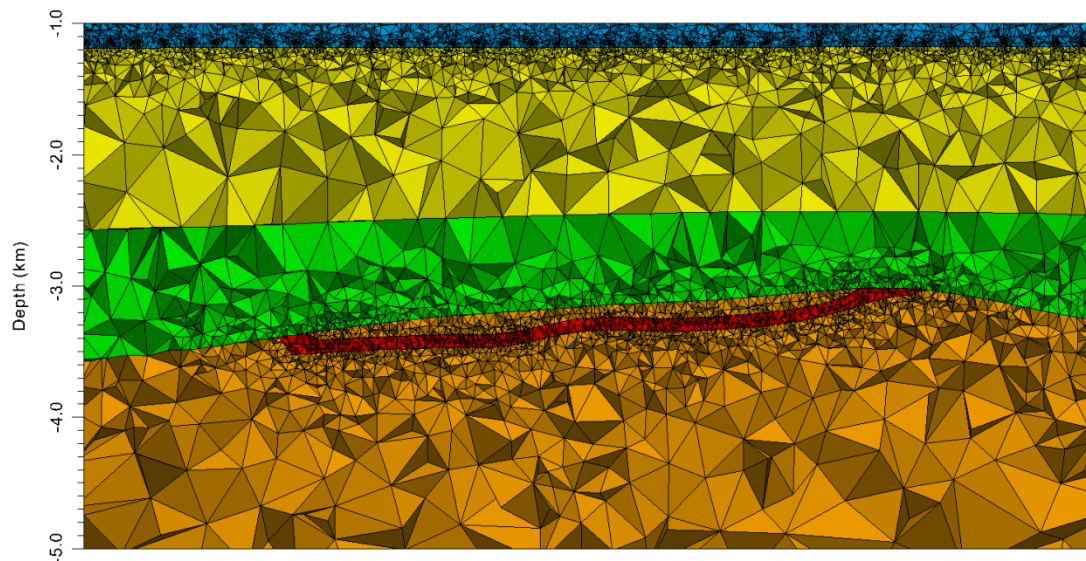


Figure 6.23: A 2D slice of the Bay du Nord reservoir mesh along the CSEM transmitter #9 and the observation locations trend northeast from RX15. This slice cuts through both of the attachment regions and the reservoir body is seen attaching to the base Cretaceous in both of these areas.

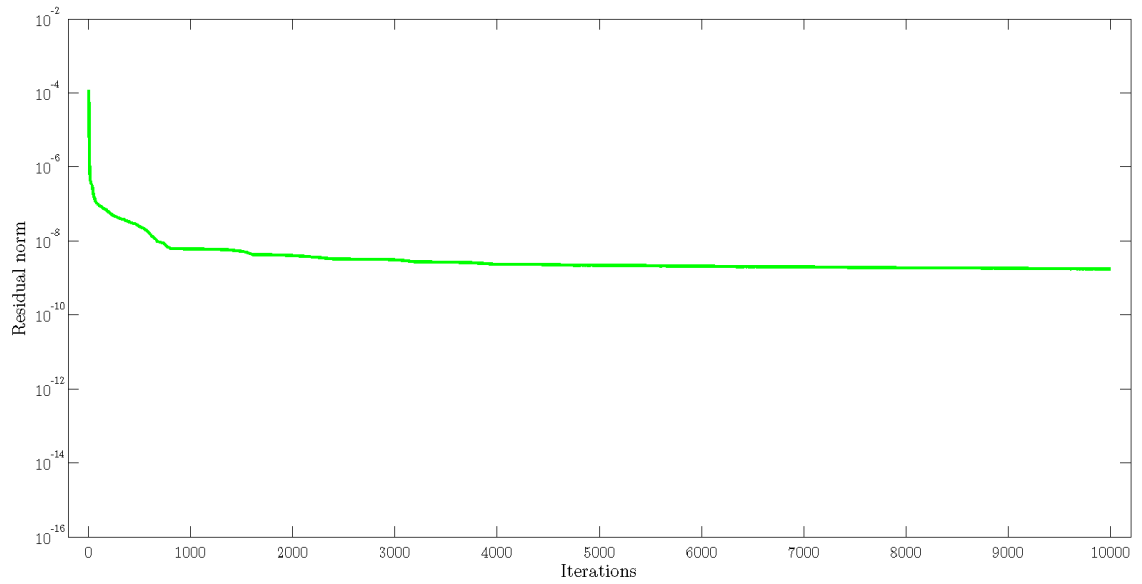


Figure 6.24: The residual norm of the Bay du Nord reservoir mesh using a Krylov subspace of 800. The decay of the residual norm is unsatisfactory and suggests improvements must be made to the mesh.

## 6.5 Debugging the Bay du Nord Reservoir mesh

The Mizzen study showed that quality data and convergence can be simulated from a simple reservoir model. Recall that the Mizzen reservoirs were represented as simple dipping slabs and they were located in the middle of the combined Cretaceous/Jurassic region (the base Cretaceous surface was not included). However, the Bay du Nord reservoir model built in the previous section has four levels of added complexity that the Mizzen reservoir model does not have:

- 1) the Bay du Nord reservoir lies just beneath the base Cretaceous,
- 2) the complex geometry of the reservoir,
- 3) the higher number of cells in the mesh, and
- 4) the Bay du Nord reservoir is physically truncating on the base Cretaceous.

Any combination of these four factors could be contributing to the poor convergence shown in Figure 6.24. Therefore, a series of tests was performed to isolate each of these factors and determine their impact on the decay of the residual norm.

### 6.5.1 Test I: Translation to the mid-Jurassic

The first test is aimed at isolating the second and third factors, but in order to do so, the influence from the first and fourth factors had to be removed. The Bay du Nord surfaces were translated vertically down 700m to remove any influence the reservoir would have on the base Cretaceous. The ‘attachment’ facets were also removed (no longer a surface to attach the reservoir surfaces to). In fact, the base-of-sand surface was the exact same as the top-of-sand surface, but shifted down 100m (this made the creation of boundary facets much easier). With the reservoir

shifted down, there is no longer a need to have refinement on the base Cretaceous surface and the original surface given in Figure 6.17(a) is used instead. As a result, the Bay du Nord reservoir is isolated in the Jurassic and subsequent simulations will only be dependent on the geometry of the reservoir and the number of cells in the mesh.

A mesh from this new ‘mid-Jurassic’ reservoir model was created using the same switches from the previous Bay du Nord reservoir model. The 500m edge-length constraints were imposed on all four surfaces (except for the nodes surrounding the observation locations on the seafloor) and no constraints were placed on the reservoir surface nodes. The resulting mesh contained 2,624,255 cells, a minimum dihedral angle of  $1.18^\circ$ , and a percentage of poor cells equating to 0.389% (10220/2624255). There is a reduction of about 200k cells from the reservoir body not being in close proximity to the base Cretaceous. Figure 6.25 shows a 2D slice of the mesh along the CSEM transmitter line #9. Notice how the placement of the reservoir body in the mid-Jurassic has removed any influence of the reservoir on the base Cretaceous. A simulation was performed on this mesh and the residual norm is shown in Figure 6.26. The residual norm appears to have reduced slightly more than for the mesh where the reservoir is attached to the base Cretaceous, but the decay is still very poor. It is difficult to deduce if isolating the reservoir body in the mid-Jurassic had any positive impact on the convergence because the minor improvement could also be attributed to the reduction of 200k cells in the mesh.

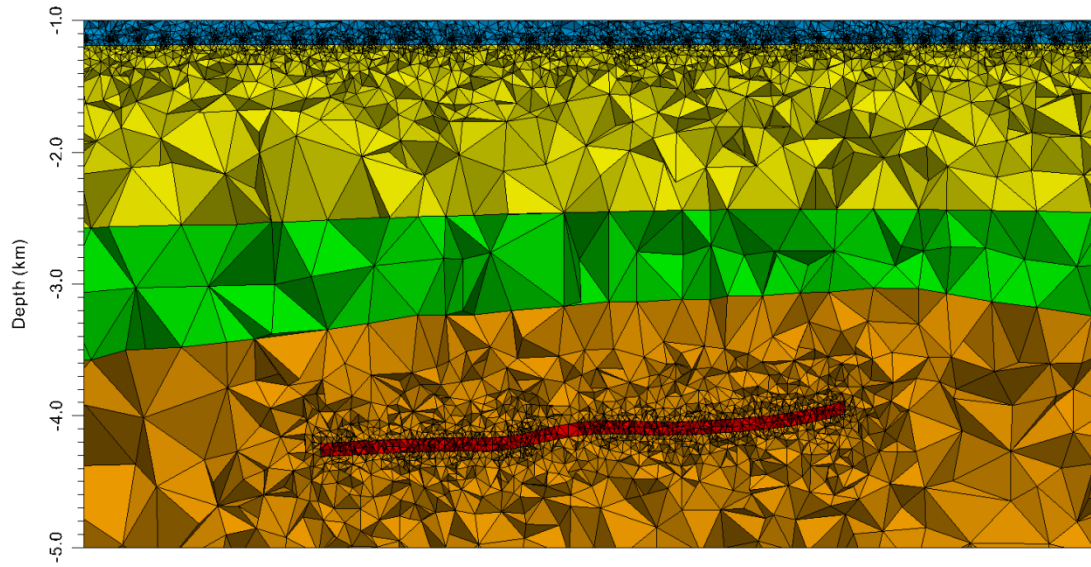


Figure 6.25: A 2D slice of the ‘mid-Jurassic’ Bay du Nord reservoir mesh along CSEM transmitter #9. The reservoir body is shifted down 700m into the mid-Jurassic and the attachment facets are removed. This removes any influence the attachment zones or refinement on the base Cretaceous may have on the numerical solver. This mesh contains 2,624,255 cells and a percentage of poor cells equating to 0.389%.

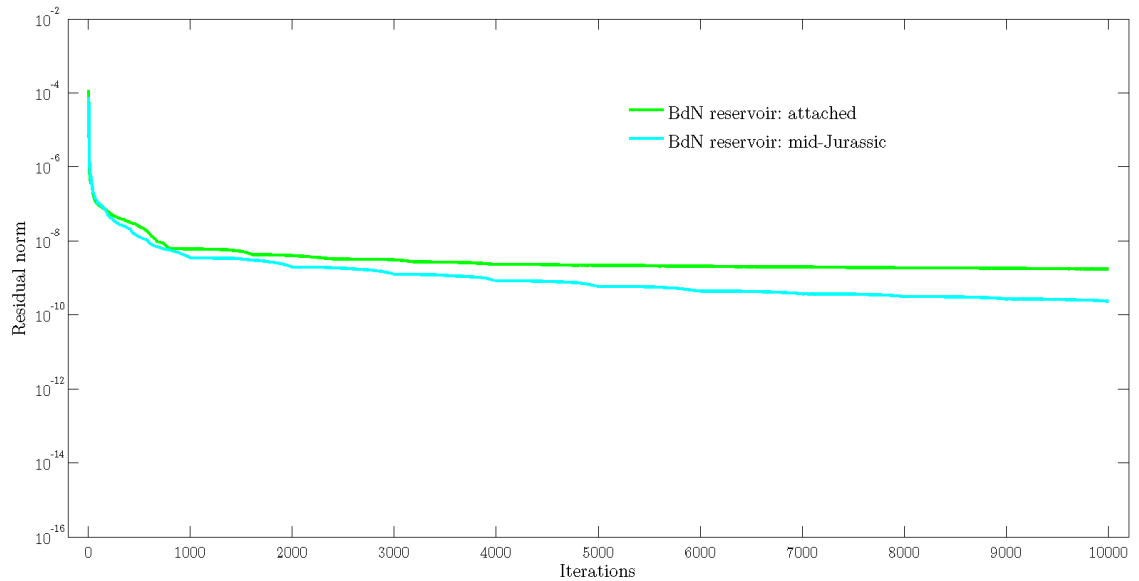


Figure 6.26: The residual norm of the ‘mid-Jurassic’ Bay du Nord mesh with the reservoir body shifted down into the mid-Jurassic and with the attachment facets removed (cyan). The residual norm from the original simulation (Figure 6.24) is shown in green.

### 6.5.2 Test II: Mid-Jurassic and reservoir constraint

After further inspection of the ‘mid-Jurassic’ reservoir mesh, it appeared the thickness of the reservoir body was being represented with 3-4 tetrahedral cells. This is unnecessary because the reservoir surfaces are represented with nodes spaced at 100m and the thickness is 100m; 1-2 cells to represent the thickness should suffice. Representing the reservoir body thickness with one cell is optimal because the edge lengths of the cells after meshing would be 100m and the resulting tetrahedra would be well-shaped.

Another mesh was created using the same model from the previous test, except an *edge length constraint of 100m was imposed on the reservoir surface nodes*. This ‘constrained mid-Jurassic’ Bay du Nord mesh contained 1,922,802 cells, a minimum dihedral angle of  $0.99^\circ$ , and a percentage of poor cells equating to 0.292% (5620/1922802). Figure 6.27 shows a 2D slice of this constrained mid-Jurassic reservoir mesh along the CSEM transmitter line #9. This 2D slice clearly shows that the degree of refinement inside and surrounding the reservoir body is significantly less. Imposing this constraint has reduced the number of cells by an additional 700k and the percentage of poor quality cells decreased as well.

A simulation was performed on this mesh and the residual norm is shown in Figure 6.28. To some surprise, the decay of the residual norm for this mesh was exceptional. The percentage of poor quality cells was reduced slightly going from the ‘mid-Jurassic’ to the ‘constrained mid-Jurassic’ mesh, so the quality of the cells *inside* the reservoir must have improved. However, it seems the *number of cells*

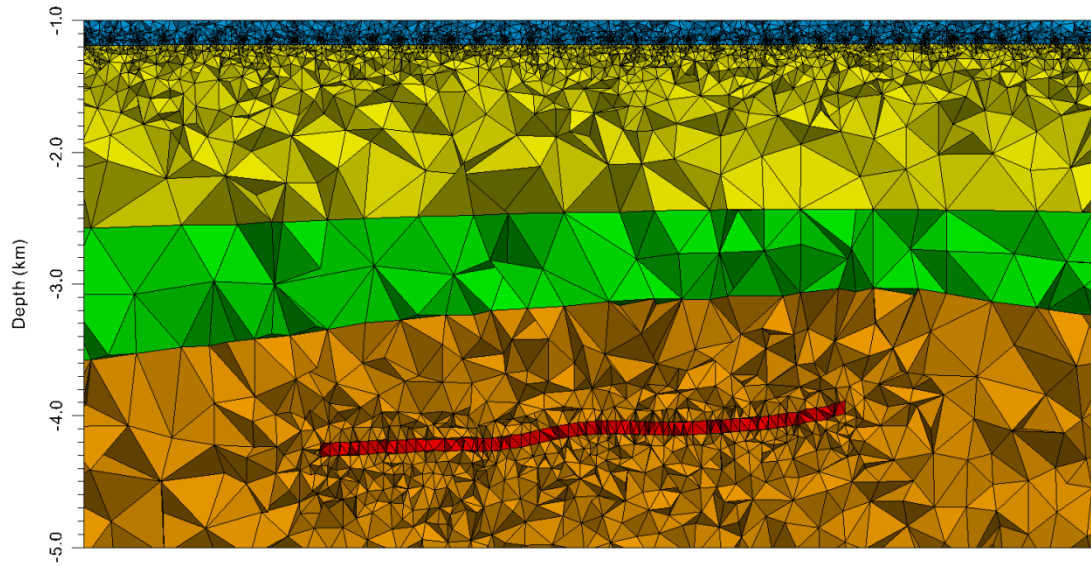


Figure 6.27: A 2D slice of the ‘constrained mid-Jurassic’ Bay du Nord reservoir mesh along CSEM transmitter #9. The reservoir body is still shifted down 700m into the mid-Jurassic with the attachment facets removed, but with a 100m edge-length constraint imposed on the reservoir surface nodes. This mesh contains 1,922,802 cells and a percentage of poor cells equating to 0.292%.

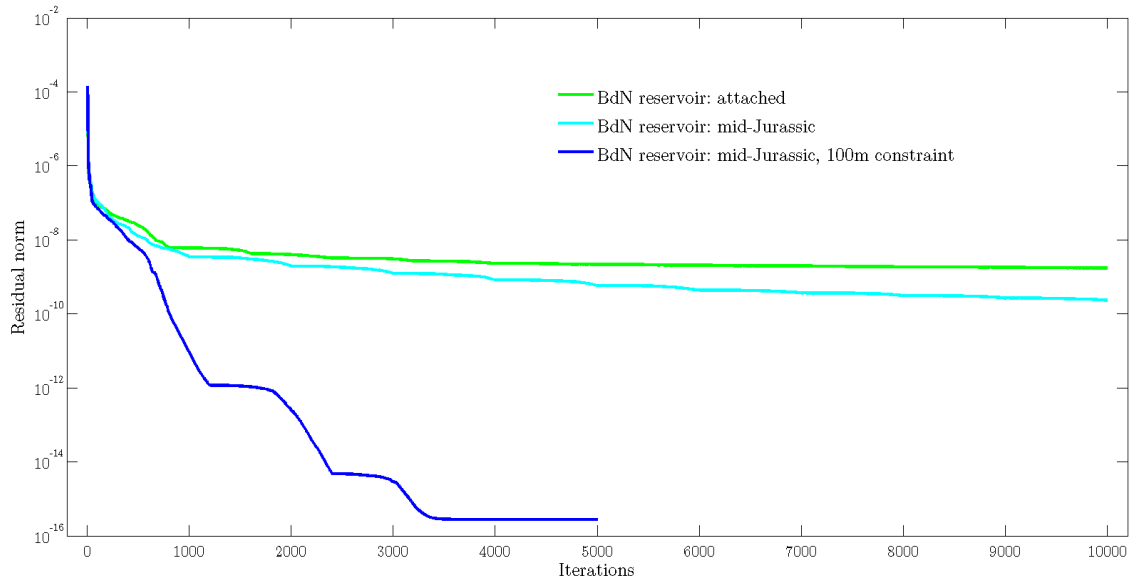


Figure 6.28: The residual norm of the ‘constrained mid-Jurassic’ Bay du Nord mesh with the reservoir body shifted down into the mid-Jurassic, with the attachment facets removed, and a 100m edge-length constraint imposed on the reservoir surface nodes (blue). The decay of the residual norm for this mesh is excellent. The residual norm from the previous tests is shown for comparison.

was the primary factor for causing poor convergence in the first test. The exceptional convergence in Figure 6.28 shows that the geometry of the reservoir is no longer a factor. The reservoir body itself has not changed (with the exception of the attachment facets). The most noteworthy change that has occurred is *how many cells are used to represent the reservoir body*. However, there are still two factors that require investigation.

### **6.5.3 Test III: No attachment with reservoir constraint**

The next factor that needed to be considered was the influence of the Bay du Nord reservoir on the base Cretaceous. Figure 6.21 clearly shows that the presence of the reservoir forces refinement on the base Cretaceous surface and this may have an impact on the convergence. The original Bay du Nord reservoir model was revisited, but the attachment facets to the base Cretaceous were again removed in order to isolate the influence of the reservoir just being in close proximity to the base Cretaceous. Even though the reservoir is quite shallow in relation to the base Cretaceous, the 100m edge-length constraints were maintained on the reservoir surface nodes. The original base Cretaceous surface with no modifications was used, but the edge-length constraints were removed on the nodes lying above the reservoir so TetGen could have the freedom to add any necessary refinement on the surface.

A mesh was generated from this new ‘shallow constrained’ Bay du Nord model using the same switches as before. The resulting mesh contained 1,992,445 cells, a minimum dihedral angle of  $1.41^\circ$ , and a percentage of poor cells equating to 0.294%

(5854/1992445). To some surprise, moving the reservoir from the mid-Jurassic to its real position situated right beneath the base Cretaceous only added about 70k cells. Figure 6.29 shows a 2D slice of this ‘shallow constrained’ Bay du Nord mesh along the EMGS transmitter line #9. There is still a minor degree of refinement reflected on the base Cretaceous surface, but the constraint on the reservoir seems to keep the level of refinement at a minimum.

A simulation was performed on this mesh and the residual norm is shown in Figure 6.30. The decay of the residual norm is still quite good, but it did not decay as much as the previous test where the reservoir body was situated in the mid-Jurassic. The size of this mesh and the mesh from the previous test (Test II) are almost the same, but it took slightly more iterations for the residual norm to reach a point where it would no longer decay for this mesh (Test III). This shows there is a slight impact on the residual norm from the reservoir body being in close proximity to the base Cretaceous, but not so much that it prevents the residual norm from reducing by a satisfactory amount.

#### **6.5.4 Test IV: Attached with reservoir constraint**

The fourth and final factor that needed to be considered was the influence of *attaching* the two Bay du Nord surfaces to the base Cretaceous. A new mesh was created by simply taking the original Bay du Nord reservoir model from Section 6.4.3 and imposing all the same constraints with the addition of the 100m edge-length constraints on the reservoir surface nodes. The resulting ‘attached and constrained’ Bay du Nord reservoir mesh contained 2,049,203 cells, a minimum

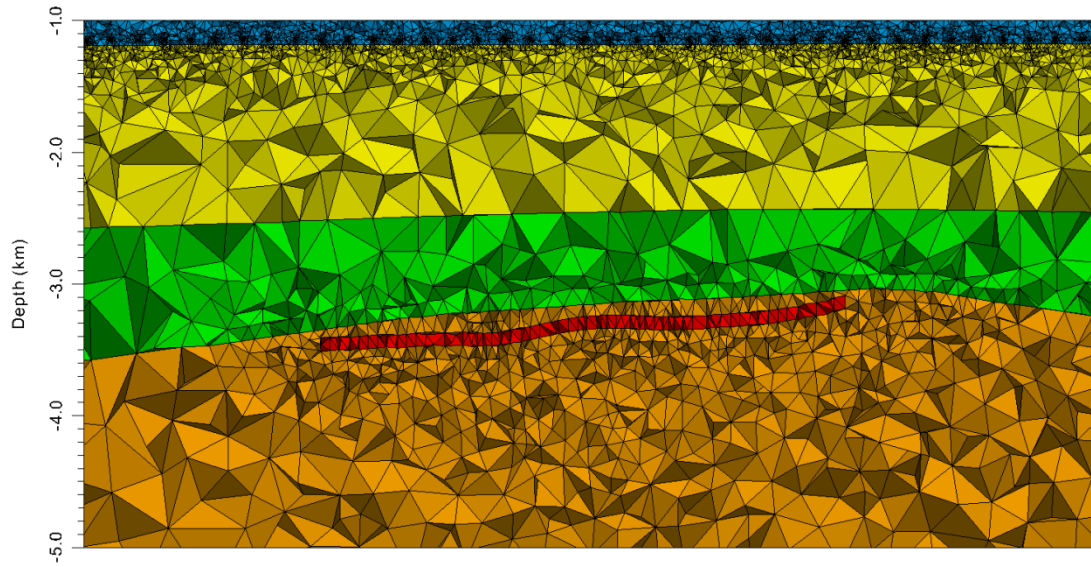


Figure 6.29: A 2D slice of the ‘shallow constrained’ Bay du Nord reservoir mesh along CSEM transmitter #9. The reservoir body is returned to its original position with the attachment facets removed, and a 100m edge-length constraint imposed on the reservoir surface nodes. This mesh contains 1,992,445 cells and a percentage of poor cells equating to 0.294%.

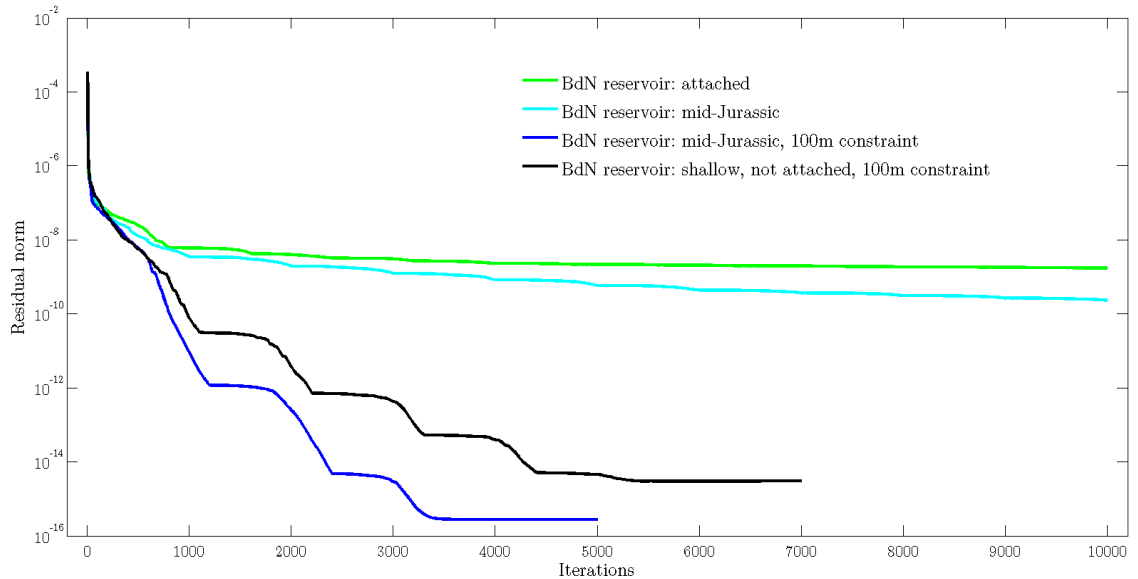


Figure 6.30: The residual norm of the ‘shallow constrained’ Bay du Nord mesh with the reservoir body at its original position with the attachment facets removed, and a 100m edge-length constraint imposed on the reservoir surface nodes (black). The decay of the residual norm for this mesh is adequate, but not as good as the residual norm from the previous test (blue).

dihedral angle of  $0.45^\circ$ , and a percentage of poor cells equating to 0.341% (6979/2049203). The attachment regions appear to have only added roughly 60k cells from the previous mesh (Test III) which is reasonable because the attachment regions account for a very small volume of the whole reservoir. There is a slight increase in the percentage of poor cells which must be attributed to the attachment regions. However, imposing this edge-length constraint has reduced the number of cells from 2,853,440 from the original mesh to 2,049,203 for this mesh (a reduction of over 800k cells).

The 2D slice of this ‘attached and constrained’ Bay du Nord mesh along the EMGS transmitter line #9 is shown in Figure 6.31. The two attachment regions are easily identifiable. Notice the reduction of cells inside and surrounding the reservoir compared to Figure 6.23 where there was no constraint on the reservoir surface nodes. A simulation was performed on this mesh and the residual norm is shown in Figure 6.32. The residual norm did decrease by many orders of magnitude, but it took far more iterations to reach a level comparable to the previous two tests (shown as blue and black). This shows that the *attachment region does in fact have an adverse effect on the decay of the residual norm*. Despite the delay of convergence for this mesh, there is still a considerable improvement over the residual norm from the original simulation (shown in green).

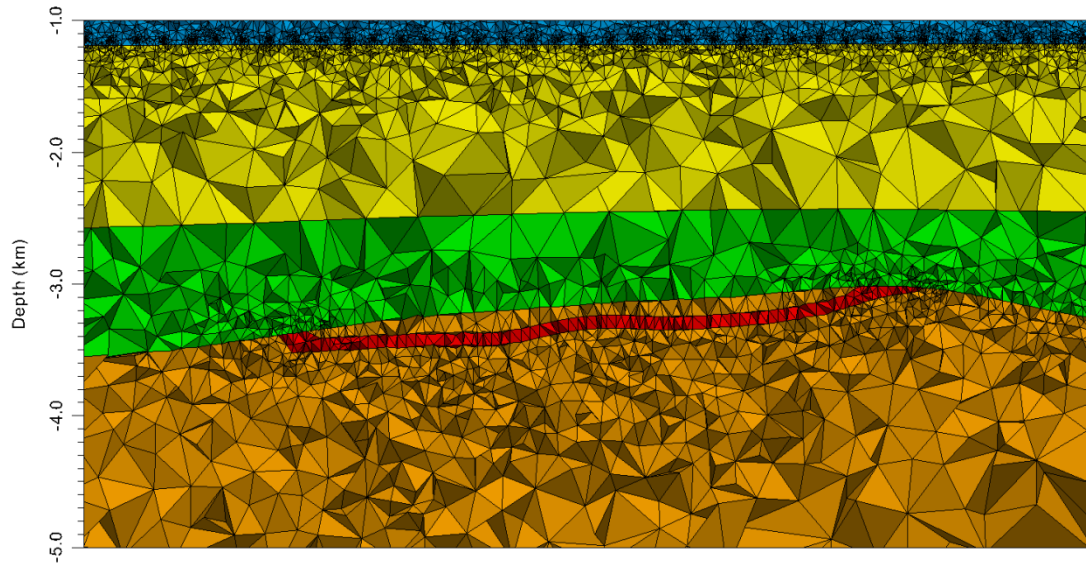


Figure 6.31: A 2D slice of the ‘attached and constrained’ Bay du Nord reservoir mesh along CSEM transmitter #9. This is the same model from Figure 6.23 (i.e. the attachment facets are reintroduced) with the only change of imposing a 100m edge-length constraint on the reservoir surface nodes. This mesh contains 2,049,203 cells and a percentage of poor cells equating to 0.341%.

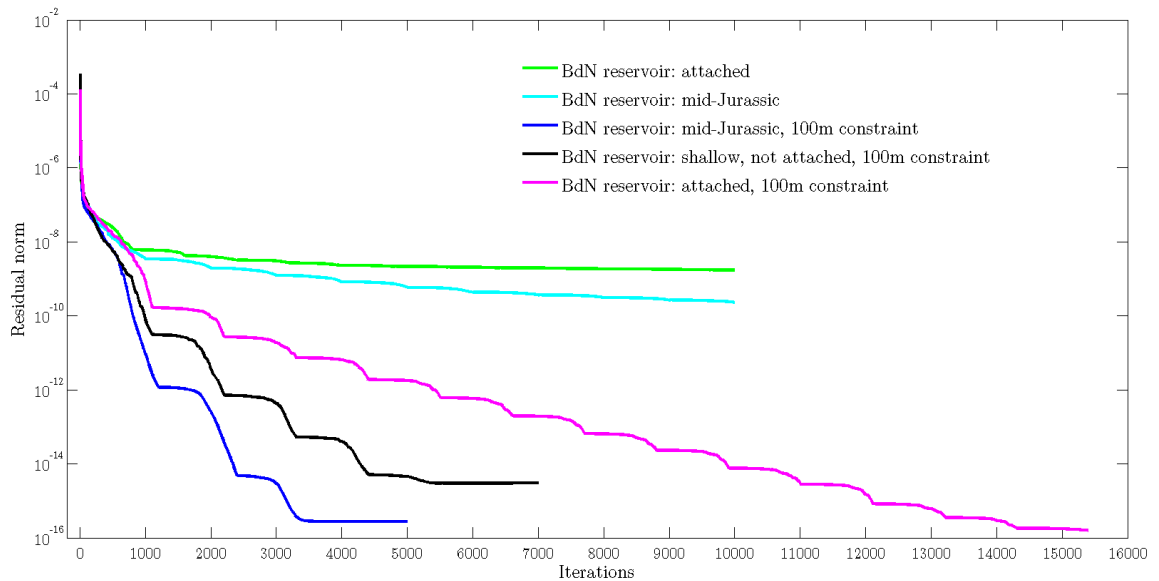


Figure 6.32: The residual norm of the ‘attached and constrained’ Bay du Nord mesh with the reservoir body attached to the base Cretaceous and containing a 100m edge-length constraint imposed on the reservoir surface nodes (purple). The decay of the residual norm for this mesh is excellent, but it takes many more iterations to converge compared to the previous test (black).

### 6.5.5 Summation and verdict

These four tests incrementally made changes to the Bay du Nord model in order to isolate four factors that were impacting the quality of the convergence. A summary of all the tests is shown in Table 6-2. The results from these tests helped choose which model would be best suited for performing numerical computations and sensitivity analyses later in this chapter.

The original mesh is clearly not appropriate because that mesh contained far too many cells and the convergence was extremely poor. The meshes investigated in Tests I and II are also not appropriate because the reservoir body was displaced from its true location for testing purposes. The meshes from Tests III and Test IV are the only two models that have any geological accuracy *and* a sufficient reduction of the residual norm. The mesh from Test IV has the most geological accuracy as the reservoir is truncating on the base Cretaceous (as suggested by the seismic data), but this model required significantly more iterations to reach convergence. Therefore, from a practical perspective, the mesh from Test III was

Table 6-2: A summary of all the simulation tests performed on variants of the Bay du Nord model.

SIMULATION TESTS	Information	TetGen quality factors	Mesh tetrahedra	Smallest dihedral angle	Percentage of poor cells	Convergence verdict
Original test	Attached	-pq1.50/16	2,853,440	0.86°	0.406%	Poor
Test I	Mid-Jurassic	-pq1.50/16	2,624,255	1.18°	0.389%	Poor
Test II	Mid-Jurassic 100m constraint	-pq1.50/16	1,922,802	0.99°	0.292%	Excellent
Test III	Not attached 100m constraint	-pq1.50/16	1,992,445	1.41°	0.294%	Good
Test IV	Attached 100m constraint	-pq1.50/16	2,049,203	0.45°	0.341%	Excellent, <i>very slow</i>

avored over that from Test IV. The model from Test III does not attach to the base Cretaceous, and subsequently, does not reflect the seismic interpretation in its entirety. However, these attachment zones only contribute a very small volume to the reservoir and their influence on the computed responses will likely be negligible. With the exception of the attachments areas, the reservoir body in Test III is identical to Test IV. As a result, the mesh from Test III (containing the 100m edge-length constraints on the reservoir surface nodes, but with the attachment facets removed) was chosen to perform the analyses remaining in this chapter.

## 6.6 Verification of Hydrocarbon Volumes

At this stage, a model for the Bay du Nord reservoir has been built and evaluated, but before any in-depth analysis is performed, the volume of the Bay du Nord reservoir body in the model needs to be verified. Again, the only information publically available that has any reference to the size of the Bay du Nord reservoir is announcements made by Statoil. On June 10, 2016, Statoil made the following announcement on their website (<http://www.statoil.com/>):

*“The appraisal and near-field exploration of the Bay du Nord discovery has reduced key reservoir uncertainties and confirmed that the volumes are within the original volume range of the **300 to 600 million barrels of recoverable oil** initially estimated by Statoil in 2013, but potentially towards the lower end of the range.”*

Therefore, an estimate for the recoverable oil of the Bay du Nord reservoir body in the model is needed in order to compare to the 300-600M barrels of recoverable oil estimate given by Statoil.

The same equations from Section 5.6.1 were used to calculate the original oil in place (*OOIP*) and recoverable oil (see Equations 5.1 and 5.2) estimates for the Bay du Nord reservoir body. However, values for the variables had to be established before any calculations could be performed. The area was found by simply calculating the area of the top-of-sand surface. This surface is represented with 6037 equally sized triangular cells with nodes spaced at 100m. The area of this surface is simply  $6037 \times 0.5 \times \text{base} \times \text{height} = 6037 \times 0.5 \times 100\text{m} \times 100\text{m} = 30.185 \text{ km}^2$ . The thickness is also fixed at 100m. The porosity can be taken directly from the C-78 well log (Figure 6.2). However, the porosity log in C-78 shows there is a different porosity for each of the sand intervals. The model made the simplification of combining all the sand bodies into *one equivalent 100m sand body*, and so only one porosity value is needed to characterize the equivalent sand body. The solution is using a weighted average porosity. The base 50m sand is quite clean and contains 32% porosity. The shallower sand body appears to have two separated 30m and 20m sands with approximately 24% and 16% porosity respectively. A thickness weighted average of these sands gives a porosity of 26.4%.

The remaining variables have a degree of uncertainty associated with them. The first to consider is the net-to-gross ratio. All the logs for C-78 (see Figure 6.2) suggest that the sand body on the interval between  $z = -3150\text{m}$  and  $z = -3200\text{m}$  is very clean. There are no breaks in the gamma ray or density signatures and the same porosity is maintained for the entire interval. However, the sand body from  $z = -3050\text{m}$  to  $z = -3100\text{m}$  appears to not be 100% sand. There are breaks in the gamma ray, resistivity, and porosity signatures suggesting the possibility of some

interbedded silt/shale zones. This suggests that the net-to-gross ratio may not be 100%, but it is too ambitious to use only one value. The net-to-gross ratio was allowed to vary between a range of 75% and 100% as indicated in Table 6-3.

A more conservative approach to choosing values for a variable containing uncertainty is to consider a *range of acceptable values* instead of just one value (using only one value for each variable is what was done in the Mizzen chapter). This removes the uncertainty of choosing just one value, and this approach was used for the remaining variables. An acceptable range for the water saturation ( $S_W$ ) was chosen to be 15-35%. The formation volume factor ( $FVF$ ) was chosen to lie between 1.30 and 1.50. Lastly, a conservative recovery factor ( $RF$ ) range was chosen to be 15-25%. All four of these variables and their respective ranges and step values are shown in Table 6-3.

Table 6-3: The start, step, and end values for four variables needed for the calculations of original oil in place (OOIP) and recoverable oil. These four variables contain uncertainty, so rather than use only one value for each variable, a range is considered.

Variable	Start value	Step	End value
Net-to-gross ratio (N/G)	75%	2.5%	100%
Water saturation ( $S_W$ )	15%	2.5%	35%
Formation volume factor ( $FVF$ )	1.30	0.01	1.50
Recovery factor ( $RF$ )	15%	0.5%	25%

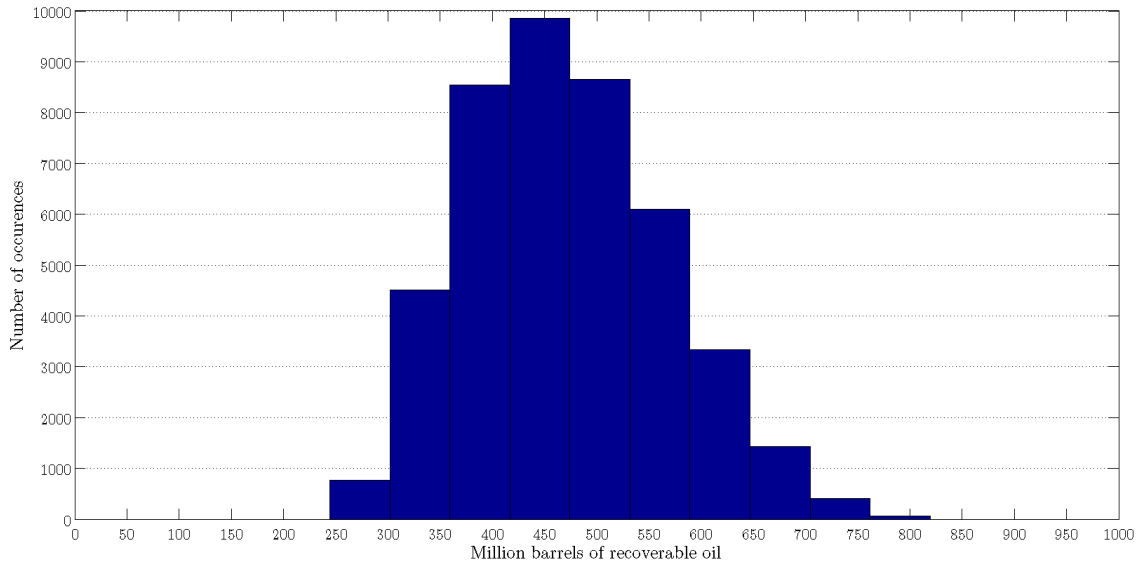


Figure 6.33: A histogram of recoverable oil calculations for the Bay du Nord reservoir body in the model. The average is 470M barrels of recoverable oil with a standard deviation of 100M.

A calculation for the *OOIP* and recoverable oil (using Equation 6.1 and Equation 6.2) was performed for each unique combination of the variables considered in Table 6-3. Based on the step sizes and ranges for each variable, there are 43,659 different combinations. A histogram showing the distribution of the recoverable oil calculations is shown in Figure 6.33. These results show an approximately normal distribution, and the average is 470M barrels of recoverable oil with a standard deviation of 100M. Therefore, the Bay du Nord reservoir body in the model has a volume range of *370-570M barrels of recoverable oil*. This estimate is in good agreement with estimate announced by Statoil (300-600M barrels of recoverable oil) and this provides supporting evidence that the size of the reservoir in the model is accurate. Based on the satisfactory convergence (Figure 6.30) and the agreement of the recoverable oil estimates, the Bay du Nord reservoir mesh is suitable for numerical simulation and sensitivity analyses.

## 6.7 Establishing Resistivities at RX15

### 6.7.1 Simulations with longitudinal resistivities

The resistivities of the various regions in the Bay du Nord model were established using the same incremental simulation technique from Chapter 5. However, in order for this approach to work, recall that many distinct meshes were needed with incremental changes in order to isolate how the resistivity of each region in the model influences the computed results. Earlier in this chapter, five different meshes were made (Section 6.3.3 and 6.5.3) which contain the necessary incremental changes going from the most basic model (only contains the seafloor surface) to the most complex model (all four surfaces and the Bay du Nord reservoir body). 2D mesh slices along  $x = 25.0$  km from each of these models are shown in Figure 6.34.

These five meshes are similar to those from the Mizzen chapter (Figure 5.47) with two main distinctions. This study was able to incorporate the base Cretaceous, so the Cretaceous and Jurassic layers are represented as two separate layers. The second distinction relates to how the sensitivities will be calculated. Recall from the Mizzen study that the sensitivities were calculated by normalizing the response with hydrocarbons up-dip to a response where all three slabs were filled entirely with *brine*. The scenario for Bay du Nord is much different. The C-78 well log did not encounter any brine saturated sands, and the reservoir extent was built using the *resistive anomaly* from the mCSEM inversion from EMGS. This implies that the Bay du Nord reservoir in the model is purely a *hydrocarbon-bearing reservoir*, and no portion is filled with brine. Brine could certainly still be encountered

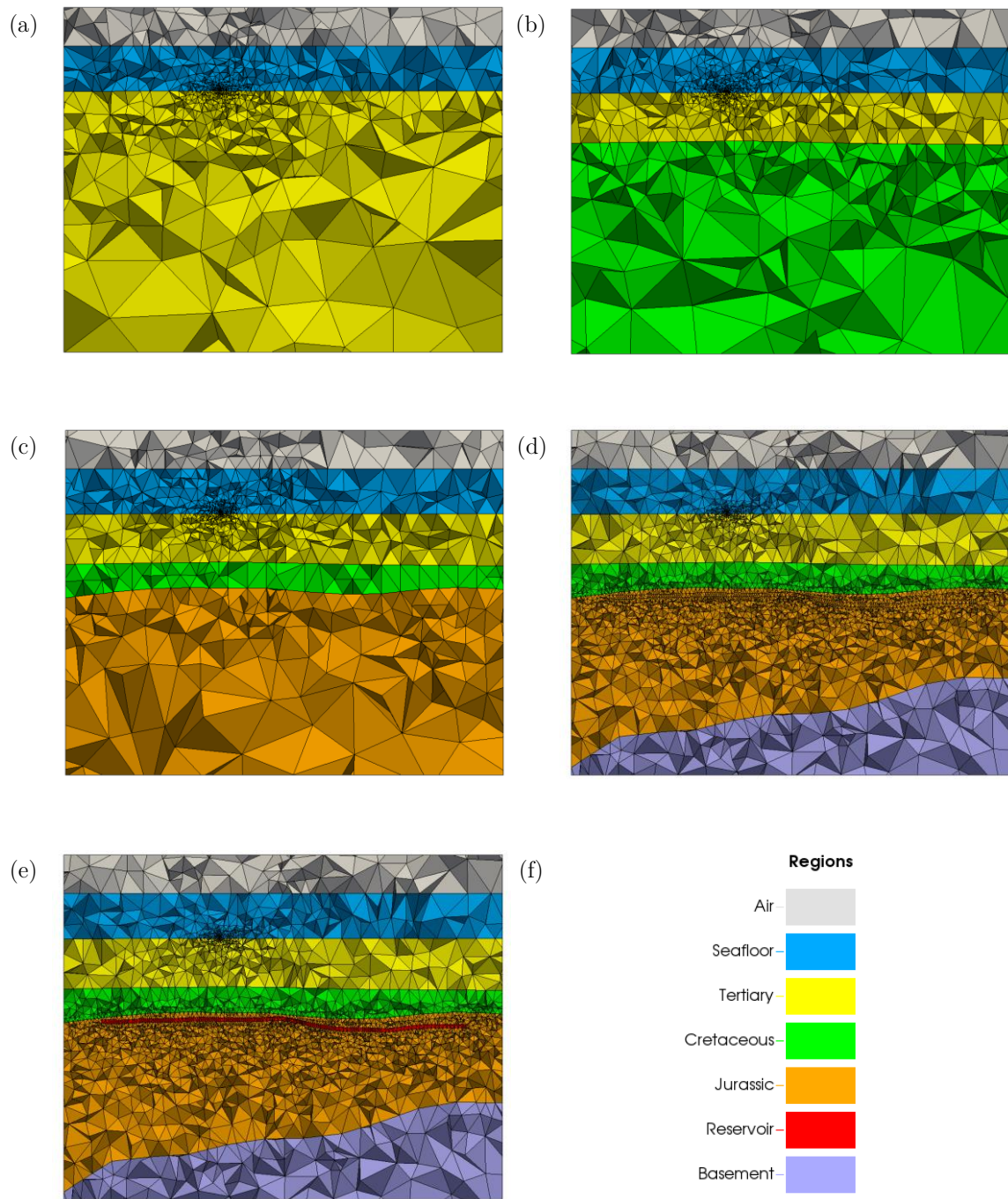


Figure 6.34: 2D mesh slices along  $x = 25.0$  km for the (a) seafloor model, (b) base tertiary model, (c) base Cretaceous model, (d) base Jurassic/background model, and (e) the reservoir model, illustrating the subsequent incremental changes between each model. Panel (f) provides a color key for the corresponding regions of all the models.

further down-dip in structure, but constraining the extent of the reservoir on a resistive anomaly excludes the potential brine portions of the reservoir. As a result, the sensitivity of the Bay du Nord reservoir was calculated by normalizing the reservoir response (Figure 6.34e) to the background response (Figure 6.34d). The same mesh is used for the normalization process where the ‘background mesh’ is the ‘reservoir mesh’, but the resistivity of the reservoir is assigned the value for the Jurassic. If two responses are normalized, they need to come from the same mesh to avoid possible minute differences in numerical results arising from any changes between two different meshes.

The five distinct meshes in Figure 6.34 contain the incremental changes necessary to isolate the contributions coming from each subsurface region, and the next step is simulating mCSEM data from these meshes. All of these meshes were initially created to reflect the necessary conditions for RX15 (see Figure 6.1) and upcoming simulations are made at RX15 because those meshes have not changed. The starting point for numerical simulations, similar to the Mizzen chapter, is using the *horizontal resistivities* derived from the C-78 well log (see Figure 6.6). Numerical simulations were performed on all five of the meshes using a frequency of 0.50 Hz. The convergence for each of the meshes was very similar to those in Figure 6.13 (surface meshes) and Figure 6.30 (reservoir mesh) and is not shown here for brevity.

The computed in-line amplitude, phase, and reservoir sensitivity are shown in Figure 6.35. To no surprise, the in-line amplitude and phase of the reservoir mesh

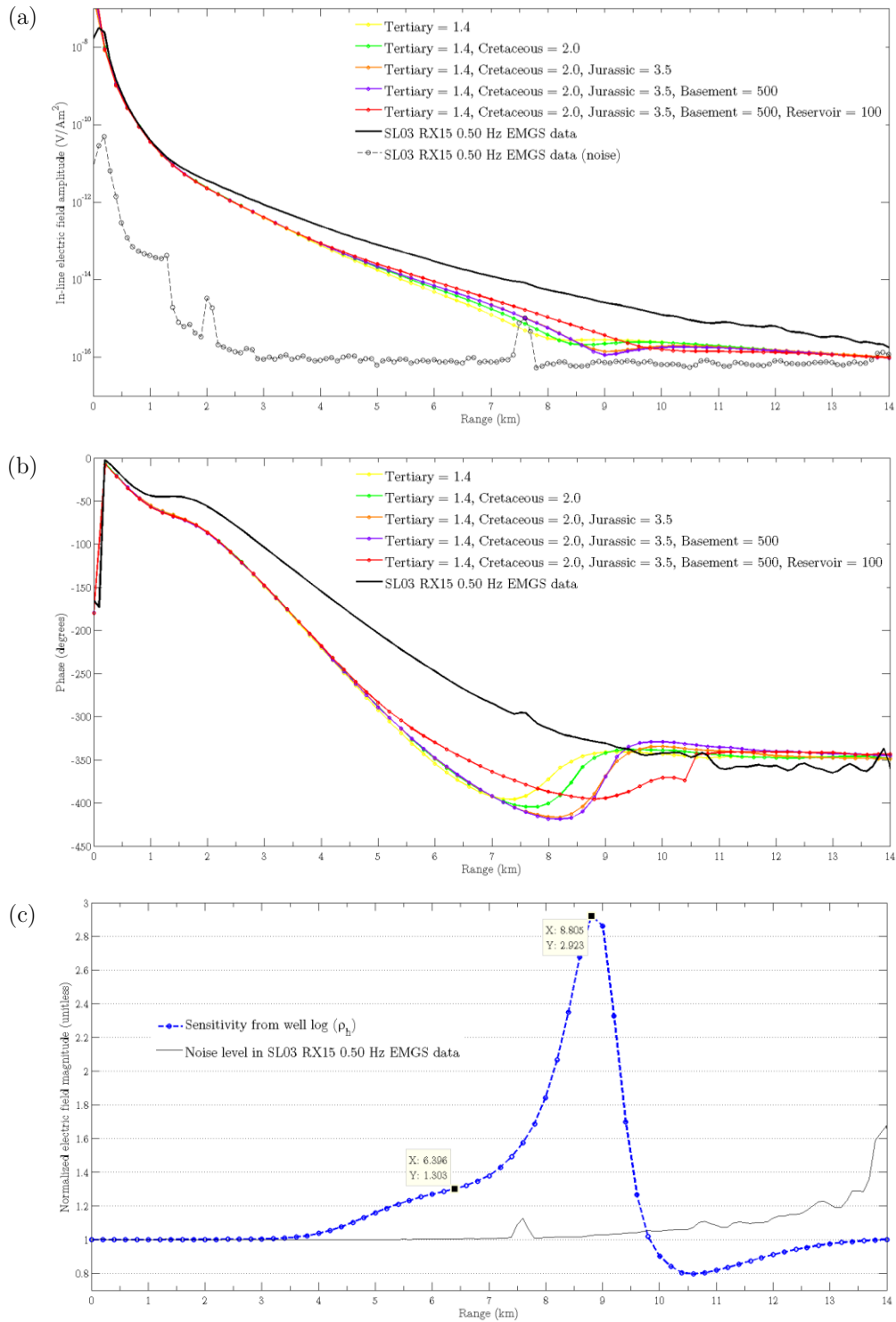


Figure 6.35: The computed (a) in-line amplitude, and (b) phase responses from each of five meshes at RX15 for  $f = 0.50$  Hz using the horizontal resistivities derived from blocking the C-78 resistivity log. Panel (c) shows the sensitivity of the Bay du Nord reservoir. The measured mCSEM data (in-line amplitude, phase, and noise) are plotted in each appropriate panel for comparison.

(red) does not match the measured mCSEM data from EMGS. This is once again a result of in-line mCSEM fields being sensitive to  $\rho_V$  and not  $\rho_h$ . An interesting phenomenon observed in these results is that the basement, or background response shows almost no difference from the Jurassic response (orange). It seems the basement is so deep that it has such a minimal impact on the computed amplitude and phase. However, this is an observation based on data simulated with *horizontal resistivities* which do not match the measured data. The horizontal resistivities make the overall skin depth of the layers above the basement (Tertiary, Cretaceous, and Jurassic) smaller, and the EM fields must decay to a point that when they reach the basement there is no signal left. However, when the resistivities of the layers above the basement are modified to match the data, the overall skin depth of these layers *will be larger* and a contribution from the basement may return.

Another key observation is that the Bay du Nord reservoir is showing a very strong sensitivity and it lies well above the noise level (Figure 6.35c). Even though this is an overestimated sensitivity from using the horizontal resistivities, the sensitivity to the Bay du Nord reservoir at RX15 is much greater than the preliminary sensitivity computed for the Mizzen reservoir at RX44 (see Figure 5.52). Already, a larger anomaly is being seen for the Bay du Nord reservoir and that was the prediction. However, to recover the *true sensitivity* of the Bay du Nord reservoir at RX15, the background resistivities must be modified so the reservoir response matches the measured data.

### 6.7.2 Recovery of vertical resistivities

The longitudinal resistivities were modified to match the measured mCSEM data at RX15 using the same incremental simulation technique from the Mizzen chapter. Again, the air and seawater are considered isotropic and their values are held constant. However, all background layers were candidates for modification (the Tertiary, Cretaceous, Jurassic, and basement). The exact same process was used from Section 5.8 and the details will not be repeated here. There was an added challenge for this scenario because the resistivities of four regions had to be determined instead of three.

Based on inspection of the measured mCSEM data, it seems the data is of good quality up to 11 km offset for  $f = 0.50$  Hz. After 11 km offset, the in-line amplitude has a distinct ‘bump’ and the phase begins to flatten suggesting a significant contribution of the airwave to the total field. Therefore, all the resistivities were determined with this kept in mind. The incremental simulation process determined the resistivities of the Tertiary, Cretaceous, and Jurassic regions to be  $2.3 \Omega\text{m}$ ,  $4.0 \Omega\text{m}$ , and  $6.0 \Omega\text{m}$  respectively. The last step in the curve matching process was fixing the Tertiary, Cretaceous, and Jurassic resistivities and then varying the basement resistivity in the base Jurassic model. Again, there is no data suggesting an appropriate value for the basement, so the basement resistivity was chosen to vary across a wide range from  $30 - 1000 \Omega\text{m}$ .

The in-line amplitude and phase responses for each of the basement resistivities are shown in Figure 6.36 with the response from the base Cretaceous model plotted for

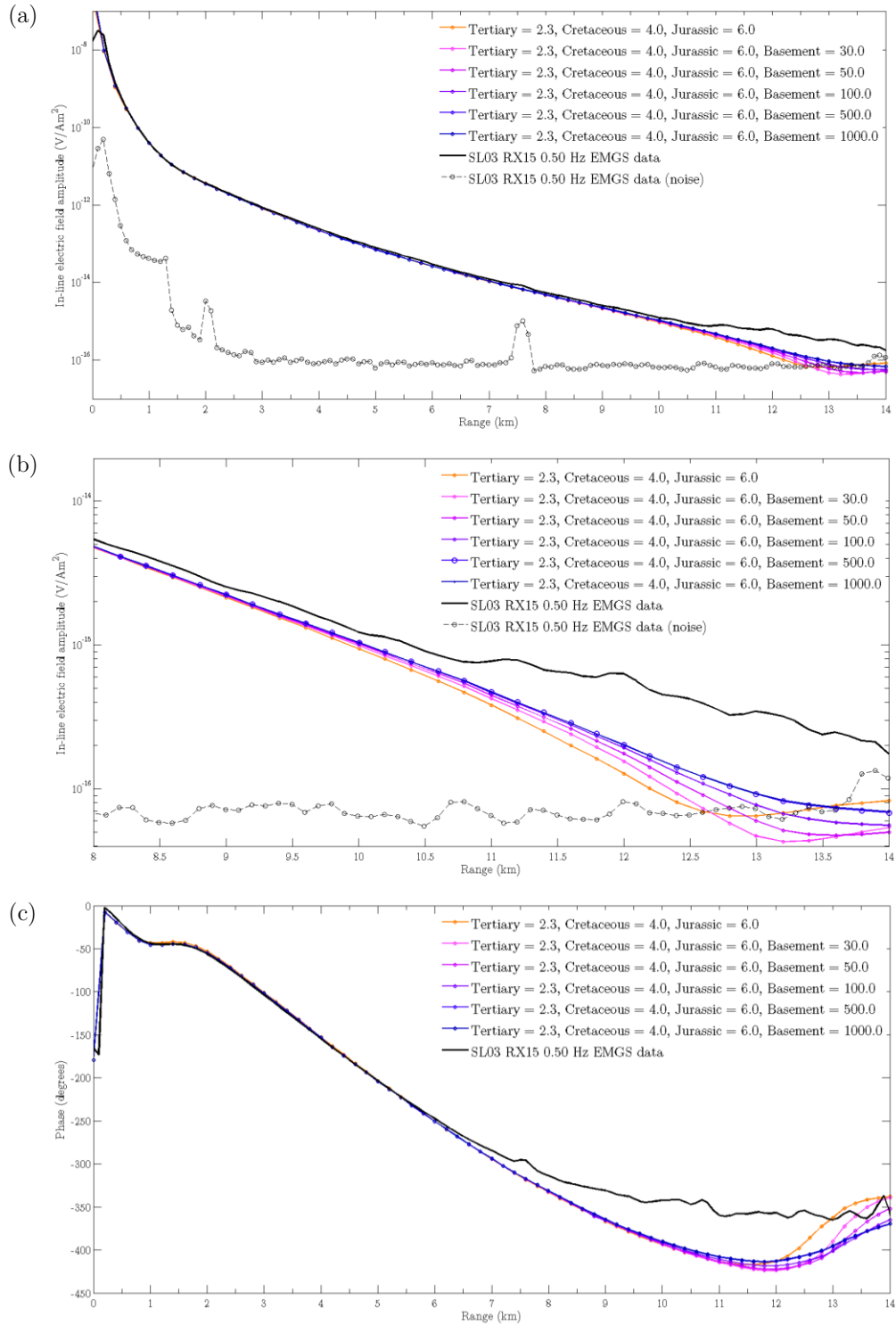


Figure 6.36: The computed (a) in-line amplitude, (b) in-line amplitude zoomed in, and (c) phase responses for varying the value of the basement region in the base Jurassic mesh at RX15 for  $f = 0.50$  Hz. The measured mCSEM data and the base Cretaceous model response (Tertiary = 2.3  $\Omega m$ , Cretaceous = 4.0  $\Omega m$ , Jurassic = 6.0  $\Omega m$ ) are shown for comparison.

comparison. As predicted, the presence of the basement region starts to influence the data once higher resistivities are assigned to the overlying layers. It seems that regardless of the basement resistivity, *all* the curves begin to deviate from the base Cretaceous model response starting around 9 km offset (recall it was 6 km for the Mizzen chapter). Starting at around 10 km offset, the curves for varying basement resistivity begin to deviate from each other. Interestingly, there is no difference in the in-line amplitude or phase between the responses containing a basement resistivity of 500  $\Omega\text{m}$  or 1000  $\Omega\text{m}$ . So it does not seem appropriate to use 1000  $\Omega\text{m}$  for the basement resistivity. The curve for 500  $\Omega\text{m}$  starts to deviate from 100  $\Omega\text{m}$  at 11.0-11.5 km offset. Either 100  $\Omega\text{m}$  or 500  $\Omega\text{m}$  were the best candidates for the basement resistivity, and the conservative decision was the choice for 500  $\Omega\text{m}$ . This is a much higher resistivity than what was used for the basement in the Mizzen chapter (30  $\Omega\text{m}$ ). However, the basement under Bay du Nord is buried much deeper than it is under Mizzen and the added compaction and overburden pressure may actually cause the basement resistivity to be higher.

The computed results for the basement response of 500  $\Omega\text{m}$  still show a small mismatch gap with the measured in-line amplitudes, but this was by design as this ‘gap’ is meant to be filled by the contribution from the reservoir. The computed in-line amplitude, phase, and sensitivity for each of the five meshes using the new resistivities derived through incremental simulation are shown in Figure 6.37. Notice that the reservoir response (red) matches the measured in-line amplitude quite well. The match to the measured phase is not as good, but matches to phase are deemed auxiliary. The emphasis is placed on matches to in-line amplitude

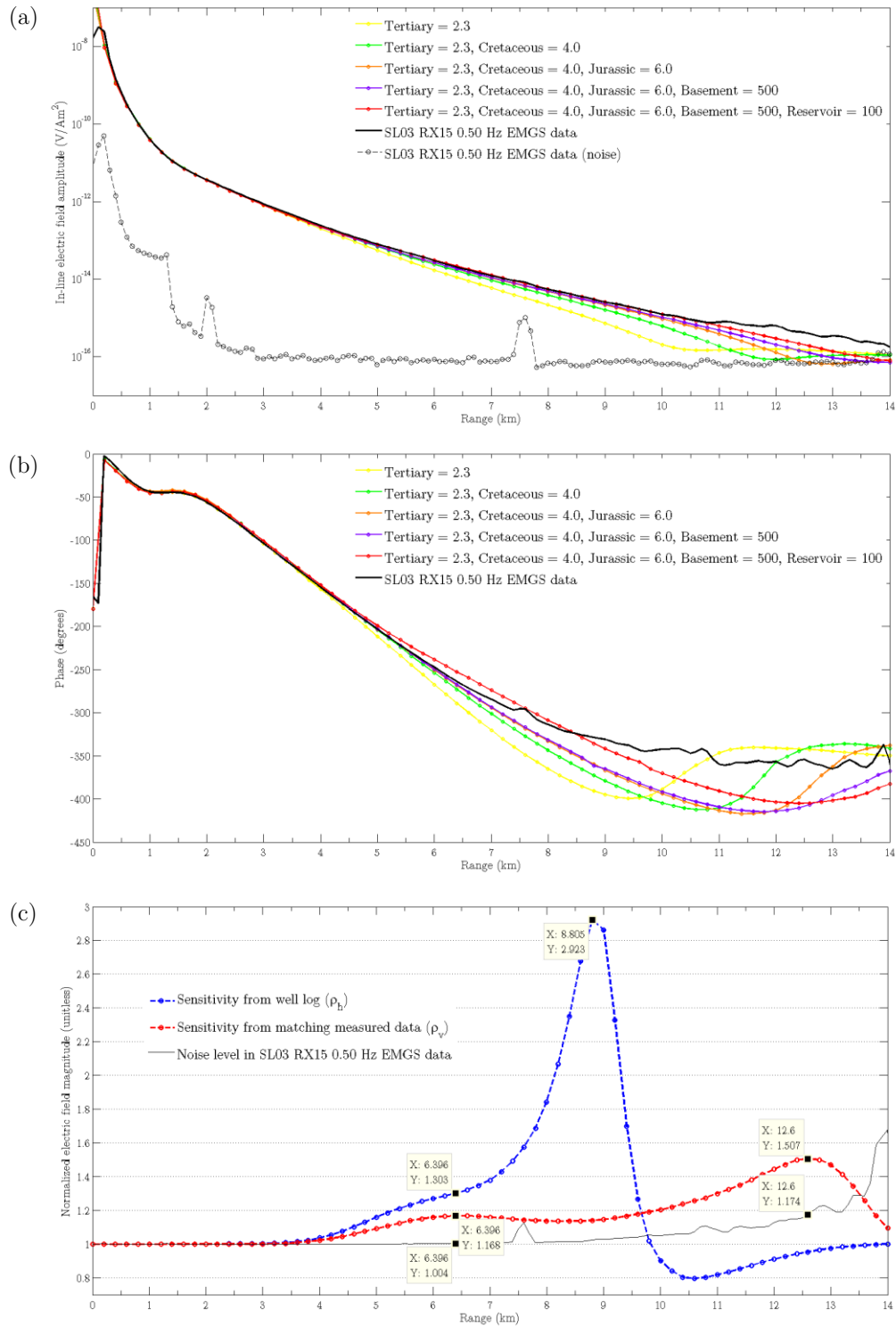


Figure 6.37: The computed (a) in-line amplitude, and (b) phase responses for each of the five meshes at RX15 for  $f = 0.50$  Hz using the final resistivities found using the incremental simulation approach. Panel (c) compares the sensitivity of the Bay du Nord reservoir using the longitudinal resistivities from the well log and the vertical resistivities found through matching the data.

because the sensitivity is calculated from in-line amplitudes. Figure 6.37(c) shows an unfortunate, yet expected phenomenon regarding the sensitivity to the reservoir. The sensitivities from the longitudinal and vertical resistivities are shown as blue and red respectively. Notice how changing the background resistivity from  $\rho_h$  to  $\rho_V$  reduced the maximum sensitivity from 192.3% to 50.7% and shifted the offsets at which these peaks occur from 8.8 km to 12.6 km. Once again, it seems the maximum sensitivity may not be detectable since about half of the signal is attributed to noise. The sensitivity at the mid-offset range decreased a significant amount as well, but these sensitivities still lie firmly above the noise level.

### 6.7.3 Updated 1D sensitivities

The changes in background resistivity going from  $\rho_h$  to  $\rho_V$  are depicted by the 1D models in Figure 6.38. With both  $\rho_h$  and  $\rho_V$ , the electrical anisotropy of the background layers can be reported. The anisotropy of the basement cannot be reported because the C-78 well did not penetrate the basement and there is no concrete data suggesting a value for  $\rho_h$ . Therefore, the basement was assumed to be *isotropic*. The calculation of the electrical anisotropy of the remaining three background regions is straightforward and they are:

$$\lambda_T = \sqrt{\frac{2.3}{1.4}} = 1.282,$$

$$\lambda_C = \sqrt{\frac{4.0}{2.0}} = 1.414,$$

$$\lambda_J = \sqrt{\frac{6.0}{3.5}} = 1.309.$$

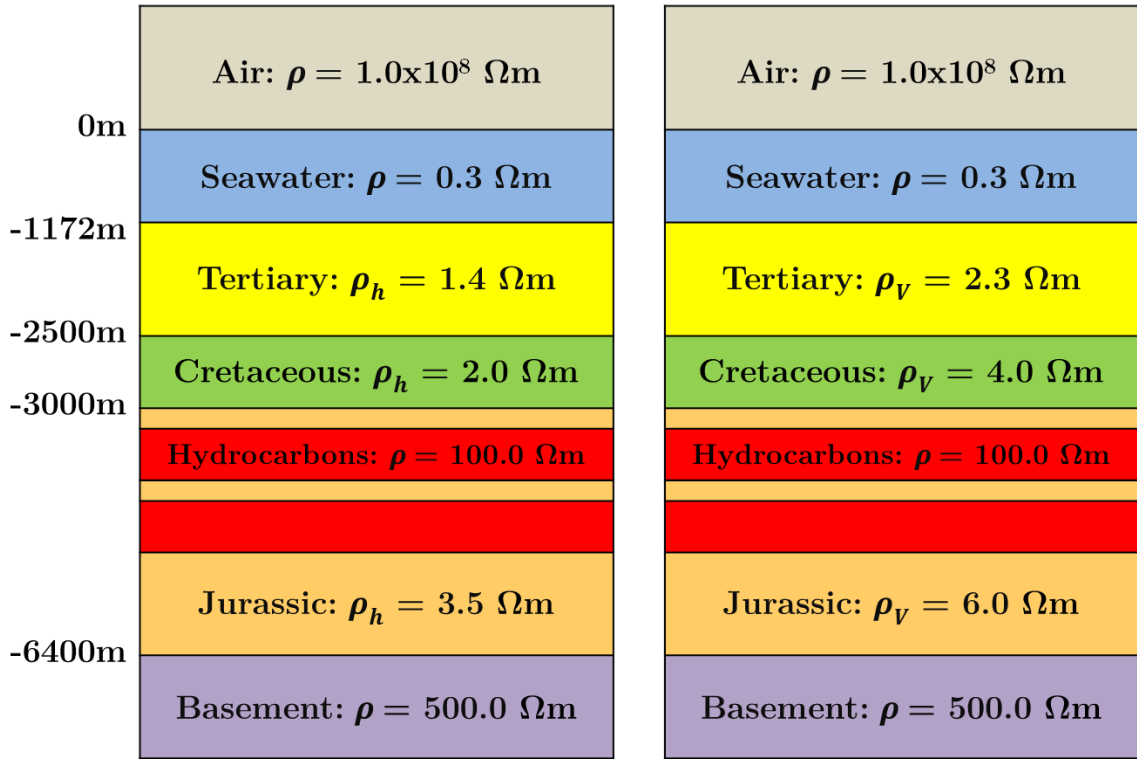


Figure 6.38: 1D resistivity models of the horizontal resistivities derived from the C-78 well log (left), and the vertical resistivities determined through the incremental simulation approach (right). These 1D models were used for the 1D simulations needed for Figure 6.39.

These values for the electrical anisotropy seem realistic. This assertion is supported by personal communication with Svein Ellingsrud from EMGS and Joe Molyneux from ExxonMobil who have both indicated that these values for electrical anisotropy are similar to what they have encountered in the Flemish Pass Basin.

An important consideration was revisiting the 1D sensitivity analysis performed in Section 6.2 with the updated vertical resistivities. In-line marine CSEM data was simulated for both the 1D models shown in Figure 6.38 using DIPOLE1D (Key, 2009). Figure 6.39 shows the corresponding 1D sensitivities to the Bay du Nord reservoir for both  $\rho_h$  and  $\rho_v$ . For each frequency, there is a clear shift in offset and

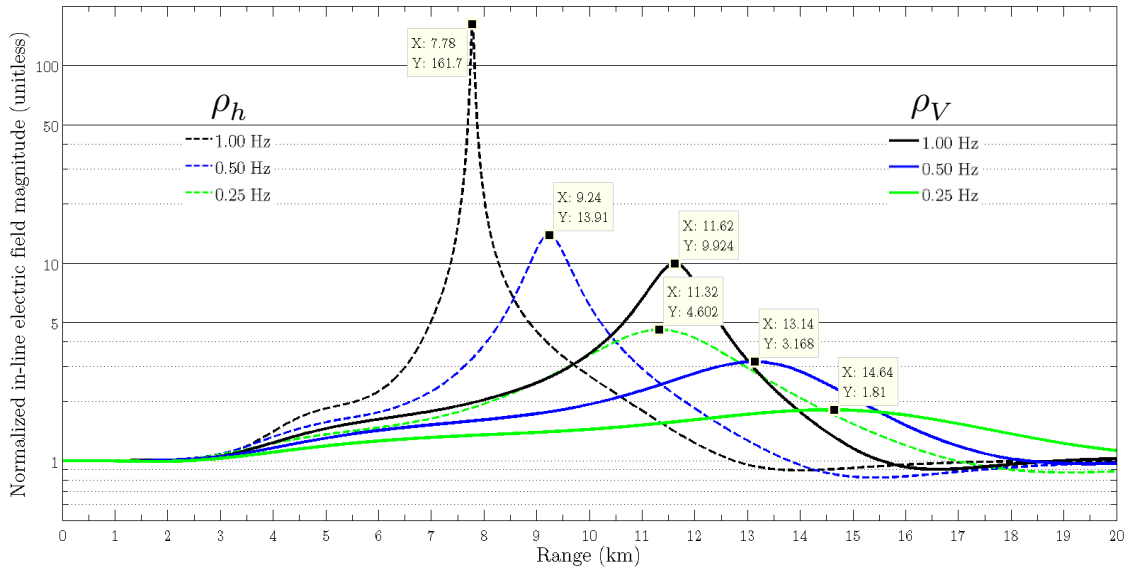


Figure 6.39: The 1D sensitivities of the Bay du Nord reservoir for both the horizontal and vertical resistivity models shown in Figure 6.38 and also for three different frequencies.

reduction of the maximum sensitivity. Interestingly enough, the sensitivity changes here in 1D match the changes to the reservoir sensitivity for 0.50 Hz in Figure 6.37(c). The 1D results in Figure 6.39 show the range at which the maximum sensitivity for  $f = 0.50$  Hz occurs is 9.24 km and 13.14 km for  $\rho_h$  and  $\rho_V$  respectively. Figure 6.37(c) shows that these same offsets in 3D occur at 8.8 km to 12.6 km for  $f = 0.50$  Hz. This shows that there is a good agreement and consistency between the synthetic 1D sensitivities and the 3D sensitivities computed from the Bay du Nord model.

## 6.8 Final results

The final component of this study is to simulate mCSEM responses at all the remaining receivers and for all the frequencies. The previous section determined the vertical resistivities necessary for matching the measured data using the incremental simulation approach. Again, for the interest of time, this curve matching process was only performed once (at RX15 for  $f = 0.50$  Hz). Recall from Figure 6.1 that there are twenty different receivers surrounding Bay du Nord that are considered for this study. The curve matching process would have to be applied *sixty times* if it was performed for each receiver and frequency. Therefore, the resistivities from the model for  $\rho_V$  in Figure 6.38 were used for all remaining receivers and frequencies. The only results shown in this section are those for RX59 and the remaining two frequencies for RX15.

### 6.8.1 Results for RX15

Section 6.7.2 synthesized results at RX15 with a frequency of  $f = 0.50$  Hz, but there are still two other frequencies to consider for this receiver. Figure 6.40 and Figure 6.41 show the amplitude, phase, and sensitivity for the frequencies of 0.25 Hz and 1.00 Hz respectively. In summary, the synthesized in-line amplitude and phase continues to match the measured mCSEM data quite well. The in-line amplitude for  $f = 0.25$  Hz in Figure 6.40 is exceptionally good and continues to match until roughly 12 km offset. An excellent match for the in-line amplitudes is also seen for  $f = 1.00$  Hz and this match continues until roughly 9 km offset. To some surprise, even the matches to the phase for both frequencies appear to be good.

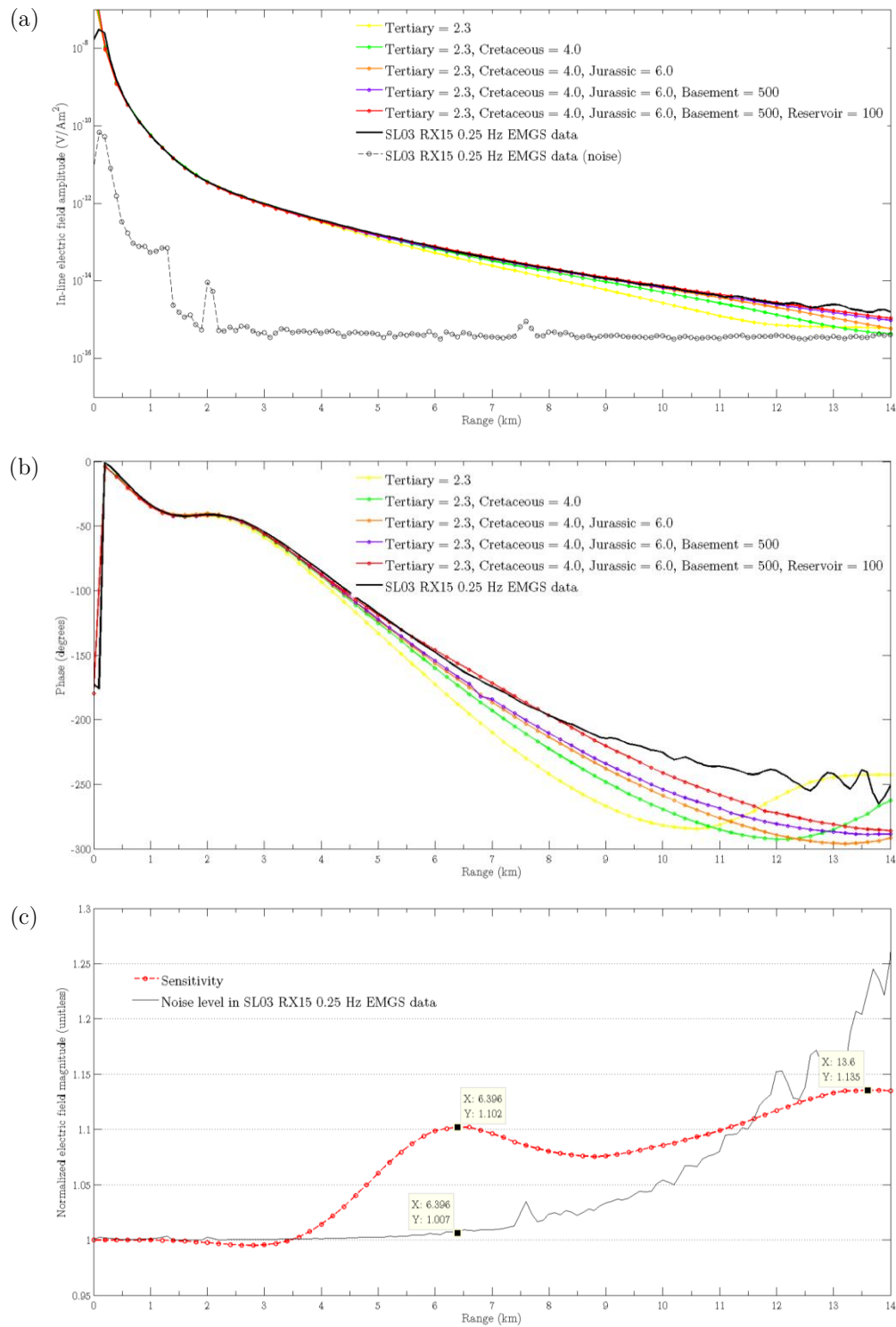


Figure 6.40: The computed (a) in-line amplitude, and (b) phase responses for each of the five meshes at RX15 for  $f = 0.25$  Hz. Panel (c) compares the sensitivity of the Bay du Nord reservoir to the measured noise level in RX15 for  $f = 0.25$  Hz.

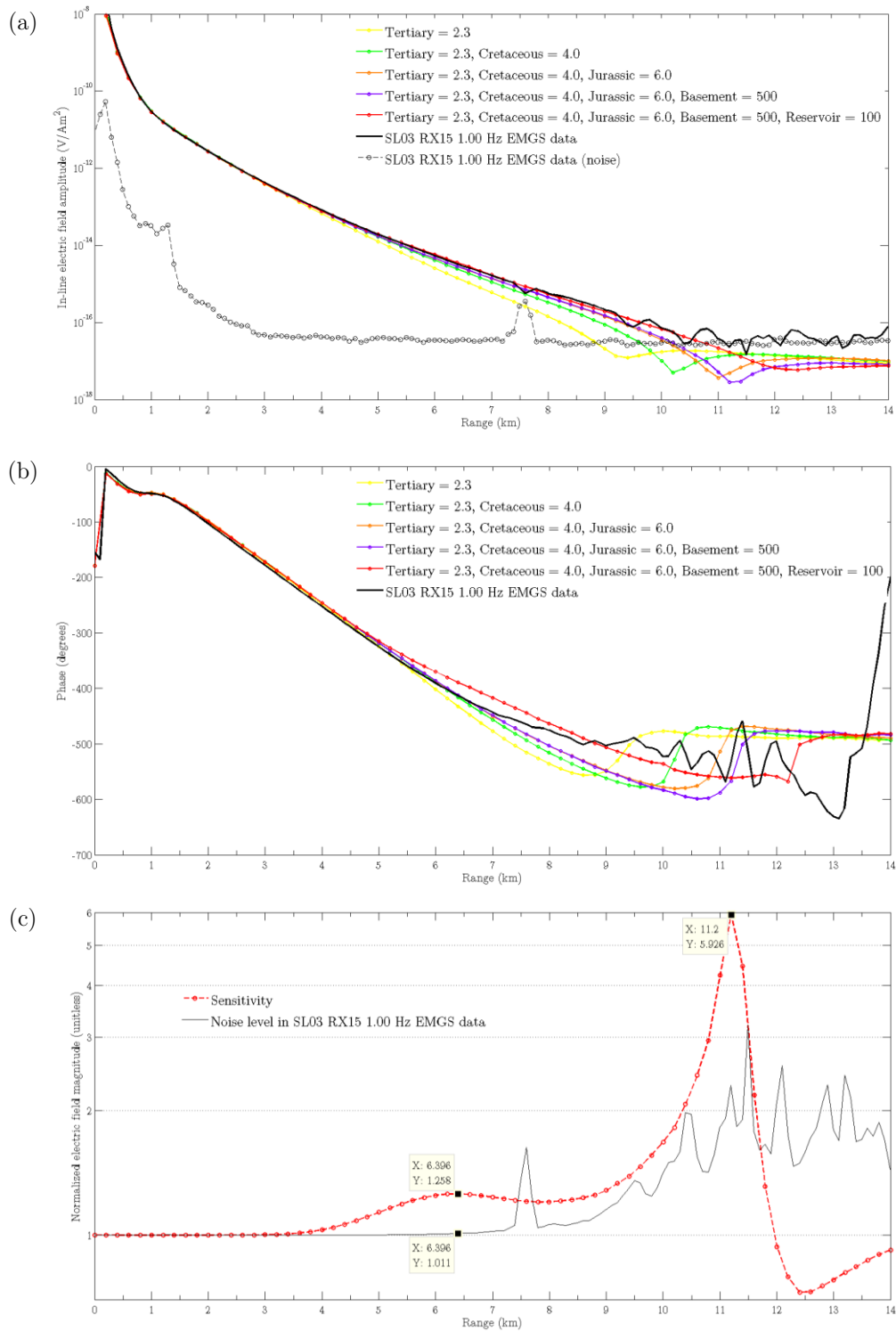


Figure 6.41: The computed (a) in-line amplitude, and (b) phase responses for each of the five meshes at RX15 for  $f = 1.00$  Hz. Panel (c) compares the sensitivity of the Bay du Nord reservoir to the measured noise level in RX15 for  $f = 1.00$  Hz.

The sensitivities for 0.25 Hz and 1.00 Hz exhibit a similar behavior to the sensitivity for 0.50 Hz shown in Figure 6.37. Still, it seems the maximum sensitivities occur at an offset that is dominated by noise in the data. However, similar to the Mizzen chapter, the sensitivities in the mid-offset range lie above the noise level. The mid-offset sensitivity peaks for 0.25 Hz and 1.00 Hz are 10.2% and 28.5% respectively, whereas the noise levels are 0.7% and 1.1%.

### **6.8.2 Results for RX59**

For all the remaining receivers, data was only simulated from the background model and the reservoir model because these were the only two pieces of data needed to calculate sensitivity. The next set of simulations was performed at RX59 (see Figure 6.1 for location). The observation locations were chosen to extend southwest from this receiver so they would pass over the prospect. Figure 6.42, Figure 6.43, and Figure 6.44 show the amplitude, phase, and sensitivity for the frequencies of 0.25 Hz, 0.50 Hz, and 1.00 Hz respectively at RX59.

The synthesized in-line amplitude and phase still matches very well at each frequency which shows that the resistivities derived at RX15 still represent the data well at another receiver. However, at the near offset range of 1-5km, the in-line amplitudes from the reservoir model at each frequency show a minor deviation from the measured data. Even though this mismatch is minor, it does suggest that the resistivities of the shallow layers (i.e. Tertiary and Cretaceous) need to be modified slightly to achieve a better fit. Aside from the minor mismatch at near offsets, the predicted in-line amplitudes for 0.25 Hz, 0.50 Hz, and 1.00 Hz match

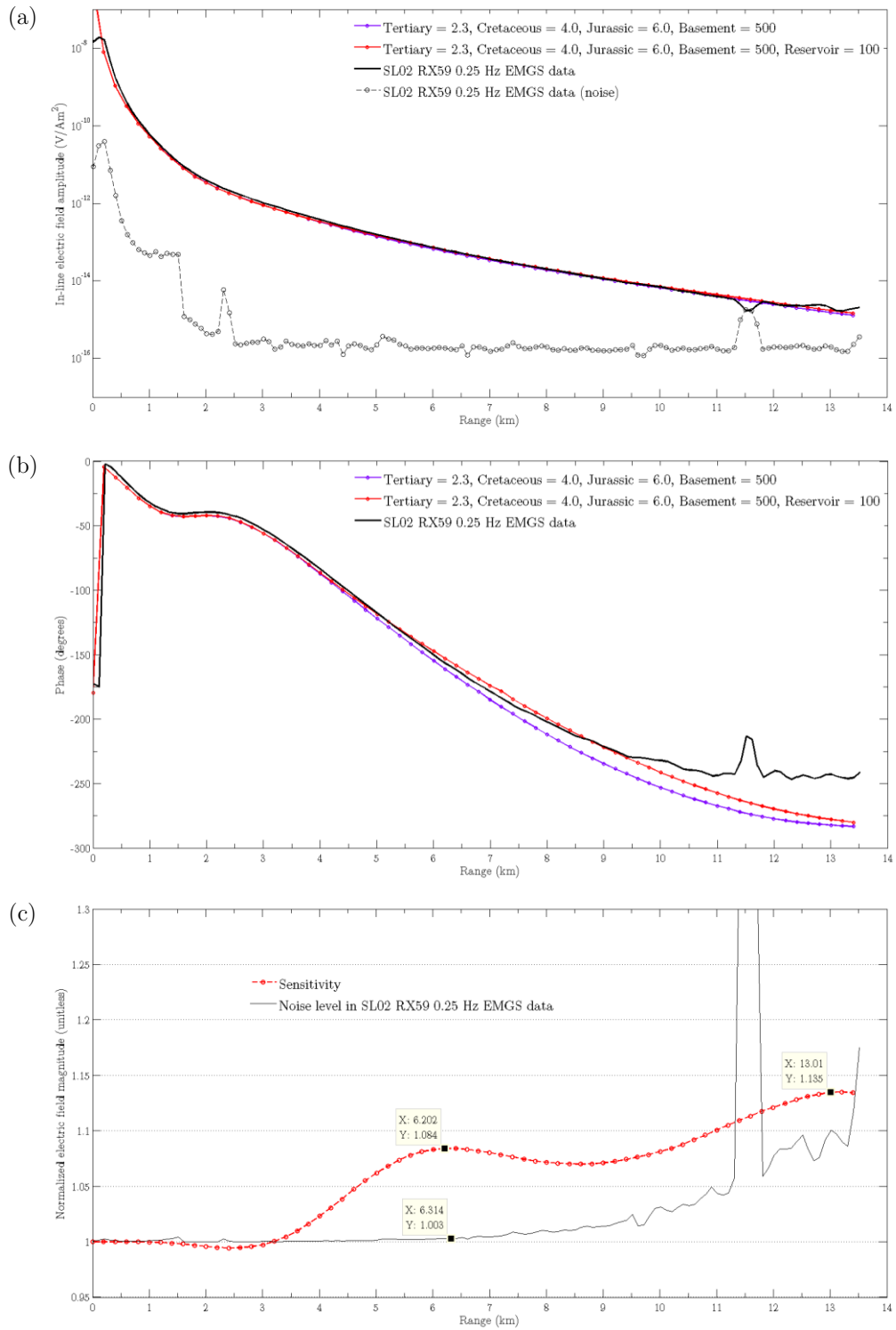


Figure 6.42: The computed (a) in-line amplitude, and (b) phase responses for the background and reservoir meshes only at RX59 for  $f = 0.25$  Hz. Panel (c) compares the sensitivity of the Bay du Nord reservoir to the measured noise level in RX59 for  $f = 0.25$  Hz.

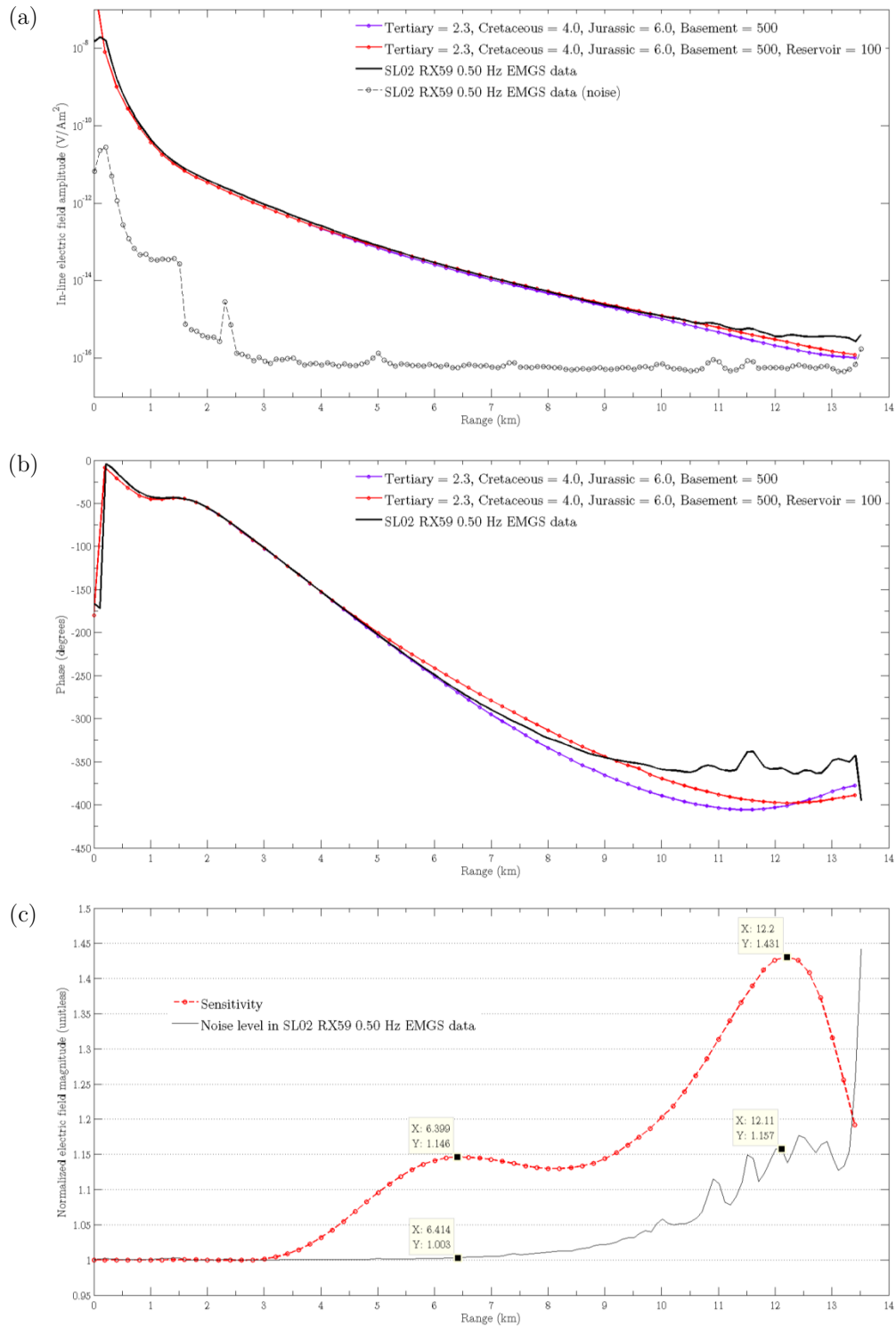


Figure 6.43: The computed (a) in-line amplitude, and (b) phase responses for the background and reservoir meshes only at RX59 for  $f = 0.50$  Hz. Panel (c) compares the sensitivity of the Bay du Nord reservoir to the measured noise level in RX59 for  $f = 0.50$  Hz.

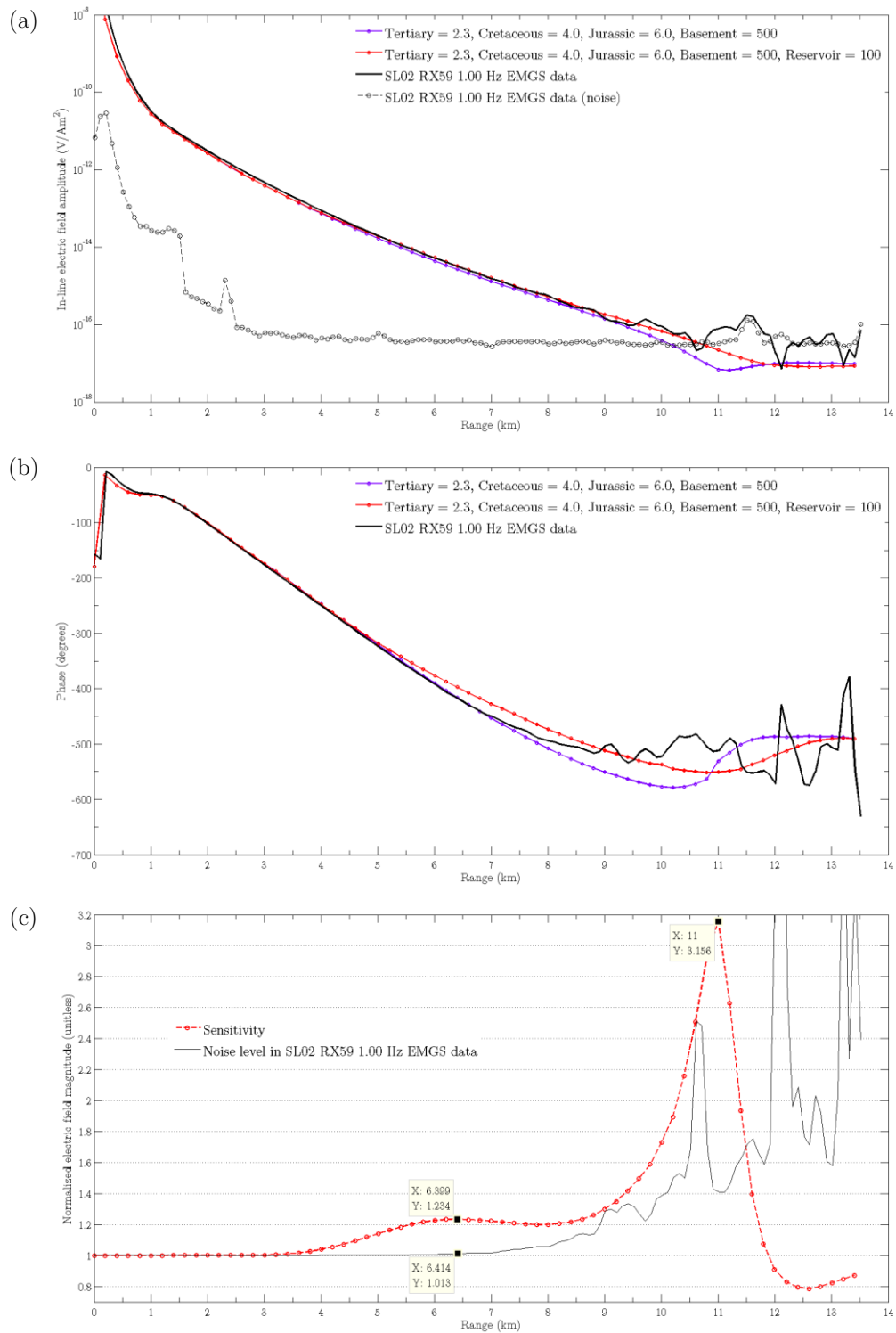


Figure 6.44: The computed (a) in-line amplitude, and (b) phase responses for the background and reservoir meshes only at RX59 for  $f = 1.00$  Hz. Panel (c) compares the sensitivity of the Bay du Nord reservoir to the measured noise level in RX59 for  $f = 1.00$  Hz.

the measured in-line amplitudes until 12 km, 11 km, and 9 km offset respectively. From a skin depth perspective, 0.25 Hz is most sensitive to deeper structure and to see the predicted amplitudes matching the measured in-line amplitudes so well provides supporting evidence that the choice of basement resistivity is correct.

The sensitivities for each frequency at RX59 exhibit similar behavior to those at RX15. The maximum sensitivities occur at an offset dominated by noise (with the exception of  $f = 0.50$  Hz; the noise accounts for roughly half of the signal). Also, the ranges at which these maximum sensitivities occur roughly align with those from the 1D sensitivities in Figure 6.39. The mid-offset ranges continue to have a sensitivity, albeit smaller, that still lies well above the noise level. The measured noise levels at these mid-offset ranges appear to be 1% or less for all three frequencies, whereas the sensitivities are 8.4%, 14.6%, and 23.4% for 0.25 Hz, 0.50 Hz, and 1.00 Hz respectively.

### 6.8.3 Sensitivity summaries

An easier way to visualize all the data from this study is through the sensitivity curves because they condense the important information from the in-line amplitudes into one curve. Figure 6.45 shows the sensitivity curves for six of the twenty receivers – three each from survey layout two and three – broken up into one panel for each frequency (see Figure 6.1 for receiver locations). Each of the three panels is plotted on the same vertical scale in order to easily see the relative sensitivity changes between each frequency. Panel (a) shows the sensitivities for the six receivers at  $f = 0.25$  Hz. There appears to be a consistency between most of

the curves as the maximum sensitivities all equate to 10-13% at an offset of 13 km. At the mid-offset range, the sensitivities equate to 8-11%. Moving to panel (b), which shows the sensitivities for 0.50 Hz, there is an obvious increase in the sensitivity for all receivers. The maximum sensitivities are 30-50% at an offset of 12 km, and the sensitivities are 14-17% for the mid-offset range. Panel (c) shows the sensitivities for 1.00 Hz and there is an even larger increase in the sensitivity of all the receivers. The maximum sensitivities equate to 150-500% (not seen) at an offset of 10 km, and for the mid-offset range the sensitivities are 23-26%.

An anomaly among these six receivers is RX49. Notice how the transmitter line associated with RX49 (CSEM Line#7 – see Figure 6.1) does not cut across the reservoir body whereas the transmitter lines for the other receivers do pass over the reservoir body. The reservoir is *broadside* to the transmitter path rather than in-line and this explains why the sensitivity is lower at this receiver for all three frequencies. Also, close inspection of the noise levels indicates that RX49 has a slightly higher noise level than the other five receivers, and there is a reasonable explanation as to why. The other five receivers are situated around the reservoir and the sensitivities are quite strong. For any given frequency, the measured noise (not % noise level) is consistent, and the presence of a reservoir will increase the value of the in-line amplitude (i.e. the signal), and by extension, increase the signal-to-noise ratio. This explains why RX49 has the *highest noise level*. The other five receivers are geometrically situated to pick up a strong signal from the reservoir, and by extension, improve their signal-to-noise ratio. However, from a geometrical standpoint, RX49 will not recover as much signal from the reservoir to

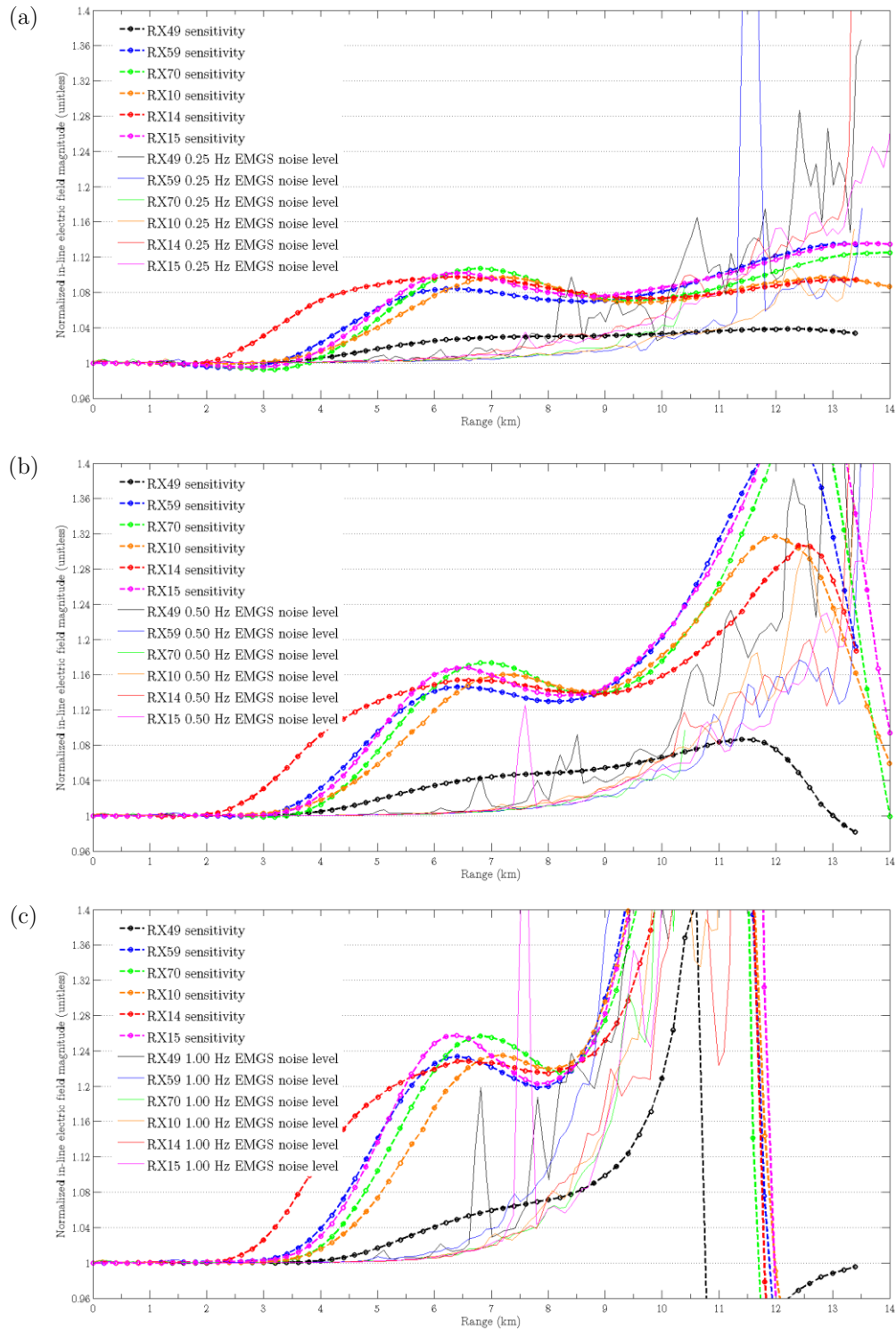


Figure 6.45: The sensitivity summaries for the Bay du Nord reservoir at six of the twenty receivers for (a)  $f = 0.25$  Hz, (b)  $f = 0.50$  Hz, and (c)  $f = 1.00$  Hz. The noise level at each receiver for each frequency is shown to help establish if the sensitivities are detectable. All three panels are plotted on the same vertical scale to indicate the relative sensitivity changes between each frequency.

increase the measured in-line amplitude, and therefore contains a higher noise level. As a whole, this phenomenon also explains why the synthesized data was able to maintain good matches with the measured data at slightly larger offsets compared to the Mizzen study. The Bay du Nord reservoir is much larger than the Mizzen reservoir, and may have a slightly higher signal-to-noise ratio for the same offset.

An effective tool to visualize the sensitivities from all of the receivers (not just six) is through *topographical maps*. The sensitivity analysis thus far has focused on the maximum sensitivity at far offsets and the smaller sensitivity anomalies in the mid-offset range. Showing these sensitivities in the form of a map will indicate *how the sensitivities vary laterally*. To do this, the maximums for the sensitivities at mid and far offsets were extracted from each receiver and each frequency. This resulted in 120 data points. A map was created for each frequency and for both the mid and far offset ranges resulting in six distinct maps. The data representation for each of these maps is quite sparse because there are only twenty data points (i.e. receivers) for each map. Consequently, it did not seem appropriate to interpolate using a dense grid spacing; instead, an arbitrary coarse grid spacing of 500m was used. For the interpolation parameters, the minimum sensitivity for each map was set to zero, and the maximum was set to the largest recorded value for *that* map. These parameters were enforced to help constrain the interpolation and prevent any artifacts from being introduced into the maps.

Figure 6.46, Figure 6.47, and Figure 6.48 show the mid-offset and far-offset sensitivity maps for 0.25 Hz, 0.50 Hz, and 1.00 Hz respectively. The locations of all

twenty receivers and the Bay du Nord reservoir extent are shown for reference. As a whole, the largest sensitivities are situated at receivers along CSEM Lines #8 and #9 because the transmitter passes over the reservoir body. For CSEM Lines #7 and #10, the transmitter path is broadside to the reservoir body and the sensitivities are subsequently smaller. Also, the receivers located directly above the reservoir body do not show a strong anomaly; the receivers situated just outside the reservoir boundary have the highest sensitivities. This is a result of the geometrical interaction between the reservoir and the position of the receiver (this same phenomenon was discussed in Section 5.9.2).

Upon inspection, it is clear the mid-offset sensitivity anomalies are consistent between all three frequencies. The sensitivities for the receivers along CSEM Line #9 seem to be slightly stronger than those along CSEM Line #8. This is likely a result of the reservoir being shallower on the eastern and southern sides (i.e. near the attachment zones) and deeper on the western and northern sides. Figure 6.46(a), Figure 6.47(a), and Figure 6.48(a) are practically useful because the stronger anomalies show the sensitivities that lie above the noise level.

The sensitivity maps for the far-offset range (i.e. the maximum sensitivity) are much different from the mid-offset sensitivity maps in that there are significant changes between frequencies. Recall the earlier statement that the reservoir body under CSEM Line #9 is shallower than it is under CSEM Line #8. However, a frequency of 0.25 Hz is more sensitive to *deeper* structure and the sensitivity anomalies surrounding the reservoir are broad. As a result, there is not much

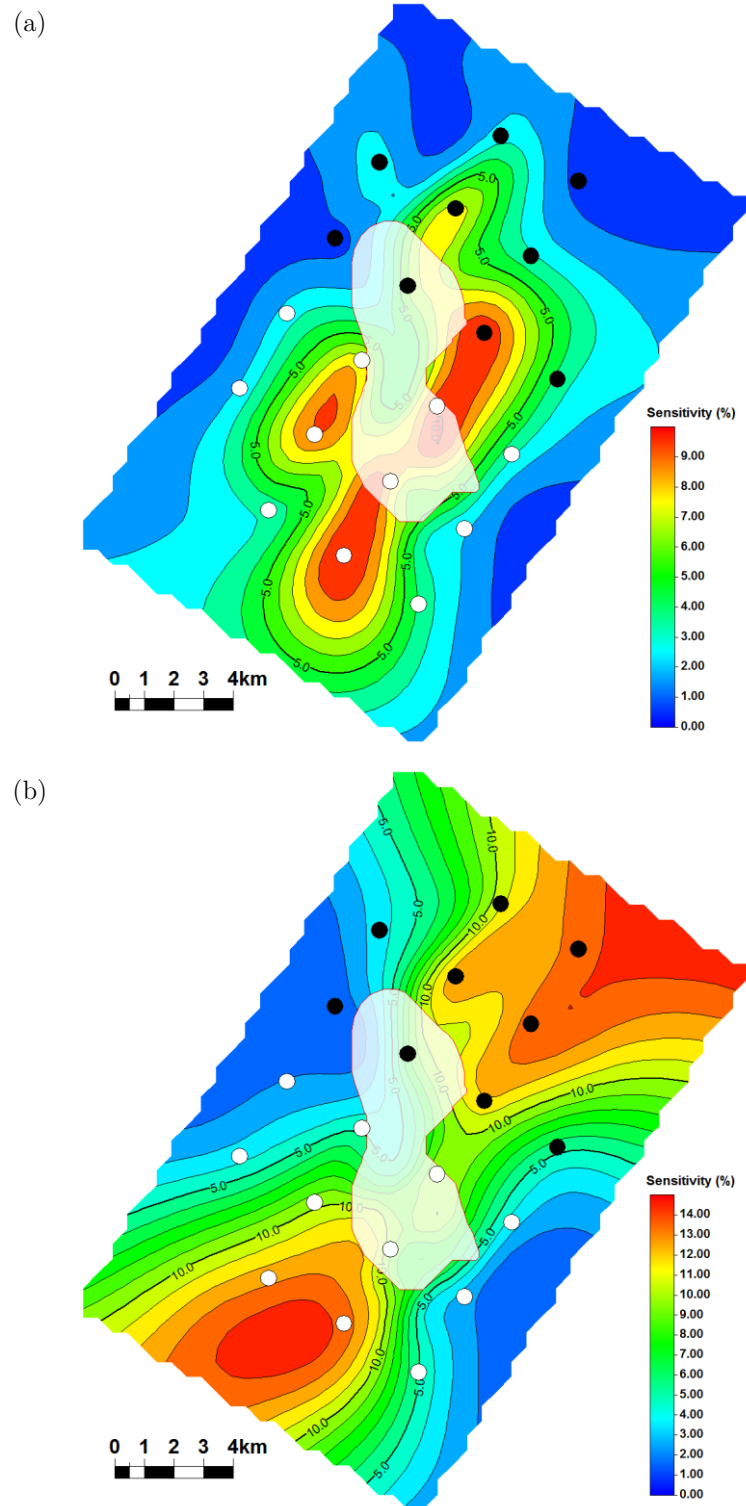


Figure 6.46: The (a) mid-offset and (b) far-offset sensitivity maps for  $f = 0.25$  Hz. The locations of all twenty receivers and the Bay du Nord reservoir extent are shown for reference. Note the difference in color bar values for panel (a) and panel (b).

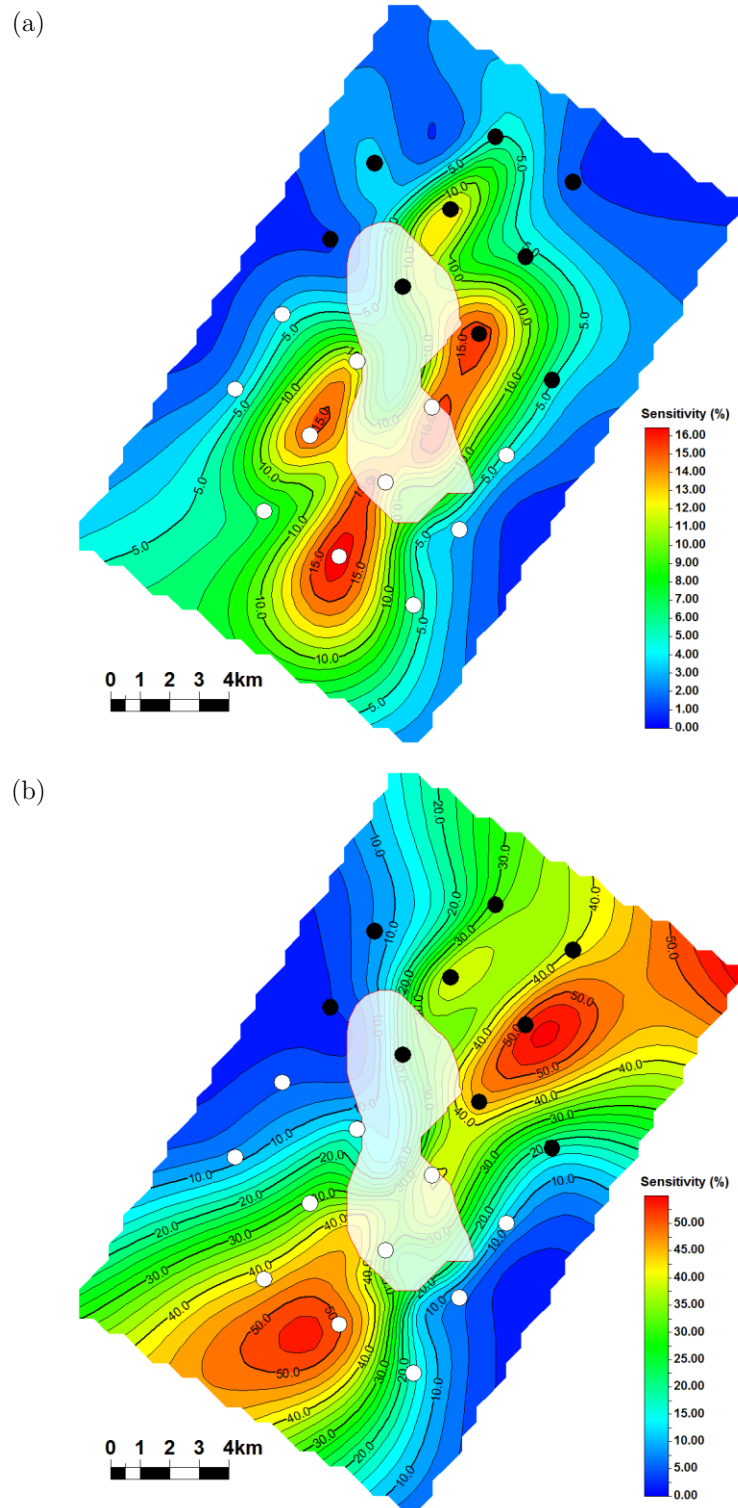


Figure 6.47: The (a) mid-offset and (b) far-offset sensitivity maps for  $f = 0.50$  Hz. The locations of all twenty receivers and the Bay du Nord reservoir extent are shown for reference. Note the difference in color bar values for panel (a) and panel (b).

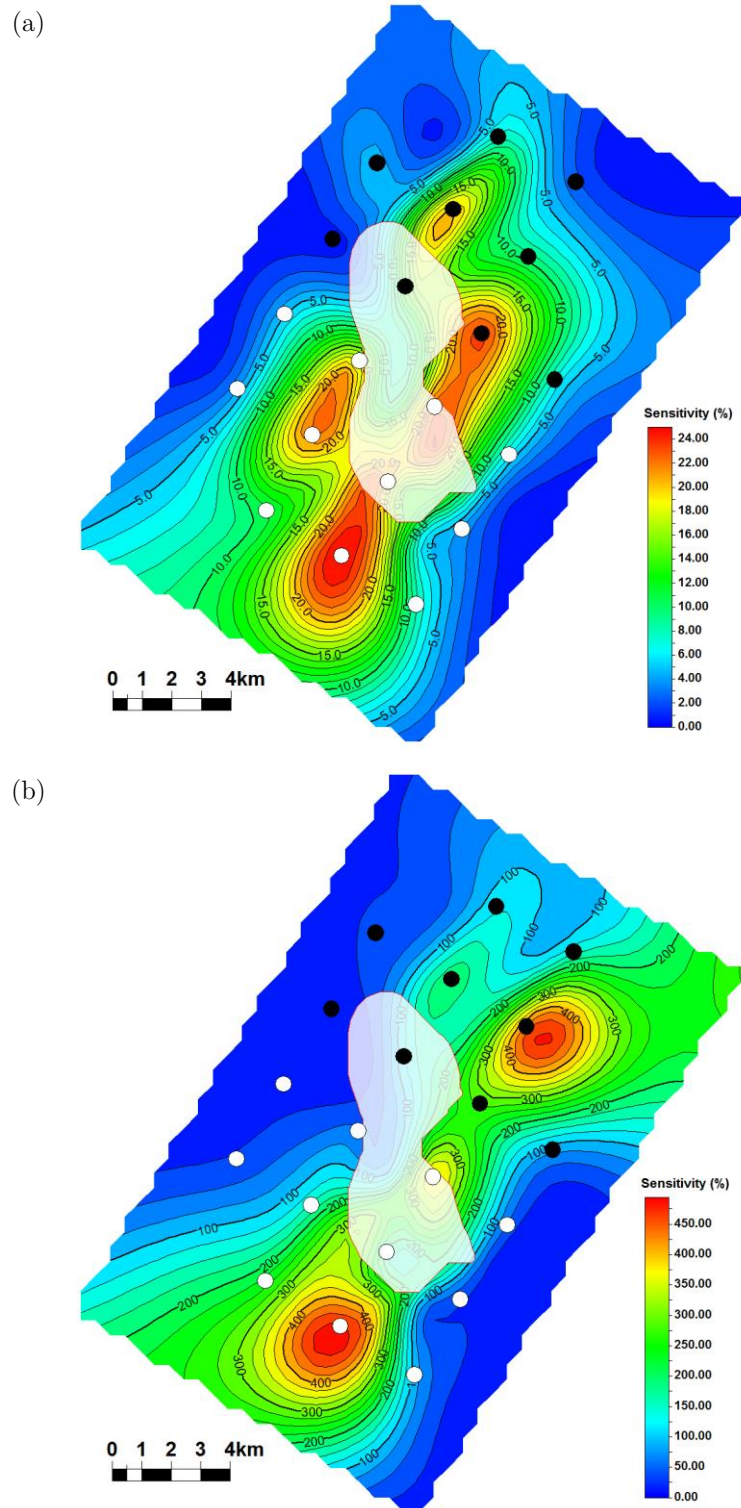


Figure 6.48: The (a) mid-offset and (b) far-offset sensitivity maps for  $f = 1.00$  Hz. The locations of all twenty receivers and the Bay du Nord reservoir extent are shown for reference. Note the difference in color bar values for panel (a) and panel (b).

difference in the sensitivity between CSEM Lines #8 and #9. As the frequencies increase to  $f = 0.50$  Hz and to  $f = 1.00$  Hz, the anomalies begin to focus towards CSEM Line #9. The sensitivity anomalies for  $f = 1.00$  Hz in Figure 6.48(b) show very strong anomalies along CSEM Line #9. Even though the sensitivities shown in Figure 6.46(b), Figure 6.47(b), and Figure 6.48(b) are likely not detectable, they do still provide a consistent and verifiable interpretation regarding the depth of the reservoir.

## 6.9 Bay du Nord Conclusions

The investigation of 3D mCSEM forward modeling at the Bay du Nord prospect was performed with two desired outcomes in mind: (1) to show that the finite-element forward modeling technique can successfully simulate data from an even more complex model, and (2) use this technique to show a more detectable sensitivity exists for a more economically sized reservoir.

Building the resistivity model for Bay du Nord used the same process for building the Mizzen model in the previous chapter. The two main differences in this model were (1) it contained four instead of three geochronologic surfaces, and (2) the reservoir body was far more complex. The base Cretaceous surface was able to be successfully included in the Bay du Nord model, whereas this surface was excluded from the Mizzen model. The improvement in seismic data coverage surrounding Bay du Nord that was available to this thesis allowed for a more complex representation of the reservoir to be built. The top-of-sand surface was built using the  $\rho_V$  inversion from EMGS and three seismic lines. Debugging the final reservoir

model showed how different components of the final reservoir mesh impacted the convergence, and these discoveries could be important for future model building studies.

The final Bay du Nord reservoir mesh certainly utilized the full benefits of an unstructured grid in many ways. Using an unstructured grid allowed the topography of the four geochronologic surfaces and the reservoir body to be accurately represented. Furthermore, using an unstructured grid allowed the mesh to have constraints (on the surfaces and reservoir body) and refinement at critical locations (observation locations). Recall that imposing constraints on the reservoir body drastically reduced the total number of cells and ultimately allowed the iterative solver to converge. Despite the two added complexities of the Bay du Nord model, the 3D finite-element forward modeling software (CSEM3DFWD) continued to successfully simulate mCSEM data.

The second desired outcome of this study was to use this forward modeling technique to show a more detectable sensitivity exists for a more economically sized reservoir. The practical motivation was different for this study because the reservoir potential at Bay du Nord is fairly certain based on the success of the C-78 well and the supporting evidence from the seismic data. Therefore, it would have been redundant to specifically assess the reservoir potential of Bay du Nord. Instead, this study took a different approach and sought to show Bay du Nord gives a stronger, more detectable mCSEM sensitivity compared to Mizzen. The larger lateral extent and recoverable oil estimate both suggested that the Bay du

Nord reservoir is undoubtedly larger than the Mizzen reservoir. Therefore, the obvious prediction was Bay du Nord would certainly have a higher sensitivity, but the question was by how much.

Table 6-4 shows a summary of the strongest sensitivities at both offset ranges for the Mizzen and Bay du Nord reservoirs. The sensitivities at each frequency for both the mid-offset and far-offset ranges were reported in Section 5.9.2 and Section 6.8.3 for the Mizzen and Bay du Nord reservoirs respectively. The sensitivity peaks for each offset interval were easy to deduce, but determining the noise levels surrounding these peaks was not trivial because the noise levels are highly variable. So, the best estimate was used to determine the noise level for all the scenarios at both prospects. Table 6-4 indicates that the sensitivity peaks at far offsets for Bay du Nord are 4-5 $\times$  greater than they are for Mizzen. This is a significant increase and is to be expected. The mid-offset sensitivities appear to be 3 $\times$  greater than they are for Mizzen.

However, when these sensitivities are interpreted in the context of the noise level in the measured mCSEM data, the maximum sensitivities still appear to be undetectable despite the Bay du Nord reservoir being much larger. This is unfortunate because the strongest difference in sensitivity between the Bay du Nord and Mizzen reservoirs occurs at the far-offset range. Nevertheless, the mid-offset range continues to hold promise. Recall from the Mizzen chapter conclusions that the sensitivities in the mid-offset range did not lie appreciably above the noise level and the reservoir was deemed borderline detectable. The noise levels at each

Table 6-4: A summary of the strongest sensitivities at both offset ranges and at the three frequencies considered for the Mizzen and Bay du Nord reservoirs. The noise levels are reported at each frequency and offset range to help determine if the sensitivities are detectable.

<b>Mizzen sensitivity summary</b>				
Frequency	Mid-offset sensitivity	Mid-offset noise level	Far-offset sensitivity	Far-offset noise level
0.25 Hz	2.0 - 3.5%	0.5 - 2.0%	3 - 4%	10 - 20%
0.50 Hz	3.5 - 6.0%	0.5 - 2.0%	7 - 11%	15 - 30%
1.00 Hz	6 - 11%	0.5 - 5.0%	30 - 90%	40 - 100%
<b>Bay du Nord sensitivity summary</b>				
Frequency	Mid-offset sensitivity	Mid-offset noise level	Far-offset sensitivity	Far-offset noise level
0.25 Hz	8 - 11%	0.5 - 2.0%	10 - 13%	10 - 16%
0.50 Hz	14 - 17%	0.5 - 2.0%	30 - 50%	15 - 25%
1.00 Hz	23 - 26%	0.5 - 6.0%	150 - 500%	50 - 100%

frequency are comparable for the Mizzen and Bay du Nord measured data, but the mid-offset sensitivities for Bay du Nord are  $3\times$  larger than they are for Mizzen. If Mizzen is borderline detectable and Bay du Nord has sensitivities that are  $3\times$  greater, then by extension, it is easy to assert that the Bay du Nord reservoir should be detectable. The vertical resistivity inversion from EMGS (see Figure 6.14) also gives concrete evidence to support this claim given the strong anomaly surrounding the C-78 well. In summary, the data suggests a more discernable and detectable sensitivity exists for the Bay du Nord reservoir.

### 6.9.1 Assumptions

The outcomes of this chapter showed this finite-element forward modeling technique continues to successfully simulate mCSEM data from even more complex models, and also showed the Bay du Nord reservoir contains a detectable sensitivity. However, it is necessary to not overlook the assumptions and simplifications required to achieve these outcomes.

A majority of the assumptions and simplifications for this chapter occurred during the reservoir building stage. Recall from the C-78 well log that there are two distinct 50m thick sand packages, and a simplification was made by representing these two sand bodies as one 100m sand package. The lateral extent of the Bay du Nord reservoir relied almost exclusively on the inversion from EMGS, so the accuracy of the lateral extent is dependent on a product that this thesis had no involvement with. Even with the lateral extent constrained, there were still only three seismic lines to constrain the *topography* of the top-of-sand surface. A substantial amount of interpolation was required in order to fill the voids. This process for determining the top-of-sand surface was only done once, and the base-of-sand surface was exactly the same as the top-of-sand surface except shifted down 100m. As a result, this assumes the reservoir is a *constant thickness* of 100m. Therefore, if there are any thinning/thickening regions of the reservoir, these are not accounted for.

The last assumption was during the numerical simulation stages of this chapter. Similar to the Mizzen study, the incremental simulation process used to determine

vertical resistivities was only performed at one receiver for a given frequency (RX15 at  $f = 0.50$  Hz). These resistivities were subsequently used for simulations at each frequency for all 19 remaining receivers. This assumes each region (i.e. Tertiary, Cretaceous, etc.) in the model contains a homogeneous resistivity. Marine sediments likely have some degree of lateral inhomogeneity, so this assumption may not hold in all cases. Any lateral changes could have been accounted for by using the incremental simulation process at each receiver, but in the interest of time this was not done. Despite this assumption, the simulated data still maintained adequate matches to the measured data at the other receivers.

# Chapter 7

## Conclusions

### 7.1 Modeling conclusions

Most research in EM numerical modeling has focused on simulating data from simple models for verification and proof of concept purposes. Specifically in regard to marine CSEM modeling, there have been many examples of forward modeling codes applied to the common synthetic canonical disk model (Weiss and Constable, 2006; Um et al., 2010). Recently, there have been some 3D finite-element EM modeling codes applied to marine CSEM examples that involve complex *synthetic* models (Puzyrev et al., 2013; Um et al., 2013). However, using a 3D finite-element CSEM forward modeling method to synthesize data from a *real* complex model built from *real data* – the focus of this thesis – is, to the best of my knowledge, a novel contribution to the field.

This thesis had two primary objectives: (1) to show the finite-element forward modeling code can synthesize data from real complex models built using

unstructured grids, and (2) use this forward modeling technique to provide additional support and interpretations for two real offshore exploration scenarios in the Flemish Pass Basin. The process of building the real complex models, generating meshes, and synthesizing data were very challenging. This process required many iterations and investigations to optimize the size of the meshes and recover quality results. Models for the Mizzen and Bay du Nord fields were built using seismic data, well logs, and other supplemental pieces of information. The finite-element code provided by Ansari and Farquharson (2014) was able to synthesize data from these large complex models built from real data. Good quality results were still able to be recovered despite the models containing many topographical surfaces, and in the case of the Bay du Nord model, a complex reservoir body.

A critical component of this thesis was being able to compare the synthesized results to measured mCSEM data from EMGS. Having access to real measured data not only helped establish the resistivities for the models through comparisons in the incremental simulations, but it also allowed the computed sensitivities to be interpreted in the context of the measured noise levels. Sensitivity to the Mizzen reservoir was found, but the sensitivities were small and likely below the detectability threshold. This is a result of the reservoir being small and uneconomical. However, the Bay du Nord reservoir was much larger and the sensitivity analysis confirmed this reservoir was detectable.

## 7.2 Improvements and considerations

The results of this thesis were insightful and show the versatility of finite-element forward modeling, but in hindsight, there are aspects of this thesis that could be improved. Many assumptions were required in creating the reservoir bodies for both the Mizzen and Bay du Nord chapters. If 3D seismic data were available then the reservoir bodies would have been much more refined and likely more accurate, but this was a consequence beyond control.

A component of this thesis that there was control over was the process to determine the vertical resistivities. This process was applied to only one receiver at one frequency for both studies, and the vertical resistivities established through the incremental simulation technique were used for all subsequent simulations. Using resistivities derived at one receiver caused minor mismatches between predicted and observed data at other receivers. As a whole, the matches to the measured data were all satisfactory, but in hindsight, if the incremental simulation process was restricted to being applied to only one receiver, then there is a more refined approach. Instead of using only one frequency at a chosen receiver, *many frequencies should have been used to refine the choices for resistivities*. Higher frequencies will be more sensitive to shallower layers (i.e. Tertiary and Cretaceous) and lower frequencies will be more sensitive to deeper layers (i.e. Jurassic and basement). Therefore, when determining the resistivities for shallower and deeper layers, the curve matching process via incremental simulation should have been applied to higher *and* lower frequencies respectively.

The analysis in this thesis was quite comprehensive, but there are still other avenues that could build upon this work. First of all, this thesis only considered simulations and comparisons to *in-line* mCSEM data. It would be insightful from a consistency standpoint to see if mCSEM data simulated from resistivities taken directly from well logs had a close match to the measured *broadside* mCSEM data. The most important consideration that was not within the scope of this thesis was considering the finite-difference method on structured grids for comparison purposes. Could the complex models considered in this thesis be represented on a *structured mesh*? In all likelihood, simplifications would have to be made (i.e. topography approximated as a stair-step pattern). Electromagnetic fields are diffusive, so how much would the synthesized data change if the model geometries were represented with something simple (structured grid) instead of something complex (unstructured grid)? In the context of marine CSEM, any advantages of the finite-element method may not truly become apparent until direct and tangible comparisons are made to the finite-difference method.

# References

- Ansari, S., and C. G. Farquharson, 2014, 3D finite-element forward modeling of electromagnetic data using vector and scalar potentials and unstructured grids: *Geophysics*, **79**, no. 4, E149-E165, <http://dx.doi.org/10.1190/geo2013-0172.1>
- Avdeev, D. B., 2005, Three-dimensional electromagnetic modelling and inversion from theory to application: *Surveys in Geophysics*, **26**, 767–799.
- Avdeev, D.B., A.V Kuvshinov, O.V Pankratov, and G.A Newman, 1997, High-performance three-dimensional electromagnetic modelling using Neumann series. Wide band numerical solution and examples: *Journal Geomagn. Geoelectr.*, **49**, no. 11-12, 1519–1539.
- Badea, B., M. Everett, G. Newman, and O. Biro, 2001, Finite element analysis of controlled-source electromagnetic induction using Coulomb gauged potentials: *Geophysics*, **66**, 786–799, doi: 10.1190/1.1444968.
- Bannister, P. R., 1968, Electromagnetic fields within a stratified earth produced by a long horizontal line source: *Radio Science*, **3**, 387–390.
- Behrens, J., The detection of electrical anisotropy in 35 Ma Pacific Lithosphere: Results from a marine controlled source electromagnetic survey and implications for hydration of the upper mantle, Ph.D. Thesis, University of California, San Diego, 2005.
- Cagniard, L., 1953, Basic theory of the magnetotelluric method of geophysical prospecting: *Geophysics*, **18**, 605–635, doi: 10.1190/1.1437915.

- Chen, J., D. W. Oldenburg, and E. Haber, 2005, Reciprocity in electromagnetics: application to modelling marine magnetometric resistivity data: *Physics of the Earth and Planetary Interiors*, 150, 45-61.
- Chiburis, E., 1993, Hydrocarbon detection with AVO: *Oilfield Review*, 42-50.
- Coggon, J. H., 1971, Electromagnetic and electrical modeling by the finite element method: *Geophysics*, **36**, no.1, 132–155, doi: 10.1190/1.1440151.
- Colombo, D., T. Keho, and G. McNeice, 2012a, Integrated seismic-electromagnetic workflow for subbasalt exploration in northwest Saudi Arabia, 2012: *The Leading Edge*, **31**, 42–52, doi: 10.1190/1.3679327.
- Commer, M., and G. Newman, 2004, A parallel finite-difference approach for 3D transient electromagnetic modeling with galvanic sources: *Geophysics*, **69**, no. 5, 1192–1202, <http://dx.doi.org/10.1190/1.1801936>.
- Constable, S., 2010, Ten years of marine CSEM for hydrocarbon exploration: *Geophysics*, **75**, no. 5, 75A67-75A81, <http://dx.doi.org/10.1190/1.3483451>.
- Constable, S., and L. J. Srnka, 2007, An introduction to marine controlled source electromagnetic methods for hydrocarbon exploration: *Geophysics*, **72**, no. 2, WA3–WA12, <http://dx.doi.org/10.1190/1.2432483>.
- Constable, S., and C. J. Weiss, 2006, Mapping thin resistors and hydrocarbons with marine EM methods: Insights from 1D modeling: *Geophysics*, **71**, no. 2, G43–G51, <http://dx.doi.org/10.1190/1.2187748>.
- Cox, C. S., 1981, On the electrical conductivity of the oceanic lithosphere: *Physics of the Earth and Planetary Interiors*, **25**, 196–201.
- Eidesmo, T., S. Ellingsrud, L. M. MacGregor, S. Constable, M. C. Sinha, S. Johanson, F. N. Kong, and H. Westerdahl, 2002, Sea bed logging (SBL), a new

- method for remote and direct identification of hydrocarbon filled layers in deepwater areas: *First Break*, **20**, 144–152.
- Fanavoll, S., P. T. Gabrielsen, and S. Ellingsrud, 2014, CSEM as a tool for better exploration decisions: Case studies from the Barents Sea, Norwegian Continental Shelf: *Interpretation*, **2**, no. 3, SH55-SH66, <http://dx.doi.org/10.1190/INT-2013-0171.1>.
- Farquharson, C. G., and M. P. Miensopust, 2011, Three-dimensional finite-element modeling of magnetotelluric data with a divergence correction: *Journal of Applied Geophysics*, **75**, 699-710, doi:10.1016/j.jappgeo.2011.09.025.
- Filloux, J. H., 1967b, Oceanic electric currents, geomagnetic variations and the deep electrical conductivity structure of the ocean-continent transition of central California: Ph.D. thesis, University of California San Diego.
- Fomenko, E. Y., and T. Mogi, 2002, A new computation method for a staggered grid of 3D EM field conservative modeling: *Earth Planets Space*, **54**, 499–509.
- Foster, D. G., and A. G. Robinson, 1993, Geological history of the Flemish Pass Basin, offshore Newfoundland: *AAPG Bulletin*, **77**, 588-609.
- Gabrielsen, P. T., P. Abrahamson, M. Panzner, S. Fanavoll, and S. Ellingsrud, 2013, Exploring frontier areas using 2D seismic and 3D CSEM data, as exemplified by multient data over the Skrugard and Havis discoveries in the Barents Sea: *First Break*, **31**, 66–73.
- Gassmann, F., 1951, Über die Elastizität Poröser Medien: *Vier. der Natur. Gesellschaft in Zürich*, **96**, 1–23.
- Harrington, R. F., 1961, *Time-harmonic electromagnetic fields*: McGraw-Hill.

- Hohmann, G.W., 1975, Three-dimensional induced polarization and electromagnetic modeling: *Geophysics*, **40**, no.2, 309–324. <http://dx.doi.org/10.1190/1.1440527>.
- Hoversten, G. M., S. C. Constable, and H. F. Morrison, 2000, Marine magnetotellurics for base-of-salt mapping: Gulf of Mexico field test at the Gemini structure: *Geophysics*, **65**, 1476–1488, doi: 10.1190/1.1444836.
- Jegen, M.D., R.W Hobbs, P. Tarits, and A.D. Chave, 2009, Joint inversion of marine magnetotelluric and gravity data incorporating seismic constraints: Preliminary results of sub-basalt imaging off the Faroe Shelf: *Earth Planet Science Lett.*, **282**, 47–55.
- Jin, J. M., 2002, *The finite element method in electromagnetics*, 2nd ed.: John Wiley & Sons.
- Key, K., 2009, 1D inversion of multicomponent, multifrequency marine CSEM data: Methodology and synthetic studies for resolving thin resistive layers: *Geophysics*, **74**, no. 2, F9–F20, <http://dx.doi.org/10.1190/1.3058434>.
- Key, K., 2016, MARE2DEM: a 2-D inversion code for controlled-source electromagnetic and magnetotelluric data: *Geophysics Journal International*, **207**, 571-588, doi: 10.1093/gji/ggw290.
- Lee, M.W., 2004, Elastic velocities of partially gas-saturated unconsolidated sediments: *Marine and Petroleum Geology*, **21**, no. 6, 641–650, doi: 10.1016/j.marpetgeo.2003. 12.004.
- Li, Y., and K. Key, 2007. 2D marine controlled-source electromagnetic modeling: Part 1 — an adaptive finite-element algorithm: *Geophysics*, **72**, no. 2, WA51–WA62, doi: 10.1190/1.2432262.

- Liu, C., Z. Ren, J. Tang, and Y. Yan, 2008, Three-dimensional magnetotellurics using edge-based finite element unstructured meshes: *Applied Geophysics*, **5**, no. 3, 170–180, doi: 10.1007/s11770-008-0024-4.
- Livelybrooks, D., 1993, Program 3Dfeem, a multidimensional electromagnetic finite element model: *Geophysics Journal International*, **114**, 443–458.
- Løseth, L., and L. Amundsen, 2007, Removal of air-response by weighting inline and broadside CSEM/SBL data: 77th Annual International Meeting, SEG Expanded Abstracts, **26**, 529–533.
- Lu, X., D. Willen, J. Zhang, and I. Gallegos, 2006, Marine CSEM data processing techniques: SEG Technical Program Expanded Abstracts 2006, pp. 704-708, <http://dx.doi.org/10.1190/1.2370356>.
- Maaø, F. A., 2007, Fast finite-difference time-domain modeling for marine-subsurface electromagnetic problems: *Geophysics*, **72**, no. 2, A19–A23, <http://dx.doi.org/10.1190/1.2434781>.
- Maillet, R., 1947, The fundamental equations of electrical prospecting: *Geophysics*, **12**, 529-556, doi: 10.1190/1.1437342.
- Mareh J., and R.S. White, 2005, Seeing through a glass, darkly: strategies for imaging through basalt: *First Break*, **23**, no. 5, 27–33.
- Mitsuhata, Y., and T. Uchida, 2004, 3D magnetotelluric modeling using the T- $\Omega$  method: *Geophysics*, **69**, 108–119, <http://dx.doi.org/10.1190/1.1649380>
- Mogi, T., 1996, Three-dimensional modeling of magnetotelluric data using finite element method: *Journal of Applied Geophysics*, **35**, no.3, 185–189.

- Nam, M. J., H. J. Kim, Y. Song, T. J. Lee, J. S. Son, and J. H. Suh, 2007, 3D magnetotelluric modelling including surface topography: *Geophysical Prospecting*, **55**, 277–287, doi: 10.1111/j.1365-2478.2007.00614.x.
- Nédélec, J. C., 1980, Mixed finite element in R3: *Numerische Mathematik*, **35**, 315–341, doi: 10.1007/BF01396415.
- Newman, G. A., and D. L. Alumbaugh, 1995, Frequency-domain modeling of airborne electromagnetic responses using staggered finite differences: *Geophysical Prospecting*, **43**, 1021–1042, doi: 10.1111/j.1365-2478.1995.tb00294.x.
- Newman, G. A., and G. W. Hohmann, 1988, Transient electromagnetic response of high-contrast prisms in a layered earth: *Geophysics*, **53**, 691–706. <http://dx.doi.org/10.1190/1.1442503>.
- Newman, G., M. Commer, and J. Carazzone, 2010, Imaging CSEM data in the presence of anisotropy: *Geophysics*, **75**, no. 2, F51–F61, <http://dx.doi.org/10.1190/1.3295883>.
- Oristaglio, M. L., and G. W. Hohmann, 1984, Diffusion of electromagnetic fields into a two-dimensional earth: A finite difference approach: *Geophysics*, **49**, 870–894. <http://dx.doi.org/10.1190/1.1441733>.
- Pridmore, D. F., G. W. Hohmann, S. H. Ward, and W.R. Still, 1981, An investigation of finite-element modeling for electrical and electromagnetic data in three dimensions: *Geophysics*, **46**, 1009–1024. <http://dx.doi.org/10.1190/1.1441239>.
- Puzyrev, V., J. Koldan, J. de la Puente, G. Houzeaux, M. Vázquez, and J. M. Cela, 2013, A parallel finite-element method for three-dimensional controlled

- source electromagnetic forward modelling: *Geophysical Journal International*, **193**, 678–693, doi: 10.1093/gji/ggt027.
- Raiche, A., 1974, An integral equation approach to three-dimensional modeling: *Geophysics Journal J. R. Astron. Soc.*, **36**, 363–376.
- Rutherford, S. R., and R. H. Williams, 1989, Amplitude-versus-offset variations in gas sands: *Geophysics*, **54**(6), 680-688.
- Saad, Y., 1990, Sparskit: A basic tool kit for sparse matrix calculations, report RIACS-90-20: Research institute for advanced computer science, NASA, AMES Research Center.
- Schwarzbach, C., R. U. Börner, and K. Spitzer, 2011, Three-dimensional adaptive higher order finite element simulation for geo-electromagnetics —A marine CSEM example: *Geophysical Journal International*, **187**, 63–74, doi: 10.1111/j.1365-246X.2011.05127.x.
- Shewchuk, J.R., 1996, Triangle: Engineering a 2D quality mesh generator and Delaunay triangulator, *in* M.C. Lin and D. Manocha, eds., *Applied computational geometry: towards geometric engineering: Volume 1148, Lecture notes in computer science*: Springer-Verlag, 203-222.
- Si, H., 2007, TetGen: A quality tetrahedral mesh generator and three-dimensional delaunay triangulator, <http://wias-berlin.de/software/tetgen/>.
- Spiess, F. N., K. C. Macdonald, T. Atwater, R. Ballard, A. Carranza, D. Cordoba, C. Cox, V. M. Diaz Garcia, J. Francheteau, J. Guerrero, J.Hawkings, R. Haymon, R. Hessler, T. Juteau, M. Kastner, R. Larson, B. Luyendyk, J. D. Macdougall, S. Miller, W. Normark, J. Orcutt, and C. Rangin, 1980, East Pacific Rise: Hot springs and geophysical experiments: *Science*, **207**, 1421–1433.

- Stratton, J. A., 1941, *Electromagnetic Theory*: MacGraw-Hill.
- Streich, R., 2009, 3D finite-difference frequency-domain modeling of controlled-source electromagnetic data: direct solution and optimization for high accuracy: *Geophysics*, **74**, no.5, F95–F105, <http://dx.doi.org/10.1190/1.3196241>.
- Sugeng, F., 1998, Modelling the 3D TDEM responses using the 3D full-domain finite-element method based on the hexahedral edge-element technique: *Exploration Geophysics*, **29**, 615–619.
- Ting, S. C., and G. W. Hohmann, 1981, Integral equation modeling of three-dimensional magnetotelluric response: *Geophysics*, **46**, 182–197. <http://dx.doi.org/10.1190/1.1441188>.
- Um, E. S., and D. L. Alumbaugh, 2007, On the physics of the marine controlled-source electromagnetic method: *Geophysics*, **72**, no. 2, WA13–WA26, doi: 10.1190/1.2432482.
- Um, E. S., M. Commer, and G. A. Newman, 2013, Efficient pre-conditioned iterative solution strategies for the electromagnetic diffusion in the earth: Finite-element frequency-domain approach: *Geophysical Journal International*, **193**, 1460–1473, doi: 10.1093/gji/ggt071.
- Um, E. S., J. M. Harris, and D. L. Alumbaugh, 2010, 3D time-domain simulation of electromagnetic diffusion phenomena: A finite-element electric-field approach: *Geophysics*, **75**, no. 4, F115–F126, doi: 10.1190/1.3473694.
- Vieira da Silva, N. V., J. V. Morgan, L. MacGregor, and M. Warner, 2012, A finite element multifrontal method for 3D CSEM modeling in the frequency domain: *Geophysics*, **77**, no. 2, E101–E115, <http://dx.doi.org/10.1190/geo2010-0398.1>.

- Wang, T., and G. W. Hohmann, 1993, A finite-difference time-domain solution for three-dimensional electromagnetic modeling: *Geophysics*, **58**, no. 6, 797–809, <http://dx.doi.org/10.1190/1.1443465>.
- Wannamaker, P.E., 1991, Advances in 3D magnetotelluric modeling using integral equations: *Geophysics*, **56**, no. 11, 1716–1728. <http://dx.doi.org/10.1190/1.1442984>.
- Wannamaker, P. E., G. W. Hohmann, and W. A. SanFilipo, 1984, Electromagnetic modeling of three-dimensional bodies in layered earths using integral equations: *Geophysics*, **49**, no. 1, 60–74. <http://dx.doi.org/10.1190/1.1441562>.
- Ward, S. H., and G. W. Hohmann, 1988, Electromagnetic theory for geophysical applications, *in* M. N. Nabighian, ed., *Electromagnetic methods in applied geophysics: Volume 1, Theory*: SEG, 130–311.
- Weaver, J. T., 1994, *Mathematical methods for geo-electromagnetic induction*: John Wiley & Sons Inc.
- Weaver, J. T., A. K. Agarwal, and X. H. Pu, 1999, Three-Dimensional Finite-Difference Modeling of the Magnetic Field in Geo-Electromagnetic Induction, in M. J. Oristaglio and B. R. Spies (eds.): *Three Dimensional Electromagnetics*, S.E.G. Geophysical Developments Series 7, pp. 426–443.
- Weiss, C. J., and G. A. Newman, 2002, Electromagnetic induction in a fully 3D anisotropic earth: *Geophysics*, **67**, no. 4, 1104–1114, <http://dx.doi.org/10.1190/1.1500371>.
- Weiss, C. J., and S. Constable, 2006, Mapping thin resistors and hydrocarbons with marine EM methods, Part II – Modeling and analysis in 3D: *Geophysics*, **71**(6), G321–G332, doi: 10.1190/1.2356908.

- Wright, D., A. Ziolkowski, and B. Hobbs, 2002, Hydrocarbon detection and monitoring with a multi-component transient electromagnetic (MTEM) survey: The Leading Edge, **21**, 852–864. <http://dx.doi.org/10.1190/1.1508954>.
- Wu, X., A. Ghazi, J. Rasmussen, B. Spindler, I. Atkinson, and D. E. Cameron, 2015, EM survey in the Flemish Pass Basin, East Canada: GeoConvention 2015, CSPG Abstract, 1-6.
- Yee, K. S., 1966, Numerical solution of initial boundary value problems involving maxwell`s equations in isotropic media: IEEE Transactions on Antennas and Propagation, **14**, 302–307, doi: 10.1109/TAP.1966.1138693.
- Young, P. D., and C. S. Cox, 1981, Electromagnetic active source sounding near the East Pacific Rise: Geophysical Research Letters, **8**, 1043–1046.
- Zhang, Y., and K. Key, 2016, MARE3DEM: A three-dimensional EM inversion based on a parallel adaptive finite element method using unstructured meshes: 86th Annual International Meeting, SEG, Expanded Abstracts, doi: 10.1190/segam2016-13681445.1.
- Zhdanov, M.S., Varentsov, I.M., Weaver, J.T., Golubev, N.G., Krylov, V.A., 1997. Methods for modelling electromagnetic fields: results from COMMEMI—the international project on the comparison of modelling methods for electromagnetic induction: Journal of Applied Geophysics, **37**, 133–271.

# Appendix A

## Triangle

The descriptions are taken directly from the Triangle manual from the website:

<http://www.cs.cmu.edu/~quake/triangle.html>

```
triangle [-prq__a__uAcDjevngBPNEIOXzo_YS__iFlsCQVh] input_file
```

- p Triangulates a Planar Straight Line Graph (.poly file).
- r Refines a previously generated mesh.
- q Quality mesh generation with no angles smaller than 20 degrees. An alternate minimum angle may be specified after the `q'.
- a Imposes a maximum triangle area constraint. A fixed area constraint (that applies to every triangle) may be specified after the `a', or varying area constraints may be read from a .poly file or .area file.
- u Imposes a user-defined constraint on triangle size.
- A Assigns a regional attribute to each triangle that identifies what segment-bounded region it belongs to.
- c Encloses the convex hull with segments.
- D Conforming Delaunay: use this switch if you want all triangles in the mesh to be Delaunay, and not just constrained Delaunay; or if you want to ensure that all Voronoi vertices lie within the triangulation.
- j Jettisons vertices that are not part of the final triangulation from the output .node file (including duplicate input vertices and vertices ``eaten'' by holes).
- e Outputs (to an .edge file) a list of edges of the triangulation.
- v Outputs the Voronoi diagram associated with the triangulation. Does not attempt to detect degeneracies, so some Voronoi vertices may be duplicated.
- n Outputs (to a .neigh file) a list of triangles neighboring each triangle.
- g Outputs the mesh to an Object File Format (.off) file, suitable for viewing with the Geometry Center's Geomview package.

- B Suppresses boundary markers in the output .node, .poly, and .edge output files.
- P Suppresses the output .poly file. Saves disk space, but you lose the ability to maintain constraining segments on later refinements of the mesh.
- N Suppresses the output .node file.
- E Suppresses the output .ele file.
- I Suppresses mesh iteration numbers.
- O Suppresses holes: ignores the holes in the .poly file.
- X Suppresses exact arithmetic.
- z Numbers all items starting from zero (rather than one). Note that this switch is normally overridden by the value used to number the first vertex of the input .node or .poly file. However, this switch is useful when calling Triangle from another program.
- o2 Generates second-order subparametric elements with six nodes each.
- Y Prohibits the insertion of Steiner points on the mesh boundary. If specified twice (-YY), it prohibits the insertion of Steiner points on any segment, including internal segments.
- S Specifies the maximum number of added Steiner points.
- i Uses the incremental algorithm for Delaunay triangulation, rather than the divide-and-conquer algorithm.
- F Uses Steven Fortune's sweepline algorithm for Delaunay triangulation, rather than the divide-and-conquer algorithm.
- l Uses only vertical cuts in the divide-and-conquer algorithm. By default, Triangle uses alternating vertical and horizontal cuts, which usually improve the speed except with vertex sets that are small or short and wide. This switch is primarily of theoretical interest.
- s Specifies that segments should be forced into the triangulation by recursively splitting them at their midpoints, rather than by generating a constrained Delaunay triangulation. Segment splitting is true to Ruppert's original algorithm, but can create needlessly small triangles. This switch is primarily of theoretical interest.
- C Check the consistency of the final mesh. Uses exact arithmetic for checking, even if the -X switch is used. Useful if you suspect Triangle is buggy.
- Q Quiet: Suppresses all explanation of what Triangle is doing, unless an error occurs.

- V Verbose: Gives detailed information about what Triangle is doing. Add more `V's for increasing amount of detail. `-V' gives information on algorithmic progress and detailed statistics.
- h Help: Displays complete instructions.

# Appendix B

## TetGen

Most of the descriptions are taken directly from the TetGen manual via:

<http://wias-berlin.de/software/tetgen/>

```
tetgen [-pYrq_Aa_miO_S_T_XMwcdzfenvgkJBNEFICQVh] input_file
```

### Common switches used

- p Tetrahedralizes a piecewise linear complex (PLC).
- q Adds new points to improve the mesh quality. TetGen enforces two quality constraints on tetrahedra: a maximum radius-edge ratio bound and a minimum dihedral angle bound. By default, these two constraints are 2:0 and 0 degrees, respectively. -q1.2/10 species a maximum radius-edge ratio of 1.2 and a minimum dihedral angle of 10 degrees.
- A Assigns attributes to tetrahedra in different regions.
- m Applies a user-defined mesh sizing function which species the desired edge lengths in the final mesh. It aims to create an adaptive mesh whose edge lengths are conforming to this function. TetGen reads a .mtr file, which stores the nodal mesh element size, i.e., the desired edge length at the location of the node in the mesh domain.
- f Outputs all faces to .face file.
- e Outputs all edges to .edge file.
- n Outputs tetrahedra neighbors to .neigh file.
- C Checks the consistency of the final mesh.
- V Verbose: Detailed information, more terminal output

### Remaining switches

- Y Preserves the input surface mesh (does not modify it).
- r Reconstructs a previously generated mesh.
- R Mesh coarsening (to reduce the mesh elements).

- a Applies a maximum tetrahedron volume constraint.
- I Inserts a list of additional points.
- O Specifies the level of mesh optimization.
- S Specifies maximum number of added points.
- T Sets a tolerance for coplanar test (default 10<sup>-8</sup>).
- X Suppresses use of exact arithmetic.
- M No merge of coplanar facets or very close vertices.
- w Generates weighted Delaunay (regular) triangulation.
- c Retains the convex hull of the PLC.
- d Detects self-intersections of facets of the PLC.
- z Numbers all output items starting from zero.
- v Outputs Voronoi diagram to files.
- g Outputs mesh to .mesh file for viewing by Medit.
- k Outputs mesh to .vtk file for viewing by Paraview.
- J No jettison of unused vertices from output .node file.
- B Suppresses output of boundary information.
- N Suppresses output of .node file.
- E Suppresses output of .ele file.
- F Suppresses output of .face and .edge file.
- I Suppresses mesh iteration numbers.
- Q Quiet: No terminal output except errors.

# Appendix C

## Refinement at Observation Locations

This MATLAB scrip reads a .node file containing the XYZ points representing the observation locations and generates four nodes to enclose each observation location in a tetrahedron of length a. The script outputs the refinement nodes to a file.

```
%% OPENING .NODE FILE

C = textread(observation_locations.node');
x = C(:,2);
y = C(:,3);
z = C(:,4);

%% Initialization of required parameters

n = length(x);
a = 5.0; % Desired edge length of tetrahedra

%% Creating the Nodes for Refinement Tetrahedra Surrounding the OBS
Locations

fileID1 = fopen(output_refinement_nodes.node','w');
num_of_nodes_1 = 4*n;
fprintf(fileID1,'%d %d %d %d\n',[(num_of_nodes_1), 3, 0, 0]);
fclose(fileID1); % This establishes the header of the output file

fid_nodes = fopen(output_refinement_nodes.node','a');
for i = 1:1:n
    % This is done on a 'per-cell' basis
    fprintf(fid_nodes,'%d\t %.6f\t %.6f\t %.6f\n',[1 + 4*(i-1), x(i),
        y(i) + (sqrt(3)/3)*a, z(i) - (sqrt(6)/6)*a]);
    fprintf(fid_nodes,'%d\t %.6f\t %.6f\t %.6f\n',[2 + 4*(i-1), x(i) +
        0.5*a, y(i) - (sqrt(3)/6)*a, z(i) - (sqrt(6)/6)*a]);
    fprintf(fid_nodes,'%d\t %.6f\t %.6f\t %.6f\n',[3 + 4*(i-1), x(i) -
        0.5*a, y(i) - (sqrt(3)/6)*a, z(i) - (sqrt(6)/6)*a]);
    fprintf(fid_nodes,'%d\t %.6f\t %.6f\t %.6f\n',[4 + 4*(i-1), x(i),
        y(i), z(i) + (sqrt(6)/3)*a - (sqrt(6)/6)*a]);
end
fclose(fid_nodes);
```

# Appendix D

## Results of Mizzen Study

All the remaining simulations from receivers and frequencies not shown in Chapter 5 are given here. The convergence curves are not given for any of these results because they all exhibited similar convergence trends to those shown in Figure 5.49. All the results are given in this order:

RX42

- 0.25 Hz
- 0.50 Hz
- 1.00 Hz

RX43

- 0.25 Hz
- 0.50 Hz
- 1.00 Hz

RX44

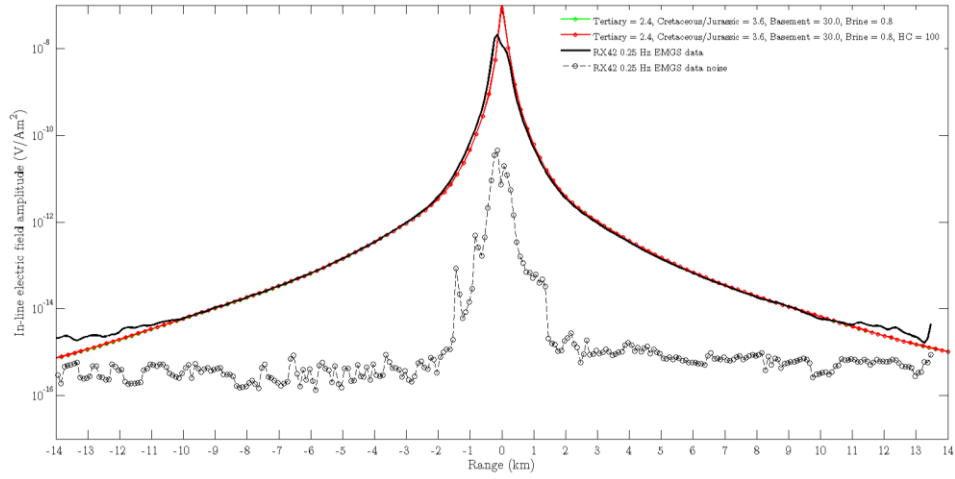
- 0.25 Hz
- 1.00 Hz

RX45

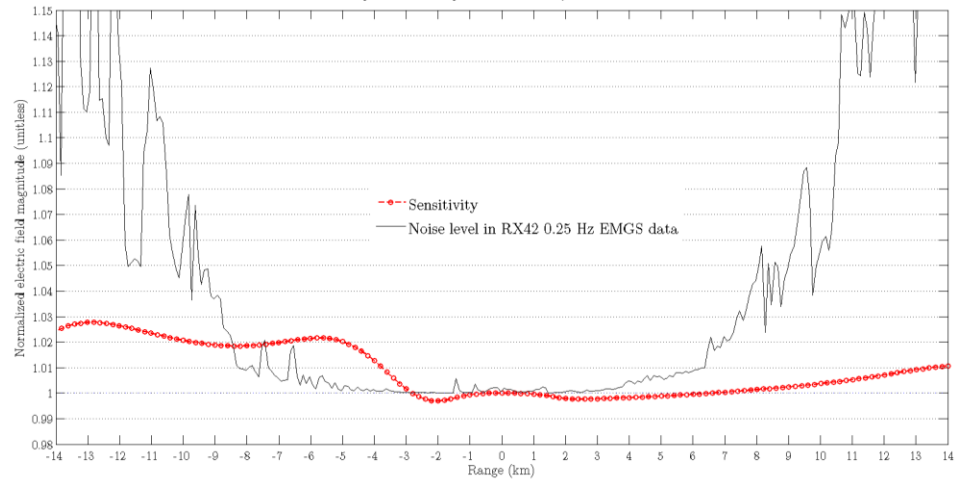
- 0.25 Hz
- 0.50 Hz
- 1.00 Hz

# RX42

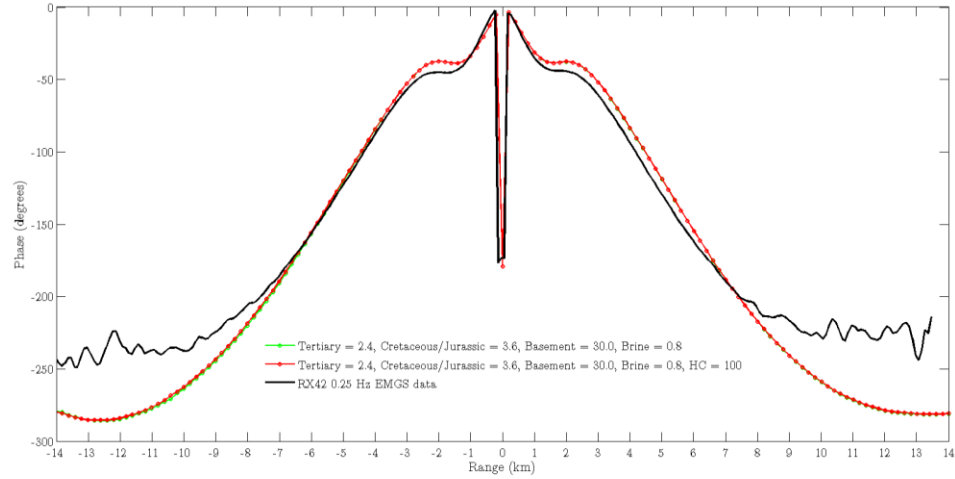
Forward model vs. measured EMGS in-line electric field amplitudes for  $f = 0.25$  Hz at RX42

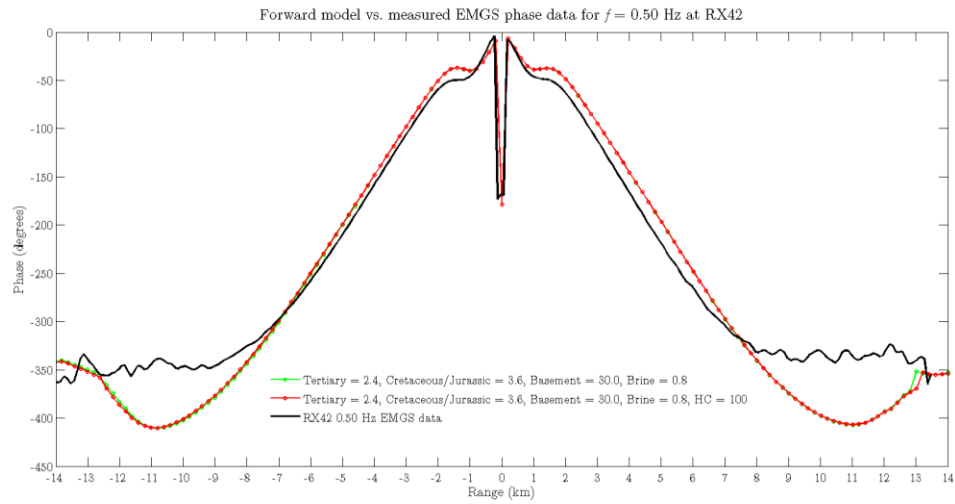
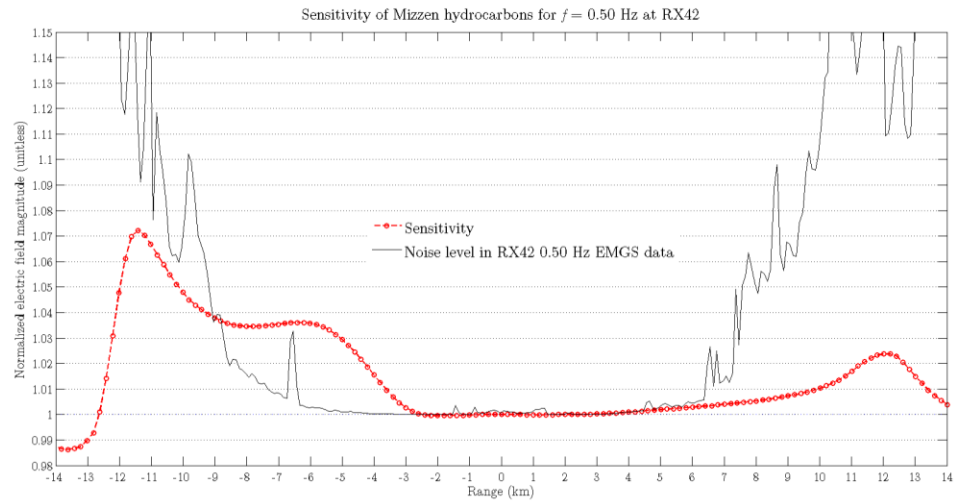
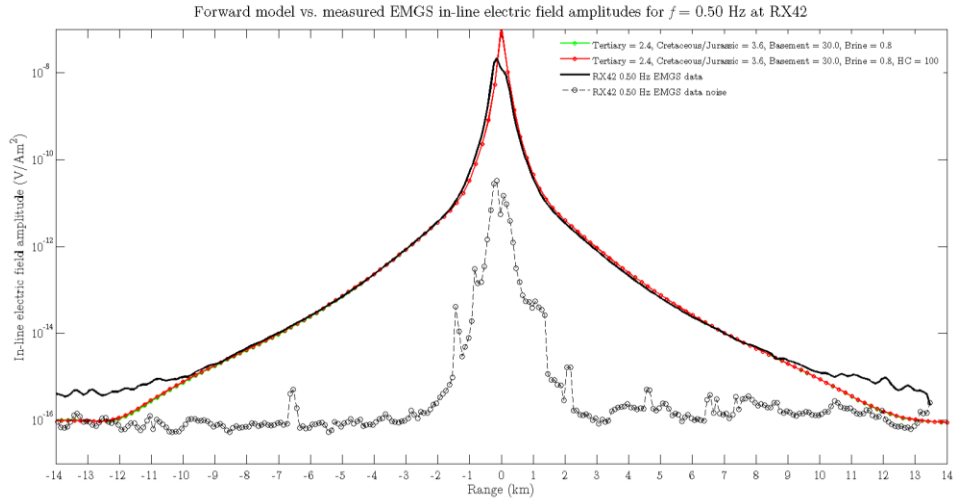


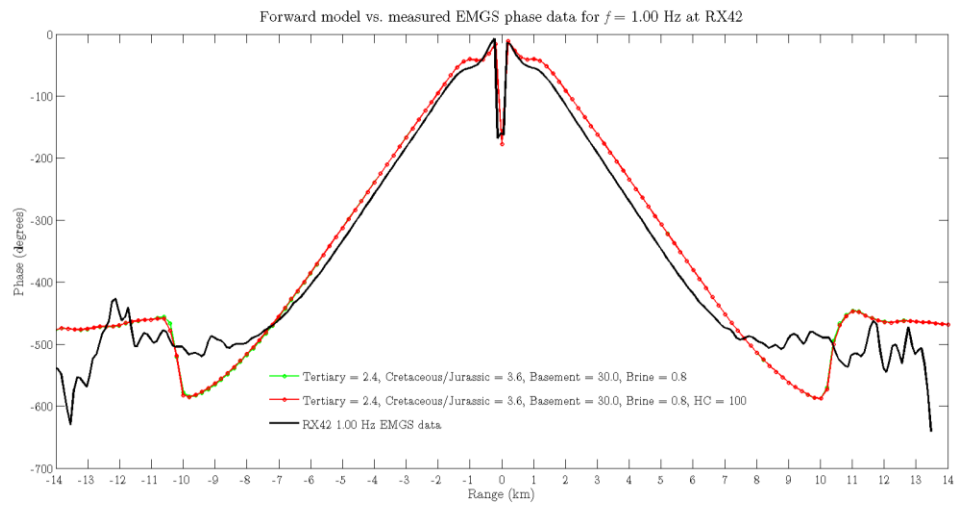
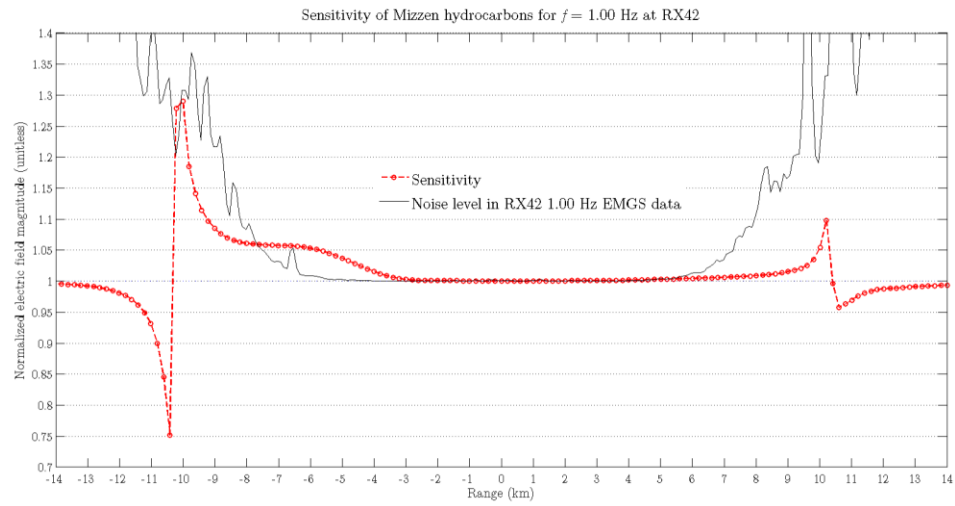
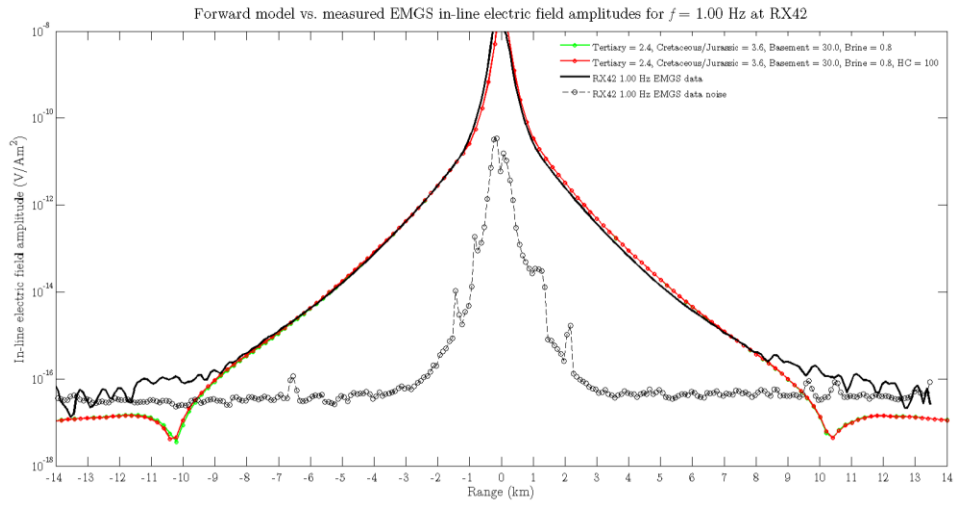
Sensitivity of Mizzen hydrocarbons for  $f = 0.25$  Hz at RX42



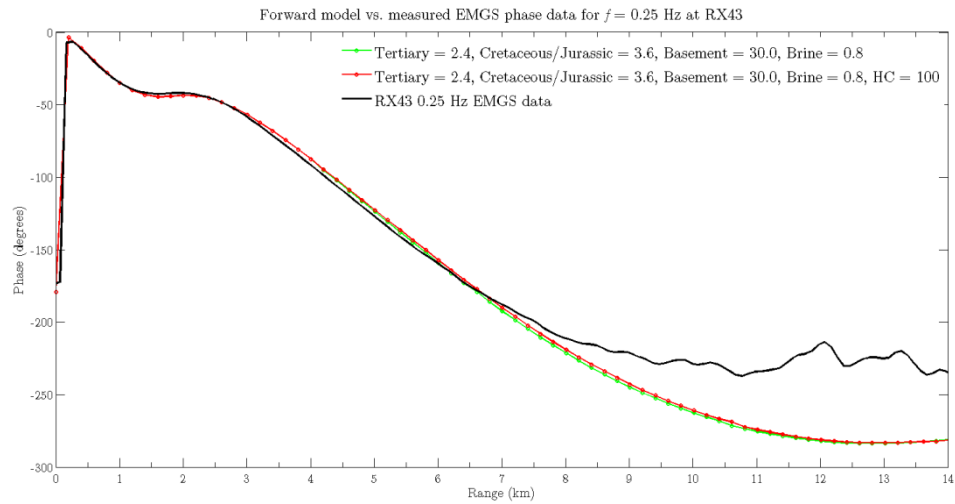
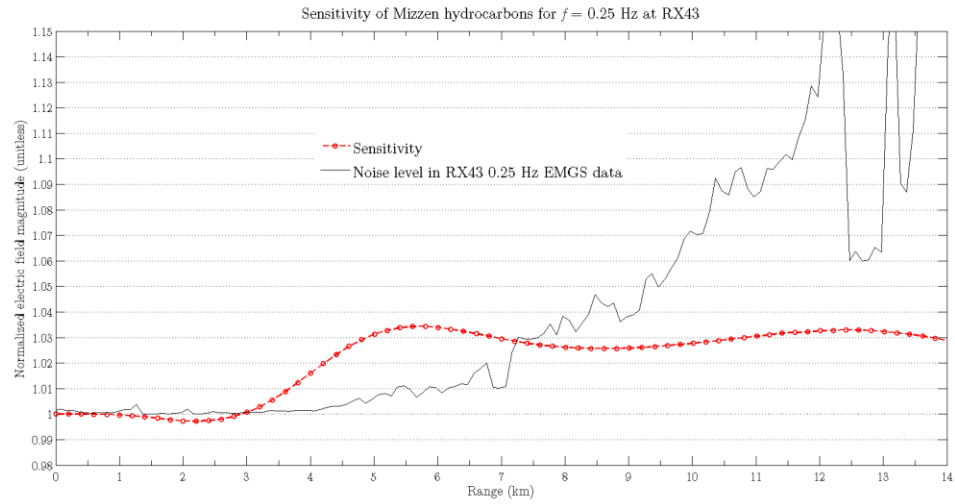
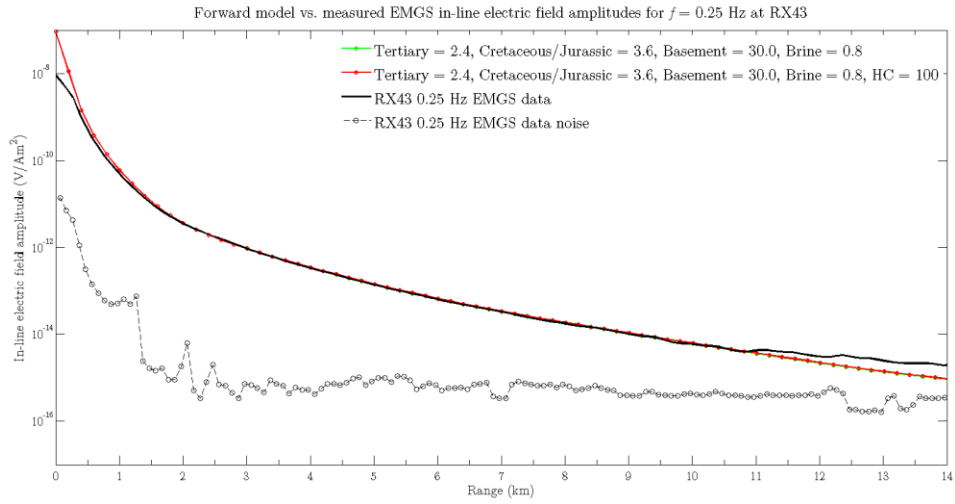
Forward model vs. measured EMGS phase data for  $f = 0.25$  Hz at RX42

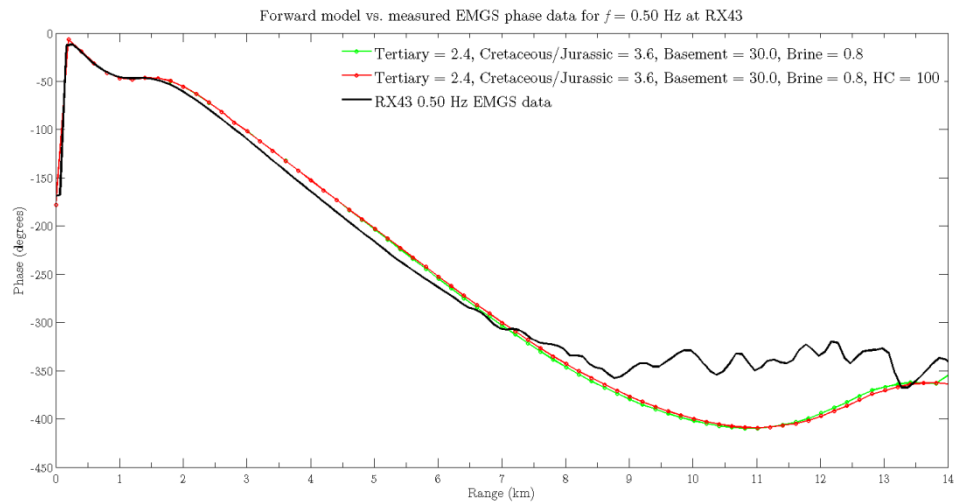
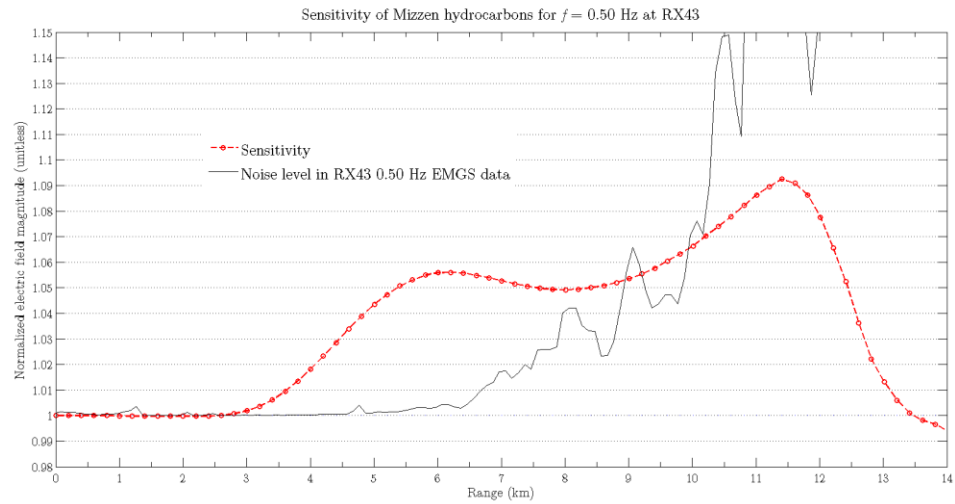
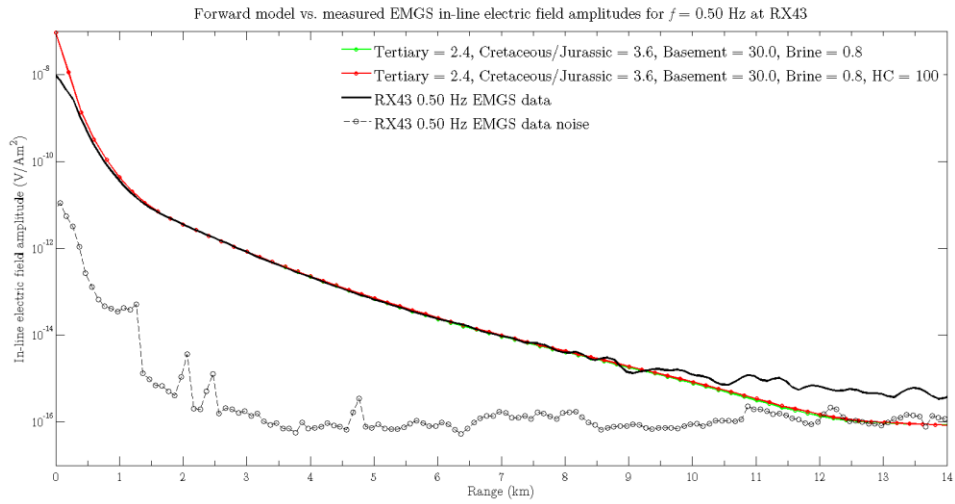


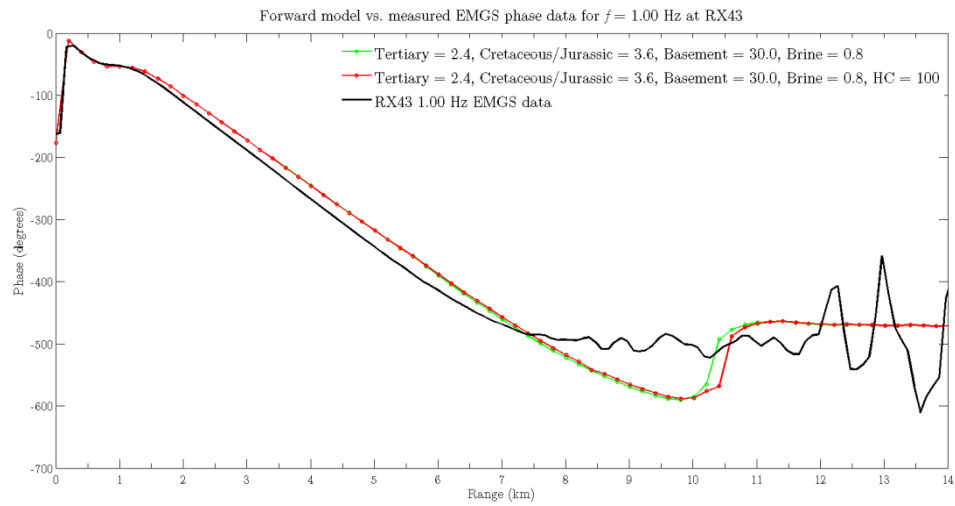
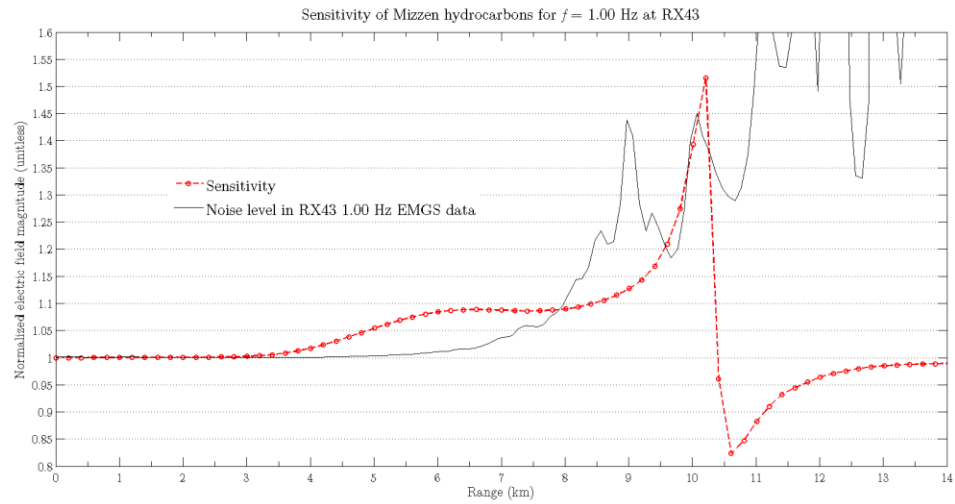
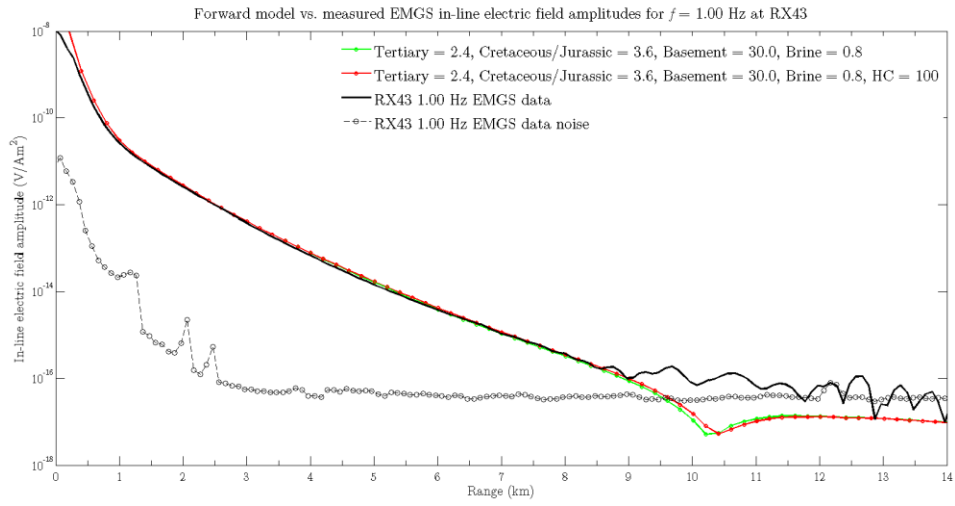




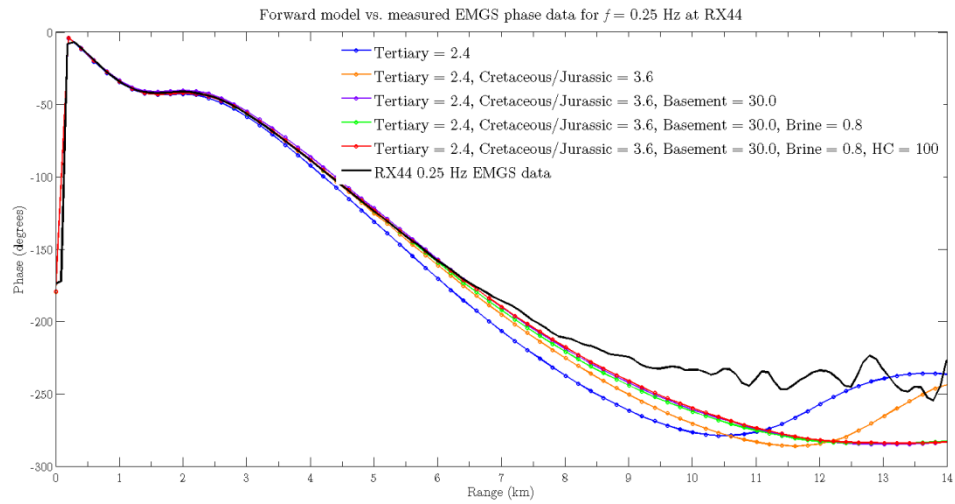
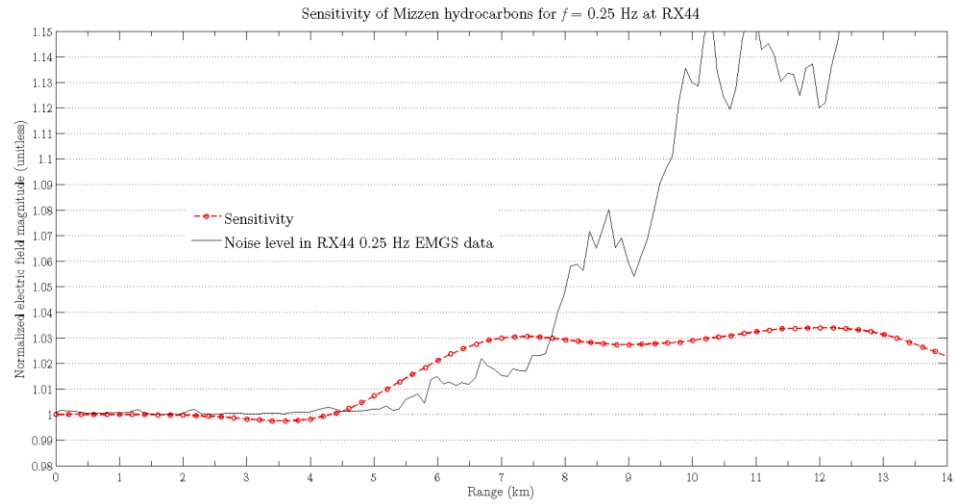
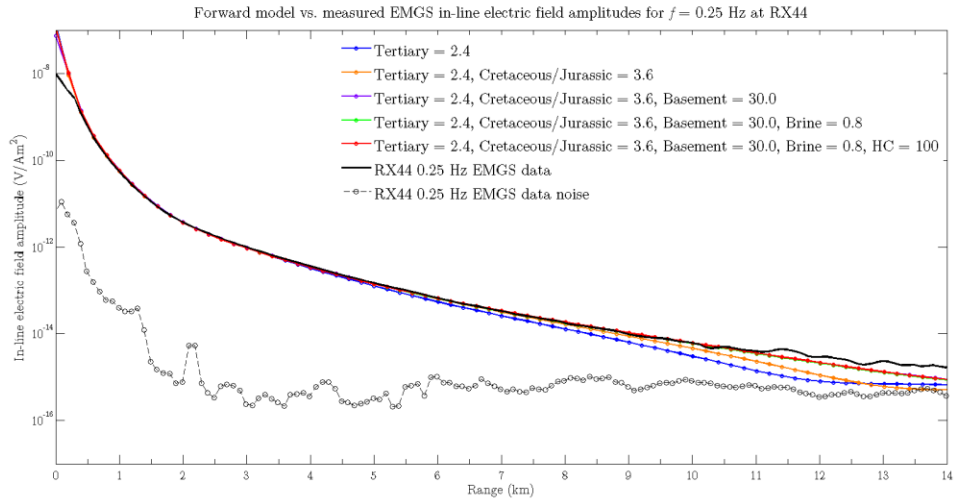
# RX43

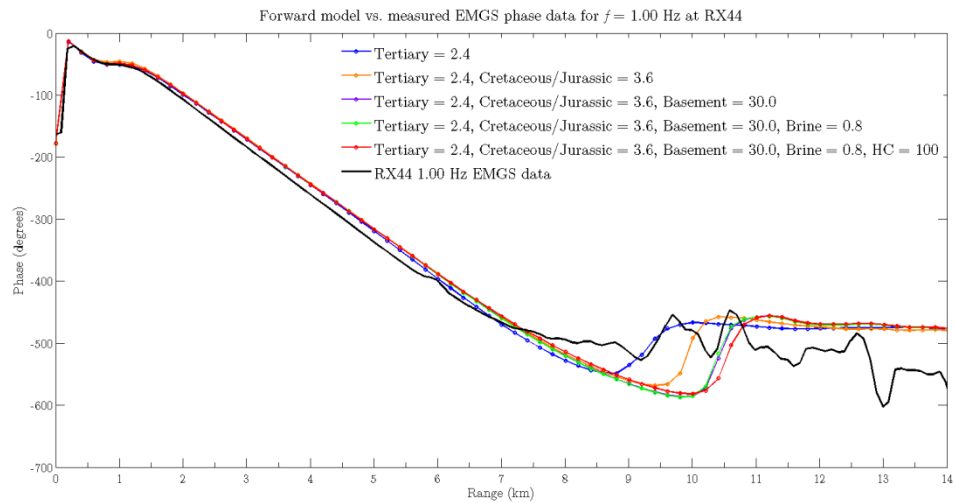
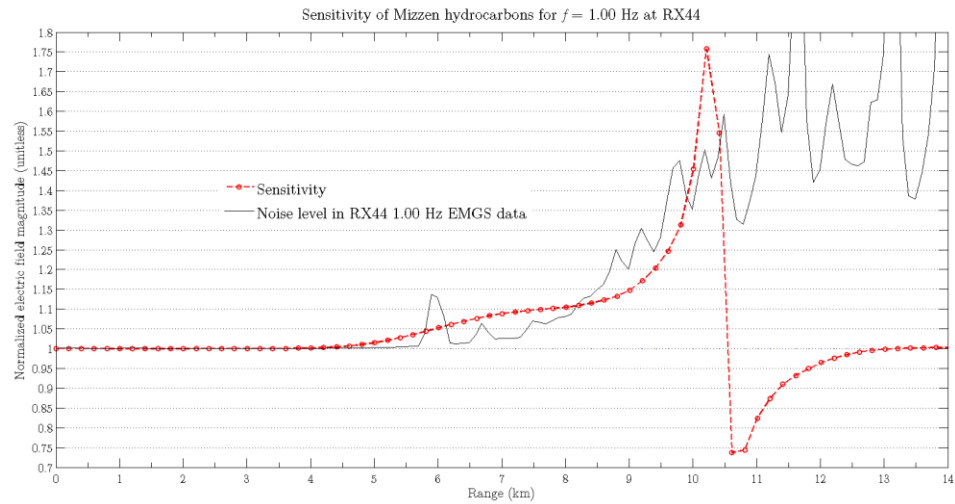
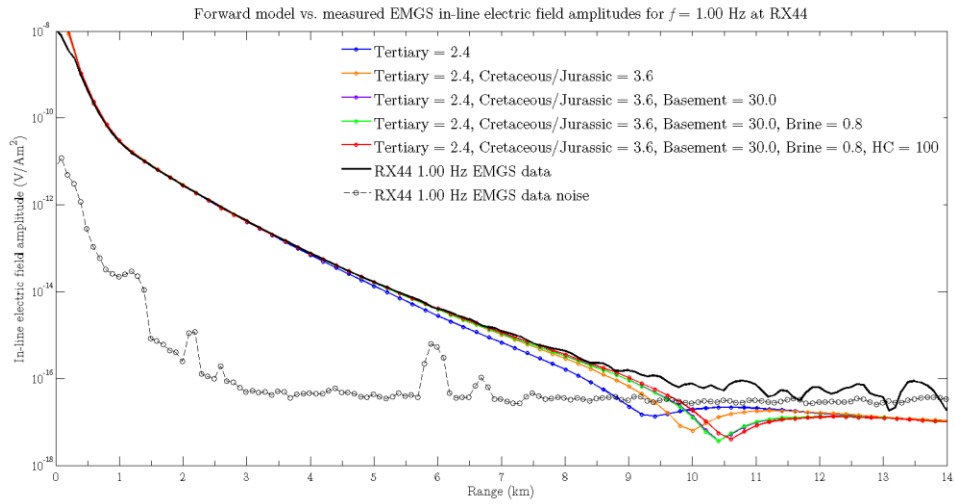






# RX44





# RX45

